DISSERTATION

# Salt-induced corrosion phenomena in physical vapor deposited nitride-based coatings

carried out for the purpose of obtaining the degree of Doctor technicae (Dr. techn.),
submitted at TU Wien, Faculty of Mechanical and Industrial Engineering,

by

**Oliver Ernst Hudak**

[redacted]

under the supervision of

Ass. Prof. Dipl.-Ing. Dr.techn. Helmut Riedl-Tragenreif

Institute of Materials Science and Technology - E308-01-2
Applied Surface and Coating Technology

Wien, December 2023

reviewed by

**Ao.Univ.-Prof. Dipl.-Ing.**
**Dr.techn. Paul Linhardt**
Institute of Chemical Technologies
and Analytics-E164-03-1
TU Wien
1060 Vienna, Austria

**Ao.Univ.-Prof. Dipl.-Ing.**
**Dr.mont. Gregor Mori**
General Analytical Chemistry
Montanuniversität Leoben
8700 Leoben, Austria

”*For you were made from dust, and to dust you will return.*”

– Genesis

The financial support by the Austrian Federal Ministry for Digital and Economic Affairs, the National Foundation for Research, Technology and Development and the Christian Doppler Research Association is gratefully acknowledged (Christian Doppler Laboratory “Surface Engineering of high-performance Components”). We also thank for the financial support of Plansee SE, Plansee Composite Materials GmbH, and Oerlikon Balzers, Oerlikon Surface Solutions AG.

*Affidavit:*

I declare in lieu of oath, that I wrote this thesis and performed the associated research myself, using only literature cited in this volume. If text passages from sources are used literally, they are marked as such. I confirm that this work is original and has not been submitted elsewhere for any examination, nor is it currently under consideration for a thesis elsewhere. I acknowledge that the submitted work will be checked electronically-technically using suitable and state-of-the-art means (plagiarism detection software). On the one hand, this ensures that the submitted work was prepared according to the high-quality standards within the applicable rules to ensure good scientific practice ”Code of Conduct” at the TU Wien. On the other hand, a comparison with other student theses avoids violations of my personal copyright.

*Date*

*Signature*

# Acknowledgments

My first and foremost gratitude goes to my supervisor **Ass. Prof. Dipl.-Ing. Dr. Helmut Riedl-Tragenreif** for your tireless motivation and support over the past years. Thank you for welcoming me into your research group CDL-SEC and being the person you are. Your expertise in the field of material science and your aspiration for excellence have helped me excel in my work and as a person.

I would also like to voice my gratitude to the **CDL-SEC Team** for always providing me with a jolly and pleasant work environment. **Christoph Fuger**, **Thomas Glechner**, **Ahmed Bahr**, **Sophie Richter**, **Anna Hirle**, **Tomas Wojcik** and **Philip Kutrowatz** — your involvement and support have been utterly valuable to me and for accomplishing my research. I want to extend special regards to my colleagues **Rainer Hahn** and **Lukas Zauner**. There are no words that describe the sweat, effort and sheer enthusiasm that we have shared over the years. Going the extra mile with you has been my privilege.

I would like to express my upmost appreciation to **Edith Asiemo**, **Christian Zaruba**, and **Werner Artner**— you have always gone out of your way to help me when I was in dire need to save 'the world' on fridays. Time was always against us, but in the end, time is what we had together. Thank you.

I would also like to extend my deepest appreciation to the industrial partners **Plansee Composite Materials** and **Oerlikon Balzers**, who have made this research possible. **Dr. Szilard Kolozsvari**, **Dr. Peter Polcik**, **Dr. Jürgen Ramm**, and **Dr. Oliver Hunold**— no coating would have seen the light of day without your support. I value the moments we had at Balzers and Reutte while contemplating about the wonders and secrets the world of coatings holds.

My deepest gratitude goes to all of my **friends in Vienna**, who have lifted my spirit in times of struggle, and have encouraged me in moments of doubt. I am so thankful for all your friendships and for making my time in Vienna so memorable.

Lastly, I would like to express my love and gratefulness to my **Family** to which I dedicate this work. **Heidi**, **Harald**, **Hannah**, **Katharina**, and **Alexander**— thank you so so much for this exciting journey, your endless support and always having my back. I love you.

# Contents

# List of Figures

# List of Symbols & Abbreviations

| | |
|---|---|
| $\boldsymbol{\alpha_0}$ | jump distance |
| $\boldsymbol{\alpha}$ | activity |
| $\boldsymbol{\alpha_a}$ | anodic symmetry factor |
| $\boldsymbol{\alpha_c}$ | cathodic symmetry factor |
| $\boldsymbol{\beta_a}$ | anodic tafel slope |
| $\boldsymbol{\beta_c}$ | cathodic tafel slope |
| $\boldsymbol{\beta_{a,bs}}$ | anodic tafel slope of the bare substrate |
| $\boldsymbol{\Delta G^\circ}$ | change in standard Gibbs free energy |
| $\boldsymbol{\Delta G_f}$ | change in Gibbs free energy of formation |
| $\boldsymbol{\Delta G_{surf.}}$ | surface/interface energy term opposing crystal formation |
| $\boldsymbol{\Delta G}$ | change in Gibbs free energy |
| $\boldsymbol{\Delta H^\circ}$ | change in standard enthalpy |
| $\boldsymbol{\Delta S^\circ}$ | change in standard etropy |
| $\boldsymbol{\eta}$ | overpotential |
| $\boldsymbol{\gamma}$ | unfavourable energy contribution related to the cluster surface |
| $\boldsymbol{\omega}$ | vibrational frequency |
| $\boldsymbol{\phi_1}$ | inner Helmholz plane |
| $\boldsymbol{\phi_2}$ | outer Helmholz plane |
| $\boldsymbol{\Phi}$ | concentration |
| $\boldsymbol{\rho}$ | pressure |

| | |
|---|---|
| $C$ | constant |
| $D_0$ | diffusion constant |
| $D$ | diffusion coefficient or diffusivity |
| $E_{\mathrm{pit}}$ | pitting potentials or breakthrough potential |
| $E^\circ$ | standard electode potential |
| $E_{corr}$ | corrosion potential |
| $E_{mp}$ | mixed electrode potential |
| $E$ | nonstandard electode potential |
| $F$ | Faraday constant |
| $H^\circ$ | enthalpy under standard conditions |
| $i_0$ | exchange current density |
| $i_a$ | anodic current |
| $i_{corr}$ | corrosion current |
| $i_c$ | cathodic current |
| $i$ | measured current density |
| $j_0$ | exchange current density |
| $J$ | molar flux |
| $j$ | electrode current density |
| $k_l$ | linear diffusion rate constant |
| $k_p$ | parabolic diffusion rate constant |
| $k_{log}$ | logarithmic diffusion rate constant |
| $K$ | absolute temperature |
| $m_i$ | mass of particle i produced |
| $M$ | molecular weight |
| $n, z$ | number of electrons transferred |

| | |
|---|---|
| $\boldsymbol{n_i}$ | particle number |
| $\boldsymbol{P}$ | open porosity |
| $\boldsymbol{Q_d}$ | activation energy |
| $\boldsymbol{Q_f}$ | energy of formation |
| $\boldsymbol{Q_m}$ | energy of migration |
| $\boldsymbol{Q}$ | total electric charge |
| $\boldsymbol{Q}$ | reaction quotient |
| $\boldsymbol{r_f}$ | forward reaction |
| $\boldsymbol{R_p}$ | polarization resistance |
| $\boldsymbol{r_r}$ | return reaction |
| $\boldsymbol{R_{p,bs}}$ | polarization resistance of the bare substrate |
| $\boldsymbol{R_{p,c}}$ | polarization resistance of the coating |
| $\boldsymbol{r}$ | radius of the adatom cluster |
| $\boldsymbol{R}$ | universal gas constant |
| $\boldsymbol{S^\circ}$ | entropy under standard conditions |
| $\boldsymbol{t}$ | elapsed time |
| $\boldsymbol{T}$ | temperature |
| $\boldsymbol{x}$ | oxide film thickness or mass gain due to oxidation |
| $\boldsymbol{x}$ | position of the solute or distance from its origin |
| **APT** | atome probe tomography |
| **CAE** | cathodic arc evaporation |
| **CE** | counter electrode |
| **CPDP** | cyclic potentiodynamic polarization |
| **DCMS** | direct current magnetron sputtering |
| **Flux** | quantifiable net drift of particles |

| | |
|---|---|
| **HC** | hot corrosion |
| **HPT** | high-pressure turbine |
| **HTHC** | high-temperature hot corrosion |
| **LPP** | linear potentiodynamic polarization |
| **LPT** | low-pressure turbine |
| **LSV** | linear sweep voltametry |
| **LTHC** | low-temperature hot corrosion |
| **MeO** | metal oxide |
| **MFC** | mass flow controler |
| **PVD** | physical vapor deposition |
| **RE** | reference electrode |
| **SHE** | standard electrode potential |
| **SIMS** | secondary ion mass spectroscopy |
| **SSC** | silver-silver chloride electrode |
| **t-EBSD** | transmission electron backscatter diffraction |
| **TEM** | transmission electron microscopy |
| **TMN** | transition metal nitride |
| **ToF** | time of flight |
| **TPB** | Tammann Pilling Bedworth parabolic law |
| **WE** | working electrode |

# Abstract

The impact of corrosion phenomena is significant across a wide range of modern technological fields. To address this challenge, protective physical vapor deposited (PVD) coatings and surface modifications present new opportunities for enhancing material properties and extending the operational lifespan of machining components. However, a lacking understanding of corrosion processes within PVD coatings has led to a limited availability of high-performance corrosion resistant thin films in industrial settings. Particularly salt-rich environments represent regimes, where PVD coated machining elements continue to suffer accelerated breakdown. Factors contributing to this issue include inherent coating defects, porosity, the presence of embedded macroparticles, and the overall columnar growth orientation, which make PVD coatings especially vulnerable to the infiltration of corrosive substances.

The first part of this thesis provides a systematic approach on highlighting preferred diffusion pathways of $Cl^-$-rich aqueous media in $Al_{0.7}Cr_{0.3}N$ PVD thin films. Intended as a model system, the study was designed to discern differences in the passive behavior between cathodic arc evaporated (CAE) and direct current magnetron sputtered (DCMS) $Al_{0.7}Cr_{0.3}N$ coatings. Through use of a three-electrode electrochemical setup in conjunction with an array of high-resolution analytical techniques (e.g., transmission electron microscopy (TEM), time-of-flight secondary ion mass spectrometry (ToF-SIMS), atom probe tomography (APT), and transmission electron backscatter diffraction (t-EBSD)), the study presents a meticulous breakdown of the most prevalent diffusion pathways taken by chemically active species. The results emphasize that accelerated infiltration occurs along embedded macroparticles in CAE $Al_{0.7}Cr_{0.3}N$ coatings, whereas preferential diffusion along under dense column boundaries constitute the predominant weak points in DCMS coatings. Subsequent investigations were directed towards assessing the level of coating passivity of pristine and unimpaired coating sites. Notably, ToF-SIMS was employed to collect $Cl^-$ diffusion profiles, which unveiled an intrinsically inferior passive behavior of DCMS coatings in comparison to their CAE counterparts. Thus, a dense coating morphology with a randomized growth orientation and minimal fast-track diffusion routes along embedded macroparticles are viewed as beneficial attributes that corrosion resistant coatings should possess.

Based on these findings, two approaches were chosen to counter the prevailing diffusion routes that were identified earlier and improve the corrosion behavior of the $Al_{0.7}Cr_{0.3}N$ system: (i) a grain-refining doping strategy for imparting complexity to the diffusion routs along grain boundaries using vanadium (V), and (ii) a subsequent annealing treatment for generating a surface-oxide that functions as a sealing layer. It was found that both, grain-refinement of the $Al_{0.7}Cr_{0.3\text{-}x}V_xN$ coatings and the development of a continuous and dense top-oxide were directly related to the amount of doped V. Through extensive electrochemical analysis, using potentiodynamic polarization techniques, it was shown that both, grain-refining effects and the formation of a dense V-rich top oxide layer translated to an improved corrosion behavior of the initial AlCrN base-system.

The second part of the thesis focuses on hot corrosion (HC) phenomena and proposes CAE $Ti_{1\text{-}x}Al_xN$ as a potential candidate for providing corrosion protection in high-temperature settings. $Ti_{1\text{-}x}Al_xN$ coatings with varying metal content ratios were deposited on an industrially established NiCoCr-based superalloy (alloy c-263) and investigated in an in-house built HC testing rig. After applying a $Na_2SO_4$-$MgSO_4$ salt mixture onto both $Ti_{1\text{-}x}Al_xN$ coated and uncoated samples, HC experiments were conducted in a $SO_x$-rich atmosphere under two distinct sets of conditions: low-temperature hot corrosion (LTHC) settings at 700 °C, and high-temperature hot corrosion (HTHC) settings at 850 °C. Here, the primary objective was to extend the understanding of the corrosion mechanisms that govern $Ti_{1\text{-}x}Al_xN$ coatings when investigated under LTHC and HTHC parameters, and to directly compare the corrosion resistance between $Ti_{1\text{-}x}Al_xN$ coated samples and the bare c-263 alloy. Notably, the $Ti_{1\text{-}x}Al_xN$ coatings demonstrated superior resistance to both LTHC and HTHC compared to the bare c-263 alloy.

Regarding the LTHC behavior of $Ti_{1\text{-}x}Al_xN$, a highly accelerated and localized attack was observed. Initiated by a nitride-to-sulphate transformation and formation of a low-melting liquid salt interface, a synergistic fluxing mechanism was found to be the dominant degradation process. Due to the acidic nature of the liquid salt interface under LTHC conditions, the development of a porous $Al_2O_3$-dominated top-oxide was observed, which is known for its enhanced stability under acidic conditions. Underneath, the corrosion scale exhibited a lamellar structure composed of $TiO_2$- and $Al_2O_3$-rich oxide domains below which a more globular scale morphology was featured.

Conversely, under HTHC conditions, a more uniform development of the corrosion scale was noted. Similar to the corrosion behavior observed under LTHC conditions, a sequential fluxing mechanism was found to be the predominant corrosion process, resulting in the formation of a layered corrosion scale. Owing to the higher melt basicity under HTHC, a porous $TiO_2$ scale was primarily formed at the salt-scale interface, followed by a layered corrosion scale of $Al_2O_3$-rich and $TiO_2$-rich domains.

In summary, this thesis emphasizes the importance of developing a fundamental understanding of the governing corrosion mechanisms in thin films, in order to help establish PVD coatings as a viable solution for highly demanding environments.

# Chapter 1

# Introduction

Corrosion is a common phenomenon that is observed in every facet of industrial ingenuity and is a manifestation of the chemical interaction between a material and its respective environment over time. Coming from the Latin word “corrodere”, meaning to gnaw to pieces, the concept of material degradation and/or transformation has been known for a long time. With an ubiquitous presence among materials design and their application, the control over the rate, under which a certain material degrades, is a beneficial tool in areas of chemical, mechanical, electrical, material, and civil engineering.

Particularly under extreme conditions, such as marine settings [1–5] or high-temperature regimes [6–9], accelerated corrosion poses a great challenge. In order to prolong the longevity of materials, the use of protective physical vapor deposited (PVD) coatings remains an attractive approach for material engineers. To extend the lifespan of materials, the use of protective physical vapor deposited (PVD) coatings presents an appealing solution for material engineers, especially when cost-effective bulk materials are unavailable or when bulk materials do not fully meet the desired property profile for a given application.

Such environments are often encountered when salt impurities (e.g., from marine environments, road salts, or combustion byproducts) interact with in-service machining surfaces. Particularly alloys and metals, which depend on their ability to form passivating oxide scales in order to circumvent further oxidation and/or corrosion, are particularly prone to the depassivating nature of salt-induced corrosion mechanisms [10]. For this reason, this study aims to evaluate the effectiveness of PVD transition metal nitride (TMN) coatings as a viable option for corrosion protection in both aqueous and high-temperature settings.

Aqueous corrosion is a prevalent form of corrosion observed in humid and marine environments. It involves an electrochemical process, which can be described using four components: An anode, where dissolution of a material occurs (oxidation half-reaction) with the release of electrons; a cathode, were an oxidation agent ($O_2$ or $H_3O^+$) is reduced through the consumption of electrons (cathodic half-reaction); an electrolyte allowing for the migration of ionic species and for retaining charge neutrality; and an electrically conductive pathway that closes the loop between the anode and cathode [11]. Pitting corrosion represents a particularly insidious form of aqueous corrosion, characterized by chloride-induced localized attack on a passive surface (pit initiation), followed by localized acidification and autocatalytic pit-growth propagation [12–14]. Given that these pits can remain concealed beneath a material's surface for extended periods, pitting is considered exceptionally pernicious. For this reason, the first part of this thesis will aim to simulate this mechanism using a three-electrode cell setup with a potentiostat workstation in order to study the corrosion behavior of $Al_{1-x}Cr_xN$-based coating materials deposited on low-alloyed steel.

Hot corrosion, on the other hand, describes the accelerated degradation of a material surface that occurs within a temperature range of 575-950 °C in the presence of a salt deposit [15, 16]. Many engineering systems operating within these temperatures, such as gas turbines [16–18], waste incinerators [19–21], power plants [22–24], and internal combustion engines [25, 26], frequently experience failures due to hot corrosion. While most metals and alloys undergo oxidation in the presence of oxygen, producing native oxides that act as a protective layer against further bulk-material oxidation [27] the presence of contaminants such as sulfates, chlorides, or vanadates can lead to the formation of low-melting eutectic mixtures. Through degradative fluxing mechanisms, the protective oxide is depassivated or even dissolved, exposing the underlying alloy and allowing for anew oxidative attack [28]. Depending on the aggregate phase of the initial salt-deposit, two distinct types of hot corrosion, high-temperature hot corrosion (HTHC) and low-temperature hot corrosion (LTHC), can be differentiated.

In order to emulate these processes in their most true way, a versatile laboratory scaled hot corrosion rig was designed and built to allow hot corrosion testing. Consisting of a quartz flow-reactor, a three-zone gradient oven, and a gas-mixing system ($SO_2$, $O_2$ and Ar), experiments can be run at various temperatures ranges (<1200 °C) and atmospheric conditions. With focus on well-established industrial materials (Ni- and Co- base super alloys) that readily find application in high-temperature settings [29–32], the objective here is to improve the hot corrosion behavior (HTHC and LTHC) of these materials, through application of protective PVD $Ti_{1-x}Al_xN$ based coatings. Additionally, the study aims to provide a fundamental understanding of the corrosion mechanisms specific to such thin films.

# Chapter 2

# Physical vapor deposition

All coatings throughout this thesis were grown by using PVD techniques. During PVD, a source material (target) is first vaporized and then transported to a desired surface (substrate), where it condenses, nucleates and grows as a thin coating [33, 34]. Depending on the method that is utilized to vaporize the target material, PVD processes can be further categorized. Two of the most common PVD techniques include cathodic arc evaporation (CAE) and direct current magnetron sputtering (DCMS), which are also the two techniques utilized throughout this thesis.

## 2.1 Sputtering

Sputtering involves the bombardment of a target material by energetic species (plasma), in order to generate a vapor. Through a momentum exchange between the plasma particles and the target surface, atoms of the target are physically removed, transported across a vacuum chamber to a substrate, where it condenses and forms the coating [33–35].

First, however, a stable plasma must be generated. In sputtering, a discharge is formed by applying a high voltage between a cathode (target) and anode (vacuum wall). Electrons and ions that are already present within the vacuum chamber (generated by cosmic radiation) are swept out by the electric field and pulled to the respective electrode. When electron emissions between the cathode and anode obtain high enough velocities, ionization of neutral gas atoms occurs. Electron-electron (valence electrons) collisions liberate secondary electrons, which are pulled towards the anode and ionize more gas atoms. This collision cascade is a favorable process and contributes to a stable and efficient plasma (see Fig.2.1). However, electrons may also recombine with ionized species, and by falling into their respective energetic positions, a photon is released that is susceptible to the human eye [35–37].

The probability of ionization is therefore proportional to the mean free path existing between the electron's origin (cathode or ionization event) and its consumption (anode or recombination processes). In order to shorten the mean-free-path, and encourage a more frequent collision

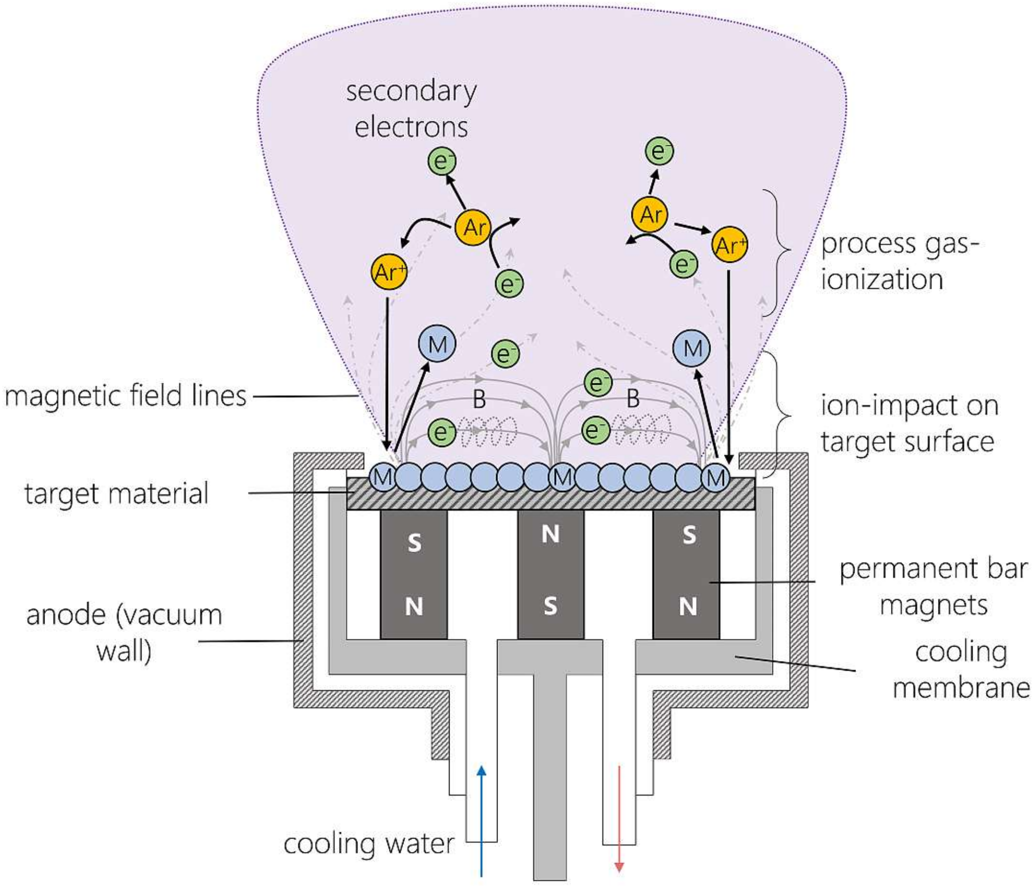

Figure 2.1: Illustration of a magnetron sputter source showing the effect of a guided electron orbit. Adapted from [36].

cascade, an external magnetic field is applied by a magnetron. This has the effect that electrons are no longer guided in a linear fashion from their origin to the anode, but instead are guided along the magnetic field lines and inherit a longer life time–or time of flight (ToF). With a longer ToF, electrons gain a significantly higher probability of ionizing gas atoms and generating a higher plasma density [36–38].

Once a stable plasma is present (consisting of neutrals, electrons and ionized process gas), the ionized species (e.g., $Ar^+$-ions) are accelerated towards the cathode (negative voltage), where they collide and interact with the surface atoms (see Fig.2.2) If the energy from its momentum transfer is high enough, surface atoms are ejected and sputtering is possible. This so-called “threshold energy” of the striking species must be reached in order to overcome the surface binding energy of the target atoms [33–38].

Once the threshold energy is exceeded, sputtering of the target material ensues. The ratio between the sputtered atoms and impinging energetic species is referred to as sputter yield. The more surface atoms are ejected through the bombardment of a striking species, the higher the sputter yield. This, however, is dependent on the final energy of the impinging species

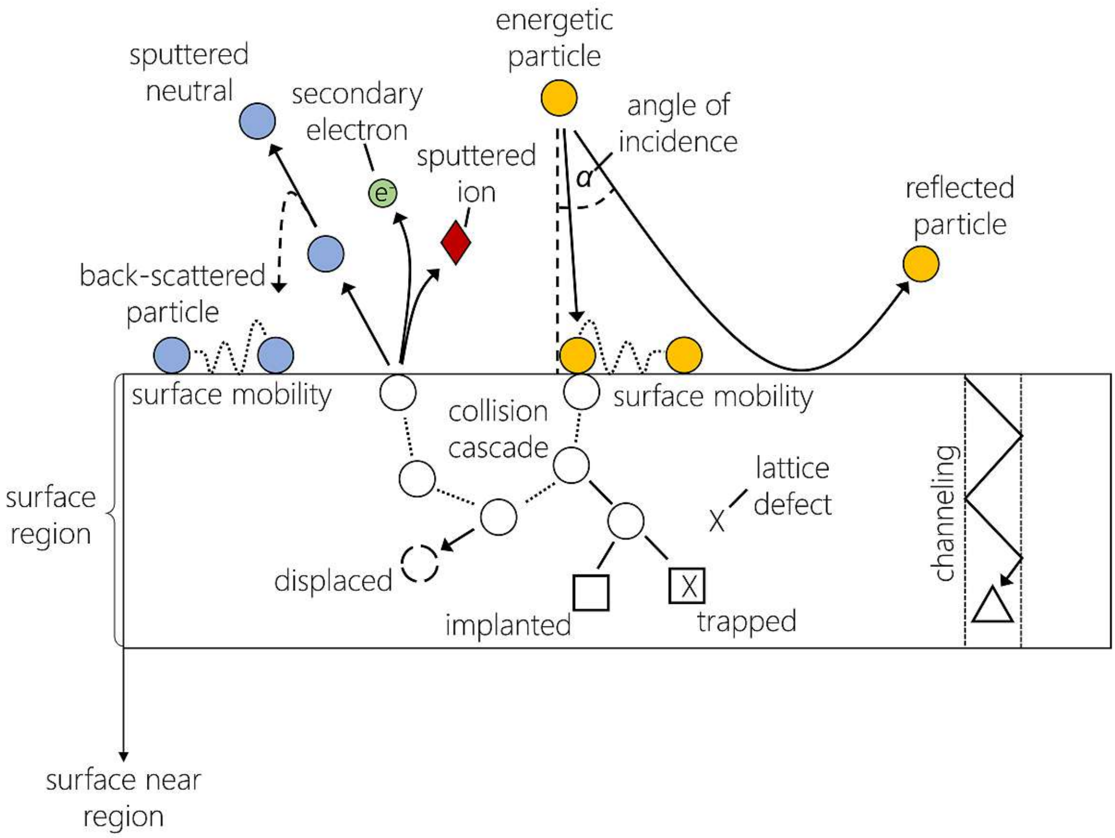

Figure 2.2: Possible collision events that occur during bombardment with energetic atomic-sized particles.

and the angle of incidence. If the energy of the energetic particle is too high, the species becomes implanted into the target lattice and does not participate into a collision cascade of surface near atoms, causing the sputter yield to decrease. Similarly, if the angle of incidence is too vertical (0°) or too shallow (>70°), the collision cascade is either not translated to surface near atoms, or the impinging species are reflected by the target surface, respectively [36–38].

There are several benefits to the sputtering deposition technique, one of which includes the used of compound targets. Since sputtering relies solely on momentum transfer between energetic species from the plasma and surface near atoms from the targets, sputtering is rather insensitive to target chemistries that are comprised of elements with varying vapor pressures. This is a particular problem for PVD processes, which hinge on thermally vaporizing the target material. Here, selective vaporization of elements with lower vapor pressures can occur, offsetting the chemical composition of the coating compared to that of the target (e.g., cathodic arc evaporation) [39].

## 2.2 Cathodic arc evaporation

Cathodic arc evaporation (CAE)uses a high-current, low-voltage arc, to thermally vaporize the target material. The high-current densities that pass through the target material during an arc-discharge thermally melt and vaporize the material in localized melting pools, or so-called "cathode spots". By introduction of a reactive process gas, such as nitrogen, ceramic films can be grown onto the substrate surface. In order to initiate the arc, a short contact is made between an auxiliary electrode and the cathode, after which it is separated again (trigger arc). Once the initial discharge is extinguished, the inductance in the arc power supply will induce a voltage spike and reignite a new arc-spot at a nearby location. Which location (in the case of random arc-systems) will be determined upon the condition of the molten cathode spot and state of the surrounding target material, particularly surface protuberances such as oxide and nitride inclusions. In general, a new arc-discharge will ignite where electrical field lines are condensed, or places where the conduction of electrons is preferential. However, the arc-movement may also be influenced by an external magnetic field, which is referred to as a steered arc [33–38].

The material that is ejected from the cathodic surfaces by arc erosion comprise thermionic electron emissions, ionized target species, neutrals, and molten droplets. Thermionic electrons are essential for the stabilization of the arc-plasma, through their collation with neutral gas atoms and generation of secondary electrons (see Fig.2.3). In contrast to sputtering techniques, where the material is primarily ionized through momentum transfer mechanisms, such as electron-atom collisions that ultimately lead to the formation of ions in the classic glow discharge regime, the arc evaporation process involves the ionization of the evaporated material primarily through the use of high-power density and elevated temperature generated by the arc-spot. The essential mechanism for arc evaporation revolves around maintaining electrons free from the conduction band within the cathode material and subsequently releasing them to the atmosphere (vacuum or gas). In the case of arcs, electrons are not liberated by individual ion impact but rather through a collective process, which involve thermionic emission, strong electric fields, or a combination of these factors. Both, thermally evaporated metallic ions, as well as ions of the reactive gas are then accelerated to the substrate, where both nucleation and condensation of a coating occurs [33, 34, 36, 38].

There are several advantages that speak for CAE. Compared to DCMS, arc evaporation provides significantly higher ionization and vaporization rates. Higher ratios of ionization of the process gas, as well as vaporized target material are therefore achieved, which generate a higher flux of ions available for sputter cleaning procedures. A higher flux of ions also provides advantages in modifying deposition processes and fine-tuning coating properties through application of a substrate bias, which promotes additional bombardment (densification) at the coating surfaces during deposition. Disadvantages on the other hand include the formation of

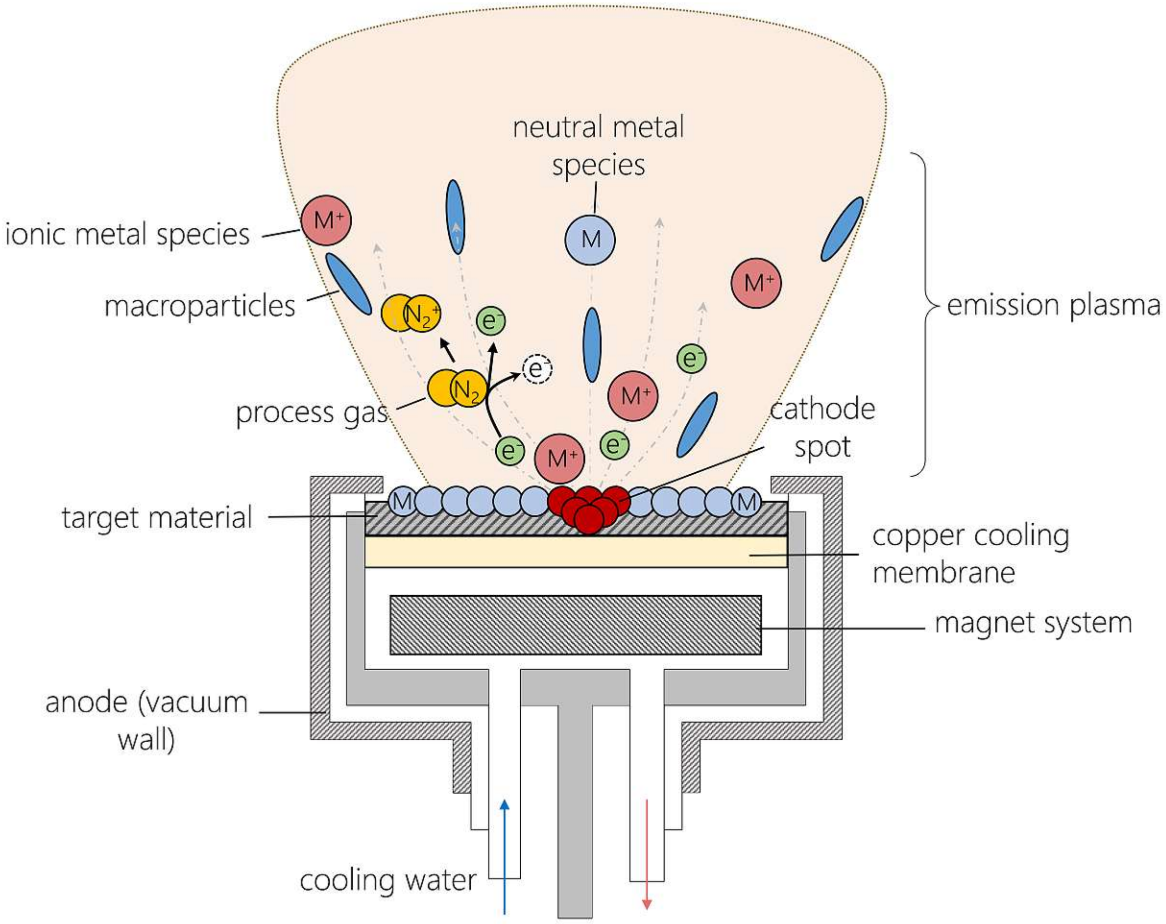

Figure 2.3: Illustration of a cathodic arc evaporation source, plasma generation and its constituents. Adapted from [36].

macroparticles during vaporization of the target surface, which incorporate into the coating structure and inherently diminish its quality [33, 34, 36, 38].

## 2.3 Transport of vaporized material

Irrespective of the method used for vaporizing the target material, the transport of the vapor across the vacuum chamber is a key element in PVD and decisive for depositing coatings with desirable properties. As atoms are ejected from the target surface and enter the vapor phase, they initially pursue a linear trajectory, while carrying a certain amount of kinetic energy. However, through a series of collisions with gas particles within the deposition chamber, a reduction of the ejection energy is caused (thermalization), as well as deflection of the initial trajectory (scattering). Naturally, higher pressures within the deposition chamber result in higher thermalization rates and increased scattering ratios, resulting in less energetic species reaching the substrate surface [33, 34, 38].

## 2.4 Condensation and film growth

After reaching the substrate surface, the vaporized atoms condensate and give off their energy (condensation energy). Depending on the energy that arriving particles carry, atoms may rearrange in order to attain the lowest, most stable energy state possible (surface diffusion). As more atoms arrive at the substrate surface and adhere (adatoms), adatoms form new bonds and agglomerate to clusters, also referred to as nucleation. In this regard, classical nucleation theory provides a rational explanation to why nucleation and subsequent crystal growth is a thermodynamically favorable process and is given by Eq.2.1. In its simplest form, the nucleation of crystals, whether they arise from solution or a vapor phase, must fulfill the requirement $\Delta \mathrm{G}_{\mathrm{bulk}} < 0$. Moreover, nucleating particles must overcome an energy barrier, which can be thought as to disconnect solute-solvent interactions, or condensation-re-evaporation processes. It is thus favorable for adatoms and early nucleating clusters to reduce their collective surfaces that stand in direct contact with their environment. In other words, the thermodynamic favorability of forming a crystal is size dependent [36, 40].

$$\Delta G_{\text{crystal}} = \Delta G_{\text{bulk}} + \Delta G_{\text{surface}} \tag{2.1}$$

where,
$\mathbf{\Delta G_{crystal}}$ is the change in Gibbs free energy of the crystal
$\mathbf{\Delta G_{bulk}}$ is the chemical potential difference of the compound in its crystalline form per volume, with respect to the solution or vapor
$\mathbf{\Delta G_{surface}}$ is the surface/interface energy term, opposing crystal formation

By assuming spherical particles as nucleating species, the above relationship can be extended by the respective geometric terms as follows:

$$\Delta G_{\text{f}} = -\frac{4}{3}\pi^3 |\Delta G_{\text{v}}| + 4\pi r^2 \gamma \tag{2.2}$$

where,
$\mathbf{\Delta G_{f}}$ is the change in Gibbs free energy of formation
$r$ is the radius of the adatom cluster
$\mathbf{\Delta G_{v}}$ is the favorable energy contribution related to the volume of the cluster
$\gamma$ is the unfavorable energy contribution related to the surface of the cluster

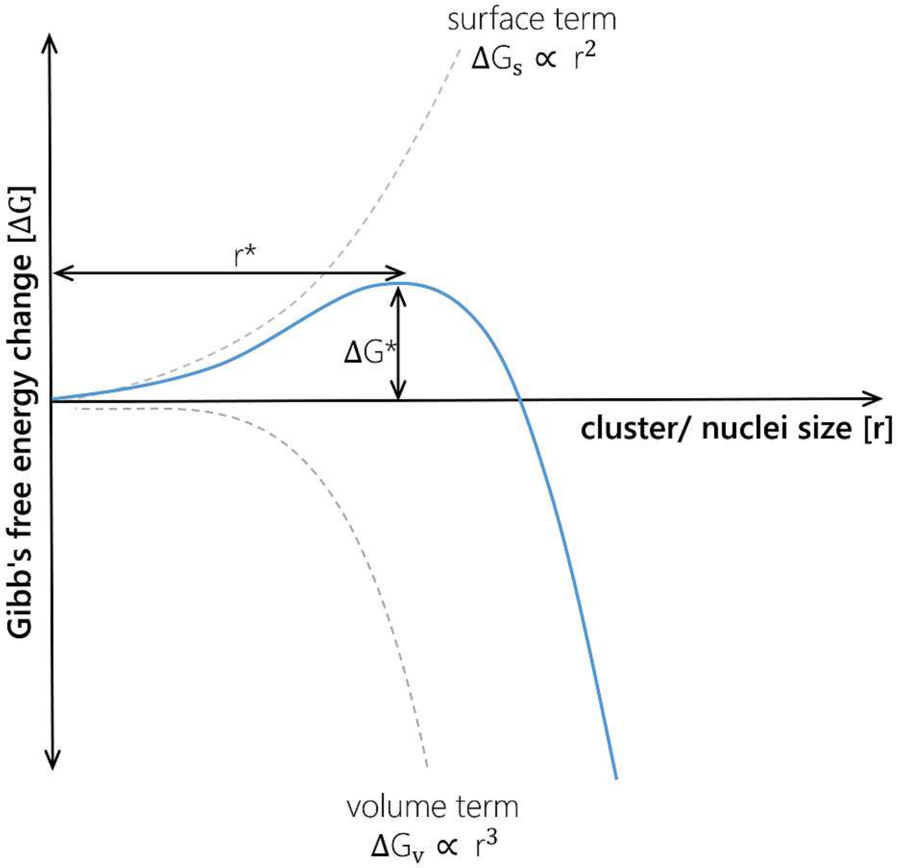

Figure 2.4: Thermodynamic barrier for nucleation. Adapted from [40].

When considering the exponential factors of both, the volume and surface contributions, it becomes apparent that the thermodynamic benefit for nucleation generated by the volume term will dominate at a certain critical cluster radius, and continue to dominate afterwards. This is visualized by Fig.2.4, where $r^*$ referrers to the critical radius of the nucleating particle, and $\Delta G^*$ refers to the nucleation barrier.

# Chapter 3

# Transport mechanisms

The significance of diffusion processes cannot be understated in thin film technologies, as they significantly influence the crystal structure, morphology, and the resulting properties of coatings. However, diffusion processes also play a pivotal role in the field of application that a coating is later indented for. Whether designed for high-temperature environments, where oxidation rates and inward oxygen diffusion dictate the efficacy of the protective coating, or intended for corrosion protection, where the diffusion of aggressive media governs the rate of coating deterioration and potential corrosion of the underlying bulk material, a thorough understanding of the specific diffusion dynamics is essential in the customization of durable coating systems [41].

Within solid materials, the movement of atoms is significantly restricted owing to the fixed arrangement of the crystal lattice. Unlike in gases and liquids, where atoms, ions, and molecules move freely due to Brownian motion, the movement of atoms and ions in solids is confined by the array of their unit cells, which collectively constitute a crystal lattice. Nonetheless, crystalline solids are not flawless structures and exhibit a notable number of crystallographic defects, which serve as the basis for diffusion processes [42].

In the domain of solid-state chemistry, diffusion mechanisms can be elucidated through thermally activated species that acquire sufficient vibrational energy to depart from their respective lattice position and move randomly to another. However, various conditions within a material can exert forces that yield a measurable mass transport or net diffusion, where the probability of certain species is more inclined to occur in one direction than in the other. Such driving forces include crystallographic defects, concentration gradients, variations in pressure, and/or thermal gradients traversing a material component [41–44].

## 3.1 Crystallographic defects

The crystallographic integrity of a solid can be disrupted through various structural flaws, which are classified as 0-, 1-, 2-, and 3-dimensional defects [42, 43, 45].

0-dimensional or point defects are by far the most common and simple impairments in crystals and comprise vacancies, substitutional, and interstitial defects, which are shown in Fig.3.1.

Further disruption of an ideal crystal lattice can be caused by linear defects or dislocations, which generate a 1-dimensional distortion of multiple crystal planes. The most common linear defects are edge dislocations and screw dislocations. While edge dislocations move parallel to an applied stress, screw dislocations progress along a perpendicular axis and are characterized by their helical appearance.

More crystallographic disturbance is caused by 2-dimensional defects, or planar defects, which are formed by either grain boundaries, phase boundaries, or stacking faults between individual crystal planes. These defects form accelerated pathways for diffusion process and greatly enhance mobility of diffusive species.

Lastly, there may also exist 3-dimensional defects, which comprise voids, precipitations, embedded macroparticles and inclusions within the crystal matrix. Particularly for thin film materials such as protective coatings, voids and macroparticles represent fast-track diffusion pathways for diffusive media and have detrimental impact on the coatings ability to function as a barrier against chemical attack [46–49].

In summary, diffusion occurs more readily on surfaces than through the tightly packed bulk of a crystal. Eq.3.1 compares and rates the above mentioned diffusion processes on the basis of their probability, as well as the rate at which diffusion will occur.

$$D_{\text{surface}} > D_{\text{phase boundary}} > D_{\text{grain boundary}} > D_{\text{bulk}} \tag{3.1}$$

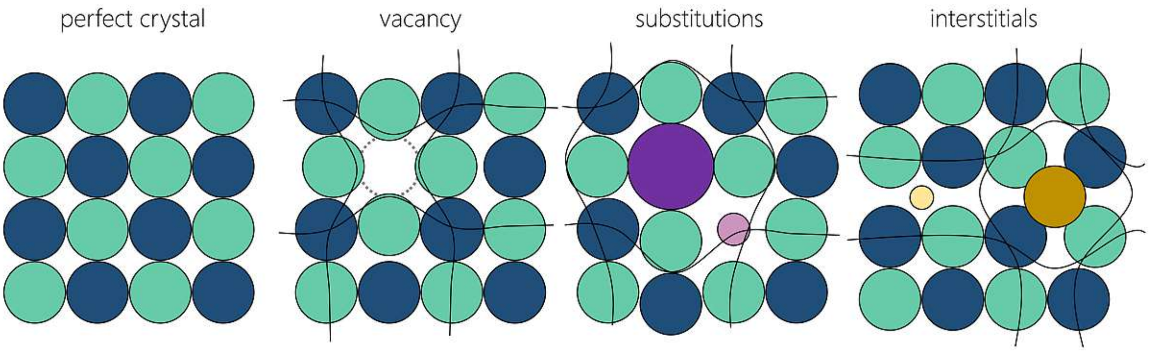

Figure 3.1: Schematic representation of 0-dimensional crystal defects.

To gain a deeper understanding about the concept of diffusion, let us examine the foundation of any transport phenomenon, known as flux. Whether it involves matter, heat, or electricity, flux is manifested as an observable movement of species from one location to another (Eq.3.2) [50].

$$flux = conductivity \cdot drivingforce \tag{3.2}$$

where,
**flux** is expressed as a quantifiable net drift of particles
**conductivity** is referred to as the diffusivity or diffusion constant (D) and describes the ease of particle mobility in a given environment
**driving force** is in most cases the presence of a concentration gradient

## 3.2 Fick's $1^{\text{st}}$ and $2^{\text{nd}}$ law of diffusion

Just like the diffusion mechanisms, which seek to rectify or improve the energetic setting of atoms in the vicinity of a crystal defect (by reducing the chemical potential of a species or Gibbs free energy), diffusion processes serve to equilibrate chemical gradients. In 1855, Adolf Fick put forward his initial proposition, suggesting that a molar flux resulting from diffusion could be directly linked to its chemical gradient (Fick's $1^{\text{st}}$ law, Eq.3.3) [41–43, 45].

$$J = -D \cdot \frac{d\Phi}{dx} = -D_0 \cdot e^{\frac{Q_\mathrm{d}}{RT}} \cdot \frac{d\Phi}{dx} \tag{3.3}$$

where,
**J** is the molar flux or the amount of substance transitioning per unit area per unit time, given in ($\mathrm{mol} \cdot \mathrm{m}^{-2} \cdot \mathrm{s}^{-1}$)
**D** is the diffusion coefficient or diffusivity, given in ($\mathrm{m}^2 \cdot \mathrm{s}^{-1}$)
$\Phi$ is the concentration, given in ($\mathrm{mol} \cdot \mathrm{m}^{-3}$)
**x** is the position of the solute or distance from its origin, given in (m)
$\mathbf{D_0}$ is the diffusion constant, given in ($\mathrm{m}^2 \cdot \mathrm{s}^{-1}$)
$\mathbf{Q_d}$ is the activation energy ($\mathrm{J{\cdot}mol}^{-1}$), given by the sum of energies of formation ($\mathrm{Q_f}$) and energies of migration ($\mathrm{Q_m}$)

By rearranging Eq.3.3 and solving for D, the following proportionality is obtained in an Arrhenius type equation, which clarifies that diffusivity is dependent on temperature (T), energies of formation ($\mathrm{Q_f}$) and energies of migration ($\mathrm{Q_m}$) [41–43, 45].

$$D = -D_0 \cdot e^{-\frac{Q_\mathrm{d}}{RT}} \tag{3.4}$$

$$D_0 = \alpha_0^2 \cdot N \cdot \omega \tag{3.5}$$

**$D_0$** here is a material specific constant and includes factors such as jump distance ($\alpha_0$), vibrational frequency ($\omega$) and crystal defect densities and is mostly determined experimentally.

Fick's 1<sup>st</sup> law is employed to depict diffusion phenomena under conditions of steady state. In such scenarios, the molar flux $\frac{d\Phi}{dx}$ across an interface remains consistent over time, rendering the process independent of time, $\frac{d\Phi}{dx}$=0. In cases where the molar flux $\frac{d\Phi}{dx}$ does not remain constant over time, thus becoming a time-dependent process, Fick's 2<sup>nd</sup> law is consulted and is represented by Eq.3.6. In this context, the time-dependent driving force is articulated as a concentration gradient [51].

$$\frac{\partial c(x,t)}{\partial t} = \frac{\partial J}{\partial x} = D \cdot \frac{\partial^2}{\partial x^2} \tag{3.6}$$

## 3.3 Oxidation

Whenever a metal is exposed to oxygen at high temperatures, it will ultimately undergo oxidation (with some exception of noble metals), leading to the formation of a thermodynamically favored metal oxide (MeO) on its surface— an electrochemical process where the metal releases electrons to an oxidizing agent that, in turn, undergoes reduction. The development of a surface oxide layer holds significant importance for various metals and alloys. As oxide scales form and expand on the metal or alloy surface, further oxidation of the underlying bulk material is impeded, thereby serving as a protective coating against subsequent oxidative attacks. The efficacy of this oxide layer depends on several factors, including the thermodynamic stability of the scales in relation to their environment, the permeability of the surface oxide layer to other reactive substances, its mechanical properties, and the interference from competing scales that may compromise the formation of a continuous and unbroken oxide structure [10][11][12].

### 3.3.1 Oxide scale-growth kinetics

In addition to the thermodynamic criteria, the kinetics of MeO development also play a crucial role. Measurement of the diffusion depth of oxygen into a material $\Delta$x (or oxide scale thickness) over time (t) allows for the description of several different oxidation rate laws, providing valuable insights into the diffusivity of oxygen through a specific material, the affinity of oxygen to form an oxide, and the passivity of the forming scale. As shown in Fig.3.2, various rate laws exist, which are dependent on temperature, oxygen pressure, as well as the surface preparation and pre-treatment of the exposed material surface [52].

### Linear oxidation kinetics

The linear rate law, presents an empirical connection between the formation of a non-protective oxide and time and can be described by Eq.3.7. Typically, as an oxide film develops, it functions as a diffusion barrier for further oxidation, resulting in a reduction in the growth kinetics over time. However, owing to the highly porous structured oxide that is formed under such circumstances, unobstructed and 'steady' oxygen diffusion remains feasible, thus leading to the generation of fresh MeO layers beneath. At specific temperatures, metals that obey to a linear growth pattern (e.g., Mo) are susceptible to catastrophic oxidation, which is often referred to as break-away corrosion [52, 53].

$$x = k_{\mathrm{l}} \cdot t \tag{3.7}$$

where,
**x** is the oxide film thickness (or mass gain due to oxidation)
$\mathbf{k_l}$ is the linear diffusion rate constant
**t** is the elapsed time

### Parabolic oxidation kinetics

The parabolic rate law (Eq.3.8), also referred to as the Tammann Pilling Bedworth parabolic law (TPB), delineates an oxide growth mechanism where the diffusion of oxygen species dictates the rate-determining step [54]. Illustrated in Fig.3.2, the decline in the oxide growth rate over time has been derived from Fick's 1st law of diffusion, indicating a decrease in the diffusivity of oxygen with the development of the oxide scale. This suggests the formation of a non-porous, continuous, and protective oxide that, unlike in the case of catastrophic oxidation, is resistant to breakaway processes [52].

For parabolic oxidation kinetics, similar assumptions are upheld as those proposed by Fick's 1st law, implying that the concentrations of diffusing species at the oxide-metal and oxide-atmosphere interface remain constant, and that the diffusion coefficient remains independent of the concentration. Generally, high-temperature oxidation of most metals follows a parabolic growth pattern.

$$x^2 = k_{\mathrm{p}} \cdot t + C \tag{3.8}$$

where,
**x** is the oxide film thickness (or mass gain due to oxidation)
$\mathbf{k_p}$ is the parabolic diffusion rate constant
**C** is a constant
**t** is the elapsed time

### Logarithmic oxidation kinetics

Finally, the logarithmic rate law (Eq.3.9) represents an empirical growth correlation without a defined mechanism. It is commonly used to analyze the development of thin oxide layers that emerge at low temperatures [42, 52, 55].

$$x = k_{\mathrm{log}} \cdot log(C \cdot t + B) \tag{3.9}$$

where,
**x** is the oxide film thickness (or mass gain due to oxidation)
$\mathbf{k_{log}}$ is the logarithmic diffusion rate constant
**B** and **C** are a constants
**t** is the elapsed time

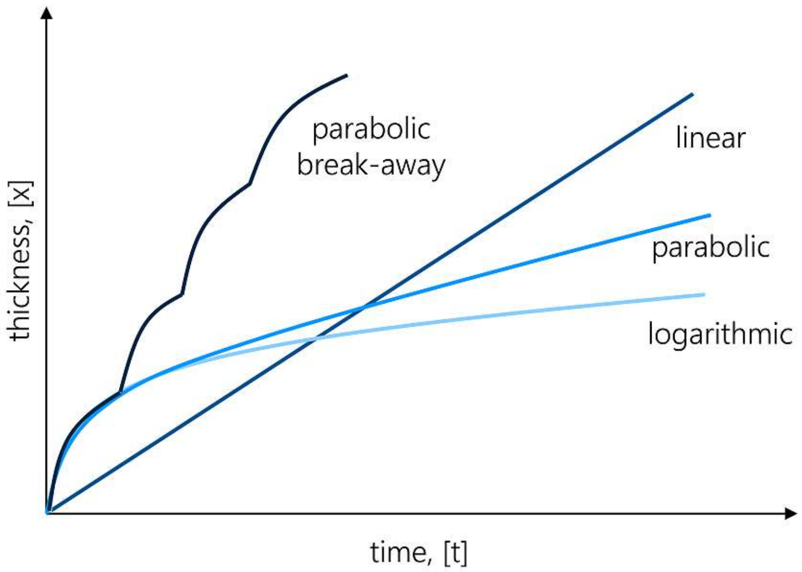

Figure 3.2: Schematic representation of different oxidation rate laws. Adapted from [56].

### Combination of simple rate laws

In numerous instances, particularly in the case of alloys, it has been demonstrated that no single rate equation (linear, parabolic, or logarithmic) is fully capable of characterizing certain oxidation processes. This holds true for both low-temperature and high-temperature oxidation growth. For instance, in the oxidation of several metals at lower temperatures, a cubic oxide growth rate was observed, indicating the presence of a combination of growth processes. Therefore, a blend of the parabolic and logarithmic rate laws has been suggested. In the case of metals undergoing oxidation at higher temperatures, a rate amalgamation between a linear and parabolic progression has been noted. This behavior involves a rapid initial oxidation, typical of a parabolic rate equation, followed by a linear pattern. Referred to as a para-linear growth rate, this phenomenon is characterized by the emergence of micro-cracks within developing oxide scales, facilitating direct gas access to the oxide-metal interface and leading to increased oxidation of the exposed metal [51, 56, 57].

# Chapter 4

# Corrosion

Ever since materials have become an integral part of human and technological advancement, the process of generating new materials has always involved the acquisition and refinement of ores, as well as purification of their minerals and elemental constituents. Energy-demanding metallurgical processes have been designed to separate stable forms, such as oxides, silicides, carbonates, sulphates etc., in order to make available the ‘ingredients’ for technologically relevant materials. However, once such materials are exposed to the environment of their utilization, their deterioration by corrosion often returns them back to their native and most stable form they were drawn from [58].

In classical thermodynamics, Gibbs free energy (G) provides the means of defining the equilibrium of a system, or by extension, the tendency of a reaction in a given direction, if the system is not at equilibrium. Under standard conditions (e.g., 298.15 K, 1 bar and activity ($\alpha$) =1) G° represents a thermodynamic standard potential that is used to calculate work of a closed and well-defined system of constant temperature (isothermic) and constant pressure (isobaric). Therefore, changes in the standard Gibbs energy (ΔG°) is related to the amount of non-volumetric work that can be obtained from a closed system, again at fixed temperature and pressure. From this came the understanding of spontaneous and non-spontaneous reactions, where a reaction occurs spontaneously at isobaric and isothermic conditions when the term $\Delta G^\circ<0$, and non-spontaneously when $\Delta G^\circ>0$ [58, 59].

$$G^\circ = H^\circ - TS^\circ \tag{4.1}$$

$$\Delta G^\circ = \Delta H^\circ - T\Delta S^\circ \tag{4.2}$$

where,
**G** is the Gibbs energy (in Joule)
**H** is enthalpy (in Joule)
**T** is temperature (in kelvin)
**S** is entropy (in Joule/kelvin)

To be able to determine the Gibbs free energy at nonstandard conditions, changes in temperature and reaction quotients have to be considered.

$$\Delta G = \Delta G^{\circ} + RT\ lnQ \tag{4.3}$$

where,
**R** is the universal gas constant ($8.314\ \mathrm{kJ} \cdot \mathrm{mol}^{-1}$)
**T** is temperature (in kelvin)
**Q** is reaction quotient

However, the Gibbs free energy criteria can only provide insight into the direction a chemical reaction will progress, while its final state ultimately hinges on the laws of chemical equilibria and chemical potentials.

The chemical potential $\mu$ is defined as the partial derivative of the Gibbs free energy with respect to the particle number ($\partial G/\partial n_i$), while keeping all other variables constant. In other words, the chemical potential of a system describes the change in Gibbs free energy $\Delta G_i$ if the number/concentration of particles $n_i$ changes, while keeping temperature and pressure constant. It's important to note that particles $n_i$ within the context of thermodynamics are not limited to atoms, but instead extend to other countable things, such as holes and electrons [59–61].

This is important when considering chemical systems and reactions, which involve the transfer of electrons– a field better known as electrochemistry.

## 4.1 Aqueous corrosion

### The electrode-potential

In the 1790s, Alessandro Volta laid the foundation for much of the electrochemical science we know today, through his invention of the voltaic pile. By stacking alternating zinc (Zn) and copper (Cu) discs, separated by a cloth socked in brine, he was the first to produce an electrical battery that could continuously generate current to a circuit. Now, having a constant source of electricity at disposal, other discoveries such as the electrical decomposition of water into oxygen and hydrogen (hydrolysis), as well as the isolation of chemical elements such as sodium, potassium, magnesium, calcium, strontium etc. by Humphry Davy became possible. Later, Davy demonstrated a relationship between chemical reactivity and electricity. He recognized that different 'galvanic powers' were needed to isolate different substances, and in doing so, postulated what is probably known as the first galvanic series [62, 63].

Classifying elements and their reactions according to an electrical potential became useful. Michael Faraday, initially an assistant to Humphry Davy, was able to demonstrate a correlation between electrical current and the quantity of metal corroded. Through a series of experiments, Faraday established two laws: (i) the amount of chemical change generated by the current at an electrode-electrolyte boundary is directly proportional to the quantity of electricity utilized, and (ii) the amount of chemical changes induced by the same quantity of electricity in different substances is directly proportional to their equivalent weights [63, 64]. Together, these laws can be written as:

$$m_i = \frac{\xi Q M}{n_e F} \tag{4.4}$$

where,
$\mathbf{m_i}$ is the mass of the species i produced
$\xi$ is the stoichiometric factor
**Q** is the total electric charge transferred
**M** is the molecular weight
**F** is the Faraday constant ($9.6485 \cdot 10^4$ C)

Through further experiments conducted by Evans, who emphasized the importance of considering the energetic impact of electrons in the form of an electrode potential, further insights were gained regarding the understanding that corrosion processes are primarily electrochemical in nature, rather than solely chemical reactions. However, in order to determine equilibrium conditions of various electrochemical reactions, and by extension their electrode-potential, an arbitrary zero-potential (reference potential) had to be established first. For this, electrochemists of the past have agreed on the standard hydrogen electrode (SHE), where the reversible electrochemical reaction (Eq.4.5) is utilized.

$$H_2 \leftrightarrow 2H^+ + 2e^- \tag{4.5}$$

where a platinized platinum wire is immersed in a 1.17 M HCl solution ($\alpha_{\mathrm{H^+}}$=1) under $\mathrm{p_{H_2}}$= 1 atm and a pH=0 [65].

In order to bridge thermodynamics of chemical reaction and the electro-potential for non-standard conditions the following equations hold true, which ultimately lead to the formulation of the Nernst equation [59–61, 66].

$$\Delta G = nFE \tag{4.6}$$

$$\Delta G^{\circ} = nFE^{\circ} \tag{4.7}$$

$$nFE = -nFE^{\circ} + RT\ lnQ \tag{4.8}$$

$$E = E^{\circ} - \frac{RT}{nF}\ lnQ \tag{4.9}$$

where,
$\mathbf{\Delta G}$ is Gibbs free energy under nonstandard conditions
$\mathbf{\Delta G^{\circ}}$ is Gibbs free energy under standard conditions
**n** is the number of electrons transferred
**F** is the Faraday constant
**E** is the electrode potential under nonstandard conditions
$\mathbf{E^{\circ}}$ is the electrode potential under standard conditions
**Q** is the reaction quotient at non-equilibrium conditions
**R** is the ideal gas constant
**T** is absolute temperature

### 4.1.1 Mixed potential theory

Electrochemical reactions (or oxidation-reduction reactions) convert chemical energy to electrical energy and vice versa. The transfer of electrons thereby occurs between two half-reactions, namely, an oxidation reaction which generates electrons, and a reduction reaction which consumes the electrons, and by doing so form a red-ox-pair. Which of the reactions will proceed as an electron donator (oxidation) and which as an electron consumer (reduction) is determined by the electrochemical half-cell potential. Whichever half-cell potential is higher will take the role of the oxidation agent, while the half-cell with the lower chemical potential will act as the reduction agent [67].

In 1938, Wagner and Traud formulated the mixed potential theory in order to better describe such electrochemical processes. By obeying the conservation of charge, the mixed potential theory postulates that the rate of electron production by oxidation reactions must equal the rate of electron consumption by reduction reactions. Thus, spontaneously occurring red-ox reactions take place at specific potentials where the two half-reactions occur at identical rates, and is referred to as the mixed potential ($E_{mp}$) [68, 69]. Unlike the standard electrochemical potentials that solely describe half-cell reactions, the mixed potential contains information of the sum of all reactions within an electrochemical system.

When considering a piece of iron (Fe) immersed in deaerated dilute HCl solution (under standard conditions), multiple reactions occur simultaneously, and are summarized by Eq.4.10 & Eq.4.11, and can be plotted in the form of an Evan's diagram (Fig.4.1).

$$\textbf{oxidation}: Fe \rightarrow Fe^{2+} + 2e^- \quad (E^{\circ}_{Fe} = -0.44\ V_{SHE}) \tag{4.10}$$

$$\textbf{reduction}: 2H^+ + 2e^- \rightarrow H_2 \quad (E^{\circ}_{H^+/H_2} = 0.00\ V_{SHE}) \tag{4.11}$$

With both half-cell reactions occurring on the Fe surface simultaneously, the system strives for an intermediate potential (corrosion potential), where the rate of electron generation by the oxidation reaction (Fe dissolution) and the rate of electron consumption by the cathode reaction (hydrogen generation) are equal, also referred to as corrosion current ($i_{corr}$). By plotting the change in current densities against changes of applied potential, the anodic branch of Fe eventually intersects with the cathodic branch of hydrogen. This intersection represents the equilibrium potential (corrosion potential, $E_{corr}$) at which the net current between metal dissolution and hydrogen generation is zero (see Fig.4.1a). In a similar manner, it is possible to determine the corrosion potential for a variety of metals, if the participating half-reactions and their electrochemical parameters are known, such as standard electrode potentials, E° and exchange current densities, $i_0$ [59–61, 67].

## 4.1.2 Kinetics of electrochemical systems

Evans diagrams also provide valuable information about the corrosion kinetics of metals. Again, we shall use Fe as an example. When considering iron (Fe) and zinc (Zn) in a deaerated HCl solution, having standard reduction potentials of -0.44 V and -0.76 V, respectively, it may be tempting to assume that Zn will corrode more likely and thus more quickly. However, when constructing a superimposed Evans diagram for both cases, a much higher corrosion current is obtained for Fe than for Zn under identical conditions (see Fig.4.1b). This emphasizes, that the thermodynamic factor of the standard electrode potential only tells us, which half-cell reaction will proceed to function as the anode, and which as the cathode, but does not reveal any information about the reaction rate. Since the corrosion current and thus the corrosion rate of a metal is defined at the potential where the net current between metal dissolution and hydrogen evolution is 0, it is clear that the exchange current of hydrogen for a specific metal has a big influence on overall corrosion rate. In other words, if the hydrogen exchange current on a metal surface is high, then the corrosion rate of that metal is also likely to be high, if the exchange current is small, then the corrosion of the metal is low.

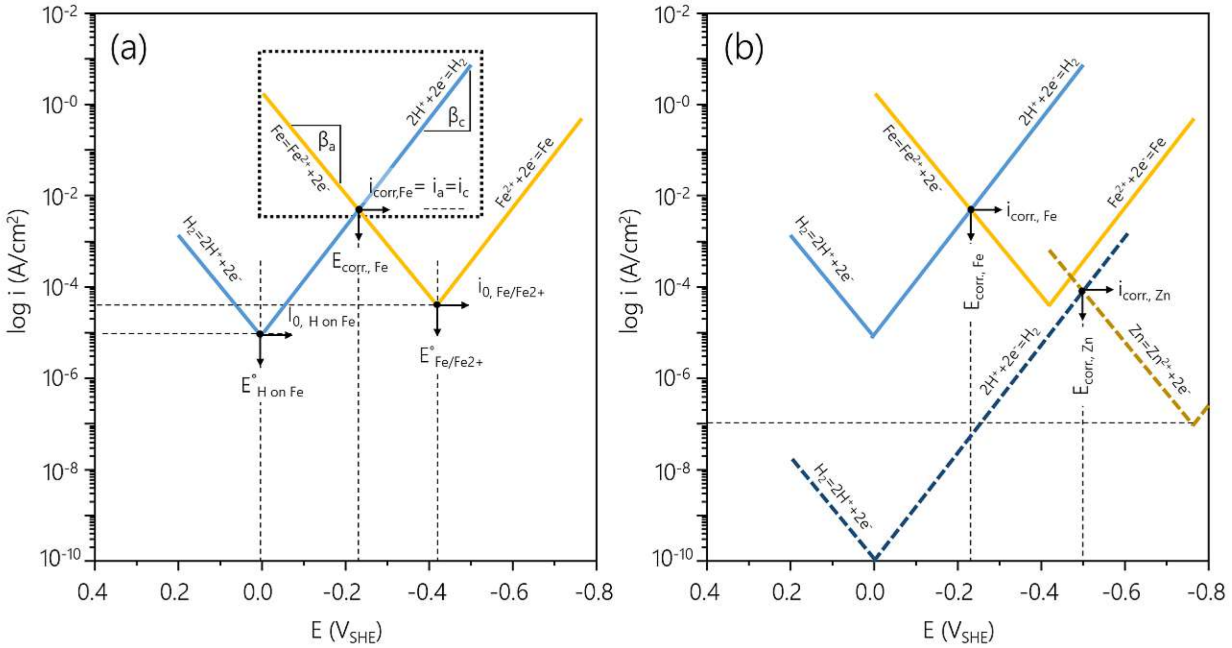

Figure 4.1: Behavior of Fe and Zn in deaerated acidic HCl-solution. Adapted from [67, 69].

In the case of Zn and Fe immersed in a deaerated HCl solution, a much higher hydrogen exchange current is featured for Fe, despite having the higher reduction potential, which ultimately translates to a faster dissolution of Fe into solution [69].

### 4.1.3 Galvanic corrosion and corrosion rate

Galvanic corrosion describes a degradative process, when two or more dissimilar materials are brought in electrical contact within the same environment (electrolyte). It is clear, that depending on the materials' thermodynamic potentials, one will act anodically, while the other will act cathodically. In the case of Fe and a noble couple (e.g., gold), which will not oxidize, a significant decrease in the exchange current density $i_{0(\mathrm{H_2\ on\ Fe})}$ is observed, while an increased exchange current density $i_{0(\mathrm{H_2\ on\ Au})}$ is featured. Moreover, an accelerate dissolution of Fe is featured when coupled with gold, than without. This effect can be seen for many galvanic couples, whose electrode potentials differ substantially. However, as discussed in the previous section, the eventual corrosion rate of the oxidizing metal is more likely determined by the exchange current $i_{0(\mathrm{H_2\ on\ noble\ metal})}$ than the relative difference of electrode potential between the noble and less-noble partners [67, 69, 70].

Once more, a great example is to consider a piece of Fe immersed in a solution of HCl, where in one case, Fe ($E°_{\mathrm{Fe}}$=0.447 V) is coupled with gold (Au) ($E°_{\mathrm{Au}}$=1.5 V), in another case with platinum (Pt) ($E°_{\mathrm{Pt}}$= 1.2 V), and in a third case remains in its original uncoupled state. Despite the larger potential difference between Fe and gold, a slower corrosion rate is observed compared to the Fe-Pt couple (see Fig.4.2).

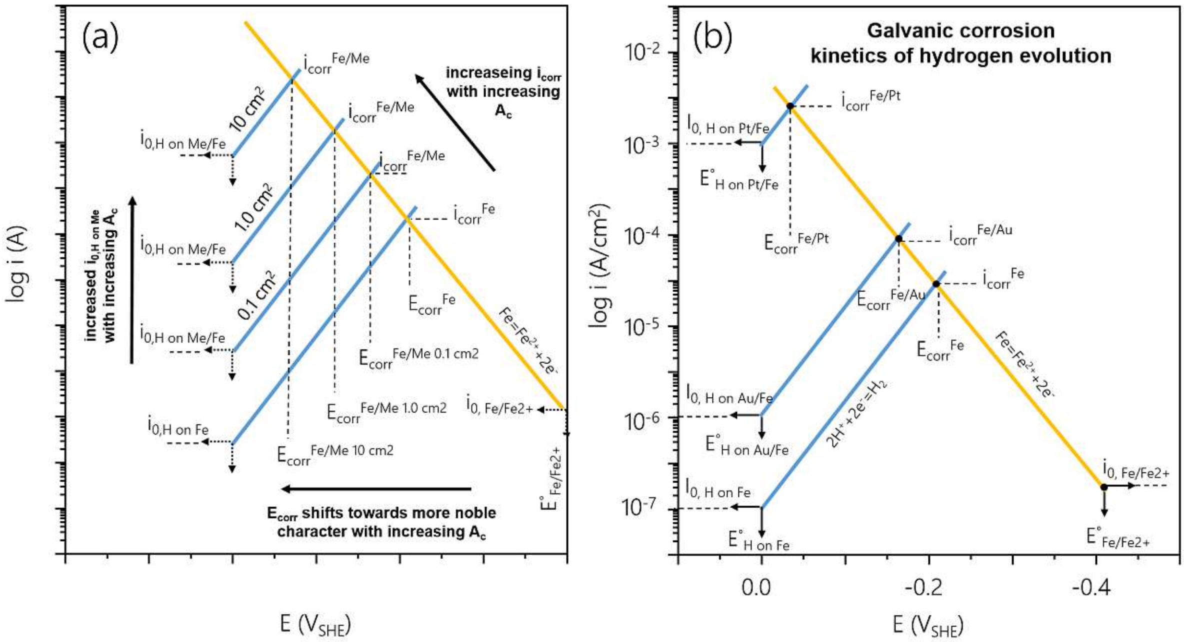

Figure 4.2: Galvanic corrosion of Fe in deaerated HCl solution. Adapted from [67, 69].

### 4.1.4 Cathode-to-anode surface ratio

With the understanding that corrosion rates of less-noble metals (anodic reaction) are dependent on the exchange current of the cathodic half-reaction, it becomes clear that the relative surface areas of the respective cathodic and anodic partial reactions have a profound influence on the corrosion current and by extension the corrosion rate. This is made clear when reviewing Fig.4.2b, which shows the corrosion rate of Fe in deaerated HCl solution under standard conditions. When Fe is not coupled with a noble metal (Me), its dissolution rate is proportional to the reaction rate of the cathodic reaction (hydrogen generation), and thus is limited by the exchange current that hydrogen experience on the Fe surface. If however, Fe is electrically coupled with a more noble metal, whose exchange current $i_{0\ (\mathrm{H\ on\ Me})} > i_{0\ (\mathrm{H\ onFe})}$, then higher dissolution rates of Fe are made possible. As the surface ratio between the noble Me and less noble Fe increases, so does the overall exchange current for the Me-Fe couple $i_{0\ (\mathrm{H\ on\ Me/Fe})}$, resulting in a higher corrosion rate of the less noble Fe partner [70, 71].

In summary, increasing the exposed cathodic-to-anodic surface ratio increases the cathodic exchange current, which in turn exerts a higher corrosion rate of the anodic metal dissolution. Moreover, the large the cathode to anode ratio is, the more noble the corrosion potential of the couple becomes.

### 4.1.5 Activation energy

A metallic electrode in solution at equilibrium will generally exhibit a forward ($r_f$) and a reverse reaction ($r_r$), between which an exchange current is flowing (net current=0). If we now consider the dissolution of a metal, formation of cationic metal-ions will accumulate at the metal-electrolyte interface while leaving behind electrons. This accumulation of charge (cationic charge build-up in the solution and electronic charge build up at the metal surface) will progress until equilibrium is reached ($r_f$=$r_r$). Respectively, separation of the opposing negative and positive charged layers generate a potential difference across the metal surface-electrolyte interface, called the Helmholtz double layer. Under standard conditions, this potential difference can be interpreted as the standard electrode potential [72]. [76]. Since water is polar, its positive dipole moment is attracted by the negative charge of the metal surface, contributing to the potential difference across the double layer. There, solvation of metallic cations occurs, which are then distanced away from the electrode surface by a hydration shell. Since such hydrated ions still experience electrostatic attraction to the metal surface, they form a second layer charge layer. While this second layer is referred to as the outer Helmholtz plane (OHP,$\varphi$2), the inner Helmholtz plane (OHP, $\varphi$1) is generated by the adsorbed water molecules by means of their dipole moment [73].

This means that for a metal atom to become dissolved, it must first overcome an energy barrier in order to dislodge from its lattice and overcome the Helmholtz layers.

### 4.1.6 Pitting corrosion

Pitting corrosion is a form of extreme localized galvanic corrosion, which is most often observed in the presence of aggressive halide-ions such as chloride-ions ($Cl^-$) and is characterized by the formation of small caverns (pits). According to Richardson and Wood [74] the state of a materials passivity (stability of the oxide scale) is determined by the rate of reoccurring depassivation and repassivation events. In the presence of $Cl^-$ however, repassivation events become dysfunctional while depassivation events continue to occur [75, 76]. Consequently, this triggers a localized breakthrough of the protective oxide, followed by the formation of a metastable pit, referred to as pit-initiation [75]. This exposes a small area of unprotected alloy (small anode), enabling the aqueous electrolyte to make contact and to forms a galvanic couple with the surrounding oxide scale (large cathode). The driving power of the large cathode (high exchange currents that occur at the cathode surface) promotes high reaction rates at the comparatively small anode, which promotes an accelerated metal dissolution at the pit initiation site (metastable pit). This represents a crucial moment within the pitting mechanism as either, the alloy repassivates the metastable pit, or the pit exceeds a critical volume after which repassivation becomes increasingly unlikely [59]. Thus, depassivation and repassivation processes are essential processes for successful engineering materials.

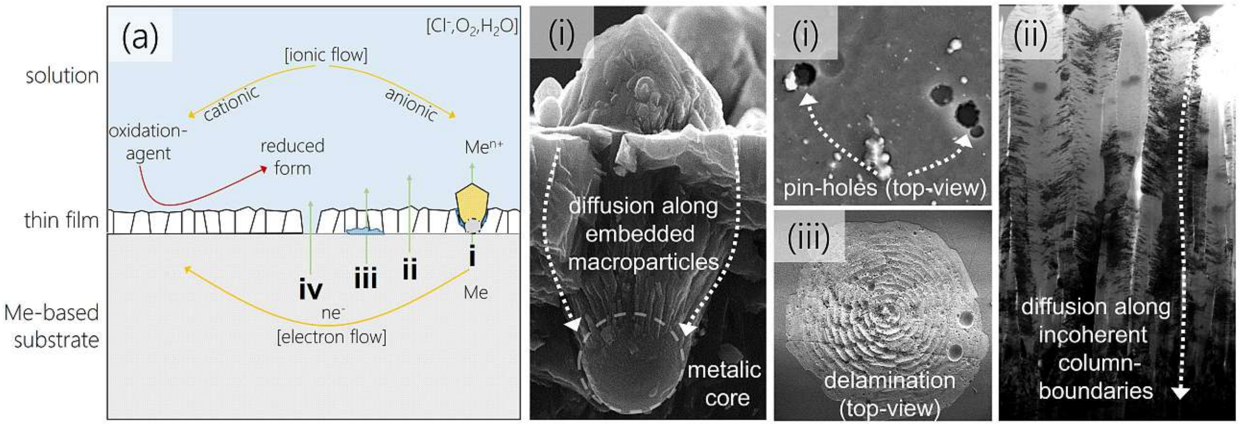

Figure 4.3: Common pit initiation events of PVD coated steel: (i) pit initiation along embedded macro-particles, (ii) diffusion along incoherent column boundaries, (iii) exposed substrate areas due to crack- formations or spallation, (iv) chemical depassivation of the coating structure itself.

Unfortunately, not all machining components self-generate a native and passivating oxide scale, but instead require protection by industrially deposited protective coatings. Such coatings, particularly ceramic transition metal nitride coatings, exhibit exceptional chemical stability (noble), but do not possess the ability to repassivate in the event of damage or other defect related occurrences. Thus, when such inert coatings are deposited on steels and are breached by an aggressive electrolyte, a galvanic couple forms and pitting initiation ensues at the coating-alloy interface [77–82].

Limiting the locations and probability for pit-initiation in PVD coated alloys is thus of upmost importance, however also extremely challenging. Due to the an array of inherent PVD coating characteristics, such as unidirectional growth orientation, columnar morphology [83], defect rich structure that include embedded macroparticles [46–49] or pin-holes [84], as well as the noble character in comparison to many alloys, pose weak points in providing exceptional corrosion protection. Therefore, PVD coatings allow for a selection of pit-initiation mechanisms, which are summarized as follows (see Fig.4.3):

i. Direct bypass of corrosion media at pin-holes, defect-sites and embedded macro-particles

ii. Local delamination of protective coating caused by inward-diffusion of corrosive media along column boundaries, followed by the formation of corrosion products and stress states at the metal-coating interface

iii. Diffusion along incoherent column boundaries

iv. Local depassivation by film breakdown, most often caused by halide-ions (mostly pertains to metallic coatings)

### Pitting mechanism

Once a metastable pit has surpassed its critical size, it begins to grow. In basic aerated solution, the Fe dissolution reaction is thermodynamically favored (anodic reaction) and is powered by the reduction of oxygen dissolved in water (reduction reaction), whose red-ox reaction is given by:

$$2Fe_{(s)} \rightarrow 2Fe^{2+}_{(aq)} + 4e^{-}(anodic) \tag{4.12}$$

$$O_{2(diss)} + 2H_2O_{(l)} + 4e^{-} \rightarrow 4OH^{-}_{(aq)}(cathodic) \tag{4.13}$$

$$2Fe_{(s)} + 2H_2O_{(l)} + O_{2(diss)} \rightarrow 2Fe(OH)_{2(s)}(redox) \tag{4.14}$$

In an aerated neutral or acidic solution, however, the dissolution of Fe occurs according to:

$$2Fe_{(s)} \rightarrow 2Fe^{2+}_{(aq)} + 4e^{-}(anodic) \tag{4.15}$$

$$O_{2(diss)} + 4H^{+}_{(aq)} + 4e^{-} \rightarrow 2H_2O_{(l)}(cathodic) \tag{4.16}$$

$$2Fe_{(s)} + O_{2(diss)} + 4H^{+}_{(aq)} \rightarrow 2Fe^{2+}_{(aq)} + 2H_2O_{(l)}(redox) \tag{4.17}$$

By reviewing the corrosion products more closely, it becomes apparent that under basic conditions, the corrosion product of Fe ($Fe(OH)_2$) is solid, while under neutral and acidic conditions, Fe remains dissolved. This is a decisive detail in the pitting mechanism, which shall be highlighted again later.

Fig.4.4a shows a schematic of the pitting mechanism of coated carbon steel in neutral aerated solution and highlights several electrochemical reactions that play an important role in promoting pit growth. Even though all reactions are occurring simultaneously, with no particular sequence, a numerated depiction is nevertheless chosen for an easier understanding of the mechanism.

When Fe dissolves into solution within the metastable pit (i, anode), its electrons are conducted to the surface (ii, cathode) where the reduction of dissolved oxygen occurs (iii, reduction reaction). As a result, hydroxyl-ions are generated and increase the alkalinity in the vicinity of the pit-opening. With Fe dissolution continuing within the pit cavity, a concentration gradient and positive charge build up develops (iv, ionic charge build up). Positively charged $Fe^{2+}$-ions build up within the cavity and diffuse down the concentration gradient to the surface of the pit, where they experience a more alkaline environment (v, diffusion of Fe to pit-mouth). Referring back to Fe dissolution under alkaline conditions (Eq.4.14), Fe will react with the hydroxyl-ions and solidify as $Fe(OH)_2$ and $Fe(OH)_3$, and

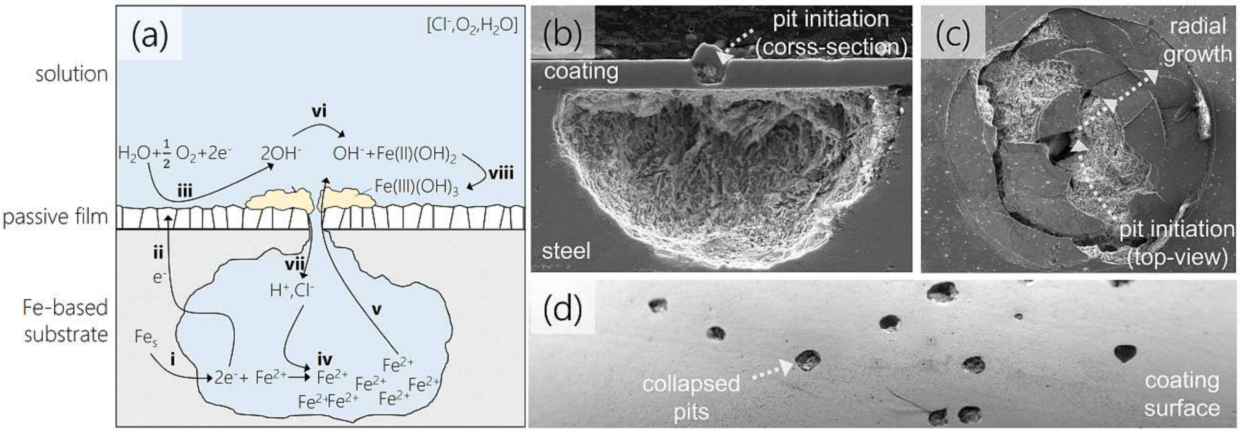

Figure 4.4: Pitting mechanism of PVD coated steel. (a) shows the correlation and synergy of various chemical processes during pitting. (b) shows an example of a matured pit forming due to an embedded macroparticle within an arc evaporated AlCrN coating. (c) illustrates a collapsed pit, due to the failing mechanical integrity of the coating structure. (d) shows a wide-view of a PVD coated steel suffering from pitting corrosion.

seals the pit opening (vi+viii, sealing of pit-opening through corrosion products). Consequently, a porous oxide scale develops, which remains penetrable for $Cl^-$ and $H^+$ (vii, high ionic mobility of $Cl^-$ and $H^+$ through porous oxide). With the consumption of $OH^-$ at the alkaline pit opening, and $Fe^{2+}$ build up at the bottom of the pit, $Cl^-$ ions are drawn to the bottom pulling along $H^+$ and acidify the pit. While the dissolution of Fe is favored at low pH levels, an autocatalytic environment is generated that allows for a continuous growth of the pit-cavern [85]. As one of the reaction products of Fe dissolution in acidic solutions is hydrogen evolution (reduction of hydronium-ions, $H_3O^+$), a gradual pressure build up will eventually rupture the cavity and elicit its collapse. SEM images of such pitting mechanism are presented in Fig.4.4b-d, which show a cross section of a matured pit cavity caused by an embedded macroparticle initiation site (Fig.4.4b), a top view of a collapse pit (Fig.4.4c) and a PVD coated steel substrate that is studded with open pit-caverns.

## 4.1.7 Assesment of corrosion

During electrochemical corrosion measurements, anodic and cathodic reactions are coupled together on the same electrode surface. Thus, when a metal or alloy corrodes in an electrolyte, the sum of all partial cathodic reactions and the sum of all partial anodic reactions are measured at the same instance. An anodic branch thus comprises all oxidation processes, while a cathodic branch represents all partial reduction processes, whose intersection (in the form of an Evans-diagram) provides the mixed potential (or corrosion potential, $E_{corr}$,) and corrosion current ($i_{corr}$) [26][27].

### 4.1.8 Corrosion potential

The measurement of the equilibrium potential of a corroding electrode (working electrode) is performed by using a non-polarizable reference electrode. By connecting the two by a voltmeter and salt-bridge, and immersing them in the same electrolyte, the open circuit potential of the freely corroding working electrode can be determined ($E_{corr}$) [26][27].

### 4.1.9 Corrosion current

Measuring the corrosion current under equilibrium conditions, however, is not possible. Since at $E_{corr}$ the current contribution from the sum of all anodic reactions is equal to the current consumption by all cathodic reactions, no net current can be measured ($i_a = -i_c = i_{corr}$ at $E_{corr}$). Since the net current for all occurring reactions at $E_{corr}$ is 0, the system must be brought out of equilibrium by application of an external voltage (overpotential, $\eta$) in order to encourage non-equilibrium reaction rates, which is referred to as polarization. While a sufficient positive overpotential induces oxidation processes ($i_a > i_c$), a sufficient negative overpotential induces reduction processes ($i_c > i_a$). In order to describe the relationship between overpotential and the change in anodic and cathodic current within a simple electrode (an electrode where reduction and oxidation processes occur on the same surface), John Butler and Max Volmer established the following equation, which is known today as the Butler-Volmer equation [59, 60, 86].

$$j = j_a + j_c = j_0 \left\{ exp\left[ \frac{\alpha_a z F}{RT}(E - E_{corr}) \right] - exp\left[ \frac{\alpha_c z F}{RT}(E - E_{corr}) \right] \right\} \tag{4.18}$$

$$j = j_a + j_c = j_0 \left\{ exp\left[ \frac{\alpha_a z F \eta}{RT} \right] - exp\left[ \frac{\alpha_c z F \eta}{RT} \right] \right\} \tag{4.19}$$

**j** is the electrode current density ($A \cdot m^{-2}$)
$\mathbf{j_0}$ is the exchange current density ($A \cdot m^{-2}$)
$\alpha_{\mathbf{a}}$ is the anodic symmetry factor ($1-\alpha_c$)
$\alpha_{\mathbf{c}}$ is the cathodic symmetry factor ($1-\alpha_a$)
**z** is the number of electrons involved in the anodic or cathodic reaction
**F** is the Faraday constant ($96\,485\ C \cdot mol^{-1}$)
**R** is the universal gas constant ($8.314\ J \cdot K^{-1} \cdot mol^{-1}$)
**E** is the electrode potential (V)
$\mathbf{E_{corr}}$ is the equilibrium potential (V)
$\eta$ is the overpotential (V)
**T** is the absolute temperature (K)

Fig.4.5a shows the relationship of the relative cathodic (blue) and anodic (yellow) current density contributions with changing overpotential on an electrode. At positive overpotentials, the net current density (purple) becomes positive with an exponentially growing anodic contribution, whereas at negative overpotentials, the net current density grows exponentially negative due to an increasing cathodic current density contribution [87].

Fig.4.5b shows the same data, however, with the current density plotted logarithmically over the electrode potential. The obtained graph, also known as a Tafel-plot, provides the necessary means for experimentally approximating the corrosion current density ($I_{corr}$). Its mathematical description, given by Eq.4.20, can further be simplified when deviating far enough away from $E_{corr}$. Thus, at high positive overpotentials Eq.4.21, the cathodic term becomes negligible, while at sufficiently low overpotentials Eq.4.22, the anodic term becomes negligible. As a result, a linear relation is given between the change in potential E and logarithm of the measured current density (log $i_{net}$), (Eq.4.23) [66].

$$i_{net} = i_{corr}\left[10^{\frac{E-E_{corr}}{\beta_a}} - 10^{-\frac{E-E_{corr}}{|\beta_c|}}\right] \tag{4.20}$$

$$E = E_{corr} + \beta_a\Big[log(i_{net}) - log(i_{corr})\Big] for\ \eta \gg 0 \tag{4.21}$$

$$E = E_{corr} - \beta_c\Big[log(i_{net}) - log(i_{corr})\Big] for\ \eta \ll 0 \tag{4.22}$$

$$\eta = \pm A \cdot log\left(\frac{i}{i_0}\right) \tag{4.23}$$

where,
$\eta$ is overpotential
**A** is the Tafel slope
**i** is the measured current density
$\mathbf{i_0}$ is the exchange current density

This allows for a rather simple way of empirically approximating the corrosion current density for a simple electrode. Making use of these linear Tafel regions, an extrapolation technique can be used to experimentally determine the corrosion current. Assuming that there are only two half-reactions occurring at on the electrode surface, the intersection point of both cathodic and anodic linear fits translates to the corrosion current. The slope of the individual Tafel slopes are referred to as Tafel-slopes ($\beta_a$ and $\beta_c$ for the anodic and cathodic Tafel-branches, respectively). The shallower the slope ($\frac{\Delta log(i)}{\Delta E}$) the higher the resistance required for the

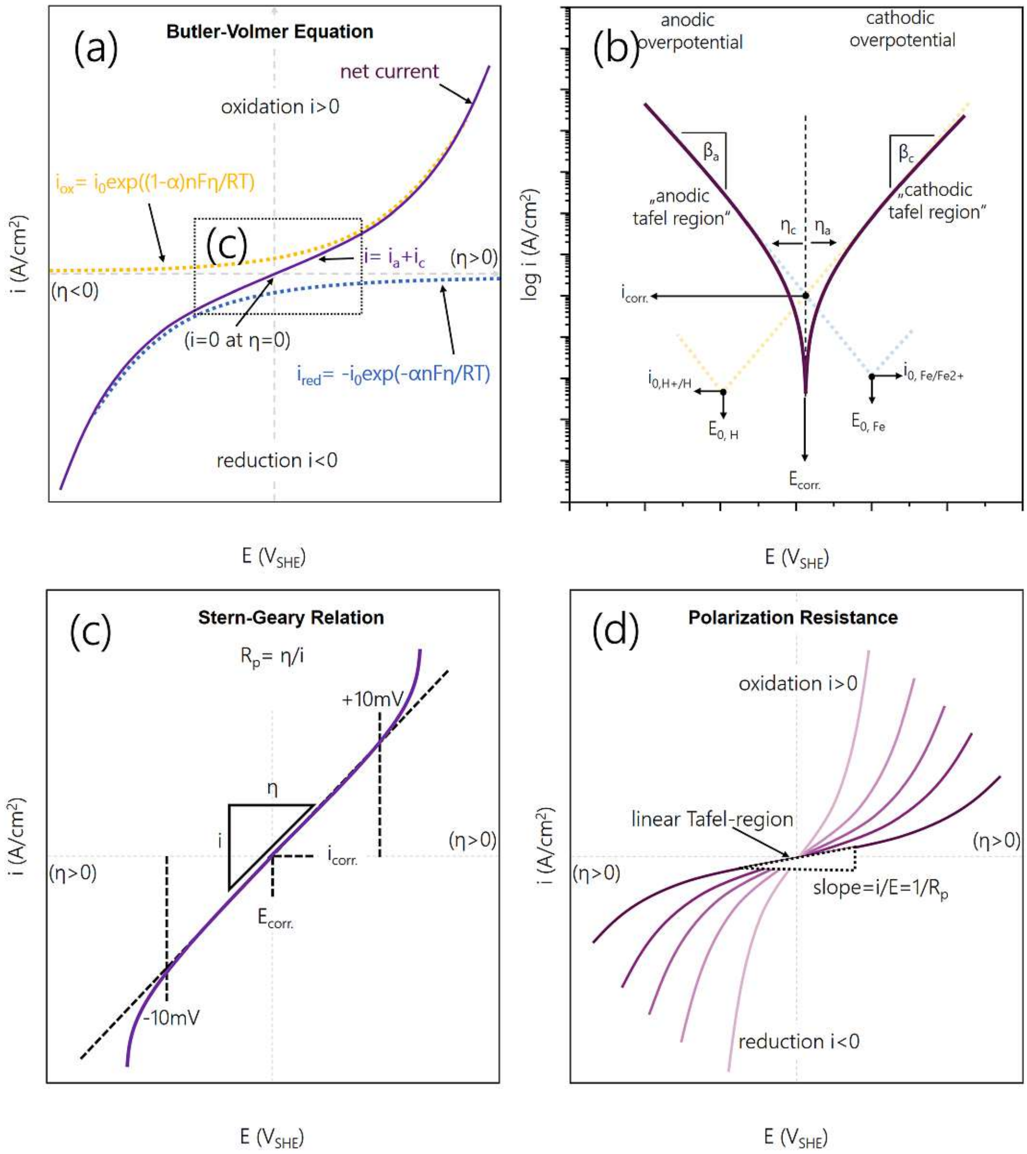

Figure 4.5: Effect of electrode polarization: (a) an i/E graph shows the net current that originates at negative and positive overpotentials. (b) illustrates the same relationship in the form of a Tafel-plot, where the net current density is plotted logarithmically. (c) illustrates the Stern-Geary relation of the linear i/E relationship at small overpotentials. (d) shows a graphical representation of a variety of i/E curves with increasing polarization resistances ($R_p$)- adapted from [66, 87, 88].

reaction and the slower the reaction rate. Naturally, the steeper the slope ($\frac{\Delta log(i)}{\Delta E}$), the lower the resistance and the faster the reaction rate.

### 4.1.10 Polarization resistance

Instead of extrapolating $i_{corr}$ from a Tafel-plot (Fig.4.5b), $i_{corr}$ can also be calculated according to the Stern-Geary relation, which provides a relationship between the polarization resistance and the corrosion current (Fig.4.5c), and is expressed as follows [59, 60, 88]:

$$i_{corr} = \frac{\beta_a \cdot |\beta_c|}{R_p \cdot 2.303(\beta_a + |\beta_c|)} = \frac{\frac{\beta_a \cdot |\beta_c|}{\beta_a + |\beta_c|}}{2.303} \cdot \frac{1}{R_p} = \frac{B}{R_p} \tag{4.24}$$

where,
$\mathbf{i_{corr}}$ is corrosion current density (A·m$^{-2}$)
$\mathbf{R_p}$ is polarization resistance Ω·m$^{-2}$
$\beta_\mathbf{a}$ is anodic Tafel slope in V/dec
$\beta_\mathbf{c}$ is cathodic Tafel slope in V/dec

Derived from the Butler-Volmer equation, the Stern-Geary relation considers the presence of a linear relationship between the potential and current at very small overpotentials (±25 mV or smaller), whose slope is referred to as the polarization resistance ($R_p$). By reviewing Eq.4.24 once more, the corrosion current, and by extension the corrosion rate, is inversely proportional to the polarization resistance of an electrochemical system [59, 60].

Since polarization resistance is a measure of the transition resistance between the electrode reactions and the electrolyte, changes to the magnitude of polarization resistance can occur due to (i) a potential drop across the electrode-electrolyte interface caused by changes of the electrical double layer, (ii) or due to insulation effects that arise through the formation of corrosion products at the electrode surface. In either cases, a high polarization resistance implies a high corrosion resistance, whereas a low polarization resistance infers poor corrosion resistance [26][27].

### 4.1.11 Open-porosity

PVD coatings offer a multitude of different defects and porosities that an electrolyte can utilize to gain access to the underlying substrate material. The subsequent formation of galvanic couples at such porosities are thus a common circumstance that material scientists need to take into consideration. Several approaches have been devised over the years to strategically obstruct open-pore transmissivity for an electrolyte, which may include increasing the overall coating thickness, the incorporation of interlayered barrier coatings, by surface treatments [89], or by thermally induced formation of a dense oxides scale.

However, in order to develop and devote such strategies to improve the passivity of a coating, analytical techniques must be able to quantify the degree of coating porosity. An easy and quick estimation of the porosity index, or open-porosity value, can be electrochemically determined at the corrosion potential of a given coating-substrate couple, assuming that the coating functions solely as the cathode and is chemically inert (Eq.4.25). Luckily, most ceramic coatings deposited on low-alloy steels fulfill this requirement in $Cl^-$-enriched neutral aqueous solutions [90].

$$P = \left(\frac{R_{p,bs}}{R_{p,c}}\right) \cdot 10^{\frac{|\Delta E_{corr}|}{\beta_a}} \tag{4.25}$$

where,
$\mathbf{R_{p,c}}$ is the polarization resistance of the coating in $\Omega \cdot m^{-2}$
$\mathbf{R_{p,bs}}$ is the polarization resistance of the bare substrate in $\Omega \cdot m^{-2}$
$\mathbf{\Delta E_{corr}}$ is the difference in the corrosion potential between coating and substrate in V
$\beta_{\mathbf{a,bs}}$ is the anodic Tafel slope of the bare substrate in V/dec

### 4.1.12 Corrosion rate

Probably one of the most coveted corrosion parameter by material scientists is the corrosion rate expressed in mass-loss over time per unit area. According to Faraday's Law and by knowing the corrosion current density of the material under investigation, the corrosion rate can be determined as follows:

$$m = \frac{1}{F} \cdot \frac{M}{n} i_{corr} \cdot t \tag{4.26}$$

with,
**m** is the mass of product removed (g)
**F** is the Farraday's constant 96 485 ($C \cdot mol^{-1}$)
**M** is the molar mass of product or atomic weight ($g \cdot mol^{-1}$)
$\mathbf{i_{corr}}$ is the corrosion current density ($A \cdot cm^{-2}$ or $C \cdot s^{-1} \cdot cm^{-2}$
**t** is time (s)
**n** is the number of electrons transferred

## 4.2 Hot corrosion

Hot gas corrosion, also known as molten salt-induced corrosion, is a phenomenon commonly observed in aviation and stationary land-based gas turbines [91]. Occurring within a temperature range of 575-950 °C, the formation of salt deposits leads to accelerated degradation of machining components, particularly affecting transition lines from the combustion chamber, as well as blades and vanes of the high-pressure turbine (HPT) and low-pressure turbine (LPT) [18]. When sulfur impurities from the kerosene (<0.3 m.%) are combusted, they oxidize entirely and form a mixture of $SO_2$ and $SO_3$ ($SO_x$), as presented by Eq.4.27-4.28 [92].

$$S + O_2 \rightarrow SO_2 \tag{4.27}$$

$$SO_2 + \frac{1}{2}O_2 \leftrightarrow SO_3 \tag{4.28}$$

When operating in marine environments, salt-rich aerosols can infiltrate the turbine sections through the air intake (e.g., NaCl, KCl, $MgCl_2$ etc.), where they react with the $SO_x$-rich exhaust gases and form high-melting sulfate-salt deposits (Eq.4.29-4.30) [91, 93].

$$2NaCl + S + 2O_2 \rightarrow Na_2SO_4 + Cl_2 \quad (T_m = 884\ °C) \tag{4.29}$$

$$MgCl_2 + S + 2O_2 \rightarrow MgSO_4 + Cl_2 \quad (T_m = 1124\ °C) \tag{4.30}$$

Over time, these adherent deposits can introduce a series of aggressive corrosion mechanism that lead to premature failure of turbine components.

One particular reason for the aggressive nature of the salt deposits is their ability to form low-melting eutectic mixtures, which can attain much lower melting temperatures than those of their individual constituents. For instance, while $Na_2SO_4$- and $MgSO_4$-deposits have melting points of 884 °C and 1124 °C, respectively, their binary system features an eutectic temperature of merely 665 °C [93]. This significantly complicates the study of hot corrosion phenomena in industrial settings, as not only temperature and atmospheric composition, but also the mole-fractions of the salt-deposit impart substantial influence on the hot corrosion mechanism.

### 4.2.1 Hot Corrosion and salt-chemistry

Hot corrosion of metals and alloys that are exposed to salt-rich environments at high temperatures can occur by a variety of degenerative mechanisms: Either through a sulfidation-oxidation mechanism, or the acidic and/or basic dissolution of the protective oxide scale (fluxing mechanism). Whether or not conditions for sulfidation or fluxing are met, depends on the chemical make-up of the protective oxide scales, temperature profile, chemical composition of the atmosphere and, as a result, on the melt basicity of the salt-deposit.

When considering a melt of pure $Na_2SO_4$, it partially dissociates into its basic ($Na_2O$) and acidic ($SO_3$) components (Eq.4.31), whereby its decomposition occurs quite slowly (>884 °C). Simultaneously, there is an exchange between the molten salt deposit and the surrounding $SO_x$-rich atmosphere, which substantially influences the character of the melt, and by extension the interaction between the melt and the protective oxide scale of a machine element. Since out of all constituents of exhaust gas ($SO_2$, $SO_3$, $O_2$, $N_2$ $CO_2$ etc.) $SO_3$ is by far the most soluble within the $Na_2SO_4$ melt, its concentration in the atmosphere and its solubility drastically influences the basicity of the melt. In other words, the higher the $\rho SO_3$ is, the more acidic the melt becomes [94].

$$Na_2SO_{4(l)} \leftrightarrow Na_2O_{(diss)} + SO_{3(g)} \tag{4.31}$$

In a sense, the sodium sulfate melt can be described by acid-base chemistry, similar to a pH-scale of aqueous solution:

$$Na_2SO_{4(l)} log(K)_{(1200K)} \leftrightarrow Na_2O_{(diss)} + SO_{3(g)} = -16.7 \tag{4.32}$$

$$log(\alpha_{Na_2O}) + log(\alpha_{SO_3}) = -16.7 \tag{4.33}$$

### 4.2.2 Solubility of protective oxides in $Na_2SO_4$

In a series of electrochemical studies, Zheng [95], Luthra and Rapp [96] have investigated the solubility of various oxides in fused $Na_2SO_4$ at 1200 K. By varying the basicity of the melt, the solubility of most oxides (with the exception of $SiO_2$) feature distinct solubility minima, and thereby indicate at which melt-basicity they are most stable. Fig.4.6a shows a compilation of such measured solubilities, where concentration of the dissolved oxide is plotted over the basicity of the melt.

When oxides come in contact with fused $Na_2SO_4$, their dissolution can occur in two ways: Basic dissolution (basic fluxing), where the oxide reacts with the basic component ($Na_2O$) of the melt, or acidic dissolution (acidic fluxing), where the oxide reacts with the acidic component of the melt ($SO_3$). Which reaction dominates depends on the chemical stability of the oxide (position of the solubility minimum). While $Al_2O_3$ and $Cr_2O_3$ are considered acidic oxides, exhibiting their solubility minima at the acidic end of the melt-basicity spectrum,

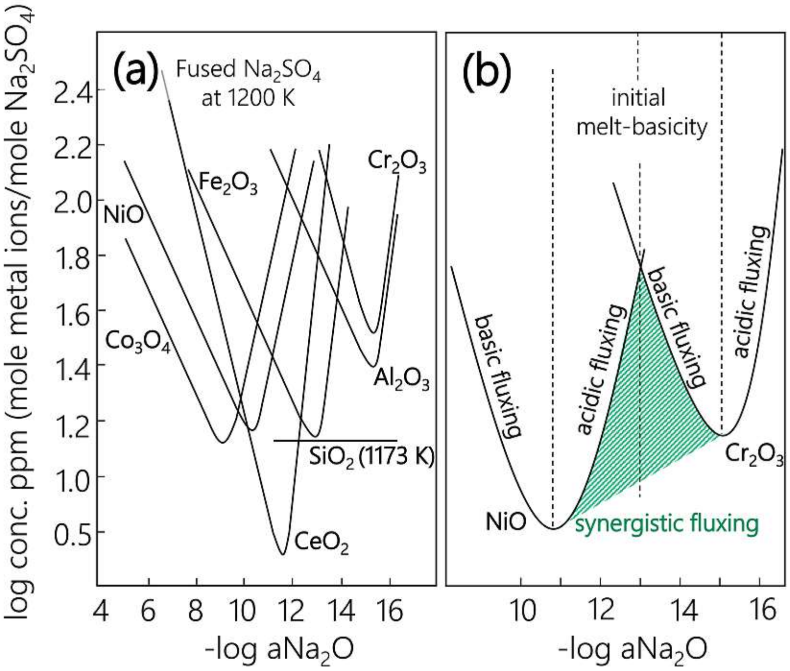

Figure 4.6: (a) Solubility diagram of common oxides in fused $Na_2SO_4$ as a function of melt-basicity (adapted from [97]), (b) region of synergistic fluxing between NiO and $Cr_2O_3$ (shaded area).

$Co_2O_3$ and NiO are viewed as basic oxides with solubility minima at the basic end of the spectrum. Therefore, $Co_2O_3$ and NiO are predominantly dissolved via an acidic fluxing mechanisms (reacts with $SO_3$), while $Al_2O_3$ and $Cr_2O_3$ are more frequently dissolved in more neutral and basic melts (basic fluxing by reacting with $Na_2O$).

### Acidic fluxing (acidic dissolution)

During acidic fluxing, dissolution of the protective metal-oxide scale occurs by reacting with $Na_2SO_4$ and by releasing $Na_2O$, to form porous metal-sulfates [44]. In the case of NiO, $NiSO_4$ and $Na_2O$ are produced and dissolve into the $Na_2SO_4$ melt (Eq.4.34-4.35). A more accurate notation of the acidic fluxing of NiO is given by Eq.4.36-4.37, which considers the solubility of the main oxidant $SO_3$ in form of disulfate (Eq.4.38), as the solubility and thus participation of $SO_2$ and $O_2$ in $Na_2SO_4$melts is negligibly low [98].

$$NiO_{(s)} + SO_{3(g)} = NiSO_{4(diss)} \tag{4.34}$$

$$NiO_{(s)} + Na_2SO_{4(l)} = NiSO_{4(diss)} + Na_2O_{(diss)} \tag{4.35}$$

$$NiO_{(s)} + Na_2S_2O_{7(l)} = NiSO_{4(diss)} + Na_2SO_{4(l)} \tag{4.36}$$

$$NiO_{(s)} + S_2O_7^{2-} = NiSO_{4(diss)} + SO_4^{2-} \tag{4.37}$$

$$SO_4^{2-} + SO_{3(g)} = S_2O_7^{2-} \tag{4.38}$$

### Basic fluxing (basic dissolution)

In the case of the basic dissolution of the protective oxide-scale (known as basic fluxing), $Na_2O$ ($O^{2-}$) present in the liquid salt film reacts with the metal oxide, resulting in the formation of soluble anionic species, as demonstrated by (Eq.4.39-4.41). However, because the availability of $O^{2-}$-ions necessary for basic-fluxing is limited by the amount of the deposited salt and its dissociation, basic-fluxing alone is not self-sustaining [97]. Thus, basic-fluxing normally predominates at higher-temperatures (HTHC 900 °C), where the production of $O^{2-}$-ions through decomposition of the salt melt is sufficiently high, and the presence of the acidic atmospheric component $SO_3$ is negligible [99].

$$NiO_{(s)} + Na_2O_{(diss)} = Na_2NiO_{2(diss)} \tag{4.39}$$

$$NiO_{(s)} + Na_2SO_{4(l)} = Na_2NiO_{2(diss)} + SO_{3(g)} \tag{4.40}$$

$$NiO_{(s)} + O^{2-}_{(diss)} = NiO^{2-}_{2(diss)} \tag{4.41}$$

### Synergistic fluxing (acid-base-dissolution)

Synergistic fluxing describes a dissolution mechanism where at least two different oxides in close proximity to one another stand in contact with the salt-melt. If the salt basicity of the melt falls between the solubility minima of the two oxides, then the solubility of the one oxide can facilitate melt conditions that accelerates the dissolution of the other (see Fig.4.6b).

Let's consider the solubility curves of NiO and $Cr_2O_3$ (common protective oxides for Ni-base superalloys) and a $Na_2SO_4$ melt basicity $-\log(\alpha Na_2O) = 11$. As the solubility minimum of NiO places left (more basic conditions) of the melt basicity, NiO will preferably undergo acidic fluxing, and in doing so, increases the local basicity of the melt according to Eq.4.42-4.43 (increases $\alpha Na_2O$). Simultaneously, $Cr_2O_3$ has its solubility minimum on the right side of the initial melt basicity, and would therefore undergo basic fluxing, whilst decreasing the melt basicity (increases $\alpha SO_3$) according to Eq.4.44-4.45.

As each fluxing mechanisms generates reaction products ($Na_2O$ or $SO_3$) which supports the dissolution of the other, a co-dissolution with a synergistic effect develops.

$$NiO_{(s)} + \mathbf{SO_{3(g)}} = NiSO_{4(diss)} \tag{4.42}$$

$$NiO_{(s)} + Na_2SO_{4(l)} = NiSO_{4(diss)} + \mathbf{Na_2O_{(diss)}} \tag{4.43}$$

$$Cr_2O_{3(s)} + \mathbf{Na_2O_{(diss)}} = 2NaCrO_{2(diss)} \tag{4.44}$$

$$Cr_2O_{3(s)} + Na_2SO_{4(l)} = 2NaCrO_{2(diss)} + \mathbf{SO_{3(g)}} \tag{4.45}$$

### 4.2.3 Two types of hot corrosion

Depending on the physical aggregate of the adhering salt-deposit, hot corrosion is further divided into two types: High temperature hot corrosion (HTHC), where the salt-deposit exits in a molten state (exposure temperature > melting temperature of salt deposit), and low temperature hot-corrosion (LTHC), where the salt adheres in a solid form (exposure temperature < melting temperature of salt deposit). However, the temperature dependent salt aggregate is not the only factor that differentiates LTHC from HTHC. With the $SO_3$-rich atmosphere being an integral part of the fluxing mechanisms, its presence or absence in the atmosphere has a huge impact on the hot corrosion mechanism. Fig.4.7a illustrates the thermodynamic and kinetic properties of the $SO_2$-$SO_3$ equilibrium reaction. Considering a homogeneous reaction (no catalytic effects), it is apparent that the formation of $SO_3$ is thermodynamically favored at low temperatures and approaches negligible amounts when approaching temperature close to 900 °C. With the kinetics behaving the other way, namely higher conversion rates with increasing temperature, it is evident that neither, very low temperatures < 500 °C nor very high temperatures > 950 °C can produce HC conditions where $SO_3$ plays a central role. Therefore, $SO_3$ driven HC reactions, such as acidic fluxing is generally expected in the LTHC regime, while basic fluxing is expected to dominate at low $\rho SO_3$ in the HTHC regime.

Fig.4.7b illustrates a summary of the aforementioned parameters that predetermine which type of HC is expected, as well as which chemical reactions tend to dominate the mechanism.

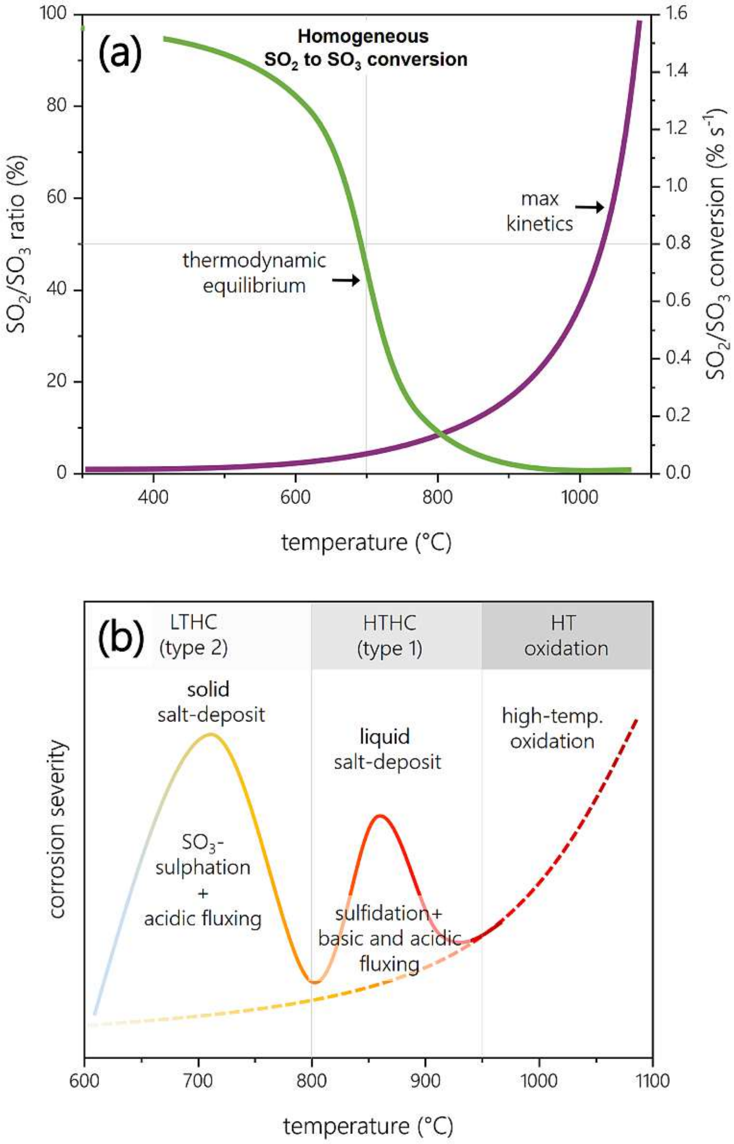

Figure 4.7: (a) Thermodynamic and kinetic properties of the homogeneous $SO_2$ to $SO_3$ conversion- adapted from [100]. (b) Illustration of the corrosion severity and predominant corrosion mechanisms of LTHC, HTHC and HT oxidation processes plotted over temperature.[101]

### Low temperature hot-corrosion (LTHC)

Considering $Na_2SO_4$ as the sole component of the salt-deposit, the presence of $SO_3$ in the environmental atmosphere is a crucial component in both the initiation, as well as subsequent propagation of the mechanism [102]. Thermodynamically favored at lower-temperatures [100], the formation of $SO_3$ in the atmosphere first facilitates an oxide to sulphate transition of the protective oxide scale. In the case of a Ni-based superalloy, this involves the sulphation of NiO scale. Once sulphation of the surface oxide has occurred, the formation of a low-melting $NiSO_4$-$Na_2SO_4$ eutectic develops. The higher the $SO_3$ content in the atmosphere, the higher the solubility of NiO in $NiSO_4$-$Na_2SO_4$ becomes, which again makes the partial pressure of $SO_3$ a controlling parameter [103]. Other protective oxides such as $Al_2O_3$ and $Co_2O_3$ may also react with $SO_3$ and form mixed metal sulfate eutectics with the $Na_2SO_4$ deposit ($NiSO_4$-$Na_2SO_4$ (671 °C), $Al_2(SO_4)_3$-$Na_2SO_4$ (640 °C) and $CoSO_4$-$Na_2SO_4$ (575 °C)) [104, 105]. This establishes a liquid oxide-salt interface that then functions as a transport medium for subsequent fluxing of the protective oxides scale [98]. It is generally accepted that a liquid salt deposit is necessary at the oxide-salt-interface to initiate the LTHC mechanism and provide a dynamic medium for accelerated dissolution reactions to occur.

From a thermodynamic perspective, many protective oxides, such as $Al_2O_3$, NiO and $Cr_2O_3$ react with $SO_3$ to form their respective sulphates. This highly depends on the temperature and partial pressure of $SO_3$ within the atmosphere. At 700 °C, however, the metal-oxide to metal-sulfate transformation for all three oxides is favored, making them all vulnerable to LTHC attack [97].

**High temperature hot corrosion (HTHC)**

HTHC occurs at significantly higher temperatures than LTHC. Premise for its initiation is an adherent molten salt-deposit, whereby two common propagation mechanisms can pursue: An alloy-induced acidic fluxing mechanism, or a basic fluxing mechanism [106]. Particularly interesting is the alloy-induced acidic fluxing, where acidic transient oxides of elements, such as W, Mo and V (solid solution hardeners in Ni-base super alloys) diffuse to the oxide scale surface and acidify the melt. For instance, $MoO_3$ reacts with $Na_2O$ from the $Na_2SO_4$ melt to form a complex metal oxide ($Na_2MoO_4$). By doing so, the local activity of NaO (basicity of the melt) is lowered, allowing for the acidic fluxing of $Cr_2O_3$ by expendable $MoO_3$ (Eq.4.46-4.47). Soluble within the $Na_2SO_4$ melt, the metal oxyanions ($MoO_4^{2-}$) and $Cr^{3+}$ cations diffuse towards the melt-surface, where $MoO_3$ evaporates (900 °C) and $Cr_2O_3$ precipitates as a porous non-protective oxide due to the higher $O^{2-}$-activity. Through the evaporation of $MoO_3$ and thus the transport of $O^{2-}$-species to the salt-gas interface, a negative concentration gradient for the $Cr_2O_3$ is ensured and provides a self-sustaining character [106].

$$Cr_2O_3 + 3MoO_3 \leftrightarrow Cr_2(MoO_4)_3 \tag{4.46}$$

$$Cr_2(MoO_4)_3 \leftrightarrow 2Cr^{3+} + 3MoO_4^{2-} \tag{4.47}$$

On the contrary, HTHC may also elicit basic fluxing of the protective oxides. Unlike acidic-fluxing, basic-fluxing is considered non-self-sustaining, and is ultimately dependent on the amount of salt-deposit available for the reactions.

Overall, it can be suggested that alloys with high contents of chromium and aluminum (chromia and alumina formers) are more prone to basic fluxing, whereas alloys with high contents of Mo, W and V are more sensitive to acidic fluxing.

# Chapter 5

# Methodology

Several analytical methods were used to experimentally test and examine the coating materials under study. This chapter will briefly touch on the most important methods, with additional information provided by the individual publications I-IV.

## 5.1 Electrochemical techniques

There is a plethora of tools that have been devised to mimic and study the corrosion phenomena that surround us. Ranging from its simplest form of 'immersing a material into a corrosive solution and observing it over time', to the more sophisticated implementation of electrochemical techniques that allow for a more accelerated and sensitive monitoring of a corrosion mechanism, the study of corrosion has come a long way from its inception in the late 1700s [107].

A powerful tool for investigating electrochemical corrosion phenomena is the three-electrode cell set-up coupled with a potentiostat. The system consist of a working electrode (sample under study, WE), a Ag/AgCl$_{(\mathrm{sat})}$ reference electrode (RE) and a Pt-counter electrode (CE), all housed within a press fit compartment that holds the electrolyte (Fig.5.1a). When in potentiostatic/potentiodynamic mode, the system will control the potential of the counter electrode against the working electrode. While the purpose of the RE is to measure the potential difference between itself and the WE, without exchanging any current, the function of the CE is to balance the current, which is generated/consumed by the working electrode. Fig.5.1b further illustrates how the individual electrodes are arranged within the cell. An external voltage is exerted by the potentiostat and passed through a control amplifier (CA). By switching the cell on and connecting the counter electrode, a potential difference is exerted against the working electrode, thereby polarizing it. Depending on the direction of the generated overpotential, either the oxidation half-reaction (electron generation) or the reduction half-reaction (electron consumption) will occur at the WE, while the CE will always host the opposite half-reaction. The generated currents are then measured by a current follower (CF) and communicated back to the system. Being operated in the

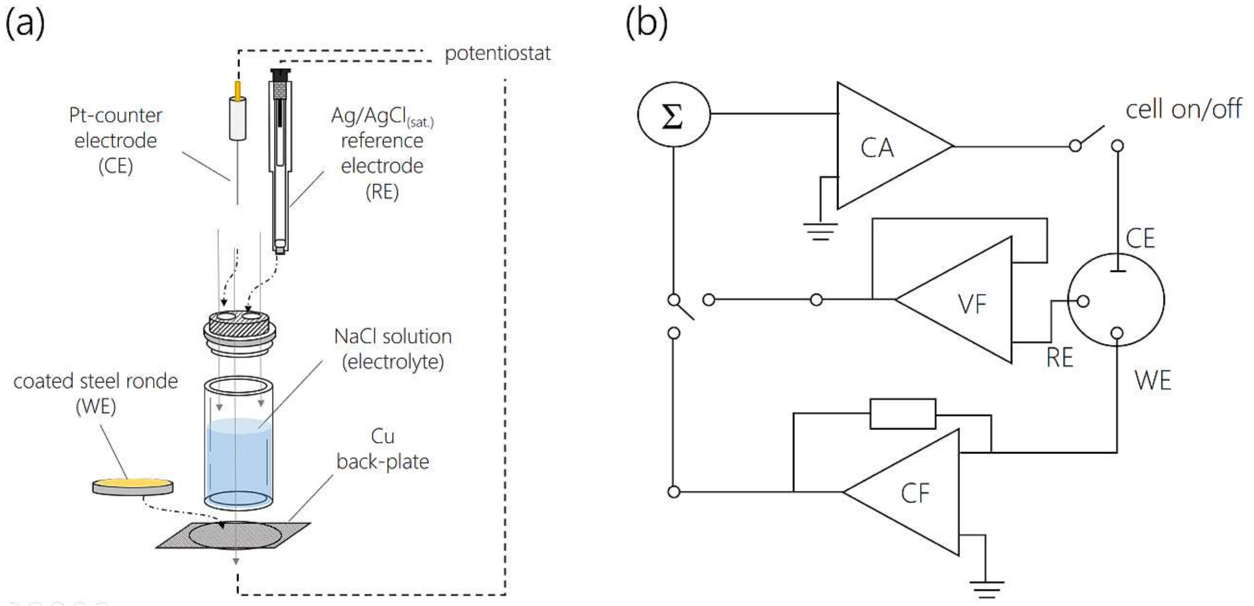

Figure 5.1: Schematic of (a) a three electrode corrosion cell and (b) its respective electrical circuit diagram-adapted from [108].

potentiostatic/potentiodynamic mode, the signal generated by the RE and voltage follower is fed back to the summation point ($\sum$), where it will be used as an input of the control amplifier.

### Linear potentiodynamic polarization (LPP)

As mentioned in previous sections, electrochemical systems can be perturbed by an external potential referred to as polarization. Electrochemical techniques that make use of such polarization phenomena by means of applying potentials include polarization resistance measurements, linear and cyclic potentiodynamic polarization experiments, as well as potentiostatic techniques. In all cases, an external potential is imposed onto an electrode, whose electrical response is monitored in the form of current. I-E plots are then generated and consulted for elucidating an electrode's electrochemical parameters, such as corrosion potential ($E_{corr}$), corrosion current density ($i_{corr}$) and polarization resistance ($R_p$). By departing further from the corrosion potential, additional electrochemical characteristics can be measured, which give further insight about the corrosion behavior of a particular material. Illustrated in Fig.5.2a is a generic representation of a potentiodynamic polarization curve highlighting distinctive electrochemical features that may be observed and interpreted when conducting such measurements.

For most metallic specimens in an aqueous environment, the cathodic branch (region of cathodic polarization) remains rather straightforward. Hydrogen evolution and oxygen reduction provide the majority of the cathodic current contribution, while the cathodic

Tafel-slope $\beta_c$ renders one of the necessary parameters for calculating (or extrapolating) the corrosion current density ($i_{corr}$). Unlike the cathodic region, the anodic branch provides much more divers correlations between the applied overpotential and measured current response. First there is the anodic Tafel slope, which, complementary to the $\beta_c$, provides a necessary parameter for the determination of $i_{corr}$. By increasing the positive overpotential further, inherent material properties, such as the ability to form a passivating oxide, have profound influence on the i-E relationship. Whereas metals which do not produce a thermodynamically stable corrosion product or passive oxides will follow an active dissolution with increasing overpotential (disregarding concentration polarization of the electrolyte), metals which do passivate follow an immediate passivation (spontaneous passivation) or activation delayed passivation (active to passive transition). In the case of the latter two, a passive region is usually featured where the measured current density does not change with increasing overpotential. At even higher potentials, localized breakdown of the previously formed passive layer can occur, which may further lead to accelerated galvanic corrosion (pitting) of the exposed alloy (if repassivation does not occur). Lastly, at sufficiently high overpotentials, dissolution and uniform breakdown of the passive oxide can ensue (transpassive dissolution), followed by the breakdown and oxidation of the aqueous electrolyte (oxygen generation) [109].

For aqueous solutions, hydrogen evolution on the cathodic spectrum and oxygen evolution on the anodic spectrum define the thermodynamic corridor within which corrosion can occur, which for neutral solutions covers a potential range of +1.23 V and -0.83 V (measured against SHE, Fig.5.2b) [110].

### Cyclic potentiodynamic polarization (CPDP)

An extension of the linear potentiodynamic polarization measurement is the cyclic potentiodynamic polarization method (CPDP). As the name infers, the applied potential is swept in a cyclic manner, where one cycle is comprised of a forward scan followed by an upper vertex point (where the potential sweep direction is reversed), and a revers scan followed by a lower vertex point, after which the potential is returned to the original start potential. Even though CPDP scans often involve multiple repetitions of such individual scans, a rudimentary execution of just one cycle can often provide sufficient information.

Fig.5.2c-d, for example illustrate such shortened cyclic potentiodynamic polarization measurements, each providing distinct electrochemical characteristics, which would have not been apparent by using the LPP method.

For instance, Fig.5.2c displays the log i-E plot of a material, which exhibits two things: Pitting corrosion and the proficiency to spontaneously passivate and repassivate. After the scan is swept through the materials initial corrosion potential (1→2, $E_{corr}$) the material enters a prolonged passive regime (2→$E_{pit}$). Subsequently, the material encounters its break-through

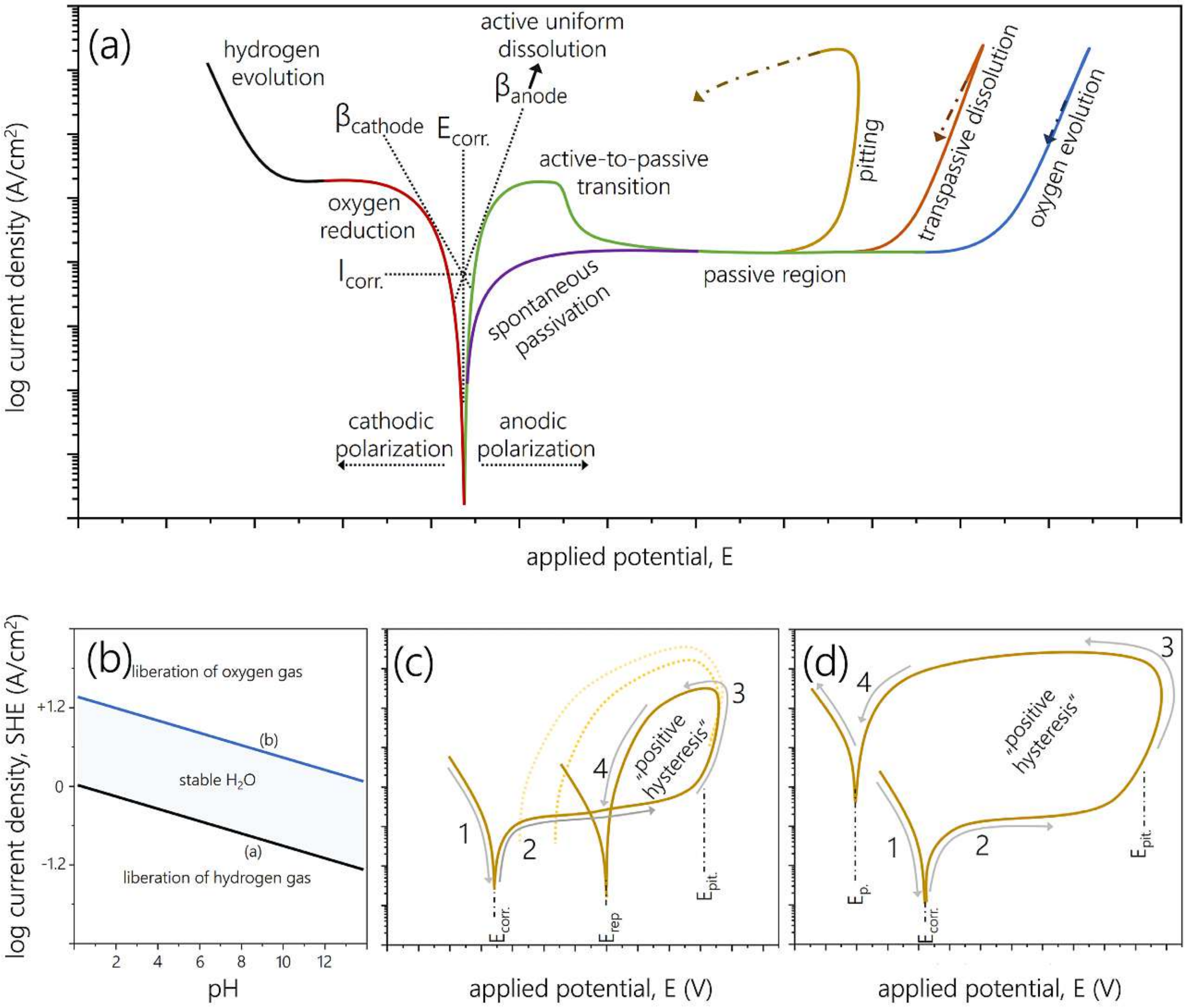

Figure 5.2: (a) shows a potentiodynamic polarization diagram that highlights the relationship between applied potential and the obtained external current densities for a variety of electrochemical processes. (b) features the Pourbaix diagram of water under standard conditions. (c-d) feature quasi-cyclic polarization measurements and highlight the effects of pitting and repassivation- adapted from [109–111].

potential (pitting potential) at which a sudden surge of current can be observed ($E_{pit}$). After reaching the measurements upper vertex point (return potential) the measured current continues to rise despite the applied potential being decreased (3). After a certain amount of time, and sufficient reduction of the overpotential, the current begins to drop and forms a positive hysteresis, which is indicative for pitting (3→4). Lastly, a second current minima is reached, however, at a significantly more noble potential then the initial $E_{corr}$, suggesting that the surface of the material has changed and produced a protective oxide. Depending on parameters such as the materials repassivation capability, the size of the forming pits, as well as the pit environment, pitting can progress more severely, which results in a larger hysteresis loop (highlighted by the dotted lines [111].

A different scenario is depicted by the cyclic measurement in Fig.5.2d. Similar to Fig.5.2c, a positive hysteresis is featured, however with the second current minima appearing at a lower potential in respect to $E_{corr}$. This infers that the material has suffered severe pitting, after which the exposed cavities are not repassivated and now provide a less noble and more active surface-electrolyte interaction. The resulting corrosion minimum is thus referred to as the new protection potential ($E_p$), which may or may not feature a higher corrosion current than the original $E_{corr}$. Such a behavior often pertains to PVD coated steel substrates, particularly for low alloy steels with no repassivation abilities [111].

## 5.2 Hot corrosion experiments

Over the years, a broad variety of techniques for analyzing hot corrosion phenomena has been devised in order to mimic hot corrosion mechanisms. Ranging from electrochemical arrangements as the likes from Rapp and Gotto [112], to crucible immersion test by Kameswary [113], to flow-reactor experiments of this work, and finally set-ups that involve real application combustion processes, all methods aim to further uncover the decisive driving forces that steer hot corrosion processes.

In order to combine the key elements of hot corrosion phenomena (e.g., $SO_x$-rich atmosphere, temperature, the dynamic flow of the atmosphere, and the influence of salt-deposits) in a lab sized and practical way, a flow-reactor set-up was chosen. Comprised of a gas-mixing system, a quartz-tube reactor, and a three-zone gradient furnace, the set-up allows for a precise modulation of the corrosion parameters, which have an immense influence on the resulting corrosion mechanism.

In order to generate a well-defined and controlled atmosphere for the hot corrosion experiments, three mass flow controlled (MFC) gas feeds were installed, each with a separate flow line to the quartz-reactor. In order to provide a continuous and homogeneous atmospheric condition, Ar was chosen as the carrier gas with the purpose of carrying and replenishing the reactive gas components throughout the reaction chamber (500-5000 sccm MFC). The reactive gases $O_2$ and $SO_2$ provide the corrosive character to the atmosphere and are controlled by 50-500 sccm and 1-10 sccm MFCs, respectively. According to reported $SO_3$ levels present in gas turbine exhaust gases [114–116], the concentrations of $SO_2$, $O_2$ and Ar were chosen such (2118 sccm(Ar), 375 sccm($O_2$), and 7 sccm($SO_2$)), that homogeneous conversion of $SO_2$ to $SO_3$ generated similar values over the course of the specific residence time of the gas mixture within the quartz-reactor [117].

For housing the corrosive atmosphere, together with the sample arrangement under study, a quartz-tube was chosen and positioned within a three-zone gradient furnace (Fig.5.3).

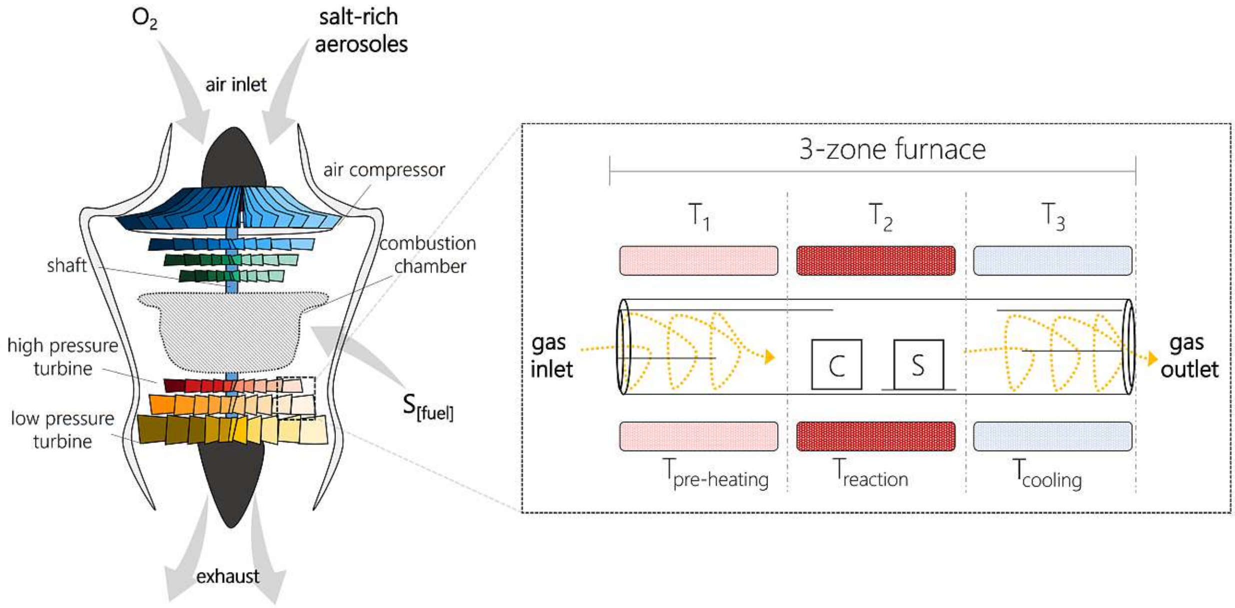

Figure 5.3: Schematic of a gas-turbine. Highlighted are sections of the HPT and LPT, whose operational condition (temperature and atmosphere) stand at the center of the HC testing rig concept. Featured is a hot corrosion quartz-tube reaction chamber, positioned within a three-zone gradient furnace, allowing for adjustments in gas-flow, temperature, composition of the atmosphere and sample positioning.

Providing excellent heat-conduction, the first heating zone ($T_1$) is devoted to the heating of the gas mixture, whereas the second heating zone ($T_2$) is designated for controlling the temperature of the corrosion reaction. The control samples (C) without salt deposits are thereby positioned before the samples loaded with salt (S) in order to avoid cross contamination through volatile salt fumes that are carried downstream. In zone $T_3$ the gas is cooled down before exiting the quartz-reactor and washed in a neutralization bath.

# Bibliography

[1] S. Li and L. H. Hihara, Journal of The Electrochemical Society **161**, C268 (2014).

[2] P. Refait, A.-M. Grolleau, M. Jeannin, C. Rémazeilles, and R. Sabot, Corrosion and Materials Degradation **1**, 198 (2020).

[3] S. Caines, F. Khan, and J. Shirokoff, Journal of Loss Prevention in the Process Industries **26**, 1466 (2013).

[4] S. X. Li and L. H. Hihara, Corrosion Engineering Science and Technology **45**, 49 (2010).

[5] J. Alcántara, D. de la Fuente, B. Chico, J. Simancas, I. Díaz, and M. Morcillo, Materials **10**, 1 (2017).

[6] N. S. Patel, V. Pavlík, and M. Boča, Critical Reviews in Solid State and Materials Sciences **42**, 83 (2017).

[7] S. H. Lee, N. J. Themelis, and M. J. Castaldi, Journal of Thermal Spray Technology **16**, 104 (2007).

[8] G. Sorell, Materials at High Temperatures **14**, 207 (1997).

[9] J. Phother-Simon, I. Hanif, T. Jonsson, and J. Liske, Fuel **357**, 1 (2024).

[10] J. Sieber, D. Broton, C. Fales, S. Leigh, B. MacDonald, A. Marlow, S. Nettles, and J. Yen, Cement and Concrete Research **32**, 1915 (2002).

[11] A. Atkinson and J. Corish, NATO ASI Series, Series B: Physics **97**, 477 (1983).

[12] R. T. Loto, Journal of Materials and Environmental Science **6**, 2750 (2015).

[13] G. T. Burstein, C. Liu, R. M. Souto, and S. P. Vines, Corrosion Engineering Science and Technology **39**, 25 (2004).

[14] S. M. Qidwai and A. C. Leung, in *A Review of Microstructural Effects on Pitting Corrosion in Stainless Steels* (2011) pp. 1–3.

[15] J. Stringer, Annual Review of Materials Research **7**, 477 (1977).

[16] S. Hu, H. Finklea, and X. Liu, Journal of Materials Science and Technology **90**, 243 (2021).

[17] N. Eliaz, G. Shemesh, and R. M. Latanision, Engineering Failure Analysis **9**, 31 (2002).

[18] B. Salehnasab, E. Poursaeidi, S. A. Mortazavi, and G. H. Farokhian, Engineering Failure Analysis **60**, 316 (2016).

[19] H. H. Krause, Journal of Materials for Energy Systems **7**, 322 (1986).

[20] Y. Kawahara, Corrosion Science **44**, 223 (2002).

[21] D. Mudgal, L. Ahuja, D. Bhatia, S. Singh, and S. Prakash, Engineering Failure Analysis **63**, 160 (2016).

[22] S. Kumar, M. Kumar, and A. Handa, Engineering Failure Analysis **94**, 379 (2018).

[23] V. Chawla, A. Chawla, D. Puri, S. Prakash, P. G. Gurbuxani, and B. S. Sidhu, Journal of Minerals and Materials Characterization and Engineering **10**, 367 (2011).

[24] P. Pan, T. Li, Y. Wang, N. Zhang, and H. Chen, Corrosion Science **203**, 110350 (2022).

[25] T. S. Sidhu, R. D. Agrawal, and S. Prakash, Surface and Coatings Technology **198**, 441 (2005).

[26] T. S. Sidhu, S. Prakash, and R. D. Agrawal, Current Science **90**, 41 (2006).

[27] S. S. Kalsi, International Journal on Emerging Technologies **7**, 4 (2016).

[28] R. A. Rapp, Corrosion Science **44**, 209 (2002).

[29] H. Bisaria and P. Shandilya, Materials and Manufacturing Processes **34**, 83 (2019).

[30] X. Zhang, Y. Chen, and J. Hu, Progress in Aerospace Sciences **97**, 22 (2018).

[31] T. M. Pollock and S. Tin, Journal of Propulsion and Power **22**, 361 (2006).

[32] N. Rao, *Advances in Gas Turbine Technology* (2011) pp. 293–314.

[33] J. L. Vossen and W. Kern, *Thin Film Processes II*, edited by J. L. Vossen and W. Kern (Academic Press Inc., San Diego, 1991).

[34] D. M. Mattox, *Film Formation, Adhesion, Surface Preparation and Contamination Control* (New Jersey, 1998).

[35] E. Blechschmidt and A. v. Hippel, *Der Einfluß von Material und Zustand der Kathode auf den Zerstäubungsprozeß*, Vol. 391 (2006) pp. 1006–1024.

[36] D. L. Smith, *Thin-film Deposition: Principles And Practice* (McGraw-Hill Professional, 1995).

[37] K. Wasa, M. Kitabatake, and H. Adachi, *Handbook of Sputter Deposition Technology* (William Andrew Publishing, New York, 2004).

[38] H. Frey and H. R. Khan, *Handbook of Thin-Film Technology* (Springer Berlin Heidelberg, Berlin, Heidelberg, 2015).

[39] D. M. Mattox, *Handbook of Physical Vapor Deposition (PVD) Processing* (2010) pp. 237–286.

[40] D. Erdemir, A. Y. Lee, and A. S. Myerson, ChemInform **40** (2009).

[41] H. Mehrer, *Fundamentals,Methods,Materials, Diffusion-Controlled Processes* (Springer Berlin Heidelberg, 2007).

[42] R. E. Smallman, *Modern Physical Metallurgy and Materials Engineering*, 6th ed. (Butterworth-Heinemann, 1999).

[43] D. Gupta and P. S. Ho, Thin Solid Films **72**, 399 (1980).

[44] C. Sabitzer, C. Steinkellner, C. M. Koller, P. Polcik, R. Rachbauer, and P. H. Mayrhofer, Surface and Coatings Technology **275**, 185 (2015).

[45] A. Paul, T. Laurila, V. Vuorinen, and S. V. Divinski, *Thermodynamics, Diffusion and the Kirkendall Effect in Solids* (Springer International Publishing Switzerland, 2014).

[46] M. L. Cedeño-Vente, J. Manríquez, G. C. Mondragón-Rodríguez, N. Camacho, A. E. Gómez-Ovalle, J. M. Gonzalez-Carmona, J. M. Alvarado-Orozco, and D. G. Espinosa-Arbelaez, Ceramics International **47**, 20885 (2021).

[47] P. Panjan, A. Drnovšek, P. Gselman, M. Čekada, M. Panjan, T. Bončina, and D. K. Merl, Coatings **9**, 1 (2019).

[48] H. W. Wang, M. M. Stack, S. B. Lyon, P. Hovsepian, and W. D. Münz, Surface and Coatings Technology **126**, 279 (2000).

[49] L. Ward, A. Pilkington, and S. Dowey, Coatings **7** (2017).

[50] R. J. Borg and G. J. Dienes, *An Introduction to Solid State Diffusion* (Academic Press Inc., London, 1988) pp. 1–360.

[51] Khanna A. S., *High Temperature Oxidation and Corrosion of Metals*, CASTI Corrosion Series (Elsevier, 2016).

[52] R. Smallman and A. Ngan, in *Modern Physical Metallurgy* (Elsevier, 2014) pp. 617–657.

[53] J.-S. Zhang, *Environmental Damage at High Temperature* (Woodhead Publishing, 2010) pp. 230–238.

[54] D. Monceau and B. Pieraggi, Oxidation of Metals **50**, 477 (1998).

[55] I. I. Kornilov, M. N. Zabrodskaya, N. G. Boriskina, and A. P. Brynza, Metal Science and Heat Treatment **19**, 387 (1977).

[56] R. Smallman and R. Bishop, in *Modern Physical Metallurgy and Materials Engineering* (Butterworth-Heinemann, 1999) pp. 376–393.

[57] D. J. Young, *High Temperature Oxidation and Corrosion of Metals*, 2nd ed., Corrosion Series (Elsevier, 2016).

[58] J. Bockris, B. E. Conway, E. Yeager, and R. E. White, *Electrochemical Materials Science*, edited by J. O. Bockris, B. E. Conway, E. Yeager, and R. E. White (Springer US, Boston, MA, 1981) pp. 1–96.

[59] N. Perez, *Springer International Publishing AG*, 2nd ed. (Springer International Publishing, Cham, 2016).

[60] H. H. Strehblow and P. Marcus, *Corrosion Mechanisms in Theory and Practice*, edited by P. Marcus (CRC Press, 2002).

[61] R. Cottis and L. L. Shreir, *Basic Concepts, High Temperature Corrosion*, 4th ed., edited by R. A. Cottis, M. J. Graham, R. Lindsay, S. B. Lyon, J. A. Richardson, J. D. Scantlebury, and F. H. Stott (Elsevier Amsterdam, Amsterdam, 2010).

[62] S. Petrovic, *Electrochemistry Crash Course for Engineers* (Springer International Publishing, Cham, 2021) pp. 1–108.

[63] J. T. Stock, *Electrochemistry, Past and Present* (American Chemical Society, Washington, DC, 1989) pp. 1–17.

[64] F. Torabi and P. Ahmadi, in *Simulation of Battery Systems* (Elsevier, 2020) pp. 55–81.

[65] G. Jerkiewicz, ACS Catalysis **10**, 8409 (2020).

[66] R. Buchanan and E. Stansbury, in *Handbook of Environmental Degradation of Materials* (Elsevier, 2012) pp. 87–125.

[67] Z. Ahmad, *Principles of Corrosion Engineering and Corrosion Control* (Elsevier, 2006) pp. 57–119.

[68] F. Mansfeld, Corrosion **62**, 843 (2006).

[69] M. Fontana, *The Polarization Resistance Technique for Measuring Corrosion Currents* (1976) pp. 163–262.

[70] H. Hack, in *Shreir's Corrosion*, Vol. 1 (Elsevier, 2010) pp. 828–856.

[71] G. A. Cragnolino, in *Techniques for Corrosion Monitoring* (Elsevier, 2008) pp. 6–45.

[72] B. Bhattacharyya, in *Electrochemical Micromachining for Nanofabrication, MEMS and Nanotechnology* (Elsevier, 2015) pp. 25–52.

[73] P. Kurzweil, in *Electrochemical Energy Storage for Renewable Sources and Grid Balancing* (Elsevier, 2015) pp. 345–407.

[74] J. Richardson and G. Wood, Corrosion Science **10**, 313 (1970).

[75] Y. F. Cheng, M. Wilmott, and J. L. Luo, Applied Surface Science **152**, 161 (1999).

[76] H. DorMohammadi, Q. Pang, P. Murkute, L. Árnadóttir, and O. B. Isgor, npj Materials Degradation **3**, 19 (2019).

[77] J. Creus, H. Idrissi, H. Mazille, F. Sanchette, and P. Jacquot, Surface and Coatings Technology **107**, 183 (1998).

[78] J. Vega, H. Scheerer, G. Andersohn, and M. Oechsner, Corrosion Science **133**, 240 (2018).

[79] W. Brandl, C. Gendig, and K. Reichel, Materials and Corrosion - Werkstoffe und Korrosion **47**, 208 (1996).

[80] M. Flores, L. Huerta, R. Escamilla, E. Andrade, and S. Muhl, Applied Surface Science **253**, 7192 (2007).

[81] C. Liu, A. Leyland, Q. Bi, and A. Matthews, Surface and Coatings Technology **141**, 164 (2001).

[82] S. Ahn, J. Lee, H. Kim, and J. Kim, Applied Surface Science **233**, 105 (2004).

[83] R. Ananthakumar, B. Subramanian, A. Kobayashi, and M. Jayachandran, Ceramics International **38**, 477 (2012).

[84] L. Cunha, M. Andritschky, L. Rebouta, and K. Pischow, Surface and Coatings Technology **116-119**, 1152 (1999).

[85] Y. Wan, J. Tan, S. Zhu, J. Cui, K. Zhang, X. Wang, X. Shen, Y. Li, and X. Zhu, Corrosion Science **152**, 226 (2019).

[86] W. S. Tait, in *Handbook of Environmental Degradation of Materials* (Elsevier, 2018) pp. 97–115.

[87] K. Kuratani, K. Fukami, H. Tsuchiya, H. Usui, M. Chiku, and S.-i. Yamazaki, Electrochemistry **90**, 22 (2022).

[88] A. Poursaee, Cement and Concrete Research **40**, 1451 (2010).

[89] S. B. Abusuilik and K. Inoue, Surface and Coatings Technology **237**, 421 (2013).

[90] J. Creus, H. Mazille, and H. Idrissi, Surface and Coatings Technology **130**, 224 (2000).

[91] S. Bose, *High Temperature Coatings*, 1st ed. (Elsevier, 2007).

[92] R. C. Brown, M. R. Anderson, and C. E. Kolb, Geographical Research Letters **23**, 3603 (1996).

[93] E. Yazhenskikh, T. Jantzen, D. Kobertz, K. Hack, and M. Müller, Calphad **72**, 102234 (2021).

[94] D. Young, *High Temperature Oxidation and Corrosion of Metals*, Vol. 1 (Elsevier Corrosion Series, 2008).

[95] X. Zheng and R. A. Rapp, Journal of The Electrochemical Society **140**, 2857 (1993).

[96] K. L. Luthra, Metallurgical Transactions A **13**, 1853 (1982).

[97] K. J. Meisner and E. J. Opila, Oxidation of Metals **94**, 301 (2020).

[98] J. M. Alvarado-Orozco, J. E. Garcia-Herrera, B. Gleeson, F. S. Pettit, and G. H. Meier, Oxidation of Metals **90**, 527 (2018).

[99] W. Gao and Z. Li, *Developments in high-temperature corrosion and protection of materials*, 1 (Woodhead Publishing Limited, 2008).

[100] Y. Sarbassov, L. Duan, V. Manovic, and E. J. Anthony, Greenhouse Gases: Science and Technology **0**, 1 (2018).

[101] Y. Garip and O. Ozdemir, Journal of Alloys and Compounds **780**, 364 (2019).

[102] D. A. Shifler, Materials at High Temperatures **35**, 225 (2018).

[103] T. Gheno and B. Gleeson, Oxidation of Metals **84**, 567 (2015).

[104] B. Grégoire, X. Montero, M. C. Galetz, G. Bonnet, and F. Pedraza, Corrosion Science **141**, 211 (2018).

Y. Wang, R. Pillai, E. Yazhenskikh, M. Frommherz, M. Müller, and D. Naumenko, Advanced Engineering Materials **22**, 1 (2020).

B. S. Lutz, J. M. Alvarado-Orozco, L. Garcia-Fresnillo, and G. H. Meier, Oxidation of Metals **88**, 599 (2017).

O. Smutok and E. Katz, Journal of Solid State Electrochemistry (2023).

Metrohm, "Nova User Manual," (2018).

S. Choudhary, K. Ogle, O. Gharbi, S. Thomas, and N. Birbilis, Electrochemical Science Advances **2**, 1 (2022).

B. J. Wiersma, The US Department of Energy , 1 (2004).

S. Esmailzadeh, M. Aliofkhazraei, and H. Sarlak, Protection of Metals and Physical Chemistry of Surfaces **54**, 976 (2018).

R. A. Rapp and Y. S. Zhang, JOM **46**, 47 (1994).

S. Kameswari, Oxidation of Metals **26**, 33 (1986).

R. L. Jones and S. T. Gadomski, Journal of Electrochemical Society **129**, 1613 (1980).

D. Fleig, K. Andersson, F. Normann, and F. Johnsson, Industrial & Engineering Chemistry Research **50**, 8505 (2011).

L. P. Belo, L. K. Elliott, R. J. Stanger, R. Spörl, K. V. Shah, J. Maier, and T. F. Wall, Energy & Fuels **28**, 7243 (2014).

A. Scheiber, *Design and Mechanical Construction of a Hot-Corrosion Testing System*, M.Sc. thesis, TU Wien (2020).

# Chapter 6

# Scientific contributions

## 6.1 Assessing the corrosion behavior of PVD coatings in chloride-rich aqueous media

*Publication I*

### Pitting corrosion – Preferred chloride diffusion pathways in physical vapor deposited AlCrN coatings

**O.E. Hudak**, A. Bahr, P. Kutrowatz, T. Wojcik, F. Bohrn, L. Solyom, R. Schuster, L. Shang, O. Hunold, P. Polcik, M. Heller, P. Felfer, G. Ball, and H. Riedl. *Corrosion Science*, 211 (2022), 110901.

The general incentive for depositing PVD hard coatings is clear- to improve the wear resistance of softer and cheaper materials (often steels) in order to make them more applicable in highly demanding environments. However, particularly for applications in energy production sectors, automotive-industries, and aviation, aggressive environments such as coolants, exhaust gases, and salt-particulates from coastal areas and road salts bring forth new, corrosion related challenges. Even though PVD hard coatings are extremely stable and chemically inert throughout a broad range of environments, they are nevertheless notorious for inducing pitting corrosion of the steel it is intended to protect. Due to their nature of having a myriad of coating defects, imperfections and porosities, salt-rich media is able to permeate the coatings protective barrier and form an aggressive galvanic couple between the coating and the underlying steel.

This study intends to showcase preferred diffusion paths that exist for cathodic arc evaporated, as well as magnetron sputtered $Al_{1-x}Cr_xN$ coatings. Using a three-electrode electrochemical approach in order to induce pitting behavior, an array of analytical methods was devoted to systematically reveal the weak spots for each coating method. Substantial EDX and SEM investigation revealed for arc evaporated $Al_{1-x}Cr_xN$ coatings, fast-tracked diffusion of the NaCl-rich electrolyte was exclusively observed along incoherently incorporated macroparticles, resulting in rapid oxidation of their metallic cores and consequent pit initiation. For sputtered $Al_{1-x}Cr_xN$ coatings, on the other hand, the most abundantly observed pit initiation mechanism resulted from diffusion routes along open column domains, with a partially coarse-grained microstructure and unidirectional column growth facilitating fast-track diffusion to the coating-substrate interface.

Lastly, high-resolution techniques, such as *t*-EBSD, APT and SIMS, provided novel insights about the distinct differences in the diffusion behavior of aggressive ions (e.g., chloride) through pristine sputtered and arc evaporated coating sites. The obtained results strongly suggest that a fine-grained morphology together with a randomly orientated growth orientation are key properties that translate to improved diffusion resistance.

### *Publication II*

## Improved corrosion resistance of cathodic arc evaporated $Al_{0.7}Cr_{0.3-x}V_xN$ coatings in NaCl-rich media

**O.E. Hudak**, P. Kutrowatz, T. Wojcik, E. Ntemou, D. Primetzhofer, L. Shang, J. Ramm, O. Hunold, S. Kolozsvári, P. Polcik, and H. Riedl. *Corrosion Science* 221 (2023), 111376.

With current state-of-the-art corrosion resistant coatings being far from optimized, saline environments remain a technological frontier, where machining elements suffer accelerated breakdown through a localized corrosion mechanism called – pitting. Particularly PVD hard coatings with their intrinsically high degree of porosities, macroparticles, and the overall columnar growth orientation makes are susceptible to inward-diffusion of corrosive media and allow for an accelerated attack at the coating substrate interface.

This study showcases two concepts for mitigating fast-track diffusion pathways in cathodic arc evaporated $Al_{0.7}Cr_{0.3}N$ coatings- a doping strategy with vanadium, and an annealing treatment- as viable approaches for improving the corrosion behavior of the previously discussed $Al_{0.7}Cr_{0.3}N$ system. In order to investigate the beneficial effects of vanadium, a series of $Al_{0.7}Cr_{0.3-x}V_xN$ coatings were deposited on a low-alloy steel, with V-contents ranging between 0 and 22.3 at.% on the metal sublattice. Electrochemical tests of the as-deposited, as well as annealed coatings were conducted in a 0.1 M NaCl solution using a three-electrode cell set up, whereupon extrapolations of Tafel-plots were used to evaluate the corrosion resistance. According to the Stern-Geary relation, polarization resistances, as well as an approximation of the related open porosity values were calculated.

The key findings of the experiments reviled a direct relationship between the V-content and grain-refinement of the coating morphology. The more V was doped to the $Al_{0.7}Cr_{0.3}N$ base system, the more refined the coating morphology turned out. Interestingly, a direct correlation was also noted between the V-content and corrosion current densities obtained from the Tafel extrapolations, leading to the belief, that grain-refinement promotes improved corrosion resistance.

Further reduction in the corrosion current densities and related open porosity values was achieved through an annealing step. In a second series of corrosion experiments, $Al_{0.7}Cr_{0.3-x}V_xN$ coatings deposited on a low-alloy steel, with V-contents ranging between 0 and 22.3 at.% on the metal sublattice were first annealed at 700 °C for 3 h before undergoing electrochemical analysis. Results showed that coatings with higher V-contents not only featured more prominent oxidation (scale formation), but also significantly lower corrosion currents. The improved corrosion resistance by $Al_{0.7}Cr_{0.3-x}V_xN$ coatings with elevated V contents was credited to the sealing of open porosities by the growing oxide scale and therefore reduced reactive sites between unprotected alloy and the electrolyte.

## 6.2 Hot corrosion behavior of arc evaporated coatings

*Publication III*

### Low-temperature hot corrosion of arc evaporated $Ti_{1-x}Al_xN$ on Ni-Cr-Co based superalloys

**O.E. Hudak**, A. Scheiber, P. Kutrowatz, T. Wojcik, L. Shang, O. Hunold, S. Kolozsvári, P. Polcik, and H. Riedl. *Corrosion Science* 224 (2023), 111565.

Throughout this study, the low-temperature hot corrosion (LTHC) resistance of arc evaporated $Ti_{1-x}Al_xN$ coatings is discussed. In a series of LTHC experiments, $Ti_{1-x}Al_xN$ coatings were deposited onto an industrially established NiCrCo-based superalloy (Nimonic c263) and treated with a $MgSO_4/Na_2SO_4$ salt-mixture (20:80 mol/mol) before annealing them at 700 °C in a 3000 ppm(volume) $SO_x$-rich atmosphere for 1, 5, 15 and 30 h. Significant reduction in the corrosion severity was exhibited by all $Ti_{1-x}Al_xN$ variants over the uncoated NiCrCo-based superalloy, which substantiates the notion that PVD coatings can be implemented as protective measures for superalloys in hot corrosion environments. Delving deeper into the specific corrosion mechanism of $Ti_{1-x}Al_xN$, a synergistic fluxing mechanism was found to be the dominant factor for film breakdown. Depending on the relative Al-to-Ti content on the metallic sublattice, differences in the coatings' corrosion and scaling behavior were observed. For compositions approaching a 1:1 Al to Ti ratio, a thin $Al_2O_3$ top-oxide, followed by a highly sequenced $TiO_2/Al_2O_3$ laminate structure was featured. Contrarily, for Al-Ti ratios >1:1, a pronounced $Al_2O_3$ top scale with a more broadened layering of the $TiO_2/Al_2O_3$ domains was noticed. The findings of this study highlight the profound interplay that exists between the chemical makeup of the protective coating and the resulting scaling behavior in HC environments.

### *Publication IV*

## High-temperature hot corrosion kinetics of arc evaporated $Ti_{1-x}Al_xN$ on Ni-Cr-Co-based superalloys

**O.E. Hudak**, A. Scheiber, P. Kutrowatz, T. Wojcik, R. Hahn, J. Ramm, O. Hunold, S. Kolozsvári, P. Polcik, and H. Riedl. Submitted at *Surface & Coatings Technology*, since 31.10.2023

$Ti_{1-x}Al_xN$ is a well-studied material class that has established its place among the most widely used protective coatings in high temperature environments, due to its high hardness, age-hardening effect an excellent oxidation resistant up to 850 °C. However, quite little is known about its behavior in hot corrosion settings at similar temperatures. For this reason, this study intents to extend the knowledge surrounding the $Ti_{1-x}Al_xN$ system by presenting new insights about the structural evolution, oxidation kinetics and scaling behavior of cathodic arc evaporated (CAE) $Ti_{1-x}Al_xN$ coatings in high-temperature hot corrosion environments. $Ti_{1-x}Al_xN$ coatings were deposited on an industrially established NiCrCo-based superalloy and tested using an in-house built hot corrosion testing rig at 850 °C in a $SO_x$-rich atmosphere. Preliminary annealing experiments were conducted over a temperature range of 700-850 °C (without salt deposits) in order to evaluate the oxygen inward diffusion behavior of $Ti_{1-x}Al_xN$ coatings in a $SO_x$-rich environments. Evaluation of EDX measurements provided oxygen diffusion profiles that best fit a quasi-cubic rate-law.

Thereafter, salt loaded experiments were performed at 850 °C by applying a $MgSO_4$-$Na_2SO_4$ salt mixture to the sample surface and corroded in a $SO_x$-rich atmosphere for a maximum of 30 h. Analysis by EDX and TEM revealed a significant increase in the oxidation kinetics when salt deposits were added under identical $SO_2$-enriched atmospheric conditions. Compared to the quasi-cubic rate laws exhibited for the c-263 alloy and $Ti_{1-x}Al_xN$ coatings in the absence of a salt deposit, the c-263 alloy now followed a compounded parabolic-linear rate law (n=1.5). At the same time, both $Ti_{0.52}Al_{0.48}N$ and $Ti_{0.34}Al_{0.66}N$ feature a parabolic-like rate behavior (n=2.3 and n=2.2, respectively). Thus, a significantly improved corrosion resistance is expressed by the cae-$Ti_{1-x}Al_xN$ samples over the bare c-263 alloy.

The HTHC mechanism was described according to the growth behavior of the corrosion scale. In summary, a sequential fluxing mechanism of Ti-rich and Al-rich oxide domains was found to be the dominating corrosion mechanism, resulting in the formation of a layered corrosion scale. Due to the more basic character of $TiO_2$ (more stable under basic conditions) over $Al_2O_3$, a porous $TiO_2$ scale predominantly develops at the scale-salt interface, followed by a voluminous Al-rich oxide band below. Lastly, no internal sulfidation was observed at the corrosion front of the $Ti_{1-x}Al_xN$-coatings, which was regarded as one of the main reasons for their improved corrosion resistance over the c-263 alloy.

## 6.3 Co-author publications

**Influence of the non-metal species on the oxidation kinetics of Hf, HfN, HfC, and $HfB_2$ coatings**

T. Glechner, **O.E. Hudak**,T. Wojcik, L. Haager, F. Bohrn, H. Hutter, O. Hunold, J. Ramm, S. Kolozsvári, E. Pitthan, D. Primetzhofer, and H. Riedl. *Materials & Design*, 211 (2021) 110136.

**TGO formation and oxygen diffusion in Al-rich $\gamma$-TiAl PVD-coatings on TNM alloys**

S. Kagerer, **O.E. Hudak**,M. Schloffer, H. Riedl, and P.H. Mayrhofer. *Scripta Materialia*, 210 (2022), 114455.

**Oxidation protection of TNM alloys with Al-rich $\gamma$-TiAl-based coatings**

S. Kagerer, **O.E. Hudak**,T. Wojcik, R. Hahn, A. Davydok, M. Schloffer, H. Riedl, and P.H. Mayrhofer. *Journal of Alloys and Compounds*, 969 (2023) 172343.

## 6.4 Supervised students

**Alexander Scheiber**

*Design and Mechanical Construction of a Hot-Corrosion Testing System*

Master thesis

Finished 11. 2020

**Bernhard Ivo Mittenecker**

*A study on the effect of V-doping on the mechanical-, oxidation-, and corrosion properties of physical vapor deposited* $(Ti,Al)_{1-x}V_xN$ *hard coatings*

Bachelor thesis

Finished 11. 2023

## 6.5 Participation at international conferences

**ICMCTF Virtual Conference 2021**

Online, 26-30.04.2021

*Corrosion induced diffusion pathways in thin film materials investigated by atom probe tomography*

O.E. Hudak, E. Aschauer, V. Dalbauer, L. Shang, O. Hunold, M. Arndt, P. Polcik, P. Felfer, and H. Riedl.

**AVS 67 Virtual Symposium 2021**

Online, 25–28.10.2021

*Corrosion induced diffusion pathways in thin film materials investigated by atom probe tomography*

O.E. Hudak, E. Aschauer, V. Dalbauer, L. Shang, O. Hunold, M. Arndt, P. Polcik, P. Felfer, and H. Riedl.

**ICMCTF 2022**

San Diego, USA, 22-27.05.2022

*Arc evaporated* $Ti_{1-x}Al_xN$ *coatings in hot corrosion settings*

O.E. Hudak, A. Scheiber, L. Shang, O. Hunold, M. Arndt, S. Kolozsvári, and H. Riedl.

**Plansee Seminar 2022**

Reutte, Austria, 30.05-03.06.2022

*Arc evaporated* $Ti_{1-x}Al_xN$ *coatings in hot corrosion settings*

O.E. Hudak, A. Scheiber, L. Shang, O. Hunold, M. Arndt, S. Kolozsvári, and H. Riedl.

**PSE 2022**

Erfurt, Germany, 12-15.09.2022

*Hot corrosion mechanisms of arc evaporated* $Ti_{1-x}Al_xN$ *coatings*

O.E. Hudak, A. Scheiber, L. Shang, O. Hunold, M. Arndt, S. Kolozsvári, and H. Riedl.

**ICACC 2023**

Daytona, USA, 22-27.01.2023

$Ti_{1-x}Al_xN$ *PVD coatings in hot corrosion environments*

O.E. Hudak, A. Scheiber, L. Shang, O. Hunold, M. Arndt, S. Kolozsvári, and H. Riedl.

# Chapter 7

# Concluding remarks

This thesis presents a framework for studying and understanding corrosion driven phenomena in physical vapor deposited coatings and intends to extend their range of application. Focusing on transition metal nitride (TMN) coatings, salt induced corrosion phenomena, such as pitting corrosion and hot corrosion, provide the scope within which the corrosion behavior of TMNs will be discussed.

As far as evaluating the corrosion resistance of PVD coated alloys goes, passivity is without doubt the most decisive property of all. Possessing the ability of structurally separating an aggressive medium from a base material, while remaining chemically stable must therefore be of upmost importance, if PVD coatings are to be considered as feasible approaches. In this regard, Publication I showcased that chemically inert PVD $Al_{0.7}Cr_{0.3}N$ coatings, whether sputtered or arc evaporated, provide substantial coating defects and diffusion routs for aggressive media to permeate the coating structure. By exposing both magnetron sputtered and arc evaporated $Al_{0.7}Cr_{0.3}N$ coated low steel using a potentiodynamic polarization technique, preferred chloride diffusion was identified along underdense column boundaries, as well as along embedded macroparticles. Moreover, Publication I provides novel insights about the degree of passivity of pristine coating sites - locations exhibiting no apparent defects. Using an array of high-resolution analytical techniques, such as atom probe tomography (APT), time of flight secondary ion mass spectroscopy (ToF-SIMS), and transmission electron back scattered diffraction (*t*-EBSD), it was possible to interrelate a higher degree of passivity with a random crystallographic growth orientation and a refined grain morphology.

Considering these findings, Publication II investigated additional approaches for increasing the passive behavior of arc evaporated $Al_{0.7}Cr_{0.3}N$ coatings in aqueous NaCl-rich solutions. By means of a doping strategy, which involved substituting Cr with V on the metal sublattice, significant grain refinement of the $Al_{0.7}Cr_{0.3-x}V_xN$ coatings compared to the original $Al_{0.7}Cr_{0.3}N$ base system was achieved. Standing in good agreement with the findings from Publication I, electrochemical investigations of the $Al_{0.7}Cr_{0.3-x}V_xN$ showed a positive correlation between grain-refined morphologies (more dense) and improved corrosion resistance. To further reduce fast-track diffusion routs along embedded macroparticles and defect related coating features, an annealing strategy was implemented in addition to the grain-refinement by V-doping. Through the formation of a coarse grained V-rich top oxide and an underlying nanocrystalline V-depleted Al-rich oxide band, additional reduction in fast track-diffusion pathways and open-porosity values was achieved, further improving the corrosion resistance and lowering of the measured corrosion current densities.

Having investigated the passive behavior of chemically inert $Al_{0.7}Cr_{0.3}N$ and $Al_{0.7}Cr_{0.3\text{-}x}V_xN$ coatings in aqueous media, where structural impairments determined the passivity of the coatings, Publication III and IV extend the scope of protective PVD coating to aggressive high temperature environments, where chemical factors such as chemical stability, oxide scale formation and corrosion rate gain in importance. To better understand the underlying driving forces that lead to the loss of passivity during hot corrosion, Publication III investigated the low-temperature hot corrosion mechanism of $Ti_{1\text{-}x}Al_xN$ at 700 °C, whereas Publication IV studied the effect of high-temperature hot corrosion of $Ti_{1\text{-}x}Al_xN$ at 850 °C, when exposed to $Na_2SO_4/MgSO_4$ salt deposits.

In Publication III, the mechanisms of LTHC stands at the forefront of the investigations, and has revealed a highly localized degradative process that is very similar to that found in Ni-based superalloys. Initiated by the oxidation of the $Ti_{1\text{-}x}Al_xN$ and growth of a mixed $TiO_2/Al_2O_3$ oxide scale, followed by an oxide-to-sulphate transformation, a synergistic fluxing mechanism has been proposed as the predominant corrosion mechanism. Alternating basic and acidic fluxing of $TiO_2$-rich and $Al_2O_3$-rich oxides contributed to an accelerated degradation of the coating structure. Lastly, $Ti_{1\text{-}x}Al_xN$ with higher Al-content have been suggested to be more effective in retarding the onset of the accelerated hot corrosion, due to the inherently better stability of the $Al_2O_3$ in acidic environments, which is imposed by the $SO_3$-rich atmosphere.

Lastly, Publication IV investigated the high-temperature hot corrosion behavior of $Ti_{1\text{-}x}Al_xN$ coatings at 850 °C in order to directly compare their proficiency against industrially established NiCrCo-superalloys. With the overall HTHC mechanisms progressing in a more uniform manner than the LTHC mechanism, evaluation of the oxidation rate constants and underlying rate-laws for was possible. In order to highlight the aggressive effect that salt deposits impose on alloys and protective coatings during hot corrosion, oxidation rates were determined for both, samples that were loaded with salt and samples annealed without salt under identical atmospheric conditions. Results showed, that the presence of salt during annealing at 850 °C in a $SO_2$-rich atmosphere elevated the oxidation rates from a quasi-cubic rate law to a compounded parabolic-linear rate law for the bare NiCrCo alloy, while an increase from a quasi-cubic rate law to only a parabolic-like rate law was observed for the $Ti_{1\text{-}x}Al_xN$ coated samples.The improved corrosion resistance of the $Ti_{1\text{-}x}Al_xN$ coatings is attributed to the lack of internal sulfidation, which is a key sequence of the HTHC mechanism found in most high-temperature alloys. Instead, the suggested rate-determining step of the HTHC mechanism for $Ti_{1-x}Al_xN$ is the nitride-to-oxide transformation, followed by the acidic and basic fluxing of the formed oxides.

In summary, this thesis provides novel insights about the passive behavior of physical vapor deposited TMN coatings in salt-rich aqueous and high temperature settings. Moreover, it provides a framework of experimental and analytical techniques that intend to systematically reveal inherent weak-points of TMN coatings as corrosion resistant coatings, and helps to develop strategies to improve their applicability in the discussed environments.

# Publication I

*Pitting corrosion – Preferred chloride diffusion pathways in physical vapor deposited AlCrN coatings*

**O.E. Hudak**, A. Bahr, P. Kutrowatz, T. Wojcik, F. Bohrn, L. Solyom, R. Schuster, L. Shang, O. Hunold, P. Polcik, M. Heller, P. Felfer, G. Ball, and H. Riedl.

*Corrosion Science* 211 (2022), 110901.

Corrosion Science 211 (2023) 110901

Contents lists available at ScienceDirect

Corrosion Science

journal homepage: www.elsevier.com/locate/corsci

# Pitting corrosion – Preferred chloride diffusion pathways in physical vapor deposited AlCrN coatings

O.E. Hudak [a,*], A. Bahr [a], P. Kutrowatz [a], T. Wojcik [a], F. Bohrn [a], L. Solyom [a], R. Schuster [b], L. Shang [c], O. Hunold [c], P. Polcik [d], M. Heller [e], P. Felfer [e], G. Ball [f], H. Riedl [a,g]

[a] *Christian Doppler Laboratory for Surface Engineering of high-performance Components, TU Wien, Austria*
[b] *Christian Doppler Laboratory for Interfaces and Precipitation Engineering CDL-IPE, Institute of Materials Science and Technology, TU Wien, 1060, Vienna, Austria*
[c] *Oerlikon Balzers, Oerlikon Surface Solutions AG, 9496 Balzers, Liechtenstein*
[d] *Plansee Composite Materials GmbH, D-86983 Lechbruck am See, Germany*
[e] *Department of Materials Science, Friedrich-Alexander-Universität Erlangen-Nürnberg, Germany*
[f] *Institute of Chemical Technologies and Analytics, TU Wien, A-1060 Wien, Austria*
[g] *Institute of Materials Science and Technology, TU Wien, A-1060 Wien, Austria*

ARTICLE INFO

*Keywords:*
PVD Coatings
Pitting Corrosion
Tafel-Plots
APT
TOF-SIMS
Chloride Diffusion

ABSTRACT

Pitting corrosion of sputtered and arc evaportaed fcc-AlCrN coated low-alloy steel substrates was studied in a 0.1 M NaCl solution, using a three-electrode-cell. Depending on the deposition technique, several diffusion mechanisms were identified by high-resolution techniques (i.e. APT, TOF-SIMS). For arc evaporated AlCrN, incoherently embedded macro-particles provided the majority of fast-track diffusion pathways and pit-initiation sites, while their pristine coating matrix proved protective against chloride inward diffusion. Contrarily, the more coarse-grained sputtered AlCrN morphology with a highly orientated crystal growth featured diffusion paths along column boundaries, where chloride permeated the coating structure and initiated pit formations at the coating-substrate interface.

## 1. Introduction

Corrosion processes epitomize the chemical interaction between a material and its surrounding, which ultimately leads to an altered or even degradative state of the material itself. Particularly saline environments represent a technological frontier, where machining elements suffer accelerated breakdown through a localized corrosion mechanism called – pitting. Being a highly insidious and self-sustaining process, pitting corrosion consistently shortens the lifespan of operating elements [1–3]. Therefore, the pitting behavior is an essential variable that, if properly understood, may drastically extend the longevity of material components.

The ingenuity of next-generation physical vapor deposited (PVD) coatings has given rise to a wide range of material concepts and has become a profitable method amongst high-tech industries. Particularly for technological avenues where there is no practicable low-priced bulk material at disposal, coatings provide a lucrative solution for protecting highly stressed machining components. For this reason, more and more industries resort to the application of protective coatings through means of sputtering and arc evaporation, rather than investing in the development of high-end bulk materials. However, with current state-of-the-art corrosion resistant coatings being far from optimized, it is of great interest to further investigate the fundamental mechanisms and underlying driving forces that dominate the degradative process.

Several corrosion mechanisms exist through which a coating can lose its protective quality: *(i)* local de-passivation by film-breakdown [4–6]; *(ii)* local delamination of the coating, caused by inward diffusion of corrosive media followed by the formation of corrosion products at the coating-substrate interface [7]; *(iii)* direct bypass of corrosive media at pin-holes [8,9]; and *(iv)* anodic dissolution of embedded metal based macroparticles [9–12], where the latter particularly pertains to cathodic arc evaporated (cae) thin films.

It is no secret that the production of metallic-macroparticles (droplets) during PVD processes poses a significant drawback in light of the coating's corrosion resistance [13]. Voids and rugged grain boundaries that surround such droplets, allow for fast-tracked diffusion of corrosive media to the substrate-coating interface. Furthermore, weakly bonded macroparticles may become dislodged from the coating matrix and

---

[*] Corresponding author.
*E-mail address:* oliver.hudak@tuwien.ac.at (O.E. Hudak).

https://doi.org/10.1016/j.corsci.2022.110901
Received 11 October 2022; Received in revised form 21 November 2022; Accepted 3 December 2022

produce pin-holes that may function as initiation sites for localized corrosion.

For instance, Abusuilik and Inoue [10] have identified surface droplets and inclusions as particularly susceptible to corrosive attack, and illustrated how intermediate surface treatments can improve the corrosion resistance of arc evaporated CrN coating-substrate systems. Furthermore, Cedeño-Vente et al. [12] highlighted the relationship between macroparticle-size, deposition conditions, and corrosion behavior in aqueous NaCl-rich media for arc evaporated CrN coatings. However, not only arc-coatings with their evenly distributed droplets are vulnerable to corrosion, but also sputtered coatings have their weak spots. A study from Panjan et al. [9] on sputtered TiAlN hard coatings also identifies growth defects and pin-holes as significant contributors for pit-formations. Also combinations of arc evaporated and sputtered coating systems have been investigated, such as the CrN/NbN multilayer system by Wang et al. [11], with similar conclusions, namely, that macroparticles and growth defects stand at the center of the pitting mechanisms.

Despite these findings, transition metal nitrides (TMN) remain a versatile representative in the realm of protective coatings, convincing with good thermal stability, outstanding hardness, as well as noticeable oxidation and corrosion resistance [14–17].

This paper aims to expose possible diffusion pathways of chloride-rich media in both, arc evaporated- and sputtered AlCrN coatings beyond the already known diffusion routes along defect-sites and embedded macroparticles. We intend to first verify the aforementioned fast-track diffusion routes, upon which the focus will be extended to diffusion pathways through pristine, unimpaired coating sites that in theory should provide the best corrosion protection possible.

## 2. Experimental methods

### 2.1. Deposition parameters

All coatings were deposited in an industrial scale deposition system (INNOVA, Oerlikon Surface Solutions AG, Balzers). AlCr (70/30 at. %) targets were powder-metallurgically manufactured by Plansee Composite Materials GmbH and used for all, arc evaporated- and sputtered-coating variants. Single-crystalline Si-stripes (100-oriented, 20x7x 0.38 mm$^3$), 0.05 mm thick steel-foil, and low-alloy steel rounds (90MnCrV8) were utilized as substrates. Whereas coated Si-strips and steel-foil were solely used for as-deposited characterizations (e.g. analysis of the coatings morphology via fracture cross-section, coating thickness measurements and crystal-phase investigations by X-ray diffraction (XRD)), the coated low-alloy steel rounds were exclusively used for electrochemical-corrosion experiments and post-corrosion analysis. All substrates were ultrasonically cleaned with acetone and ethanol before mounting them into the deposition chamber. With a base pressure of at least $5\cdot10^{-3}$ Pa, the substrates were further cleaned for 25 min by a central-beam etching procedure (Oerlikon Surface Solutions AG).

All sputtered coatings were deposited at 500 °C, at a deposition pressure of 1.3 Pa, with a DC-bias voltage of −160 V and an Ar/N$_2$ ratio of 70/30, respectively. The arc evaporated coatings were grown at slightly lower temperature (480 °C), in a pure N$_2$ atmosphere at 3.2 Pa and a bias voltage of up to −100 V.

### 2.2. Structural and morphological characterization

For studying the morphology of the coatings, such as thickness, surface texture, and the integrity of the substrate-coating interfaces, a Zeiss Sigma 500 VP high-resolution field emission gun scanning electron microscope (FEGSEM) was used. With an acceleration voltage, ranging between 3 kV and 7 kV, characterization of coating thickness and coating morphology were performed on fracture cross sections of coated steel-foil substrates. Equipped with an EDAX Octane elect system, energy dispersive spectroscopy (EDS) was utilized for quantitative elemental investigations. Moreover, transmission electron back scattered diffraction (t-EBSD) was done to obtain an averaged evaluation of the as-deposited grain-size distribution of both, sputtered and arc evaportaed samples, as well as to gain knowledge about possible texturisation and preferred growth orientations (Velocity Super, EDAX).

For a more detailed investigation of the coating morphologies, transition electron microscopy (TEM, FEI TECNAI F20) was conducted. Bright field (BF) imaging was utilized to learn more about the microstructure, crystallinity and texture. For the preparation of the TEM lamella, a standard lift-out procedure during focused-ion beam (FIB) milling was utilized (Scios 2 DualBeam system, ThermoFisher Scientific).

For crystallographic investigations, Bragg-Brentano X-ray diffraction was utilized, using a PANalytical XPert Pro MPD system equipped with a Cu-Kα radiation source (wavelength $\lambda = 1.54$ Å).

### 2.3. Electrochemical corrosion experiments

Linear potentiodynamic polarization experiments were performed using a three-electrode set-up. With a saturated Ag/AgCl reference electrode (SSC), a Pt-counter electrode (CE) and the coated-steel sample as working electrode (WE), the pitting-corrosion resistance was measured in a 0.1 M NaCl solution. Each sample was mounted into a press-fit corrosion cell, accomodating a sample contact area of 1.58 cm$^2$. All samples were left to equilibrate for 20 min, after which the open circuit potential (OCP) was measured over an additional duration of 5 min. Linear sweep voltammetry (LSV) measurements were started cathodically at OCP- 300 mV and swept into the anodic region with a sweep-rate of 1 mV/s up to + 1.2 V$_{SSC}$. With a current-density cut-off value set to 1 mA/cm$^2$, the electrochemical tests were controlled and monitored by a potentiostat (Autolab PGSTAT302N, Metrohm).

Additional cyclic potentiodynamic polarization experiments were carried out using the same three-electrode and potentiostat set-up. In an identical manner, the samples were left to equilibrate for 20 min in a 0.1 M NaCl solution and the OCP was measured over the course of an additional 5 min. With a sweep-rate of 20 mV/min, the measurements were started at OCP, swept to an upper vertex potential of + 1.2 V$_{SSC}$, and stopped at a potential of −0.8 V$_{SSC}$ (see Fig. 1). If, however, an anodic current limit of 1 mA/cm$^2$ was reached, the scan direction was reversed instantaneously at the corresponding potential $E_{rev} \leq +1.2$ V$_{SSC}$.

By conducting Tafel-extrapolations and evaluating the cyclic potentiodynamic polarization curves, electrochemical parameters such as the breakdown voltage (E$_b$), the passive current density (i$_p$), as well as the protection or re-passivation potential (E$_{prot}$) were determined, see Fig. 1.

### 2.4. Characterization of electrochemically tested surfaces

Corroded samples were embedded in a conductive polymer-matrix, their cross-sections ground and polished, and analyzed via SEM and EDX. Accordingly, pit-formations, coating-substrate adherence, and fast-track diffusion routes of the electrolyte were examined.

High-resolution analytical techniques such as Time-of-Flight Secondary Ion-Mass-Spectroscopy (TOF-SIMS) and Atom Probe Tomography (APT) were consulted for tracing chloride species across pristine coating sites (no macroparticles, pin-holes, voids, etc.). For the TOF-SIMS measurements a TOF-SIMS 5 instrument (IONTOF GmbH, Münster, Germany) was used. Depth profiles were acquired in a high vacuum (~$4\cdot10^{-7}$ Pa) using a 25 keV Bi$^+$ primary ion beam. A high current bunched mode (HCBU) was used for depth profile measurements, which require a high mass resolution and low limit of detection. [18–21] As non-metal elements were the focus of the research, a 2 keV Cesium gun was used as the sputter source with the polarity set to negative and a cycle time of 60 µs. Low energy electron flooding of 21 V was used to reduce surface charging. In HCBU, the analysis area was set

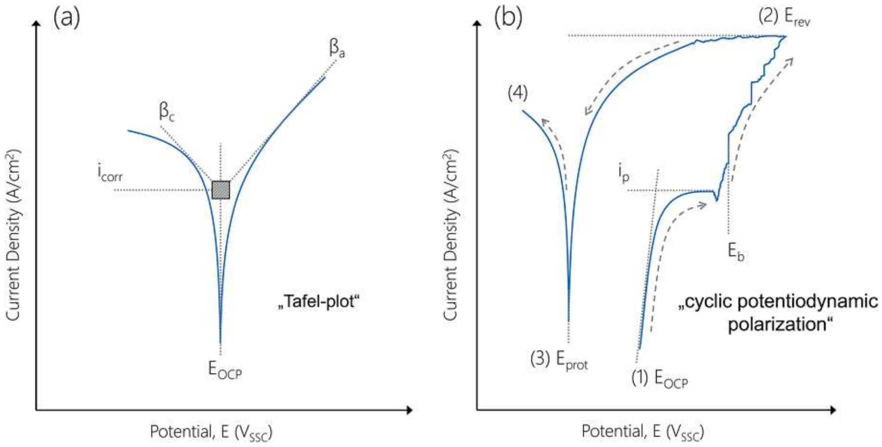

**Fig. 1.** Schematic of (a) Tafel-Plot and (b) course of a cyclic potentiodynamic polarization measurement. The scan starts with (1) the open circuit potential (OCP), sweeps at 20 mV/min to (2) the reverse potential ($E_{rev}$) + 1.2 $V_{SSC}$ (or any lower potential if a current density value larger than 1 mA/cm$^2$ was reached). From $E_{rev}$ the scan returns through (3) the re-passivation/protection potential ($E_{prot}$) and (4) stops at −0.8 $V_{SSC}$.

to 100 × 100 μm$^2$ with 1 shot/pixel, whereas the sputter crater was set to 300 × 300 μm$^2$ to ensure homogeneous material removal at the measurement site. The measurements were stopped after around 8000s

Lastly, APT was chosen as a quantitative method for measuring the diffused Cl-content within surface-near coating regions. At pristine coating sites of electrochemically stressed samples, tip lift-outs of 2 μm length were prepared by a focused ion beam (Scios 2 DualBeam system, ThermoFisher Scientific). Prior to the milling process, a thin protective tungsten layer was deposited in order to preserve the surface vicinity of the coating. The final sharpening of the tips was performed with 30 kV acceleration voltage and 50 pA, after which a clean-up sequence ensued with 5 kV and 28 pA for generating a Ga damage-free tip. The APT analysis was carried out on a Cameca LEAP 4000X HR in pulsed laser mode, equipped with a 355 nm UV laser and a reflection lens. The experiments were done with a laser pulse energy of 50–90 pJ with a pulse rate of 200 kHz at a target evaporation rate of 1 %, whose mass-spectra were then analyzed using a MATLAB tool-box for quantifying the diffused Cl-contents. [22].

## 3. Results and discussion

### 3.1. Microstructure and compositional analysis

The as-deposited SEM cross-sections, as well as respective top-view micrographs are illustrated in Fig. 2 and highlight the intrinsic differences in coating microstructure and texture. Coating thicknesses of 2.5, 5.1, and 7.5 μm were obtained for the arc evaporated depositions, compared to 2.8, 4.9 and 7.1 μm for the sputtered variants (see Fig. 2a-f, respectively). While all coatings feature a typical columnar structure, the sputtered coatings produced a more pronounced and textured morphology. This is related to the inherently lower energetics and ion-flux, as well as lower ion-mobility of arriving species present during sputtering (decreased self-surface diffusion and densification of the coating morphology) [23]. Top-view SEM-micrographs (Fig. 2a*-f*), further highlight the differences in the coating morphology and surface-texturing between arc evaporated and sputtered coatings. Whereas no surface texturing is visible for any of the arc evaporated samples, distinct pyramidal features dominate the surface of the sputtered coatings, particularly with increasing coating thickness (see Fig. 2f*).

Fig. 3 presents the diffractograms and peak-patterns for all as-deposited coatings. All coatings feature a face-centered-cubic (fcc) crystal-structure with mixed [111]/[200] growth orientations. Here as well, the texture of the sputtered coatings stands out, as the diffractograms clearly display a shift from a highly [200] orientated crystal structure (see Fig. 3d) to a preferred [111] crystal orientation (see Fig. 3f), with increasing coating thickness.

All in all, the as-deposited states can be summarized as follows: The arc evaporated coatings share a columnar and dense morphology with a fcc-crystal structure composed of mixed [111] and [200] crystal orientations. Similarly, all sputtered coatings feature a fcc-crystal structure with a pronounced columnar morphology. However, with higher coating thicknesses, the crystal growth orientation changes from a mixed [111]/[200] to a preferred [111] orientation, which results in the formation of a highly faceted surface. Lastly, by utilizing EDX analysis, the metal content ratios for the sputtered- and arc evaporated coatings were determined to be $Al_{0.67}Cr_{0.33}N$ and $Al_{0.68}Cr_{0.32}N$, respectively.

### 3.2. Electrochemical corrosion properties

The Tafel-plots of the bare 90MnCrV8 alloy and the AlCrN coated samples are shown in Fig. 4a. The corrosion current ($i_{corr}$) and open circuit potential ($E_{OCP}$) were determined from the intersection of the extrapolated anodic and cathodic Tafel-branches (Fig. 1a) [27]. All extrapolations were performed manually with no additional software package for data analysis. The corrosion potential of the uncoated steel substrate leveled at about −569 $mV_{ssc}$, whereas the open circuit potentials of the AlCrN coated samples all settled within the range of −378 $mV_{ssc}$ to −326 $mV_{ssc}$ ($OCP_{(mean)}$= −352 $mV_{ssc}$), regardless of the deposition route used. The positive shift from −569 $mV_{ssc}$ to −352 $mV_{ssc}$ indicates reduced anodic activity of the AlCrN-coated samples over the bare alloy. Minimal improvement in $i_{corr}$ was measured for all AlCrN coated samples over the bare substrate, again with similar values across all coating variants (see Table 1).

Fig. 4b and c illustrate the cyclic potentiodynamic polarization curves of all arc evaporated coatings and sputtered coatings, respectively. Starting from the corrosion potential ($E_{OCP}$) and sweeping into the anodic region, all samples show a similar corrosion behavior. From about +100 $mV_{ssc}$ upwards, the AlCrN-coated samples enter their passive region, where the current densities ($i_{pass}$) of the sputtered coatings measure slightly lower than those of the arc evaporated variants. Also within each coating group (sputtered and arc evaporated), the obtained passive current values decrease with increasing coating thickness (see Table 1). Despite being rather small reductions in the measured currents, it may be suggestive of a sealing-effect of initial defect sites and open porosities. In other words, initial fast-track diffusion routes may be

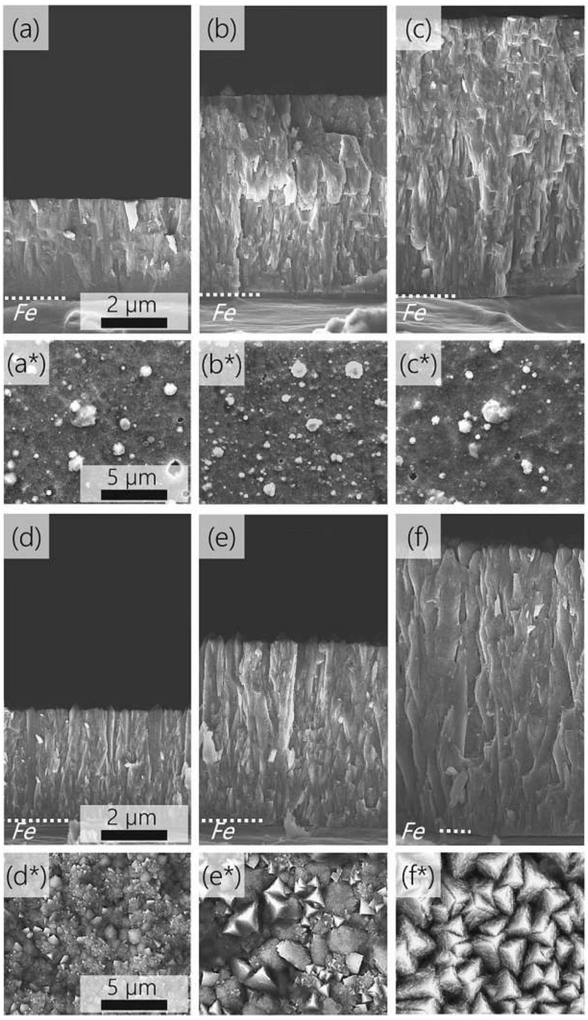

**Fig. 2.** As-deposited SEM cross-sections of arc evaporated coatings (a-c) with thicknesses of 2.5, 5.1, and 7.5 µm, and sputtered coatings (d-f) with thicknesses of 2.8, 4.9 and 7.1 µm, respectively. Related top-view morphologies are shown in (a*-f*).

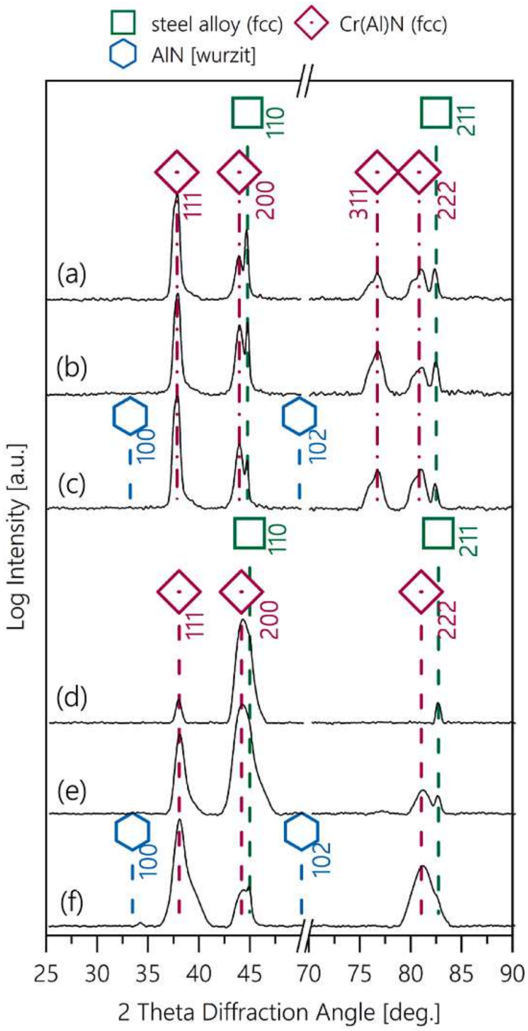

**Fig. 3.** XRD spectra of the as-deposited arc evaporated fcc-AlCrN coatings (a-c) with thicknesses of 2.5, 5.1 and 7.5 µm, respectively, as well as sputtered fcc-AlCrN coatings (d-f) with thicknesses of 2.8, 4.9, and 7.1 µm, respectively. Reference patterns were taken from Ref. [24–26].

overgrown by longer deposition times and result in an improved passive behavior of the coating. When increasing the applied potential further, all measurements indicate a drop in the current density values at ~300 mV$_{ssc}$, followed by a spike in the measured current shortly after, which we interpreted as the breakdown potential ($E_b$) for each coating. This is indicative for the equilibria reaction $Fe^{2+}+2OH^- \rightarrow Fe(OH)_2$, prematurely passivating the pit-mouth openings. Subsequent internal acidification then leads to a rapid elevation in the alloy dissolution and drastically increases the corrosion current values. Interestingly, despite the coating thickness within the arc evaporated and sputtered groups, all arc evaporated AlCrN samples reach the current cut-off value (1 mA/cm$^2$) at similar potentials ($E_{rev}$= ~360 mV$_{ssc}$), whereas $E_{rev}$ for all sputtered variants is found more anodic ($E_{rev}$= ~420–450 mV$_{ssc}$). A summary of the electrochemical properties is presented in Table 1. Together with the results from the Tafel-plots, these findings further strengthen the argument, that coating thickness plays a subordinate role in the corrosion mechanism of AlCrN-coated low alloy steel samples. For this reason, from here onwards, further investigations will focus solely on the ~5 µm thick arc evaporated- and sputtered coatings.

### 3.3. *Morphological investigations of preferential pitting sites*

SEM cross-sections of the electrochemically stressed AlCrN samples are shown in Figs. 5–7, highlighting the preferred diffusion pathways and pit-initiation sites for both, arc evaporated and sputtered coating variants. Cross-sections of the arc evaporated AlCrN samples (see Figs. 5 and 6) evidently single out intrinsically deposited macroparticles as the dominating weak-spot for pit-formations. Fig. 5a shows the polished cross-section of an as deposited arc evaporated AlCrN coating. Visible through the mass-contrast is the bright chrome-rich inner core of the droplet, which has been verified by EDX analysis. Also highlighted are porous domains below the core that have evolved through shadowing effects throughout the growth of the macroparticle. While exposed to NaCl-rich aqueous media during electrochemical testing, these metallic cores are prone to accelerated oxidation. Whereas some droplets only suffer premature oxidation (Fig. 5b), others oxidize much more severely, depending on how coherently the droplets sit within the coating matrix. Fig. 5c and the respective EDX line-scan illustrate such a matured state. Specifically, the EDX line-scan emphasizes the oxygen enriched

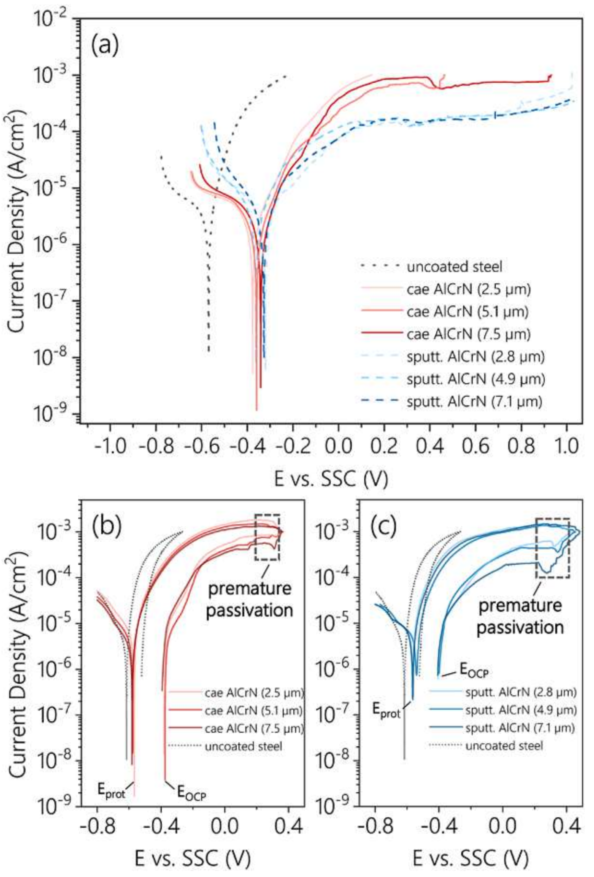

**Fig. 4.** Electrochemical measurements in 0.1 M NaCl solution: (a) Tafel-Plots of cae-AlCrN coatings (solid red lines), sputtered-AlCrN coatings (dashed blue lines), and uncoated low alloy steel substrate (dotted grey line), (b-c) cyclic potentiodynamic polarization curves of cae-AlCrN coatings and sputtered-AlCrN coatings, respectively.

chromium core, as well as surrounding areas, where the corrosive media has permeated the droplet-coating boundaries.

Particularly, droplets located near the coating-substrate interface and permeate the entire coating structure (see Fig. 6a-c), offer fast-track diffusion routes along the particle-coating interface. Once a pit has initiated (Fig. 6b), the exchange of both, corrosion product out of the pit, as well as transport of the aqueous media into the pit, occurs simultaneously along these pathways. In Fig. 6d and the respective EDX maps this ion-exchange is further exemplified. While the pristine coating matrix remains chemically and structurally unchanged (alloy and metallic droplets are the only chemically active species) an accelerated metal dissolution of the substrate is observed (pit growth).

Fig. 7, on the other hand, illustrates the most abundantly observed pit-initiation route for the sputtered AlCrN coating. Owed to the inherently fewer number of defect-sites, other diffusion routes must be present. The cross-sections in Fig. 7a-c reveal vertical channels that form throughout the corrosion experiments. Analogous to the diffusion paths along macroparticle boundaries in arc evaporated coatings, these channels allow for inward and outward diffusion of corrosion products and chloride/hydroxide-ions. The formation of channels can be related to the more pronounced columnar morphology of the sputtered coatings, as well as the intrinsically lower packing/density of the overall microstructure. Similar to the arc evaporated sample, Fig. 7d and the respective EDX maps suggest that the surrounding sputtered AlCrN coating matrix is chemically stable. Homogeneous distribution of aluminum and chromium, with no indication of coating deterioration through oxidation confirms this impression. Furthermore, the EDX maps highlight the exchange of iron and oxygen between the pit and surface by channels that trend along the column boundaries.

### 3.4. *Surface near examination of chloride inward diffusion by APT*

In order to reveal more about the actual passivity of the intact coating morphology to chloride species (no fast-track diffusion pathways, e.g. droplets, macroparticles and/or underdense columnar morphology), APT lift-outs were taken from pristine coating sites of cyclic potentiodynamic polarized samples (see Fig. 4). Fig. 8a shows the positions chosen for the lift outs, whereas Fig. 8b-c illustrate two of the tip preparation steps (milling and sharpening, respectively). The mass spectra of the corroded arc evaporated coatings (see Fig. 8d) and sputtered coating (see Fig. 8e) originate from the surface near regions of the electrochemically stressed coatings. These spectra quantitatively highlight the amount of diffused chloride for the duration of the corrosion experiment. Labeled are the individual chlorine-containing fragments that substantiate the presence of diffused chloride species through the pristine coating morphologies. The interpretation and quantification of the dataset (chlorine containing signals) render a chloride concentration of 600 ppm for the arc evaporated coating, whereas a 28 times higher chloride concentration of 16,800 ppm was determined for the sputtered AlCrN film (comparing the same volume). This clearly demonstrates that pristine coating morphologies, particularly the topmost regions, are indeed permeable to chloride. As expected, a significantly lower chloride concentration was measured for the arc evaporated coating, suggesting that the arc evaporated coating has a more coherent and compact coating morphology than its sputtered equivalent. This also emphasizes the dominant role of embedded macroparticles in the pitting initiation mechanism of arc evaporated coatings. In contrast,

**Table 1**
Electrochemical properties from the cyclic potentiodynamic polarization experiments in 0.1 M NaCl solution. $E_{OCP}$, corrosion potential; $E_{prot}$, protection potential; $E_b$, breakdown potential; $i_p$, passive current density; $i_{corr}$, corrosion current density.

| Coating | Thickness (µm) | $E_{OCP}$ (mV$_{ssc}$) | $E_{prot}$ (mV$_{ssc}$) | $E_b$ (mV$_{ssc}$) | $i_p$ (A/cm$^2$) | $i_{corr}$ (A/cm$^2$) |
|---|---|---|---|---|---|---|
| bare alloy | – | -569 | -616 | – | – | $2.65 \times 10^{-6}$ |
| cae-AlCrN | 2.5 | -381 | -567 | 324 | $7.52 \times 10^{-4} \pm 1.10 \times 10^{-5}$ | $9.76 \times 10^{-7}$ |
|  | 5.1 | -374 | -576 | 318 | $5.13 \times 10^{-4} \pm 5.28 \times 10^{-5}$ | $8.87 \times 10^{-7}$ |
|  | 7.5 | -392 | -580 | 334 | $4.01 \times 10^{-4} \pm 1.13 \times 10^{-5}$ | $9.11 \times 10^{-7}$ |
| sputt.-AlCrN | 2.8 | -406 | -567 | 329 | $5.56 \times 10^{-4} \pm 4.92 \times 10^{-6}$ | $1.09 \times 10^{-6}$ |
|  | 4.9 | -398 | -539 | 357 | $4.36 \times 10^{-4} \pm 3.91 \times 10^{-6}$ | $1.54 \times 10^{-6}$ |
|  | 7.1 | -405 | -562 | 371 | $1.92 \times 10^{-4} \pm 5.47 \times 10^{-6}$ | $1.51 \times 10^{-6}$ |

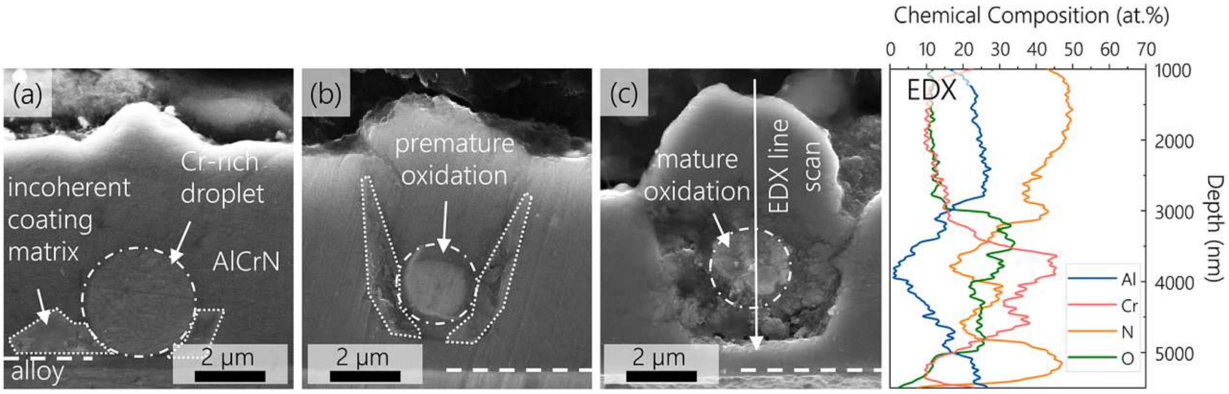

**Fig. 5.** SEM cross-section images of (a) as deposited arc evaporated- AlCrN coating, (b) prematurely corroded droplet within the arc evaporated AlCrN coating matrix, and (c) matured corrosion of the metallic droplet core with the respective EDX analysis as indicated by the arrow.

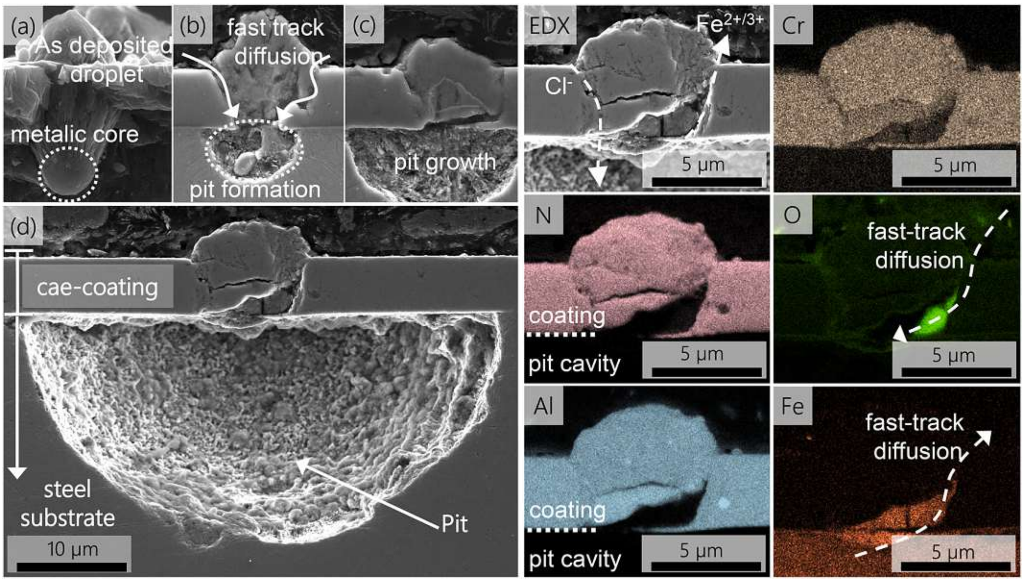

**Fig. 6.** SEM investigations of preferred diffusion routes in cae-AlCrN coatings: (a) as-deposited droplet routed within the coating matrix; (b-c) pit initiation and propagation stages; (d) fully developed pit cavern with respective EDX color maps that highlight diffusion exchange pathways between cavity and coating surface.

significantly higher chloride concentrations were measured for the sputtered AlCrN coating. With its more directional columnar growth and inferior packing density, the sputtered coating matrix proves extremely pervious to chloride and provides no adequate diffusion barrier. In order to extend the scope from coating surface near regions towards the coating-substrate interface, it was of great interest to examine the chloride diffusion across the overall coating thickness.

### 3.5. Depth profiling of chloride diffusion by TOF-SIMS

In order to investigate the chloride diffusion qualitatively throughout the entire span of the pristine coating matrix, TEM analysis, as well as TOF-SIMS depth-profile measurements were carried out for both, arc evaporated (Fig. 9a-e) and sputtered coatings (Fig. 9f-j). Selected area electron diffractograms (SAED) and TEM bright field images of the measured coatings provide localized information about the coating's crystallinity and help to interpret the obtained TOF-SIMS data. The collected depth-profiles of the anionic Cl and Al species are presented in Fig. 9e and j, respectively. Based on this analysis, the progression of chloride (diffusion front) was assessed. While the dotted lines represent the measurements of the as-deposited samples (considering a native Cl-contamination), the solid profiles represent the measurements of the electrochemically stressed samples. The shaded regions enclosed by both, solid and dotted lines, highlight the loading behavior and diffusion front in both, cae and sputtered samples.

By looking at the depth-profiles of the arc evaporated AlCrN coatings, a more or less typical diffusion curve is observed (Fig. 9e). With a chloride-enriched surface region, reaching about 500 nm into the coating, a gradual decline in chloride concentration follows for about 3 µm, after which the concentration gradient bleeds out at the coating substrate interface. When examining the respective bright-field TEM image in Fig. 9d, a homogeneous morphology with discontinuous column boundaries is featured. SAEDs of the surface near (Fig. 9a), centered (Fig. 9b) and interface near regions (Fig. 9c) exhibit random crystal orientations of the coating matrix with defined diffraction dots.

On the other hand, Fig. 9j shows the chloride diffusion behavior of the electrochemically stressed sputtered AlCrN coating, featuring a uniform chloride loading profile. Only towards the coating-substrate

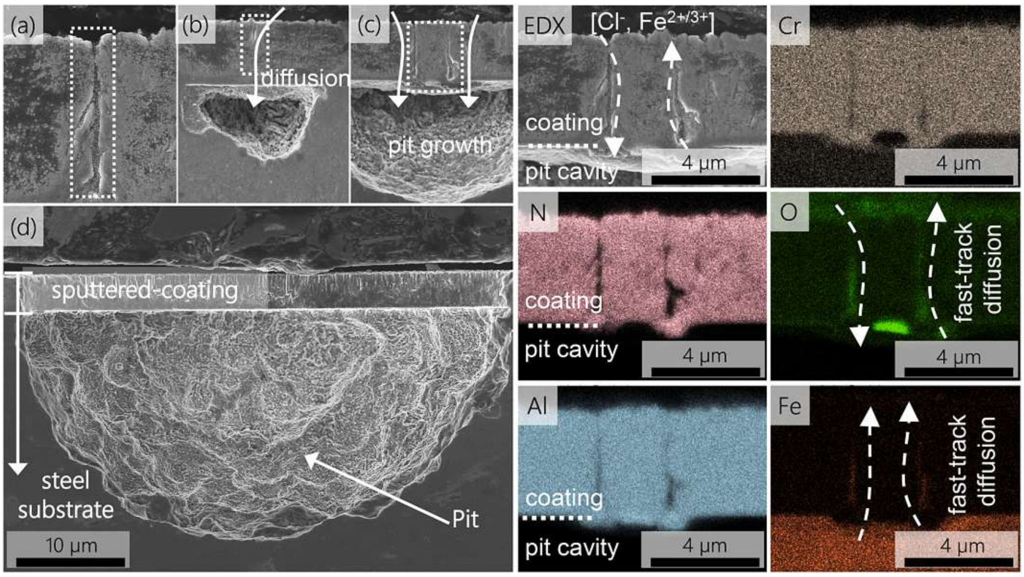

**Fig. 7.** SEM investigations of preferred diffusion routes in sputtered-AlCrN coatings: (a) incoherent column boundary; (b-c) pit initiation and propagation stages; (d) fully developed pit cavern with respective EDX color maps that highlight diffusion exchange channels between cavity and coating surface.

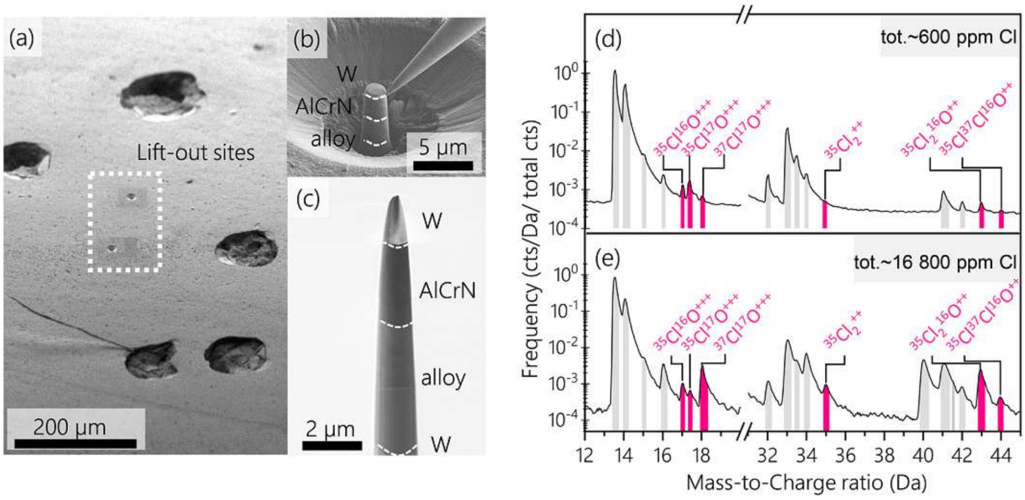

**Fig. 8.** Illustration of (a) the APT tip-site selection (b) lift-out operation and (c) sharpening sequence of a stressed arc evaporated AlCrN coating. (d) Features the APT mass-spectra of the arc evaporated and (e) of the sputtered coatings. Two cut-outs (12–20 Da & 30–45 Da) highlight the chloride-containing fragments, as labeled, whose integration was used to quantify the respective Cl-contents.

interface, a decrease in the chloride concentration occurs. Evident from the TEM bright-field images and SAED patterns, the difference in the diffusion profile must be, at least partially, due to the variation in the microstructure. Whereas the SAEDs that were collected near the surface and center of the coating show diffraction patterns with distinct diffraction dots, the SAED from near the coating-substrate interface features smeared dots, indicative of a more nanocrystalline microstructure. It may be this property that translates to an improved diffusion barrier, and is responsible for the prevention of pitting at the coating-substrate interface. This may also explain why the corrosion behavior did not improve with increasing coating thickness.

Overall, it can be asserted that the arc evaporated AlCrN morphology exhibits a relatively uniform grain size distribution throughout the entire coating thickness, providing a sufficient diffusion barrier for the duration of the corrosion experiments (diffusion front ~3.2 µm into the sample). Moreover, the sputtered microstructure features an increasing grain and column size distribution from the interface to the surface near regions that allow for accelerated chloride loading throughout most of the coating thickness until the nanocrystalline morphology at the interface is reached (diffusion front ~4.8 µm into the sample).

### 3.6. *Preferred growth orientations and coating texture*

Lastly, it was of great interest to further substantiate the aforementioned differences in microstructure, especially grain orientation and grain-size distribution. For this, we resorted to transmission electron back-scatter diffraction and performed an averaged evaluation of the grain-size distribution of the AlCrN-coated samples. In this case, the goal

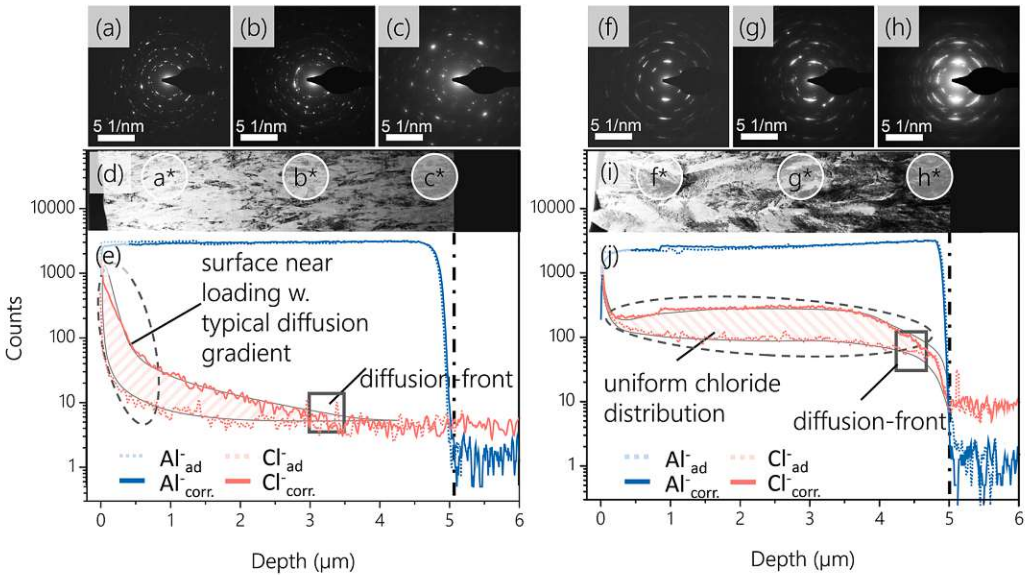

**Fig. 9.** TEM and TOF-SIMS analysis: (a-c) SAED images indicating differences in crystallinity of surface-near, centered, and interface near arc evaporated coating regions, respectively; (d) bright-field TEM image of the arc evaporated coating morphology; (e) TOF-SIMS depth-profile highlighting the chloride inward diffusion gradient (shaded region) and diffusion front (box) of the arc evaporated AlCrN coating. The illustrations (f-j) corresponds to the sputtered coating variant with identical assignment.

was to link the diffusion profiles obtained from the TOF-SIMS and APT analysis, to the morphological characteristics observed during TEM. Fig. 10 shows the TEM lamellas of the ~5 μm thick arc evaporated and sputtered AlCrN coatings (see Fig. 10a and d), the respective inverse pole figure maps (Fig. 10b and e), as well as inverse pole figures (Fig. 10c and f) calculated from the t-EBSD data. Correlating with the results from the XRD analysis, the inverse pole figures reveal a highly orientated {001} growth direction for the 5 μm sputtered coating, whereas a mostly random growth orientation, with a weak preference in the {211} plane, is featured by the arc evaporated coating variant. At this point, we would like to point out that the difference in the color range interval used for the arc evaporated sample (Fig. 10c) and sputtered-sample (Fig. 10f). Whereas the {211} orientation of the arc evaporated morphology occurs merely three times as often as for a random distribution of christallographic orientations, the {001} orientation in the sputtered matrix appears more than twenty times as often.

From the EBSD data, averaged grain sizes of 72 and 120 nm in horizontal diameter were calculated for the as-deposited arc evaporated and sputtered samples, respectively. These numbers, again substantiate the notion that the highly orientated {001} morphology and the larger grain sizes, in combination with the open column boundaries of the sputtered sample, allow for unimpeded diffusion along its grain boundaries. In this manner, fast bridging of the protective coating and subsequent pit initiation at the coating-substrate interface is granted in a similar way, as would be observed for arc evaporated coatings with their droplet-streaked morphology.

## 4. Conclusion

With near to identical pitting behavior by electrochemical investigation, in-depth analysis of AlCrN thin films has yielded distinct diffusion mechanisms that pertain exclusively to either arc evaporated or sputtered AlCrN coating morphologies.

For arc evaporated AlCrN coatings, fast-tracked diffusion of the electrolyte was exclusively observed along incoherently incorporated macroparticles, resulting in rapid oxidation of the metallic cores and a consequent dislodging from their surrounding coating structure. It has been found that the formation of cavities functions as the most frequently observed pit-initiation site. Delving deeper into other possible diffusion routes, pristine coating sites (droplet free) were investigated by APT and TOF-SIMS. Both analyses revealed surface near inward diffusion of chloride (600 ppm Cl), however no chloride was detected close to the coating-substrate interface. Featuring a depth profile with a rapidly decreasing chloride concentration gradient, the pristine coating morphology demonstrates excellent diffusion resistance against chloride species. By consulting t-EBSD for a detailed understanding of the coating structure, we appoint the fine-grained morphology (~70 nm) and randomly orientated growth orientation as one of the decisive properties for improved diffusion resistance.

On the other hand, the most abundantly observed pit-initiation mechanism for the sputtered AlCrN samples resulted from diffusion routes along open column domains. The partially coarse-grained microstructure and unidirectional column growth facilitated fast-track diffusion to the coating-substrate interface, allowing for an eased breaching of the coating structure. APT and TOF-SIMS analysis of pristine coating sites exhibited uniform chloride loading throughout most of the sputtered morphology (16800 ppm Cl), which is 28 times higher than for the arc evaporated coating. Unlike for the arc evaporated coating, t-EBSD of the sputtered sample revealed a coarse-grained morphology (~120 nm) with significant coating texturing in the {100} direction. A sufficient diffusion barrier was only observed at the coating-substrate interface, where a sufficiently fine-grained microstructure, as well as randomized growth orientations prevailed.

To perfectly protect the underlying alloy and to prevent pitting, sufficient diffusion resistance to $Cl^-$ must be warranted by the AlCrN coating morphology. Despite being chemically inert to the oxidative electrolyte, both, sputtered and arc evaporated coatings have shown distinctly different diffusion routes, which allow for the initiation of pits at the coating-substrate interface.

## CRediT authorship contribution statement

O. E. H. and H. R. conceived the research. L. S. and O. E. H. conducted the coating depositions, as well as the electrochemical corrosion

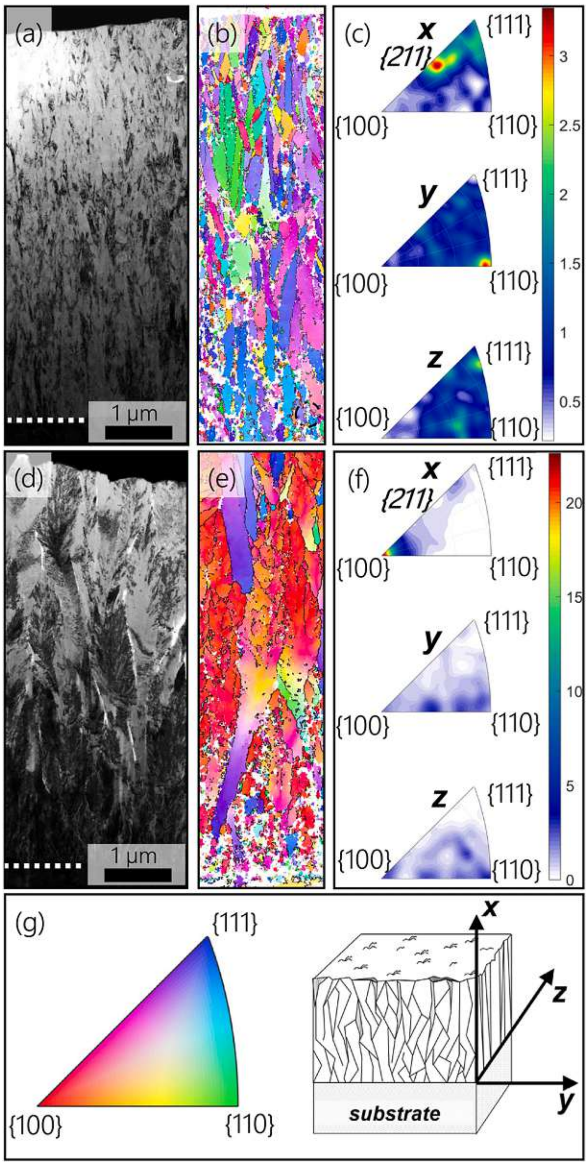

**Fig. 10.** TEM bright-field images (a, d), EBSD inverse pole figure maps colored with respect to x (b, e) and related inverse pole figures for directions x, y and z (c, f), of the as-deposited arc evaporated and sputtered coatings, respectively. (g) shows the color legend and viewing direction for the IPF maps.

tests. G. B. assisted with the set-up of the electrochemical methods and provided support with their implementation and evaluation. P. K. prepared the TEM and t-EBSD lamella, whereas T. W. conducted the TEM and t-EBSD measurements. R. S. assisted in the evaluation and interpretation of the t-EBSD data. A. B., M. H. and P. F. conducted the preparation and measurements of the atom probe tips, whereas F. B. carried out the ToF-SIMS measurements. O. H. and P. P. supported the research by providing indispensable funding, while L. S. assisted the research with her thematic expertise. H. R. also provided funding acquisition and oversaw the research as supervisor. Finally, all authors have contributed in revising and approving the final version of the manuscript.

## Declaration of Competing Interest

The authors declare the following financial interests/personal relationships which may be considered as potential competing interests: Oliver E. Hudak reports financial support was provided by Christian Doppler Research Association.

## Data availability

Data will be made available on request.

## Acknowledgments

The financial support by the Austrian Federal Ministry for Digital and Economic Affairs, the National Foundation for Research, Technology and Development and the Christian Doppler Research Association is gratefully acknowledged (Christian Doppler Laboratory "Surface Engineering of high-performance Components"). We also thank for the financial support of Plansee SE (Austria), Plansee Composite Materials GmbH (Germany), and Oerlikon Balzers, Oerlikon Surface Solutions AG (Liechtenstein). In addition, we want to thank the X-ray center (XRC) of TU Wien for beam time as well as the electron microscopy center - USTEM TU Wien - for providing the SEM and TEM facilities. The authors acknowledge TU Wien library for financial support through its Open Access Funding Program.

## Appendix A. Supporting information

Supplementary data associated with this article can be found in the online version at doi:10.1016/j.corsci.2022.110901.

## References

[1] K.V. Akpanyung, R.T. Loto, Pitting corrosion evaluation: a review, J. Phys. Conf. Ser. 1378 (2019), https://doi.org/10.1088/1742-6596/1378/2/022088.
[2] P. Aldhous, R. Akid, R. Leiva-Garcia, S. Zhou, Evaluating the effects of environmental aging on the pitting corrosion of steam turbine blade steels, Mater. Corros. (2022), https://doi.org/10.1002/maco.202213384.
[3] Y. Mollapour, E. Poursaeidi, O. Pedram, Study of pitting corrosion under actual operating conditions of a first stage compressor blade, Eng. Fail. Anal. 131 (2022), 105822, https://doi.org/10.1016/j.engfailanal.2021.105822.
[4] H. DorMohammadi, Q. Pang, P. Murkute, L. Árnadóttir, O.B. Isgor, Investigation of chloride-induced depassivation of iron in alkaline media by reactive force field molecular dynamics, Npj Mater. Degrad. 3 (2019), https://doi.org/10.1038/s41529-019-0081-6.
[5] L. D'Avico, R. Beltrami, N. Lecis, S.P. Trasatti, Corrosion behavior and surface properties of PVD coatings for mold technology applications, Coatings 9 (2019) 1–12, https://doi.org/10.3390/coatings9010007.
[6] A. Perez, A. Billard, C. Rébéré, C. Berziou, S. Touzain, J. Creus, Influence of metallurgical states on the corrosion behaviour of Al-Zn PVD coatings in saline solution, Corros. Sci. 74 (2013) 240–249, https://doi.org/10.1016/j.corsci.2013.04.048.
[7] C. Liu, A. Leyland, Q. Bi, A. Matthews, Corrosion resistance of multi-layered plasma-assisted physical vapour deposition TiN and CrN coatings, Surf. Coat. Technol. 141 (2001) 164–173, https://doi.org/10.1016/S0257-8972(01)01267-1.
[8] P. Panjan, M. Čekada, M. Panjan, D. Kek-Merl, F. Zupanič, L. Čurković, S. Paskvale, Surface density of growth defects in different PVD hard coatings prepared by sputtering, Vacuum 86 (2012) 794–798, https://doi.org/10.1016/j.vacuum.2011.07.013.
[9] P. Panjan, A. Drnovšek, P. Gselman, M. Čekada, M. Panjan, T. Bončina, D.K. Merl, Influence of growth defects on the corrosion resistance of sputter-deposited TiAlN hard coatings, Coatings 9 (2019) 1–16, https://doi.org/10.3390/coatings9080511.
[10] S.B. Abusuilik, K. Inoue, Effects of intermediate surface treatments on corrosion resistance of cathodic arc PVD hard coatings, Surf. Coat. Technol. 237 (2013) 421–428, https://doi.org/10.1016/j.surfcoat.2013.09.026.
[11] H.W. Wang, M.M. Stack, S.B. Lyon, P. Hovsepian, W.D. Münz, The corrosion behaviour of macroparticle defects in arc bond-sputtered CrN/NbN superlattice coatings, Surf. Coat. Technol. 126 (2000) 279–287, https://doi.org/10.1016/S0257-8972(00)00554-5.
[12] M.L. Cedeño-Vente, J. Manríquez, G.C. Mondragón-Rodríguez, N. Camacho, A. E. Gómez-Ovalle, J.M. Gonzalez-Carmona, J.M. Alvarado-Orozco, D.G. Espinosa-Arbelaez, Application of a transmission line model to evaluate the influence of structural defects on the corrosion behavior of arc-PVD CrN coatings, Ceram. Int. (2021), https://doi.org/10.1016/j.ceramint.2021.04.087.

[13] M. Fenker, M. Balzer, H. Kappl, Corrosion protection with hard coatings on steel: Past approaches and current research efforts, Surf. Coat. Technol. 257 (2014) 182–205, https://doi.org/10.1016/j.surfcoat.2014.08.069.

[14] C.M. Koller, S.A. Glatz, S. Kolozsvári, H. Bolvardi, P.H. Mayrhofer, Thermal stability and oxidation resistance of architecturally designed Ti–Al–N- and Ti–Al–Ta–N-based multilayers, Surf. Coat. Technol. 385 (2020), 125444, https://doi.org/10.1016/j.surfcoat.2020.125444.

[15] E. Aschauer, T. Wojcik, P. Polcik, O. Hunold, M. Arndt, V. Dalbauer, P. H. Mayrhofer, P. Felfer, H. Riedl, Ultra-high oxidation resistance of nano-structured thin films, Mater. Des. 201 (2021), 109499, https://doi.org/10.1016/j.matdes.2021.109499.

[16] P. Mohamadian Samim, A. Fattah-Alhosseini, H. Elmkhah, O. Imantalab, Structure and corrosion behavior of ZrN/CrN nano-multilayer coating deposited on AISI 304 stainless steel by CAE-PVD technique, J. Asian Ceram. Soc. 8 (2020) 460–469, https://doi.org/10.1080/21870764.2020.1750102.

[17] D.D. Kumar, N. Kumar, S. Kalaiselvam, S. Dash, R. Jayavel, Wear resistant super-hard multilayer transition metal-nitride coatings, Surf. Interfaces 7 (2017) 74–82, https://doi.org/10.1016/j.surfin.2017.03.001.

[18] A. Benninghoven, Surface analysis by secondary ion mass spectrometry (SIMS), Surf. Sci. 299–300 (1994) 246–260, https://doi.org/10.1016/0039-6028(94)90658-0.

[19] A. Benninghoven, Chemical analysis of inorganic and organic surfaces and thin films by static time-of-flight secondary ion mass spectrometry (TOF-SIMS), Angew. Chem. Int. Ed. Engl. 33 (1994) 1023–1043, https://doi.org/10.1002/anie.199410231.

[20] M. Kubicek, G. Holzlechner, A.K. Opitz, S. Larisegger, H. Hutter, J. Fleig, A novel ToF-SIMS operation mode for sub 100nm lateral resolution: application and performance, Appl. Surf. Sci. 289 (2014) 407–416, https://doi.org/10.1016/j.apsusc.2013.10.177.

[21] R.N.S. Sodhi, Time-of-flight secondary ion mass spectrometry (TOF-SIMS):—versatility in chemical and imaging surface analysis, Analyst 129 (2004) 483–487, https://doi.org/10.1039/B402607C.

[22] P. Felfer, Matlab Toolbox for APT analysis, Github, n.d., (n.d.). 〈https://github.com/peterfelfer/Atom-Probe-Toolbox〉.

[23] C. Yang, B. Jiang, Z. Liu, J. Hao, L. Feng, Structure and properties of Ti films deposited by dc magnetron sputtering, pulsed dc magnetron sputtering and cathodic arc evaporation, Surf. Coat. Technol. 304 (2016) 51–56, https://doi.org/10.1016/j.surfcoat.2016.06.083.

[24] International Center of Diffraction Data, Powder diffraction file 01–083-5613, 2016.

[25] International Center of Diffraction Data, Powder diffraction file 00–046-1200, 1996.

[26] International Center of Diffraction Data, Powder diffraction file 04–014-0360, (2010).

[27] R.A. Buchanan, E.E. Stansbury, 4 Electrochemical Corrosion, (2012).

# Publication II

## *Improved corrosion resistance of cathodic arc evaporated $Al_{0.7}Cr_{0.3\text{-}x}V_xN$ coatings in NaCl-rich media*

**O.E. Hudak**, P. Kutrowatz, T. Wojcik, E. Ntemou, D. Primetzhofer, L. Shang, J. Ramm, O. Hunold, S. Kolozsvári, P. Polcik, and H. Riedl.

*Corrosion Science* 221 (2023), 111376.

Corrosion Science 221 (2023) 111376

Contents lists available at ScienceDirect

Corrosion Science

journal homepage: www.elsevier.com/locate/corsci

# Improved corrosion resistance of cathodic arc evaporated $Al_{0.7}Cr_{0.3-x}V_xN$ coatings in NaCl-rich media

O.E. Hudak [a,*], P. Kutrowatz [a], T. Wojcik [a], E. Ntemou [b], D. Primetzhofer [b], L. Shang [c], J. Ramm [c], O. Hunold [c], S. Kolozsvári [d], P. Polcik [d], H. Riedl [a,e]

[a] Christian Doppler Laboratory for Surface Engineering of high-performance Components, TU Wien, Austria
[b] Department of Physics and Astronomy, Uppsala University, 75120 Uppsala, SE, Sweden
[c] Oerlikon Balzers, Oerlikon Surface Solutions AG, 9496 Balzers, Liechtenstein
[d] Plansee Composite Materials GmbH, D-86983 Lechbruck am See, Germany
[e] Institute of Materials Science and Technology, TU Wien, A-1060 Wien, Austria

## ARTICLE INFO

*Keywords:*
PVD coatings
Cathodic arc evaporation
Pitting
Corrosion resistance
Open porosity

## ABSTRACT

The corrosion resistance of cathodic arc evaporated $Al_{0.7}Cr_{0.3-x}V_xN$ coatings with a vanadium content up to 22.3 at% has been electrochemically tested in a 0.1 M NaCl-solution. Significant improvement in the open porosity and corrosion rate was observed for coatings with higher V-contents, due to a denser and more refined coating morphology. Further reduction in the open porosity rate was achieved through an annealing step in air at 700 °C. Here, the formation of an $AlVO_4$ top-oxide and underlying oxygen-rich V-depletion zone provides additional sealing of the coating surface, whilst reducing the corrosion current density to a final $1.59 \times 10^{-9}$ A/cm$^2$.

## 1. Introduction

One of the biggest drawbacks regarding the application of corrosion protective PVD coatings on bulk materials (e.g. steels) is the presence of open porosities. Pores or defect sites (e.g. embedded macroparticles, porosity due to highly orientated columnar growth, pin holes, etc.) allow the corrosive medium to travel unhindered to the coating/substrate interface and generate galvanic couples [1–3]. Depending on the materials that make up this galvanic cell, coatings may either act as the anodic element (providing sacrificial protection) [4], or act as the cathodic element, in which anodic dissolution and pitting of the substrate material ensues [5]. For the latter case, which pertains to most ceramic protective coatings, the coating itself remains inert, whereas the steel underneath suffers detrimental corrosion [6–11].

In recent years, a great number of strategies have been pursued to minimize the open-porosity values in protective PVD coatings and limit the probability of the electrolyte to make contact with less noble substrates. Whether this is achieved by: i) increasing the coating thickness [12–14], ii) incorporating a dense interlayer between the substrate and coating (interlayer designs) [6,7,15,16], iii) disrupting the columnar growth orientation by means of multilayer architectures [17–20], or iv) by refining the coating morphology altogether through alloying routs [21], all approaches aim to obstruct fast-track diffusion pathways between the electrolyte and the substrate in order to improve the corrosion behavior of the system.

Following a doping strategy, this study provides novel insights into the positive impact that V-doping imparts on the corrosion behavior of cathodic arc evaporated AlCrN thin films in NaCl-rich media. An $Al_{0.7}Cr_{0.3}N$ chemistry was chosen as the base system, whereupon chromium was progressively substituted with vanadium. In a series of $Al_{0.7}Cr_{0.3-x}V_xN$ depositions, with vanadium contents ranging from x = 0–22.3 at% on the metal sublattice, two strategies are being pursued: *i)* improving the corrosion behavior solely by means of vanadium-doping, and ii) further improving the corrosion resistance of the $Al_{0.7}Cr_{0.3-x}V_xN$ series through an annealing step and consequent development of a vanadium-rich top-oxide scale. Thus, the first part of this study will focus on the effect of vanadium content in the as-deposited state, by considering changes in microstructure and crystal phase composition, while the second part will provide a detailed investigation on the oxide scale formation and diffusion mechanisms of the annealed samples.

## 2. Experimental methods

All coatings were deposited in an industrial scale deposition system

---

* Correspondence to: TU Wien- Institute of Materials Science and Technology Getreidemarkt 9/ E308-01, A-1060 Wien, Österreich
*E-mail address:* oliver.hudak@tuwien.ac.at (O.E. Hudak).

https://doi.org/10.1016/j.corsci.2023.111376
Received 21 March 2023; Received in revised form 2 June 2023; Accepted 1 July 2023

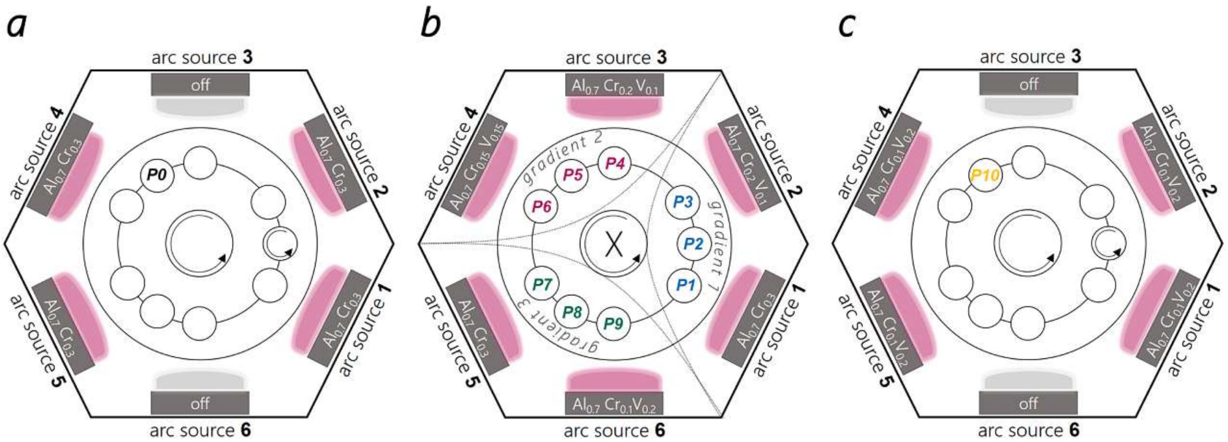

**Fig. 1.** : Schematic of the cathodic arc evaporation deposition chamber, showing target arrangements, sample positions used for all $Al_{0.7}Cr_{0.3-x}V_xN$ coatings. a) shows a rotary deposition run equipped with $Al_{0.7}Cr_{0.3}$ targets (P0). b) shows a stationary deposition run with varying target arrangements used for P1-P9. Gradient 1 (P1-P3) was placed between $Al_{0.7}Cr_{0.3}$ and $Al_{0.7}Cr_{0.2}V_{0.1}$ targets, Gradient 2 (P4-P5) was placed between $Al_{0.7}Cr_{0.2}V_{0.1}$ and $Al_{0.7}Cr_{0.15}V_{0.15}$ targets, and Gradient 3 (P7-P9) was positioned between $Al_{0.7}Cr_{0.3}$ and $Al_{0.7}Cr_{0.1}V_{0.2}$ targets. c) shows a rotary deposition run equipped with $Al_{0.7}Cr_{0.1}V_{0.2}$ targets (P10).

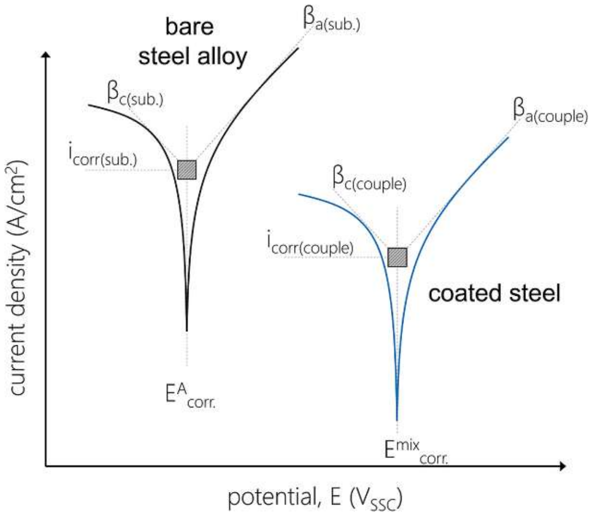

**Fig. 2.** : A schematic of a Tafel Plot from which several electrochemical parameters can be obtained: $E^{A}_{corr.}$, corrosion potential of the bare steel; $E^{mix}_{corr}$, mixed corrosion potential of the deposited coatings on steel; $i_{corr}$, corrosion current density; $\beta_{c(alloy)}$, $\beta_{a(alloy)}$, cathodic and anodic Tafel-slopes of the bare alloy; $\beta_{c(couple)}$, $\beta_{a(couple)}$, cathodic and anodic Tafel-slopes of the coating-alloy couple.

(INNOVA, Oerlikon Balzers, Liechtenstein) by cathodic arc evaporation. $Al_{0.7}Cr_{0.3-x}V_x$ targets were powder-metallurgically manufactured by Plansee Composite Materials GmbH and used for all coating variants. Steel foil with 0.05 mm thickness, and low-alloy steel discs (90MnCrV8) were utilized as substrates. Whereas the steel-foil was solely appropriated for as-deposited characterization purposes (e.g. analysis of the coatings morphology via fracture cross-section, coating thickness measurements and crystal-phase investigations by X-ray diffraction), the coated steel discs were exclusively used for electrochemical-corrosion experiments and post-corrosion analysis. All substrates were ultrasonically cleaned in acetone and ethanol before they were mounted into the deposition chamber. With a base pressure of $< 5.0^{-4}$ Pa, the substrates were further cleaned for 25 min by an argon plasma etching procedure (Oerlikon Surface Solutions AG).

All arc evaporated coatings were deposited in a pure $N_2$ atmosphere at 3.5 Pa, with a DC-bias of up to − 100 V at 480 °C. Regarding the corrosion behavior, all coatings were grown to a thickness ~5 µm for optimal comparison.

### 2.1. *Gradient coating procedure*

Fig. 1 shows the schematic of the deposition chamber equipped with six arc-sources. A total of 11 $Al_{0.7}Cr_{0.3-x}V_xN$ coatings with varying V-content were deposited (designated P0-P10, by using several target compositions: $Al_{0.7}Cr_{0.3}$, $Al_{0.7}Cr_{0.2}V_{0.1}$, $Al_{0.7}Cr_{0.15}V_{0.15}$ and $Al_{0.7}Cr_{0.1}V_{0.2}$ at%.

P0 designates the $Al_{0.7}Cr_{0.3}$ $V_xN$ base coating with the lowest V-content (0 at% V). The deposition system was equipped with four $Al_{0.7}Cr_{0.3}$ targets and operated with a two-fold substrate rotation, as shown in Fig. 1a.

P1-P9 represent $Al_{0.7}Cr_{0.3-x}V_xN$ coatings with varying V-contents that come from a stationary deposition mode (no substrate rotation). Three substrates were placed between two adjacent arc sources, equipped with different target compositions, as shown in Fig. 1b. Depending on the V content of each target, together with the relative distance of the substrates to each of the two respective arc-sources, a slightly different coating composition was obtained.

P10 denotes the $Al_{0.7}Cr_{0.3-x}V_xN$ coating with the highest V-content. The deposition system was equipped with four $Al_{0.7}Cr_{0.1}V_{0.2}$ targets and operated with a two-fold substrate rotation (Fig. 1c).

### 2.2. *Annealing experiments in air*

Isothermal annealing experiments were conducted in air at 700 °C. For each treatment, the chamber furnace (Medlin & Naber GesmbH, Vienna, Austria) was preheated to 700 °C and let equilibrate for a minimum of 12 h. All temperature profiles were monitored using a Naber Temperature TP1 processor in conjunction with a mounted type K thermoelement. The coated samples were then placed into the preheated chamber and annealed isothermally for 3 h.

### 2.3. *Characterization of as-deposited and annealed coatings*

For studying the morphology of the coatings (coating thickness, surface texture, and the integrity of the substrate-coating interfaces), a Zeiss Sigma 500 VP high-resolution field emission gun scanning electron microscope (FEGSEM) was used. With an acceleration voltage, ranging between 3 kV and 7 kV, characterization of coating thickness and

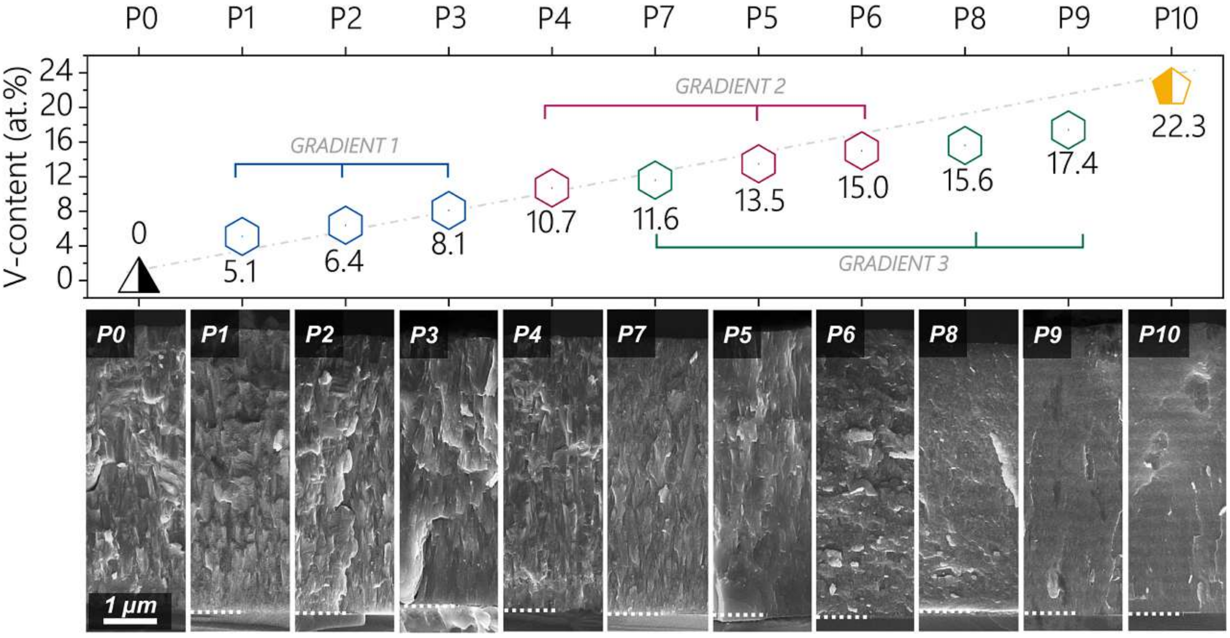

**Fig. 3.** : SEM micrographs showing fracture cross-sections of as-deposited $Al_{0.7}Cr_{0.3-x}V_xN$ with varying vanadium contents (P0 to P10). Their respective vanadium contents (at% on the metal sublattice) are presented above.

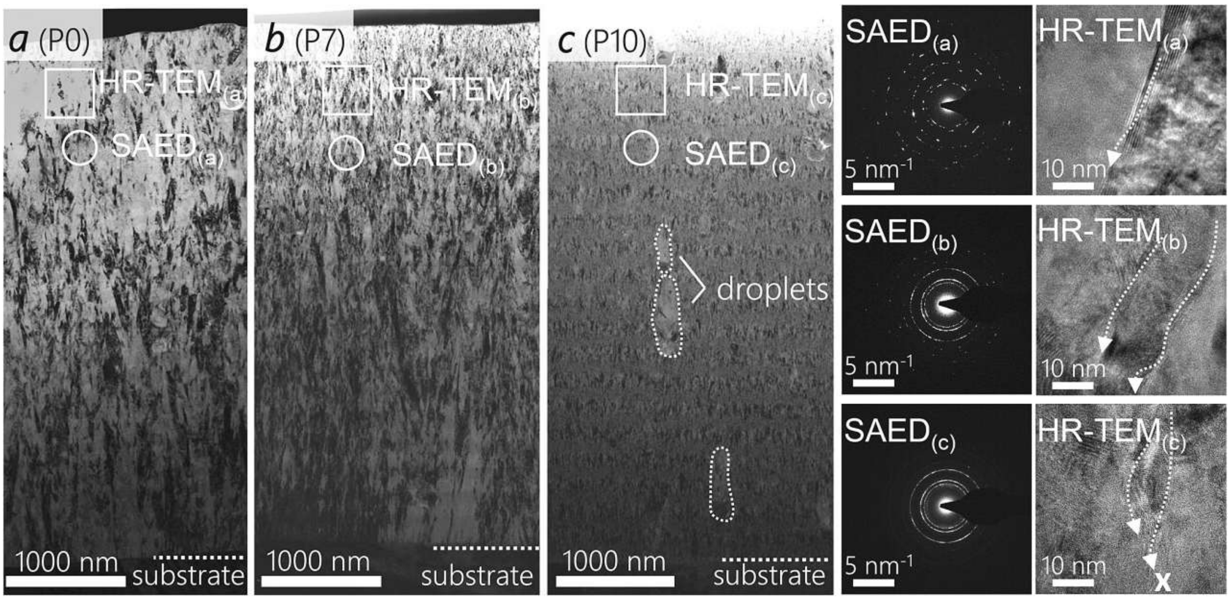

**Fig. 4.** : TEM investigations highlighting grain-refinement, as a consequence of V-doping. a-c feature bright-field images of as-deposited cross sections of the $Al_{0.7}Cr_{0.3}N$, $Al_{0.7}Cr_{0.19}V_{0.11}N$ and $Al_{0.7}Cr_{0.08}V_{0.22}N$ coatings, respectively. Further SAED and HR-TEM images render information about the crystallinity, as well as manifestation of grain-boundaries that comprise the coating matrix.

coating morphology were performed on fracture cross sections of coated steel-foil substrates. Equipped with an EDAX Octane elect system, energy dispersive X-ray spectroscopy (EDX) was utilized for quantitative elemental investigations.

Complementary to the EDX measurements, Time-of-Flight Heavy Ion Elastic Recoil Detection Analysis (ToF-HIERDA) was employed. All measurements were performed at the 5 MV 15SDH-2 Pelletron tandem accelerator at Uppsala University [22] employing $^{127}I^{8+}$ projectiles with a primary energy of 36 MeV with an incident angle of 67.5° with respect to the surface normal and a recoil detection angle of 45° with respect to the incident beam direction. Elemental composition depth profiles were determined using the CONTES software package [23] with the total systematic and statistical uncertainties estimated to be below 5% of the deduced value for the major constituents. For a more detailed description of the analytical set-up, we refer the reader to Ström et. al. [24].

For a more detailed investigation of the coating morphologies,

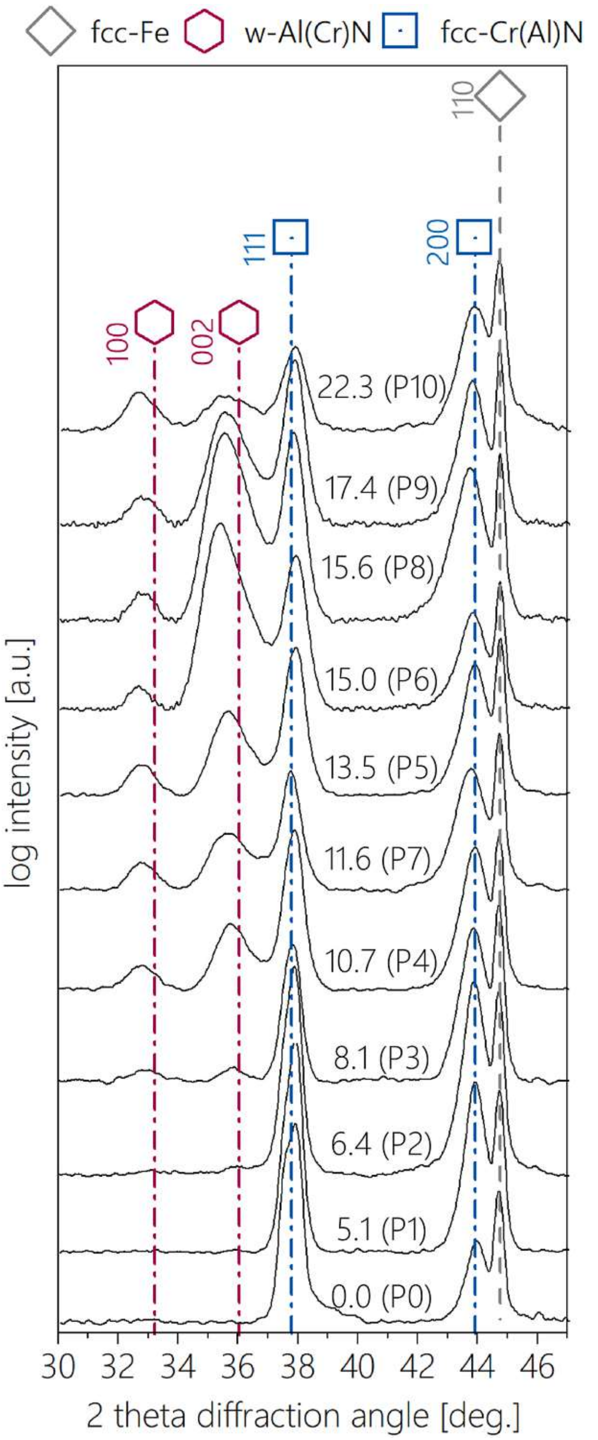

**Fig. 5.** : XRD spectra of the as-deposited arc evaporated $Al_{0.7}Cr_{0.3-x}V_xN$ coatings with increasing V-contents (at% V on the metal sublattice). Reference patterns were taken from Ref. [25–27].

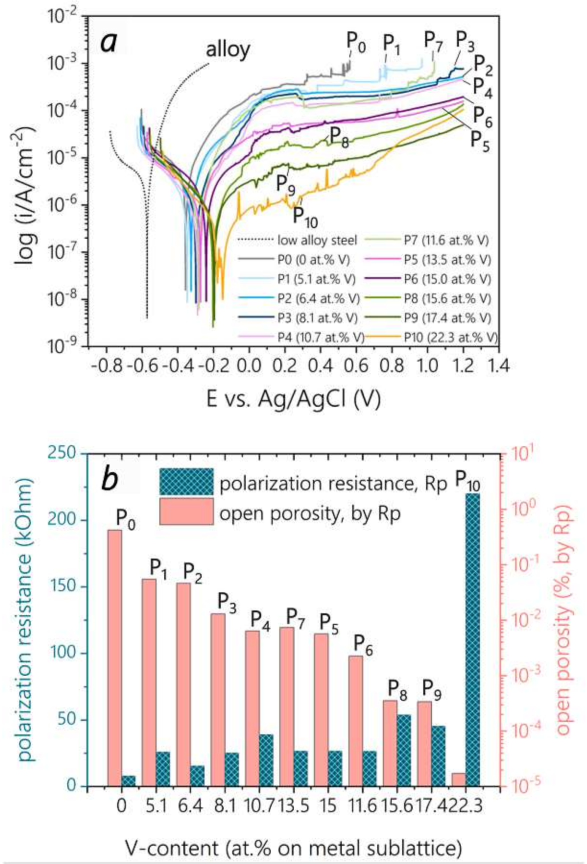

**Fig. 6.** : Electrochemical investigations of as-deposited $Al_{0.7}Cr_{0.3-x}V_xN$ coatings with varying vanadium-content (at% V on metal sublatice): a) Shows the original Tafel-plots measured in 0.1 M NaCl-solution, from which b) polarization resistance and open porosity values were calculated.

transmission electron microscopy (TEM, FEI TECNAI F20, equipped with a field emission gun and operated at an accelerating voltage of 200 kV) was conducted. Bright field (BF) imaging was utilized to learn more about the microstructure, crystallinity, and texture. For the preparation of the TEM lamellas, a standard lift-out procedure during focused-ion beam etching (FIB) milling was utilized (Scios 2 DualBeam system, ThermoFisher Scientific).

For crystallographic investigations, Bragg-Brentano X-ray diffraction (BBHD) was utilized, using a PANalytical XPert Pro MPD system equipped with a Cu-Kα radiation source (wave length $\lambda = 1.54$ Å).

Electrochemically corroded samples were embedded in a conductive polymer-matrix, their cross-sections ground and polished, and analyzed via SEM and EDX. Accordingly, pit-formations, coating-substrate adherence, and fast-track diffusion routes of the electrolyte were examined.

### *2.4. Electrochemical corrosion experiments*

Linear potentiodynamic polarization experiments were performed using a three-electrode set-up. With a saturated Ag/AgCl reference electrode (SSC), a Pt-counter electrode (CE) and the coated steel sample as working electrode (WE), the electrochemical experiments were conducted in a 0.1 M NaCl solution. Each sample was mounted into a press-fit corrosion cell, which accommodated a sample contact area of 1.58 cm$^2$. All samples were left to equilibrate for 20 min, after which the corrosion potential ($E_{corr.}$) was measured. Once the measured potential drops below a time derivative limit (dE/dt= $1 \times 10^{-6}$ V/s), the recorded potentials from the last 5 s was averaged and taken as $E_{corr}$. The linear sweep voltammetry (LSV) measurements were started cathodically at $E_{corr.} - 300$ mV and swept into the anodic region with a sweep-rate of

**Table 1**

Electrochemical properties of as-deposited $Al_{0.7}Cr_{0.3-x}V_xN$ coated low-alloy steel substrates in 0.1 M NaCl solution. $E_{corr.}$, corrosion potential; $I_{pass}$, passive current density; $i_{corr}$, corrosion current density; $\beta_c$, cathodic Tafel-slope; $\beta_a$, anodic Tafel-slope; $R_p$, polarization resistance; $P_{Rp}$, open porosity deduced from $R_p$.

| *material* | *V-content on metal- sublattice (at%)* | $E_{corr.}$ (mV) | $I_{pass.}$ (A/cm$^2$) | $I_{corr}$ (A/cm$^2$) | $\beta_c$ (mV/dec) | $\beta_a$ (mV/dec) | $R_p$ (kΩ×cm$^2$) | $P_{Rp}$ (%) |
|---|---|---|---|---|---|---|---|---|
| *low-alloy steel* | *n.a.* | -560 | *n.a.* | $3.17\times10^{-6}$ | 363.6 | 76.9 | 8.6 | *n.a.* |
| *AlCrN* | 0 (P0) | -375 | $6.60\times10^{-4} \pm1.12\times10^{-4}$ | $2.57\times10^{-6}$ | 115.7 | 81.7 | 8.0 | $4.22\times10^{-1}$ |
| $Al_{0.7}Cr_{0.3-x}V_xN$ *as-deposited* | 5.1 (P1) | -344 | $4.03\times10^{-4} \pm3.00\times10^{-5}$ | $8.50\times10^{-6}$ | 129.4 | 84.7 | 25.9 | $5.48\times10^{-2}$ |
| | 6.4 (P2) | -323 | $2.45\times10^{-4} \pm1.51\times10^{-5}$ | $1.64\times10^{-6}$ | 191.2 | 85.1 | 15.4 | $4.61\times10^{-2}$ |
| | 8.1 (P3) | -297 | $1.94\times10^{-4} \pm1.52\times10^{-5}$ | $9.69\times10^{-7}$ | 146.0 | 93.6 | 25.3 | $1.29\times10^{-2}$ |
| | 10.7 (P4) | -288 | $1.38\times10^{-4} \pm5.85\times10^{-6}$ | $5.93\times10^{-7}$ | 150.4 | 84.4 | 39.1 | $6.38\times10^{-3}$ |
| | 11.6 (P7) | -280 | $1.33\times10^{-4} \pm9.77\times10^{-6}$ | $6.89\times10^{-7}$ | 109.6 | 69.4 | 26.6 | $7.39\times10^{-3}$ |
| | 13.5 (P5) | -271 | $5.36\times10^{-5} \pm2.89\times10^{-6}$ | $9.43\times10^{-7}$ | 178.6 | 86.7 | 26.6 | $5.65\times10^{-3}$ |
| | 15.0 (P6) | -240 | $6.02\times10^{-5} \pm3.07\times10^{-6}$ | $9.85\times10^{-7}$ | 135.7 | 109.6 | 26.4 | $2.24\times10^{-3}$ |
| | 15.6 (P8) | -202 | $1.99\times10^{-5} \pm2.31\times10^{-6}$ | $5.41\times10^{-7}$ | 149.0 | 125.0 | 53.9 | $3.52\times10^{-4}$ |
| | 17.4 (P9) | -195 | $9.08\times10^{-6} \pm4.25\times10^{-7}$ | $3.68\times10^{-7}$ | 77.3 | 78.6 | 45.5 | $3.39\times10^{-4}$ |
| | 22.3 (P10) | -148 | $4.07\times10^{-6} \pm6.64\times10^{-7}$ | $1.03\times10^{-7}$ | 151.3 | 81.1 | 220.0 | $1.72\times10^{-4}$ |

1 mV/s up to + 1.2 $V_{SSC}$. With a current-density cut-off value set to 1 mA/cm$^2$, the electrochemical tests were controlled and monitored by a potentiostat (Autolab PGSTAT302N, Metrohm).

### *2.5. Deductions based on polarization measurements*

Since protective coatings are prone to coating defects or open porosities, the measured galvanic current densities of the coated steel samples will depend on the contact ratio of the electrolyte and the coating/substrate surfaces. In other words, when the electrolyte is brought in contact with a "porous" coating surface, part of the electrolyte will contact the coating and part of the substrate material beneath, generating a galvanic couple.

From the Tafel-plots, the cathodic and anodic Tafel-slopes ($\beta_c$ and $\beta_a$), as well as corrosion current density values ($i_{corr}$) and corrosion potential ($E_{corr.}$) were extrapolated (see Fig. 2). By using the Stern-Geary Equation (see Eq. 1), the polarization resistance ($R_p$) could be calculated for the uncoated substrate, as well as all $Al_{0.7}Cr_{0.3-x}V_xN$ coated samples.

$$Stern - Geary \quad Equation(R_p) = \frac{\beta_c * \beta_a}{2.33 * i_{corr}(\beta_c+\beta_a)} \tag{1}$$

Finally, according to the following relation (Eq. 2), the porosity of the coating was calculated:

$$P = \frac{R_{p(substrate)}}{R_{p(coating)}} * 10^{-\left(\frac{|\Delta E_{corr}|}{\beta_{a(substrate)}}\right)} \tag{2}$$

where P denotes the open porosity of the coating, $R_{p(substrate)}$ is the polarization resistance of the uncoated substrate material, $R_{p(coating)}$ is the polarization resistance of the coated substrate, $\Delta E_{corr.}$ refers to the difference in the corrosion potential between the uncoated and coated substrate, and $\beta_{a(substrate)}$ to the anodic Tafel-slope of the bare substrate – also see Fig. 2.

Lastly, by combining the corrosion current density ($I_{corr}$) with Faraday's Law (see Eq.3), the corrosion rate (CR) may be calculated (see Eq.4).

$$W = \frac{A_w Q}{zF} \tag{3}$$

where W is the mass material removed, $A_w$ is the atomic weight of the sample, Q is the total charge passed through the system and z is the number of electrons transferred in the reaction.

$$CR = W * \frac{As}{\rho} \tag{4}$$

where $A_s$ is the exposed surface area and ρ is the density of the material.

## 3. Results and discussion

### *3.1. Microstructure and composition analysis*

The as-deposited microstructures of all $Al_{0.7}Cr_{0.3-x}V_xN$ coatings are shown in Fig. 3. The fracture cross section labeled P0 represents the as-deposited microstructure of the base system $Al_{0.7}Cr_{0.3}N$ with 0 at% vanadium. We would like to point out that this coating does not come from a stationary deposition run, but instead was deposited in a conventional manner with rotation and four identical target compositions. P1 to P9, on the other hand, do originate from the stationary gradient deposition and are numerated according to the arrangement within the chamber (revisit Fig. 1). P10 represents the microstructure of the coating with the highest V-content and was also deposited with substrate rotation and four identical $Al_{0.7}Cr_{0.1}V_{0.2}$ targets mounted within the deposition chamber. Above the cross-sectional SEM images the corresponding V-contents are plotted (at% on the metal sublattice, determined by EDX and verified by ERDA). For a complete overview of the chemical compositions, we refer to Appendix A.

First observations of the as-deposited microstructures indicate a gradual grain-refinement with increasing vanadium content. While a distinct columnar growth morphology exists for chemistries ≤ 10.7 at% of V on the metal sublattice (P0-P3), a reduction in the column sizes can be noticed for contents ≥ 10.7 but ≤ 15.0 at% (P4, 5 and 7). From 15.0 at% upwards, the microstructure transitions into a coarse grained microstructure (P6 and P8) after which a featureless morphology predominates (P9 and P10).

TEM investigations further substantiate these observations. Fig. 4 shows the bright-field cross-sections of the as-deposited coatings P0, P7 and P10 with V-contents of 0, 11.6 and 22.3 at%, respectively (at% V on metal sublattice). Standing in good agreement with the previously shown SEM images, the effect of grain-refinement is clearly visible as the vanadium content increases. An initial refinement of the columnar structure is observed between P0 and P7, after which a featureless morphology develops. Selected area electron diffractograms (SAED), as well as high resolution TEM (HR-TEM) images were collected near the coating surfaces, to provide localized information about the coatings' crystallinity. Starting with the $Al_{0.7}Cr_{0.3}N$ coating with 0 at% V-content (P0), the $SAED_{(a)}$ provides a diffraction pattern with distinct diffraction dots, which is indicative of a crystalline morphology. The respective $HR\text{-}TEM_{(a)}$ image features a well-defined column-boundary, which would, in case of a subsequent corrosion experiment, offer a preferential diffusion path for chloride species. Such fast track diffusion pathways for chloride species have been investigated in a previous study [1], and deemed to be a significant draw-back in effectively providing corrosion protection. As vanadium is substituted for chromium, first to 11.6 at% (P7) and then further to 22.3 at% V-content (P10), the SAEDs feature

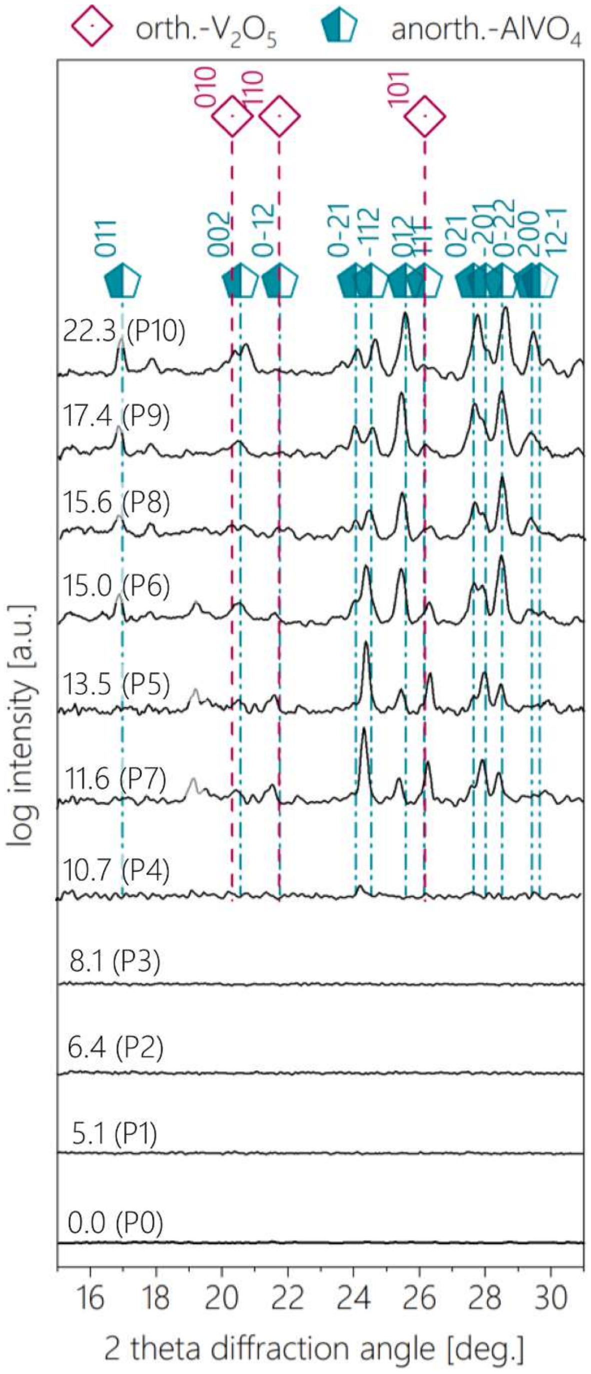

**Fig. 7. :** XRD spectra of the arc evaporated $Al_{0.7}Cr_{0.3-x}V_xN$ coatings isothermally annealed at 700 °C in air for 3 h with increasing V-content (at% V on metal sublattice) from bottom to top (P0 to P10, respectively). Reference patterns were taken from Ref. [30,31].

smeared diffraction dots ($SAED_{(b)}$), or even a ring-like diffraction pattern ($SAED_{(c)}$). Together with the respective HR-TEM images ($HR\text{-}TEM_{(b)}$ and $HR\text{-}TEM_{(c)}$), which indicate narrowing of distinct column boundaries, both HR-TEM and SAED analysis point out that the microstructure transitions into a more nanocrystalline structure with a discontinuous columnar arrangement (highlighted by the x in the $HR\text{-}TEM_{(c)}$ image of Fig. 4).

### 3.2. *Structural evolution in relation to V-content*

Fig. 5 features X-ray diffractograms and peak-patterns for the as-deposited $Al_{0.7}Cr_{0.3-x}V_xN$ samples P0 to P10. Analogous to Fig. 3, the vanadium contents and chamber locations are listed next to each diffractogram with increasing V-content from bottom to top.

The $Al_{0.7}Cr_{0.3}N$ base system with no vanadium content (P0) features a face-centered-cubic (fcc) crystal structure and exhibits a single-phase Cr(Al)N solid solution with mixed [111]/[200] growth orientations. As chromium is replaced by vanadium in the AlCrN-base-system, the crystal lattice is able to maintain the fcc-Cr(Al,V)N solid solution up to a vanadium content of 6.4 at% on the metal sublattice (P1 = 5.1 at% V and P2 = 6.4 at% V). However, as more vanadium is added (P3 = 8.1 at %), the solubility limit for Al in the fcc-Cr(Al,V)N structure is reached, and the formation of the wurzite-Al(Cr,V)N phase is favored. Consequently, from P4 (10.7 at% V) to P9 (17.4 at% V), a dual-phase, consisting of the fcc-Cr(Al,V)N and w-type Al(Cr,V)N phases make up the coating structures. While we identify the onset for the formation of w-Al (Cr,V) at a V-content of about 8.1 at% (Fig. 5, P3) and the formation of a dual-phase crystal structure thereafter (Fig. 5, P4 to P10), we can relate the competitive growth orientations between the w-Al(Cr,V)N and fcc-Cr(Al,V)N to the gradual grain-refinement first observed at P4 (Fig. 3). Based on this, we propose that the nucleation of the competitive w-Al (Cr,V)N phase with increasing V-content inhibits the growth of the opposing fcc-Cr(Al,V)N crystallites.

Also interesting is the maximum phase-fraction of the w-type Al(Cr, V)N to fcc-Cr(Al,V)N peaking at 15 at% V (P6), after which the fcc-Cr (Al,V)N or rather fcc-V(Cr,Al)N phase is again stabilized and the w-type Al(Cr,V)N phase recedes. This observation is solely made upon the intensity-evolution of the predominant w-AlN 002 reflex.

### 3.3. *Electrochemical corrosion properties*

Tafel-plots of the bare 90MnCrV8 alloy (low alloy steel) and as-deposited $Al_{0.7}Cr_{0.3-x}V_xN$ coated samples are shown in Fig. 6a. Tafel-extrapolations were made manually with no additional software package for data analysis. From the intersection of the anodic and cathodic Tafel-branches the corrosion currents ($I_{corr}$) and corrosion potentials ($E_{corr.}$) have been determined for all samples (listed in Table 1).

### 3.4. *Current density vs. V-content*

Firstly, the corrosion currents ($i_{corr}$) and passivation currents ($i_{pass}$) that were measured decrease significantly with increasing vanadium-to-chromium-ratio. Whereas quite similar $i_{corr}$ values were obtained for the uncoated alloy and the $Al_{0.7}Cr_{0.3}N$-coated samples with 0 at% V-content ($3.17 \times 10^{-6}$ and $3.32 \times 10^{-6}$ A/cm$^2$, respectively), a gradual reduction of the corrosion current densities was measured in accordance with the substitution of chromium with vanadium. In more detail, for a V-content of 5.1 at% on the metal sublattice (P1), $I_{corr}$ was determined to be $1.23 \times 10^{-6}$ A/cm$^2$, whereas for V-contents of 11.6 and 22.3 at% (P7 and P10), the measured $I_{corr}$ values decreased to $6.01 \times 10^{-7}$ and $9.81 \times 10^{-8}$ A/cm$^2$, respectively.

### 3.5. *Corrosion potential vs. V-content*

Secondly, a significant positive shift of the $E_{corr.}$ can be observed from the uncoated alloy (low alloy steel= −569 mV$_{ssc}$) to all $Al_{0.7}Cr_{0.3-x}V_xN$ coated samples (P0 = −354 mV$_{ssc}$), which indicates a reduced anodic activity of the coated sample over the bare alloy. Further positive shifting of the $E_{corr.}$ is measured as the vanadium-to-chromium-ratio increases for the $Al_{0.7}Cr_{0.3-x}V_xN$ coatings. The most noble $E_{corr.}$ is therefore obtained by the coating with 22.3 at% V on the metal sublattice (P10 = −148 mV$_{SSC}$). At this point, we again would like to point

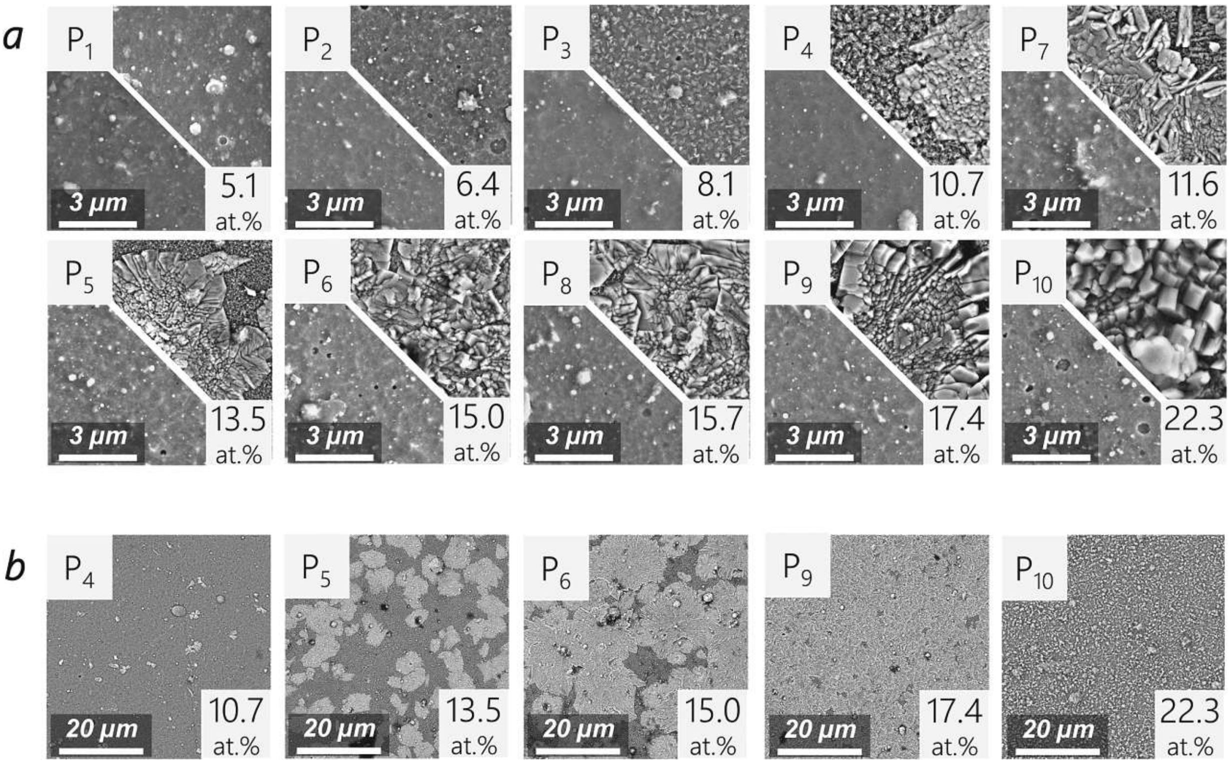

**Fig. 8.** : SEM top-view images of $Al_{0.7}Cr_{0.3-x}V_xN$ coatings with varying V-contents (at% V on metal sublattice): a) shows combined images consisting of as-deposited (bottom) and annealed states (top, 700 °C for 3 h in air). b) features selected annealed coating surfaces at lower magnification.

out that the measured $E_{corr.}$ for all coated samples are mixed potentials between the coating and substrate material, owed to open porosities and coating defects.

### 3.6. *Open Porosity vs V-content*

When considering that porosities and fast track diffusion sites along incoherent grain boundaries contribute to a more anodically active galvanic couple (coating/alloy), control over the open porosity of protective coatings is of great importance [1]. Therefore, we would like to put the aforementioned electrochemical data in context with the open porosity values (Eqs.1–2). Fig. 6b shows a bar chart visualizing the correlation between the V-content the open porosity ($P_{Rp}$) and the polarization resistance ($R_p$) of all as-deposited coatings. Standing in good agreement with the SEM and TEM analysis, a gradual decrease in the open porosity rate ($P_{Rp}$) is observed with increasing V-content. Naturally, with less contact area between the electrolyte and the substrate alloy, the polarization resistance of the coating/substrate couple increases with increasing V-content. All values are also listed in Table 1.

### 3.7. *Isothermal annealing of $Al_{0.7}Cr_{0.3-x}V_xN$ coatings*

Now that the microstructure, open porosity, and corrosion behavior have been thoroughly discussed in light of the vanadium content in the $Al_{0.7}Cr_{0.3-x}V_xN$ coatings, we wish to further investigate the corrosion resistance of their respective annealed states. With the goal to develop a vanadium-rich top-oxide scale — intended to function as an additional sealing barrier and to minimize fast-track diffusion junctions to the coating-substrate interface — we first investigated the oxidation behavior of the annealed coatings. Fig. 7 shows the Bragg-Brentano X-ray diffractograms for $Al_{0.7}Cr_{0.3-x}V_xN$ samples P0 to P10, that have been annealed isothermally at 700 °C for 3 h in air. As 700 °C is well below the phase transition temperature of fcc-Cr(Al)N to w-Al(Cr)N (>900 °C) for the $Al_{0.7}Cr_{0.3}N$ system, we can assume that the overall phase-stability of the $Al_{0.7}Cr_{0.3-x}V_xN$ remains stable throughout the annealing treatment [28]. Moreover, 700 °C also falls well below the oxidation temperature of the fcc-$Al_{0.7}Cr_{0.3}N$ system, where temperatures of $>$ 900 °C have been reported necessary for producing $Cr_2O_3$ and $Al_2O_3$ scales [29]. We therefore expect a distinct vanadium threshold content, where predominanltly vanadium-oxides form upon annealing at 700 °C. Analogous to the XRD analysis of the as-deposited coatings (Fig. 5), the vanadium contents (at% V on metal sublattice) are listed next to each diffractogram with increasing V-content from bottom to top, together with their respective deposition chamber positions. A reduced corridor of diffraction angles was chosen for the illustration, as i) most of the oxides, ($Cr_2O_3$, $Al_2O_3$, VO, $V_nO_{2n+1}$, $V_nO_{2n-1}$, $V_nO_{2n}$) feature their prominent Bragg diffractions between 15 and 30 degrees, and ii) any diffraction reflexes larger than 30° would overlap with the fcc-Cr(Al,V)N and w-Al(Cr,V)N peaks [25–27,30–36]. Evident from the diffractograms in Fig. 7, no oxide peak was detected for any of the annealed $Al_{0.7}Cr_{0.3-x}V_xN$ coatings with a V-content up to 8.1 at% (P0 to P3). At a V-content of 10.7 at%, however, first indications of oxidation are noticeable (P4). A similar V-threshold has been reported by Tillmann *et al.*, observing an oxidation onset at 10.7 at% V, however, with slightly different Al and Cr metal ratios [37]. At V-contents of 11.6 at% and higher, significant oxidation of the coating surfaces is measured with the most prominent Bragg-reflexes identified as a mixed anorthic-$AlVO_4$ and orthorhombic-$V_2O_5$ scale.

This sudden onset of the mixed V-oxide evolution is also observed by SEM-analysis. Fig. 8a shows combined top-view images of the as-deposited (bottom half) and its respective annealed coating surfaces (top-half) for all vanadium containing $Al_{0.7}Cr_{0.3-x}V_xN$ coated samples. Standing in good agreement with the XRD measurements, a distinct onset of a developing surface-oxide is seen for the sample P4 (10.7 at% V

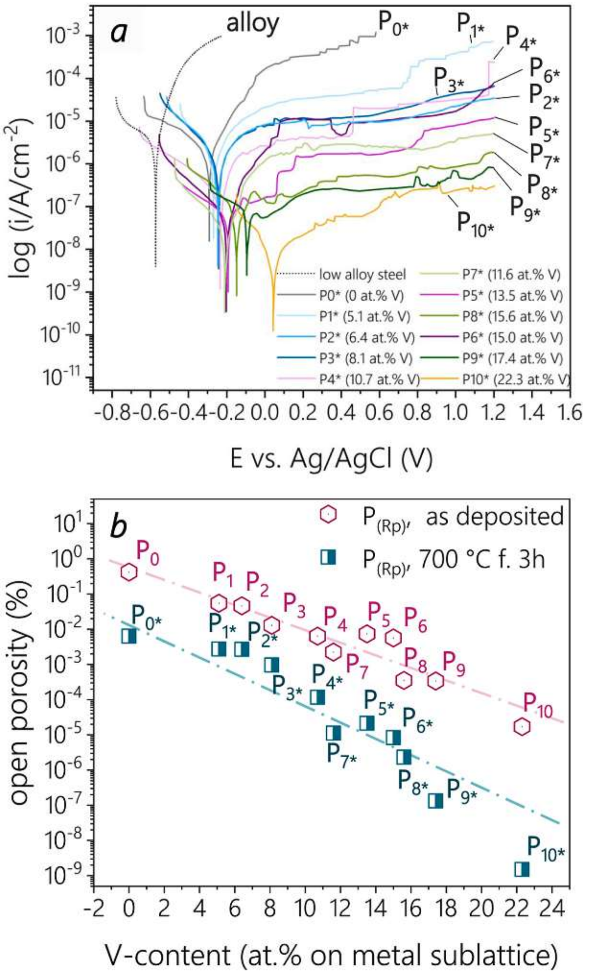

**Fig. 9.** : Electrochemical data of $Al_{0.7}Cr_{0.3-x}V_xN$-coated steel samples with varying V-content (at% on metal sublattice) annealed at 700 °C in air: a) Tafel plots and b) calculated open-porosity values for all $Al_{0.7}Cr_{0.3-x}V_xN$ coatings in their as-deposited state, as well as annealed state.

on metal sublattice), where nucleation-islands of vanadium-oxides stud the coating surface. At slightly higher vanadium-concentrations (11.6 at % V on metal sublattice, P7), a converging of the nucleation islands results in a more pronounced oxide scale, which develops thicker and more matured as more vanadium is available within the $Al_{0.7}Cr_{0.3-x}V_xN$ system (P5, P6, P8 and P9). Finally, with a V-content of 22.3 at% on the metal sublattice (P10), distinct vanadium oxide crystals grow, that appear more ordered than the oxide scale at lower V-contents.

Another interesting effect, related to the V-content, is observed at slightly lower magnification, see Fig. 8b. While all samples have been annealed for the same duration of 3 h at 700 °C, a faster growth of the vanadium-oxides-islands is featured for coatings with higher V-contents. While only remote nucleation sites of surface oxides are observed at a V-contents of 10.7 at% on the metal sublattice (P4), considerable spawning of vanadium-oxide patches evolve at a V-content of 13.5 at% (P5). At even higher V-contents (15.0 at% and 17.4 at% V on metal sublattice for P6 and P9, respectively), larger oxide islands develop, which converge to fully cover the coating surface. This is the case for P10 (22.3 at% V on metal sublattice), where a continuous and crystalline vanadium oxide scale has developed on top of the coating.

### 3.8. *Electrochemical investigations of annealed $Al_{0.7}Cr_{0.3-x}V_xN$-coated samples*

LSV measurements of the annealed samples were conducted in an identical manner to the electrochemical investigations of the as-deposited $Al_{0.7}Cr_{0.3-x}V_xN$ coated samples. Fig. 9a shows the Tafel-plots of the isothermally annealed $Al_{0.7}Cr_{0.3-x}V_xN$ coated samples, as well as the bare alloy (not annealed). As the V-content of the coatings increases, a shifting of the $E_{corr.}$ into more positive potentials is observed, accompanied by an anew decreasing in the corrosion currents ($i_{corr}$). Tafel-extrapolations again provide the electrochemical parameters, such as cathodic and anodic Tafel-slopes ($\beta_c$ and $\beta_a$, respectively), corrosion current densities ($i_{corr}$) and corrosion potentials ($E_{corr.}$), that were then used for calculating the coatings' porosities (according to Eq. 1 and Eq. 2). The porosity values for all as-deposited and annealed $Al_{0.7}Cr_{0.3-x}V_xN$ samples are plotted in Fig. 9b, with the intention to better illustrate the improved values between the as-deposited and annealed states, as well as to further highlight the beneficial effect of the V-content. A summary of the extrapolated electrochemical values, as well as the calculated values, such as polarization resistance and open porosities are also listed in Table 2.

Lastly, corrosion rates of the as-deposited, as well as annealed coated steel samples were calculated. As there are no indications of dissolution or oxidation processes of the coating material, it is expected that the current densities measured during the electrochemical experiments must come from the low alloy steel substrate (dissolution of iron). In this case, together with Faraday's Law, the mass-loss of the substrate was calculated by correlating the corrosion currents ($i_{corr}$) with the dissolution of iron (Eq. 3 and Eq. 4). Fig. 10 shows the individual corrosion rates (mg/cm$^2$ per year) for each $Al_{0.7}Cr_{0.3-x}V_xN$-steel couple. Evident is the gradual reduction in mass-loss with increasing V-content within the coatings and an even further reduction in the corrosion rate for the annealed series. With the exception of the as-deposited $Al_{0.7}Cr_{0.3}N$ coating (P0, 0 at% V), all $Al_{0.7}Cr_{0.3-x}V_xN$ coated steel samples exhibit reduced corrosion rates over the uncoated steel substrate.

Reason for this slightly increased corrosion rate of the $Al_{0.7}Cr_{0.3}N$ coated samples, despite the intended protective character of the coating, is the galvanic couple that forms when the electrolyte makes contact with both, the coating matrix and the steel substrate. The more noble coating surface thereby acts as the cathode, whereas the steel-substrate adopts the role of the anode. Due to the vastly larger contact area made between the coating surface (large cathode) compared to the small contact area made between the diffused electrolyte and the steel alloy (small localized anode), accelerated oxidation occurs. As vanadium quite drastically refines the morphology of the $Al_{0.7}Cr_{0.3-x}V_xN$ system, it yields fewer porosities (direct diffusion pathways) for the NaCl-electrolyte to reach the coating-substrate interface. Accordingly, with fewer contact area between the electrolyte and the steel substrate, lower corrosion currents (corrosion rates) are generated. We therefore see a strong correlation between the open-porosity values and the calculated corrosion rates of the $Al_{0.7}Cr_{0.3-x}V_xN$-steel couples.

### 3.9. *Vanadium-oxide scale investigation by TEM*

To further answer why the annealed $Al_{0.7}Cr_{0.3-x}V_xN$ sample with the highest V-content (P10 w. 22.3 at% V) performs best in light of its corrosion resistance, additional TEM analysis have been conducted. Here, the aim was to verify the crystal-structures that have been identified by XRD measurements in earlier sections, as well as to take a closer look at the diffusion profiles that evolved during the annealing process. For this, SAEDs together with TEM bright-field images of the coating's surface near region provide localized information about the crystal structure and crystallinity. Shown in Fig. 11a is a bright-field TEM image, which highlights three distinctly different morphologies: a crystalline top-oxide, a nanocrystalline oxygen enriched band underneath, and the pristine coating matrix at the bottom (as found in the as deposited state).

**Table 2**
Electrochemical properties of annealed $Al_{0.7}Cr_{0.3-x}V_xN$ coated low-alloy steel substrates in 0.1 M NaCl solution. $E_{corr.}$, corrosion potential; $I_{pass}$, passive current density; $i_{corr}$, corrosion current density; $\beta_c$, cathodic Tafel-slope; $\beta_a$, anodic Tafel-slope; $R_p$, polarization resistance; $P_{Rp}$, open porosity deduced from $R_p$.

| material | V-content on metal- sublattice (at%) | $E_{corr.}$ (mV) | $I_{pass.}$ (A/cm$^2$) | $I_{corr}$ (A/cm$^2$) | $\beta c$ (mV/dec) | $\beta a$ (mV/dec) | $R_p$ (kΩ×cm$^2$) | porosity (%) |
|---|---|---|---|---|---|---|---|---|
| $Al_{0.7}Cr_{0.3-x}V_xN$ annealed at 700 °C f. 3 h in | 0 (P0*) | -291 | $2.61\times10^{-4}$<br>$\pm1.81\times10^{-5}$ | $4.39\times10^{-6}$ | 127.6 | 67.2 | 43.1 | $6.34\times10^{-3}$ |
| | 5.1 (P1*) | -269 | $2.23\times10^{-5}$<br>$\pm2.03\times10^{-6}$ | $3.60\times10^{-7}$ | 86.1 | 86.5 | 51.1 | $2.75\times10^{-3}$ |
| | 6.4 (P2*) | -248 | $8.80\times10^{-6}$<br>$\pm8.12\times10^{-7}$ | $8.99\times10^{-7}$ | 108.0 | 127.8 | 27.9 | $2.70\times10^{-3}$ |
| | 8.1 (P3*) | -242 | $5.96\times10^{-6}$<br>$\pm7.54\times10^{-7}$ | $2.45\times10^{-7}$ | 93.4 | 61.8 | 65.2 | $9.66\times10^{-4}$ |
| | 10.7 (P4*) | -233 | $1.72\times10^{-6}$<br>$\pm1.79\times10^{-7}$ | $3.31\times10^{-8}$ | 117.4 | 43.1 | 408.9 | $1.18\times10^{-4}$ |
| | 11.6 (P7*) | -210 | $6.79\times10^{-7}$<br>$\pm1.13\times10^{-7}$ | $2.30\times10^{-8}$ | 128.4 | 102.1 | 1132.0 | $2.13\times10^{-5}$ |
| | 13.5 (P5*) | -194 | $1.72\times10^{-6}$<br>$\pm6.38\times10^{-7}$ | $9.15\times10^{-9}$ | 92.9 | 65.1 | 1794.4 | $8.34\times10^{-5}$ |
| | 15.0 (P6*) | -203 | $4.90\times10^{-6}$ $\pm1.08\times10^{-6}$ | $8.58\times10^{-9}$ | 74.2 | 66.3 | 1751.5 | $1.12\times10^{-5}$ |
| | 15.6 (P8*) | -147 | $1.40\times10^{-7}$<br>$\pm3.60\times10^{-8}$ | $1.60\times10^{-8}$ | 111.5 | 124.8 | 1580.9 | $2.32\times10^{-6}$ |
| | 17.4 (P9*) | -95 | $5.26\times10^{-8}$<br>$\pm2.64\times10^{-8}$ | $8.18\times10^{-9}$ | 181.8 | 283.3 | 5813.9 | $1.33\times10^{-7}$ |
| | 22.3 (P10*) | -47 | $1.61\times10^{-8}$<br>$\pm1.58\times10^{-9}$ | $1.59\times10^{-9}$ | 129.2 | 206.6 | 21,511.0 | $1.50\times10^{-9}$ |

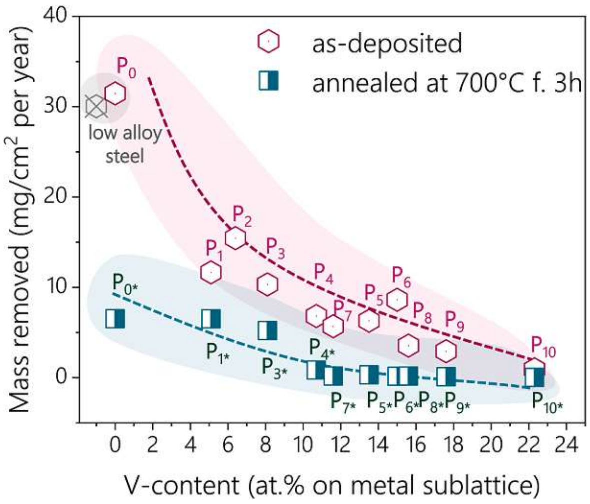

**Fig. 10. :** Comparison of the corrosion rates of as-deposited $Al_{0.7}Cr_{0.3-x}V_xN$ coated and annealed $Al_{0.7}Cr_{0.3-x}V_xN$ coated low-alloy steel substrates with varying V-contents (at% V on metal sublattice).

Starting with the top-oxide, single-crystalline domains are detected, as is evident from the spot-pattern of the $SAED_a$ in Fig. 11b. Indexing of the pattern renders a triclinic (anorthic) crystal structure of the $AlVO_4$-oxide with the space group $P\overline{1}$, which stands in excellent agreement with the findings from the XRD measurements and results from Franz et. al. [38,39].

Moving below the granular top-oxide, the $SAED_b$ in Fig. 11c features a combination of an amorphous material with a characteristic halo-ring pattern, as well as a nanostructured polycrystalline matrix, with typical smeared diffraction rings that appear further away from the primary beam. The decomposition of the original polycrystalline matrix to a semi-amorphous morphology can be attributed to the oxidation process during annealing, where oxygen inward diffusion is accompanied by simultaneous dissipation of nitrogen. By integrating the $SAED_b$ ring-pattern and plotting it over the reciprocal of the lattice-spacing, an intensity plot with broadened but still defined peaks is generated, which is shown in Fig. 11f. Again, we can deduce that the broadened peaks convey an amorphous character of the coating matrix, whereas more defined [200] and [220] reflexes of the fcc-CrN crystal structure suggest residue fragments of the original coating structure. The fact that only fcc-CrN residues appear in the intensity plot suggests a faster degradation mechanism of the hexagonal phase fraction, which greatly affects the diffusion of oxygen and other alloyed elements, such as vanadium. Lastly, $SAED_c$ and $SAED_d$ are intended to show the pristine dual fcc-Cr(Al,V)N and w-type Al(Cr,V)N phases. Furthermore, they reveal significant differences in the crystallinity of the coating morphology that is in close proximity of the oxygen-diffusion front ($SAED_c$) and the morphology that is further away ($SAED_d$). Evident from SAEDs in Fig. 11d and Fig. 11e, similar diffraction rings are obtained, whose integration in Fig. 11f also show close to identical intensity plots and, as expected, render the correct D-spacings for the fcc-Cr(Al,V)N and w-Al(Cr,V)N crystal structures. We therefore conclude that there is a sharp oxygen diffusion front, with little to no lattice distortion after.

### 3.10. *Description of diffusion mechanisms*

Next, the diffusion mechanisms are investigated in more detail. In accordance with the TEM analysis in Fig. 11, the same region of the annealed sample is chosen. First, we would like to direct the reader's attention to a top view SEM image in Fig. 12a and emphasize that the entire coating surface is homogeneously studded with a highly crystalline $AlVO_4$ top-oxide, which is otherwise not apparent from other cross-section images. Fig. 12b then shows a scanning TEM (STEM) image of the cross-section, which was chosen for subsequent EDX analysis. Several defined layers are visible through the generated mass contrast of the different coating domains. While areas with heavier elements appear brighter, regions with lighter elements produce a darker contrast in the image. First, an EDX line-scan was conducted across the entire field of view in order to take a closer look on the oxygen diffusion profile (Fig. 12c). Clearly evident is the sudden drop at the oxygen diffusion front (as labeled in Fig. 12b), where a simultaneous surge of nitrogen is

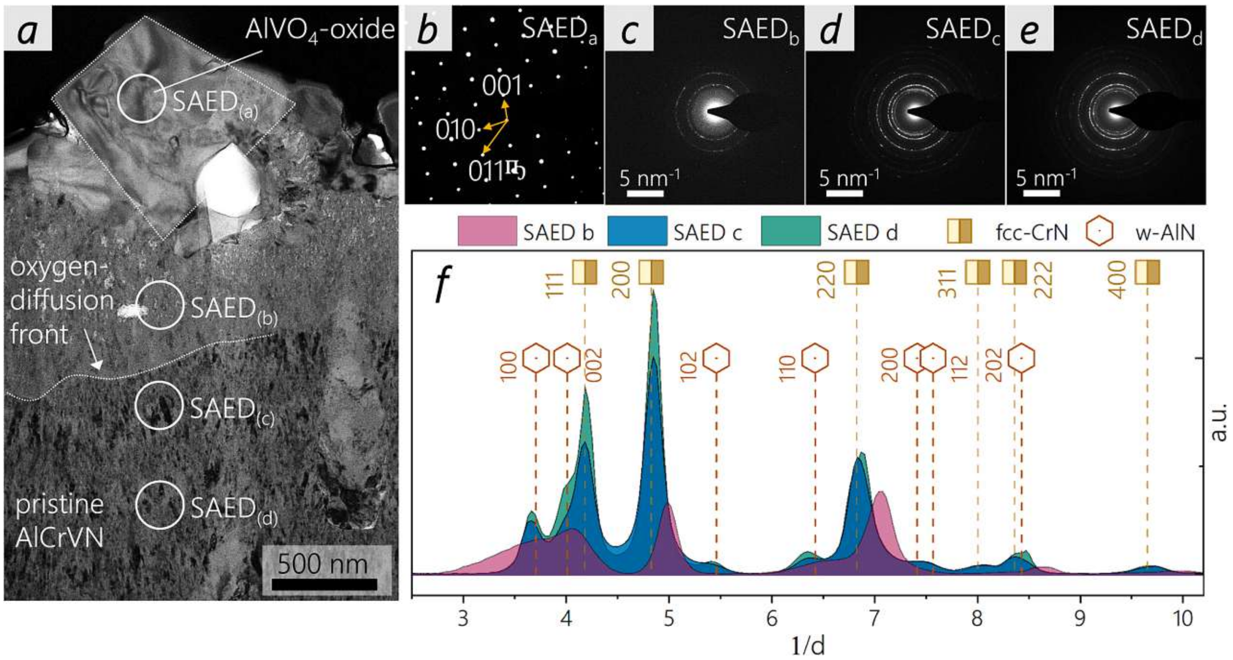

**Fig. 11.** : TEM investigations highlighting the oxidation behavior of $Al_{0.7}Cr_{0.08}V_{0.22}N$ coating isothermally annealed at 700 °C in air for 3 h. a) shows a bright-field image, highlighting the most prominent structural features, as well as the positions of $SAED_{(a\text{-}d)}$ measurements. (b-e) show the SAED-patterns that originate from the positions labeled in sub-figure (a). f) features the integrated ring-patterns from $SAED_{(b\text{-}d)}$.

recorded. This coincides with the understanding that there is a sharp interface between the oxidized coating and the remaining pristine coating matrix underneath. Also evident is a vanadium depletion layer, which results from an outward diffusion of vanadium in order to form a crystalline $AlVO_4$-top oxide. These migration dynamics become clearer when looking at the individual EDX maps in Fig. 12d. The respective nitrogen and oxygen maps substantiate the sharp interface between the oxidized coating and the remaining pristine coating morphology. Moreover, a distinct vanadium depletion layer is shown. Standing in good agreement with the findings from the line-scan, the presence of the depletion layer suggests an outward directed diffusion of vanadium for the formation of the $AlVO_4$-oxide. Chromium also indicates outward directed diffusion, however only to a marginal degree. As Cr does not participate in the formation of a top oxide, it instead concentrates at the grain-boundaries of the $AlVO_4$-crystals as shown in Fig. 12c, as well as EDX map of 12d. Lastly, aluminum shows little migration across the oxygen/nitrogen diffusion-front. This observation suggests that sufficient aluminum is originally present for the formation of the $AlVO_4$-top oxide, with no chemical gradient that will instigate further Al diffusion to the surface.

### *3.11. Overview of electrochemical parameters of various coating systems*

Lastly, we wish to place the corrosion resistance of the presented $Al_{0.7}Cr_{0.3-x}V_xN$ coatings into context with other material-systems deposited by this research group. Fig. 13 shows an overview of $I_{corr}$ vs. $E_{corr}$ values of various coating materials deposited on low alloy steel (90MnCrV8) that have been electrochemically tested in an identical manner, as described in the previous experimental section (deposition parameters and electrochemical data can be found in Appendix B). Quite evident is the significant spread of $i_{corr}$ and $E_{corr}$ values across the presented material classes. However, also within a family, such as the nitrides, significant variance in the electrochemical behavior is present, proving just how sensitive corrosion resistance of PVD coatings is to slight changes chemical composition and/or coating morphology. With this overview, we would like to emphasize the need for more detailed investigations devoted to specific material families, in order to systematically improve the corrosion resistance of PVD coatings in NaCl-rich media. Moreover, we would like to stress that both, alloying strategies and post deposition treatments such as annealing in air, pose viable approaches in significantly improving the corrosion resistance of cathodic arc evaporated $Al_{0.7}Cr_{0.3-x}V_xN$ coatings.

## 4. Conclusion

To improve the corrosion resistance of cathodic arc evaporated AlCrN-based coatings in NaCl-rich media, this study has provided two effective approaches: i) a doping-strategy with vanadium, and ii) an annealing strategy at 700 °C in air for 3 h.

In a deposition series of $Al_{0.7}Cr_{0.3-x}V_xN$ coatings, a direct correlation was found between the V-content, the coatings' crystallinity, and their corrosion current densities during electrochemical investigation. With increasing vanadium fractions, more refined coating morphologies were obtained, as well as lower current densities during the corrosion experiments. We propose that the reason for the progressive grain refinement is attributed to the nucleation of the favorable w-Al(Cr,V)N phase at higher vanadium contents, which inhibits the growth of the opposing fcc-Cr(Al,V)N crystallites. As a result, diffusion paths from the coating surface to the coating-substrate interface become increasingly branched, as more grain boundaries impede the migration of the electrolyte through the coating. In a series of 10 $Al_{0.7}Cr_{0.3-x}V_xN$ coatings with varying V-contents, ranging from 5.1 to 22.3 at% on the metal sublattice, each raise in the V-fraction lowered the corrosion currents noticeably, and resulted in a positive shift of the respective corrosion potential. Using the Stern-Geary equation together with the assumption that the coating material remains inert throughout the electrochemical experiment (only the steel substrate accounts for the anodic current), an approximation of the coatings' open porosity was made [3]. Appropriately, the approximation revealed a significant decline in the coatings' porosity values, which is a result of the observed grain-refinement due to

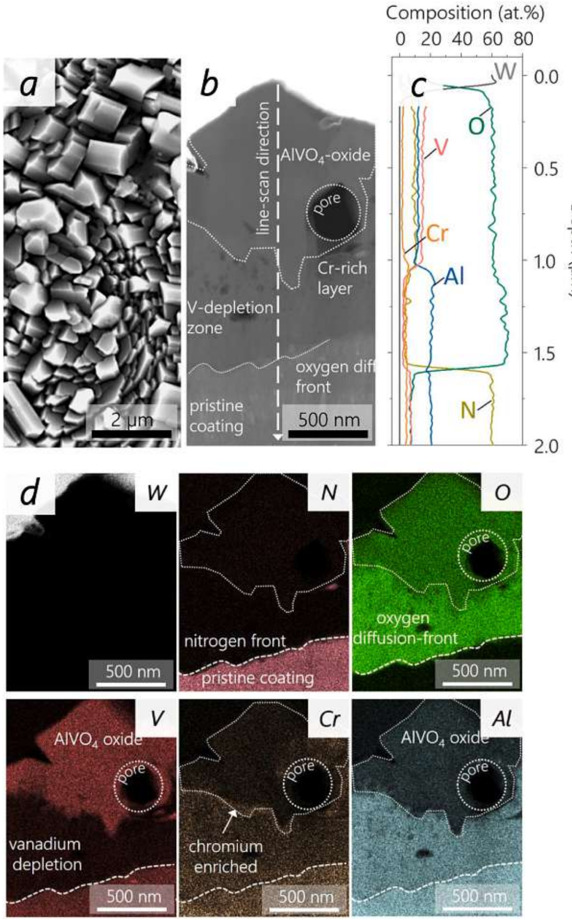

**Fig. 12.** **:** EDX investigations highlighting the diffusion behavior of the $Al_{0.7}Cr_{0.08}V_{0.22}N$ coating isothermally annealed at 700 °C in air for 3 h. a) shows a top-view SEM image of the crystalline top-oxide. b) features a STEM cross-section image of the top-most section of the annealed coating with the most prominent features labeled. c) displays an EDX-line scan that belongs to the segment shown sub-figure (b). d) displays EDX-maps, originating from the same segment as shown in sub-figures (b and c).

increasing V-fractions.

Moreover, a second series of $Al_{0.7}Cr_{0.3-x}V_xN$ coatings with V-contents ranging from 5.1 to 22.3 at% on the metal sublattice was annealed at 700 °C for 3 h in air and electrochemically tested in a 0.1 M NaCl-solution. For all annealed samples, significant shifting of the $E_{corr.}$ into more positive potentials was measured, accompanied by an anew decreasing in the corrosion currents ($i_{corr}$). Compared with the electrochemical values from the doping strategy, further improvement was obtained through the additional annealing step at 700 °C. We attribute this enhanced corrosion resistance to the formation of a ~1 µm thick $AlVO_4$-top oxide, followed by a ~0.5 µm thick oxygen-enriched (vanadium depleted) nanocrystalline layer underneath. We propose that this combination of top-oxide formation and formation of a near amorphous oxygen enriched layer below, drastically reduces the open-porosity rates of the coating structure as a whole and renders improved corrosion protection.

## CRediT authorship contribution statement

O. E. H. and H. R. conceived the research. O. E. H. conducted the coating depositions, as well as the electrochemical corrosion tests. P. K. prepared the TEM lamellas, whereas T. W. conducted the TEM measurements. E. N. and D. P. conducted the ToF-HIERDA measurements. O. H. and P. P. supported the research by providing indispensable funding, while L. S., J. R., and S. K. assisted the research with their thematic expertise. H. R. also provided funding acquisition and oversaw the research as supervisor. Finally, all authors have contributed in revising and approving the final version of the manuscript.

## Declaration of Competing Interest

The authors declare the following financial interests/personal relationships which may be considered as potential competing interests: Oliver E. Hudak reports financial support was provided by Christian Doppler Research Association.

## Data Availability

Data will be made available on request.

2

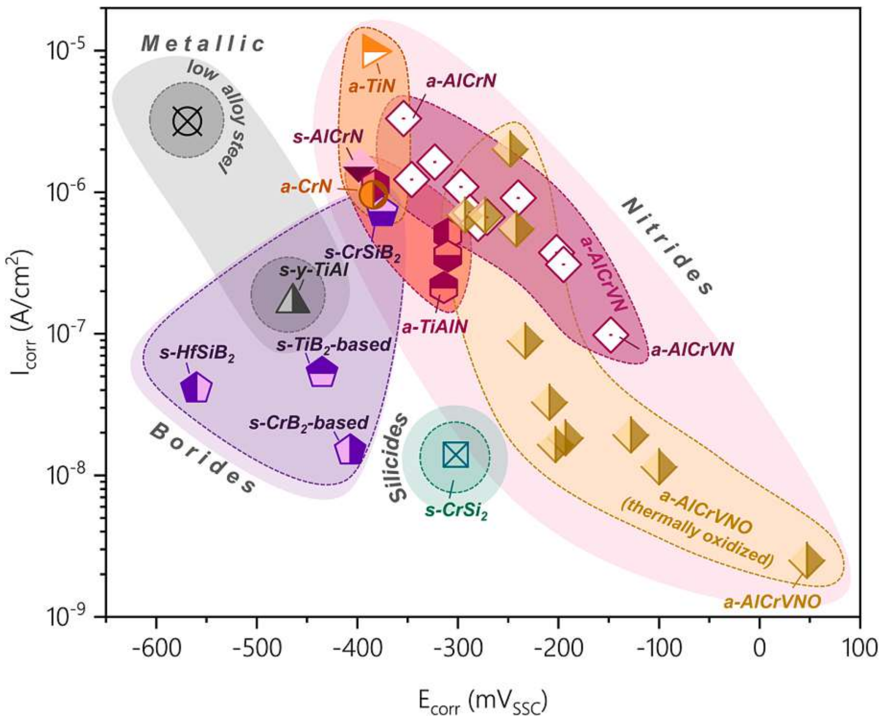

**Fig. 13.** : Summarized electrochemical data showing $I_{corr}$ vs. $E_{corr}$ values of various coating materials (s = sputtered, a= arc evaporated) measured in 0.1 M NaCl solution.

**Table A1**
Overview showing the chemical compositions of the as-deposited $Al_{0.7}Cr_{0.3-x}V_xN$ coatings. All listed values reflect EDX measurements that have been corrected according to ERDA measurements. Accordingly, ERDA values from samples P4 and P10, with compositions equivalent to $Al_{0.32}(Cr,V)_{0.19}N_{0.49}$, provided the correction standard.

| sample | V-content (at%) | Al-content (at%) | Cr-content (at%) | N-content (at%) | impurities (Oxygen) (at%) | Al- content on metal sublattice (at%) | Cr-content on metal sublattice (at%) | V- content on metal sublattice (at%) |
|---|---|---|---|---|---|---|---|---|
| P0 | 0.0 | 32.8 | 14.9 | 48.9 | 3.5 | 68.8 | 31.2 | 0.0 |
| P1 | 2.7 | 34.7 | 15.9 | 45.5 | 1.2 | 65.1 | 29.8 | 5.1 |
| P2 | 3.2 | 32.5 | 14.5 | 47.2 | 2.5 | 64.7 | 28.9 | 6.4 |
| P3 | 4.0 | 32.7 | 13.2 | 47.4 | 2.6 | 65.5 | 26.4 | 8.1 |
| P4 | 5.2 | 32.4 | 10.9 | 48.2 | 3.2 | 66.8 | 22.5 | 10.7 |
| P5 | 7.2 | 31.9 | 9.1 | 48.4 | 3.3 | 66.1 | 18.9 | 15.0 |
| P6 | 6.6 | 31.4 | 10.6 | 48.2 | 3.2 | 64.7 | 21.8 | 13.5 |
| P7 | 5.6 | 31.4 | 11.2 | 48.4 | 3.3 | 65.1 | 23.3 | 11.6 |
| P8 | 7.6 | 30.5 | 10.4 | 48.3 | 3.3 | 63.3 | 21.4 | 15.6 |
| P9 | 8.4 | 30.7 | 9.4 | 48.2 | 3.2 | 63.3 | 19.4 | 17.4 |
| P10 | 10.6 | 30.3 | 6.5 | 48.9 | 3.7 | 63.9 | 13.8 | 22.3 |

**Table A2**
Overview of deposition parameters, as well as electrochemical parameters ($I_{corr.}$ and $E_{corr.}$) measured in 0.1 M NaCl solution, pertaining to Fig. 13.

| sample | deposition technique | $T_{dep}$ ($C^\circ$) | $P_{dep.}$ (Pa) | atmosphere | bias (V) | $I_{dep.}$ (A) | ref. | $E_{corr.}$ (mV) | $I_{corr}$ ($A/cm^2$) |
|---|---|---|---|---|---|---|---|---|---|
| AlCrN | cae | 480 | 3.5 | $N_2$ | $\geq -100$ |  | [1] | -375 | $2.57 \times 10^{-6}$ |
| AlCrVN | cae | 480 | 3.5 | $N_2$ | $\geq -100$ |  | - | -148 | $1.03 \times 10^{-7}$ |
| AlCrVNO | cae | 480 | 3.5 | $N_2$ | $\geq -100$ |  | - | -47 | $1.59 \times 10^{-9}$ |
| CrN | cae | 500 | 3.5 | $N_2$ | -80 | 150 | [40] | -384 | $9.57 \times 10^{-7}$ |
| TiN | cae | 500 | 0.8 | $N_2$ | -80 | 160 | [40] | -385 | $9.89 \times 10^{-6}$ |
| TiAlN | cae | 500 | 3.0–3.2 | $N_2$ | -40 to − 80 | 200 | [40,41] | -314 | $2.12 \times 10^{-7}$ |
| AlCrN | sputtering | 500 | 1.3 | $Ar/N_2$ | -160 |  | [1] | -398 | $1.54 \times 10^{-6}$ |
| y-TiAl | sputtering | $\leq 300$ | 0.4 | Ar | -50 | - | [42] | -464 | $1.65 \times 10^{-7}$ |
| $HfSiB_2$ | sputtering | 550 | 0.56 | Ar | -40 | 0.4 | [43] | -560 | $4.11 \times 10^{-8}$ |
| $TiB_2$-based | sputtering | 500 | 0.4 | Ar | -50 | 0.4 | [44] | -435 | $5.29 \times 10^{-8}$ |
| $CrB_2$-based | sputtering | 550 | 0.7 | Ar | -40 | 0.4 | [45] | -407 | $1.50 \times 10^{-8}$ |
| $CrSiB_2$ | sputtering | 550 | 0.56 | Ar | -40 | 0.5 | [43] | -375 | $7.24 \times 10^{-7}$ |
| $CrSi_2$ | sputtering | 400 | 0.4 | Ar | -50 | 0.4 |  | -302 | $1.40 \times 10^{-8}$ |

## Acknowledgments

The financial support by the Austrian Federal Ministry for Digital and Economic Affairs, the National Foundation for Research, Technology and Development and the Christian Doppler Research Association is gratefully acknowledged (Christian Doppler Laboratory "Surface Engineering of high-performance Components"). We also thank for the financial support of Plansee SE, Plansee Composite Materials GmbH, and Oerlikon Balzers, Oerlikon Surface Solutions AG. In addition, we want to thank the X-ray center (XRC) of TU Wien for beam time as well as the electron microscopy center - USTEM TU Wien - for providing the SEM and TEM facilities. The authors acknowledge TU Wien library for financial support through its Open Access Funding Program.

## Appendix

See Table A1 and A2.

## References

[1] O.E. Hudak, A. Bahr, P. Kutrowatz, T. Wojcik, F. Bohrn, L. Solyom, R. Schuster, L. Shang, O. Hunold, P. Polcik, M. Heller, P. Felfer, G. Ball, H. Riedl, Pitting corrosion – Preferred chloride diffusion pathways in physical vapor deposited AlCrN coatings, Corros. Sci. 211 (2023), 110901, https://doi.org/10.1016/j.corsci.2022.110901.

[2] A.Y. Adesina, Z.M. Gasem, A. Madhan Kumar, Corrosion resistance behavior of single-layer cathodic Arc PVD nitride-base coatings in 1M HCl and 3.5 pct NaCl solutions, Metall. Mater. Trans. B Process Metall. Mater. ProcessSci 48 (2017) 1321–1332, https://doi.org/10.1007/s11663-016-0891-7.

[3] B. Avci, K. Kazmanli, B. Evren, M. Urgen, Contribution of galvanic coupling with TiN, TiAlN, and CrN to the corrosion of steel in neutral and acidic chloride solutions, Mater. Corros. (2023) 1–10. https://doi.org/10.1002/maco.202313848.

[4] C. Charrier, P. Jacquot, E. Denisse, J.P. Millet, H. Mazille, Aluminium and Ti/Al multilayer PVD coatings for enhanced corrosion resistance, Surf. Coat. Technol. 90 (1997) 29–34, https://doi.org/10.1016/S0257-8972(96)03080-0.

[5] J. Creus, H. Mazille, H. Idrissi, Porosity evaluation of protective coatings onto steel, through electrochemical techniques, Surf. Coat. Technol. 130 (2000) 224–232, https://doi.org/10.1016/S0257-8972(99)00659-3.

[6] J. Creus, H. Idrissi, H. Mazille, F. Sanchette, P. Jacquot, Improvement of the corrosion resistance of CrN coated steel by an interlayer, Surf. Coat. Technol. 107 (1998) 183–190, https://doi.org/10.1016/S0257-8972(98)00646-X.

[7] J. Vega, H. Scheerer, G. Andersohn, M. Oechsner, Experimental studies of the effect of Ti interlayers on the corrosion resistance of TiN PVD coatings by using electrochemical methods, Corros. Sci. 133 (2018) 240–250, https://doi.org/10.1016/j.corsci.2018.01.010.

[8] W. Brandl, C. Gendig, K. Reichel, Corrosion behaviour of hybrid coating systems, Mater. Corros. Werkst. Und Korros. 47 (1996) 208–214, https://doi.org/10.1002/maco.19960470405.

[9] M. Flores, L. Huerta, R. Escamilla, E. Andrade, S. Muhl, Effect of substrate bias voltage on corrosion of TiN/Ti multilayers deposited by magnetron sputtering, Appl. Surf. Sci. 253 (2007) 7192–7196, https://doi.org/10.1016/j.apsusc.2007.02.203.

[10] C. Liu, A. Leyland, Q. Bi, A. Matthews, Corrosion resistance of multi-layered plasma-assisted physical vapour deposition TiN and CrN coatings, Surf. Coat. Technol. 141 (2001) 164–173, https://doi.org/10.1016/S0257-8972(01)01267-1.

[11] S.H. Ahn, J.H. Lee, H.G. Kim, J.G. Kim, A study on the quantitative determination of through-coating porosity in PVD-grown coatings, Appl. Surf. Sci. 233 (2004) 105–114, https://doi.org/10.1016/j.apsusc.2004.03.213.

[12] F. Lang, Z. Yu, The corrosion resistance and wear resistance of thick TiN coatings deposited by arc ion plating, Surf. Coat. Technol. 145 (2001) 80–87, https://doi.org/10.1016/S0257-8972(01)01284-1.

[13] J. Barranco, F. Barreras, A. Lozano, M. Maza, Influence of CrN-coating thickness on the corrosion resistance behaviour of aluminium-based bipolar plates, J. Power Sources 196 (2011) 4283–4289, https://doi.org/10.1016/j.jpowsour.2010.11.069.

[14] H.A. Jehn, Improvement of the corrosion resistance of PVD hard coating-substrate systems, Surf. Coat. Technol. 125 (2000) 212–217, https://doi.org/10.1016/S0257-8972(99)00551-4.

[15] Y. Massiani, A. Medjahed, J.P. Crousier, P. Gravier, I. Rebatel, Corrosion of sputtered titanium nitride films deposited on iron and stainless steel, Surf. Coat. Technol. 45 (1991) 115–120, https://doi.org/10.1016/0257-8972(91)90213-G.

[16] F. Vacandio, Y. Massiani, M. Eyraud, S. Rossi, L. Fedrizzi, Influence of various nickel under-layers on the corrosion behaviour of AlN films deposited by reactive sputtering, Surf. Coat. Technol. 137 (2001) 284–292, https://doi.org/10.1016/S0257-8972(00)01110-5.

[17] M. Nordin, M. Herranen, S. Hogmark, Influence of lamellae thickness on the corrosion behaviour of multilayered PVD TiN/CrN coatings, Thin Solid Films 348 (1999) 202–209, https://doi.org/10.1016/S0040-6090(99)00192-3.

[18] C.S. Lin, C.S. Ke, H. Peng, Corrosion of CrN and CrN/TiN coated heat-resistant steels in molten A356 aluminum alloy, Surf. Coat. Technol. 146–147 (2001) 168–174, https://doi.org/10.1016/S0257-8972(01)01484-0.

[19] M. Herranen, U. Wiklund, J.O. Carlsson, S. Hogmark, Corrosion behaviour of Ti/TiN multilayer coated tool steel, Surf. Coat. Technol. 99 (1998) 191–196, https://doi.org/10.1016/S0257-8972(97)00525-2.

[20] P.E. Hovsepian, D.B. Lewis, W.D. Münz, S.B. Lyon, M. Tomlinson, Combined cathodic arc/unbalanced magnetron grown CrN/NbN superlattice coatings for corrosion resistant applications, Surf. Coat. Technol. 120–121 (1999) 535–541, https://doi.org/10.1016/S0257-8972(99)00439-9.

[21] L. Shan, Y.R. Zhang, Y.X. Wang, J.L. Li, X. Jiang, J.M. Chen, Corrosion and wear behaviors of PVD CrN and CrSiN coatings in seawater, Trans. Nonferrous Met. Soc. China (Engl. Ed. 26 (2016) 175–184, https://doi.org/10.1016/S1003-6326(16)64104-3.

[22] P. Ström, D. Primetzhofer, Ion beam tools for nondestructive in-situ and in-operando composition analysis and modification of materials at the Tandem Laboratory in Uppsala, J. Instrum. 17 (2022), https://doi.org/10.1088/1748-0221/17/04/P04011.

[23] M. Janson, CONTES Conversion of Time-Energy- Spectra-A Program for ERDA Data Analysis Users Manual, 2004.

[24] P. Ström, P. Petersson, M. Rubel, G. Possnert, A combined segmented anode gas ionization chamber and time-of-flight detector for heavy ion elastic recoil detection analysis, Rev. Sci. Instrum. 87 (2016), https://doi.org/10.1063/1.4963709.

[25] International Center of Diffraction Data, Powder diffraction file 00–046-1200, 1996.

[26] International Center of Diffraction Data, Powder diffraction file 04–014-0360, 2010.

[27] International Center of Diffraction Data, Powder diffraction file 01–083-5613, 2016.

[28] Y.P. Feng, L. Zhang, R.X. Ke, Q.L. Wan, Z. Wang, Z.H. Lu, Thermal stability and oxidation behavior of AlTiN, AlCrN and AlCrSiWN coatings, Int. J. Refract. Met. Hard Mater. 43 (2014) 241–249, https://doi.org/10.1016/j.ijrmhm.2013.11.018.

[29] C. Tritremmel, R. Daniel, C. Mitterer, P.H. Mayrhofer, M. Lechthaler, C. Tritremmel, R. Daniel, C. Mitterer, Oxidation behavior of arc evaporated Al-Cr-Si-N thin films, Oxid. Behav. arc evaporated Al-Cr-Si-N. Thin films 061501 (2015), https://doi.org/10.1116/1.4748802.

[30] International Center of Diffraction Data, Powder diffraction file 00–039-0276, 1989.

[31] International Center of Diffraction Data, Powder diffraction file 01–072-0433, 2020.

[32] International Center of Diffraction Data, Powder Diffraction file 00–015-0629, 1965.

[33] International Center of Diffraction Data, Powder Diffraction file 04–001-9278, 2011.

[34] International Center of Diffraction Data, Powder Diffraction file 04–015-8610, 2012.

[35] International Center of Diffraction Data, Powder Diffraction File 04–025-1918, 2021.

[36] International Center of Diffraction Data, Powder Diffraction File 01–076-0146, 2020.

[37] W. Tillmann, D. Kokalj, D. Stangier, M. Paulus, C. Sternemann, M. Tolan, Investigation on the oxidation behavior of AlCrVxN thin films by means of synchrotron radiation and influence on the high temperature friction, Appl. Surf. Sci. 427 (2018) 511–521, https://doi.org/10.1016/j.apsusc.2017.09.029.

[38] R. Franz, J. Neidhardt, C. Mitterer, B. Schaffer, H. Hutter, R. Kaindl, B. Sartory, R. Tessadri, M. Lechthaler, P. Polcik, Oxidation and diffusion processes during annealing of AlCrVN hard coatings, J. Vac. Sci. Technol. A Vac. Surf. Film. 26 (2008) 302–308, https://doi.org/10.1116/1.2841508.

[39] R. Franz, J. Schnöller, H. Hutter, C. Mitterer, Oxidation and diffusion study on AlCrVN hard coatings using oxygen isotopes 16O and 18O, Thin Solid Films 519 (2011) 3974–3981, https://doi.org/10.1016/j.tsf.2011.01.100.

[40] C. Sabitzer, C. Steinkellner, C.M. Koller, P. Polcik, R. Rachbauer, P.H. Mayrhofer, Diffusion behavior of C, Cr, and Fe in arc evaporated TiN- and CrN-based coatings and their influence on thermal stability and hardness, Surf. Coat. Technol. 275 (2015) 185–192, https://doi.org/10.1016/j.surfcoat.2015.05.020.

[41] S.A. Glatz, C.M. Koller, H. Bolvardi, S. Kolozsvári, H. Riedl, P.H. Mayrhofer, Influence of Mo on the structure and the tribomechanical properties of arc evaporated Ti-Al-N, Surf. Coat. Technol. 311 (2017) 330–336, https://doi.org/10.1016/j.surfcoat.2017.01.001.

[42] S. Kagerer, O.E. Hudak, M. Schloffer, H. Riedl, P.H. Mayrhofer, TGO formation and oxygen diffusion in Al-rich gamma-TiAl PVD-coatings on TNM alloys, Scr. Mater. 210 (2022), 114455, https://doi.org/10.1016/j.scriptamat.2021.114455.

[43] T. Glechner, H.G. Oemer, T. Wojcik, M. Weiss, A. Limbeck, J. Ramm, P. Polcik, H. Riedl, Influence of Si on the oxidation behavior of TM-Si-B2±z coatings (TM = Ti, Cr, Hf, Ta, W), Surf. Coat. Technol. 434 (2022), 128178, https://doi.org/10.1016/j.surfcoat.2022.128178.

[44] C. Fuger, R. Hahn, A. Hirle, P. Kutrowatz, M. Weiss, A. Limbeck, O. Hunold, P. Polcik, H. Riedl, Revisiting the origins of super-hardness in TiB2+z thin films – Impact of growth conditions and anisotropy, Surf. Coat. Technol. 446 (2022), https://doi.org/10.1016/j.surfcoat.2022.128806.

[45] L. Zauner, A. Steiner, T. Glechner, A. Bahr, B. Ott, R. Hahn, T. Wojcik, O. Hunold, J. Ramm, S. Kolozsvári, P. Polcik, P. Felfer, H. Riedl, Role of Si segregation in the structural, mechanical, and compositional evolution of high-temperature oxidation resistant Cr-Si-B2±z thin films, J. Alloy. Compd. 944 (2023), 169203, https://doi.org/10.1016/j.jallcom.2023.169203.

# Publication III

***Low-temperature hot corrosion of arc evaporated $Ti_{1\text{-}x}Al_xN$ on Ni-Cr-Co based superalloys***

**O.E. Hudak**, A. Scheiber, P. Kutrowatz, T. Wojcik, L. Shang, O. Hunold, S. Kolozsvári, P. Polcik, and H. Riedl.

*Corrosion Science* 224 (2023), 111565.

Corrosion Science 224 (2023) 111565

Contents lists available at ScienceDirect

Corrosion Science

journal homepage: www.elsevier.com/locate/corsci

# Low-temperature hot corrosion of arc evaporated $Ti_{1-x}Al_xN$ on Ni-Cr-Co based superalloys

O.E. Hudak [a,*], A. Scheiber [a], P. Kutrowatz [a], T. Wojcik [a], L. Shang [b], O. Hunold [b], S. Kolozsvári [c], P. Polcik [c], H. Riedl [a,d]

[a] Christian Doppler Laboratory for Surface Engineering of high-performance Components, TU Wien, Austria
[b] Oerlikon Balzers, Oerlikon Surface Solutions AG, 9496 Balzers, Liechtenstein
[c] Plansee Composite Materials GmbH, D-86983 Lechbruck am See, Germany
[d] Institute of Materials Science and Technology, TU Wien, A-1060 Wien, Austria

ARTICLE INFO

*Keywords:*
Low temperature hot corrosion
PVD coatings
Arc-evaporation
Superalloy

ABSTRACT

Cathodic arc evaporated $Ti_{1-x}Al_xN$ coatings were deposited on a Nimonic c-263 superalloy and tested under low temperature hot corrosion conditions. Treated with a $MgSO_4/Na_2SO_4$ salt-mixture, all samples were annealed at 700 °C in a 2800 $ppm_{(volume)}$ $SO_x$-rich atmosphere for 1, 5, 15 and 30 h. A significantly reduced corrosion severity was exhibited by all $Ti_{1-x}Al_xN$ variants over the uncoated NiCrCo alloy. A synergistic fluxing mechanism was found to be the dominant factor for the coating breakdown. Depending on the relative Al-to-Ti content on the $Ti_{1-x}Al_xN$ sublattice, differences in the coatings' corrosion and scaling behavior were observed.

## 1. Introduction

Superalloys are well known for their excellent mechanical strength, creep-profiles and fatigue properties at high-temperatures, as well as good corrosion and oxidation resistance in highly demanding environments [1–4]. Finding wide application in industrial gas turbines (IGT) and jet engines, superalloys represent an indispensable material class in energy generation sectors and modern aviation [1,5–8]. However, superalloys are also known for their susceptibility to molten salt-induced corrosion – better known as hot corrosion (HC) [5,9–12].

For this reason, protective coatings provide a lucrative solution in combatting HC-attack of turbine elements [13]. Many coating systems have shown improved oxidation and corrosion resistance in high temperature settings, such as metallic NiCrAlY coatings [14–16], metallic gradient coatings [17], ceramic oxide coatings [18], nitride coatings [19–22], silicides [23–25], and enamel [26,27], but remain far from being optimal. The variety of these studies not only demonstrates the complexity of hot corrosion phenomena, but also confirms that there is a need for a more refined understanding of the corrosion mechanisms in thin films.

With focus on industrially established Ni-Cr-Co- base superalloys, the objective of this study is to provide a detailed analysis of the hot corrosion behavior of protective physical vapor deposited $Ti_{1-x}Al_xN$ coatings. Cathodic arc evaporated (CAE) $Ti_{1-x}Al_xN$ depicts one of the most established coating system in diverse industrial sectors, based on its unique combination of thermo-mechanical properties. However, the use in HC environments is relatively unexplored and detailed understanding of ongoing mechanisms are rare.

### 1.1. Hot corrosion in gas turbines

When salt-rich aerosols from marine environments enter the combustion chamber through the air intake (e.g. NaCl, $MgCl_2$, etc.), they react with oxygen and sulfur baring combustion gases and form high-melting sulfate salts (e.g. $Na_2SO_4$ and $MgSO_4$) [28–31] (Eqs. 1–4). When exiting the combustion chamber, these highly stable salts can build up on hot sections of the gas-turbines, where they adhere and cause severe degradation of the material surfaces. Especially components, which come in direct contact with the combustion gases, such as transition lines from the combustion chamber, as well as blades and vanes of the high-pressure turbine (HPT) and low-pressure turbine (LPT) are vulnerable to hot gas corrosion.

$$S+O_2\rightarrow SO_2 \tag{1}$$

$$SO_2+1/2O_2+\frac{(M)}{catalyst}\leftrightarrow SO_3 \tag{2}$$

---

[*] Corresponding author.
*E-mail address:* oliver.hudak@tuwien.ac.at (O.E. Hudak).

https://doi.org/10.1016/j.corsci.2023.111565
Received 10 July 2023; Received in revised form 19 September 2023; Accepted 28 September 2023

$$2NaCl + S + 2O_2 \rightarrow \alpha - Na_2SO_4 + Cl_2 \quad T_{m(Na_2SO_4)} = 884^\circ C \tag{3}$$

$$MgCl_2 + S + 2O_2 \rightarrow MgSO_4 + Cl_2 \quad T_{m(MgSO_4)} = 1124^\circ C \tag{4}$$

Depending on the physical aggregate of these salt-deposits, one of two corrosion mechanisms can ensue: Low temperature hot-corrosion (LTHC, 575–800 °C), where the salt adheres in a solid form, or high temperature hot corrosion (HTHC, 800–950 °C), where the deposit exits in a molten state.

The corrosion of alloys and coatings by hot gas corrosion then proceeds in several key steps: An incubation stage, an initiation stage, a propagation stage, followed by failure [32,33] The incubation stage features the formation of stable oxide scales (e.g. $TiO_2$, $Al_2O_3$, NiO, and $Cr_2O_3$), whereby a steady state (passivity) against further oxidation is provided. The incubation state is especially interesting when considering coated superalloys, as the oxides that form on the coating surface typically differ from those of the bulk material.

The subsequent initiation stage comprises a sequence of changes in the materials environment that establishes the conditions where accelerated corrosion/degradation occurs. During this stage several processes take place, such as the deposition of a salt-film, the melting of the salt deposit (HTHC), and/or the formation of low-melting eutectics between the salt-deposit and metal oxide surface (LTHC). Furthermore, changes in the melt-basicity, and local depassivation of the oxide scale allows for accelerated attack of the underlying alloy/metal.

The initiation is then followed by the propagation, where an accelerated progression of both, depassivation of the protective metal oxide scale, and internal sulfidation and oxidation of the now unprotected bulk material occurs.

Lastly, after a given duration, the corrosion front has infiltrated the material to such extend, that the integrity of the component fails.

### *1.2. Depassivation via fluxing mechanisms*

When protective oxides such as $Al_2O_3$, $TiO_2$, NiO or $Cr_2O_3$ come in contact with fused $Na_2SO_4$, their dissolution can occur in one of two ways: Basic dissolution (basic fluxing), where the oxide reacts with the basic component ($Na_2O$) of the melt, or acidic dissolution (acidic fluxing), where the oxide reacts with the acidic component of the melt ($SO_3$) (Eq. 5).

$$Na_2SO_{4(l)} \leftrightarrow Na_2O_{(diss.(basic))} + SO_{3(g,(acidic))} \tag{5}$$

In a series of electrochemical studies, Zheng [34], Rapp and Luthra [35] investigated the solubility of various oxides in fused $Na_2SO_4$ at 1200 K. By varying the basicity of the melt, the solubility of most oxides (with the exception of $SiO_2$) features distinct solubility minima. Fig. 1a shows a compilation of such measured solubilities, by plotting the concentration of the dissolved oxide over the basicity of the melt.

Which reaction dominates (acidic dissolution or basic dissolution) depends on the chemical stability of the oxide (position of the solubility minimum). While $Al_2O_3$ and $Cr_2O_3$ are considered acidic oxides (stable in acidic conditions), $Co_2O_3$ and NiO are viewed as basic oxides (stable in more basic conditions). Therefore, $Co_2O_3$ and NiO are predominantly dissolved via an acidic fluxing mechanism (reacts with $SO_3$), while $Al_2O_3$ and $Cr_2O_3$ are readily dissolved in more neutral and basic melts (basic fluxing by reacting with $Na_2O$).

However, when different oxides are situated in close proximity to one another and stand in contact with a fused salt deposit, a superimposed mechanism can take place, referred to as synergistic fluxing. This is particularly dangerous for alloys and coatings which rely on a mixed and/or layered oxide scale, in order to combat hot corrosion. If the salt basicity of the melt falls between the solubility minima of such two oxides, the solubility of the one oxide can facilitate melt conditions that accelerates the dissolution of the other (Fig. 1b).

As the oxidation of $Ti_{1-x}Al_xN$ coatings is dominated by the formation of $Al_2O_3$ and $TiO_2$, a central point of discussion throughout this study are synergistic effects in the fluxing mechanism. Thus, the authors intend to provide a fundamental understanding of the respective LTHC mechanisms for arc-evaporated $Ti_{1-x}Al_xN$ coatings, by showcasing how different Al to Ti contents influence the corrosion behavior.

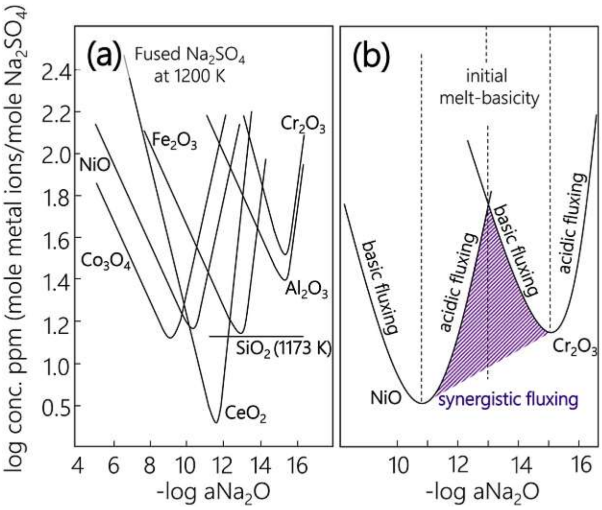

**Fig. 1.** (a) Solubility diagram of common oxides in fused $Na_2SO_4$ as a function of melt-basicity (reworked from [36]), (b) region of synergistic fluxing between NiO and $Cr_2O_3$ (shaded area).

## 2. Experimental

### *2.1. Coating depositions*

All $Ti_{1-x}Al_xN$ coatings were deposited using an industrial scale cathodic arc-evaporation system (Innova 1.0, Oerlikon Surface Solutions AG). 10 µm thick $Ti_{1-x}Al_xN$ coatings with varied Al contents ($Ti_{0.52}Al_{0.48}N$ and $Ti_{0.34}Al_{0.66}N$) were deposited using TiAl (50/50 at%) and TiAl(34/66 at%) targets, respectively (Plansee Composite Materials GmbH). The coatings were grown in a pure $N_2$ atmosphere at a pressure of 3.5 Pa and a deposition temperature of 450 °C. Furthermore, a target current of 200 A and a bias potential up to − 40 V were chosen for all depositions.

Single-crystalline Si stripes (100-oriented, 20×7x 0.38 mm) and Nimonic c-263 (VDM-Metals, Germany) were used as substrate materials. Whereas coated Si-substrates were solely used for coating-characterization purposes (e.g. analysis of the coatings morphology via fracture cross-section, and coating thickness measurements), the coated Nimonic c-263 alloys (detailed chemical composition, see Table 1) were exclusively used for hot corrosion experiments and post-corrosion analysis.

Prior to the depositions, all substrates were ultrasonically cleaned with acetone and ethanol before mounting them onto the carousel of the deposition chamber. With a base pressure of $< 5.0^{-4}$ Pa, the substrates were further cleaned for 25 min by a central-beam argon plasma etching procedure (Oerlikon Surface Solutions AG).

### *2.2. Corrosion experiments*

The hot gas corrosion testing-rig was conceptualized in three sections: (i) the gas-mixing system (inlet), (ii) a reaction module, and (iii) a gas-treatment system (outlet). For the composition of the experiment's atmosphere, a combination of three gas-inlet feeds were controlled via mass-flow controllers. A total gas-flow (total pressure, p) of 2500 sccm was chosen, comprised of 2118 sccm [Ar], 375 sccm [O], and 7 sccm [$SO_2$]. This translates to partial pressures of $p_{[Ar]} = 8.47 \times 10^{-1}$ atm,

**Table 1**
Nominal chemical composition (wt%) of the Nimonic c-263 superalloy.

| | *Ni* | *Co* | *Cr* | *Mo* | *Ti* | *Al* | *Fe* | *Si* |
|---|---|---|---|---|---|---|---|---|
| *Nimonic c-263* [4] | 47–54 | 19–21 | 19–21 | 5.6–6.1 | 1.9–2.4 | 0.3–0.6 | 0–0.7 | 0–0.4 |

$p_{[O]} = 1.5 \times 10^{-1}$ atm and $p_{[SO2]} = 2.8 \times 10^{-3}$ atm, respectively. The mixed gases then enter the reaction chamber, positioned inside a three-zone gradient oven (Carbolite Gero GmbH & Co. KG). A quartz-tube flow-reactor safely accommodates the aggressive $SO_x$-rich atmosphere in liaison with the high temperatures (700 °C) needed for the HC experiments. Lastly, the exhaust gases are washed in a NaOH bath before exiting the set-up. A detailed illustration of the HC-testing rig is provided in Appendix Figure A1.

For every corrosion experiment, two sets of sample-arrangements were considered: (i) a control-arrangement, were no salt was added to the sample surfaces, and (ii) an experimental-arrangement, where samples were prepped with salt-coupons to mimic hot-corrosion conditions.

A mixture of anhydrous $MgSO_4$ and $Na_2SO_4$ (Merck KGaA) with a molar ratio of 20:80, or mass ratio of 15.21:84.78, respectively, was chosen for all experiments. A saturated aqueous solution was then prepared. Using a pipette, small droplets were applied onto the sample surfaces and dried under ambient conditions for several days.

With reference to the calculated binary-phase diagram from Yazhenskikh et. al., a solidus temperature of ~725 °C and a liquidus temperature of ~810 °C were estimated for the salt-coupons, which was later confirmed in a series of annealing experiments [31]. In order to remain below the liquidus temperature of the salt-mixture (prerequisite for LTHC is a solid aggregate state), a temperature of 700 °C was chosen for all corrosion experiments.

After loading the quartz tube with the control-arrangement and the salt-loaded samples, the chamber was sealed and purged for 10 min with 2000 sccm Ar. Subsequently, the furnace was turned on whilst continuing purging with Ar. With a ramp-rate of 20 °C/min, 45 min were allocated for reaching the desired 700 °C, after which an additional 15 min were allotted for ensuring a homogeneous temperature distribution within the quartz-tube. Following the heat-up sequence, the Ar, $O_2$, and $SO_2$ mass-flow controllers were set to 2118 sccm, 375 sccm and 7 sccm (2800 ppm $SO_2$ by volume), respectively, and their hand valves opened, marking the beginning ($t_{0\,h}$) of the corrosion experiment. After the desired duration of the experiment has elapsed (e.g. t = 1, 5, 15, and 30 h), the furnace was turned off, the hand-valves for the $O_2$ and $SO_2$ feeds closed, and the chamber purged with 2000 sccm Ar until the temperature within the quartz-tube was < 200 °C.

### 2.3. Analytical methods

For studying the morphological properties, such as coating thickness and the integrity of the substrate-coating interfaces, a Zeiss Sigma 500 VP high-resolution field emission gun scanning electron microscope (FEGSEM) was used. With an acceleration voltage, ranging between 3 kV and 6 kV, characterization of coating thickness and morphology were performed on fracture cross sections of coated Si-substrates. Furthermore, the FEGSEM, combined with an EDAX Octane elect system for energy dispersive X-ray spectroscopy (EDX), was used for quantitative chemical investigations.

For crystallographic analysis, Bragg-Brentano X-ray diffraction (BBHD) was utilized, using a PANalytical XPert Pro MPD system equipped with a Cu-Kα radiation source (wave length $\lambda = 1.54$ Å).

For post corrosion characterization, top-view images were taken, using a digital light microscope. For salt loaded samples, the deposit was carefully removed and any remnant salt washed off with distilled water, in order to expose the oxidized coating surfaces. Subsequently, anew XRD measurements were conducted, after which the samples were embedded in a conductive polymer-matrix, their cross-sections thoroughly grinded, polished, and analyzed using a Zeiss Sigma 500 VP high-resolution FEGSEM. EDX line-scans, as well as EDX-mapping, were utilized for identifying diffusion pathways, phase-transformations, and coating breakdown.

Lastly, transmission electron microscopy (TEM), FEI TECNAI F20, equipped with a field emission gun and operated at an accelerating voltage of 200 kV) was conducted. Bright-field (BF) imaging was utilized to learn more about the microstructure, diffusion processes and the overall corrosion mechanism. For the preparation for the TEM lamella a standardized focused-ion beam (FIB) lift-out technique was used (Scios 2 DualBeam system, ThermoFisher Scientific).

## 3. Results

### 3.1. Structure and morphology

The as-deposited fracture cross-sections of both, low-Al content $Ti_{0.52}Al_{0.48}N$ and high Al-content $Ti_{0.34}Al_{0.66}N$ coatings are shown in Figs. 2a and 2b, respectively. With a thickness of 9.8 μm ($Ti_{0.52}Al_{0.48}N$) and 10.1 μm ($Ti_{0.34}Al_{0.66}N$) both coating variants feature a homogeneous and dense columnar microstructure. The chemical compositions normalized to the metallic sublattice, $Ti_{0.52}Al_{0.48}N$ and $Ti_{0.34}Al_{0.66}N$, were determined by EDX and deviate only slightly from their target compositions (50/50 and 35/65 at%, respectively). Structural analysis by XRD indicate a dominant cubic-Ti(Al)N crystal structure for both coating variants, with only slight indications of the thermodynamically

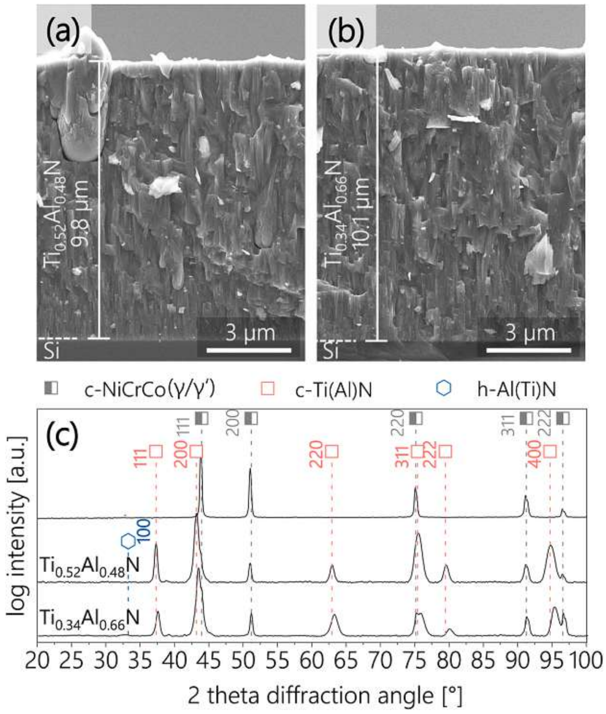

**Fig. 2.** Characterization of as-deposited $Ti_{1-x}Al_xN$ coatings: (a-b) show the fracture cross-sections of the $Ti_{0.52}Al_{0.48}N$ and $Ti_{0.34}Al_{0.66}N$ on Si, respectively, whereas (c) features XRD spectra of the $Ti_{1-x}Al_xN$ coatings and NiCrCo substrate material. Reference patterns were taken from ref. [37–39].

favored wurzite-Al(Ti)N phase visible for the high Al-content $Ti_{0.34}Al_{0.66}N$ coating see Fig. 2c.

### 3.2. *Low temperature hot corrosion experiments*

Fig. 3 features top-view images of all samples that have been subject to the hot-corrosion experiments. At 700 °C and a partial pressure of $p_{[SO2]} = 2.8 \times 10^{-3}$ atm (2800 ppm by volume), all samples were exposed to the same corrosive atmosphere and annealed for 1, 5, 15 and 30 h. Shown on the left is the so-called control group (samples without salt deposit), consisting of the uncoated NiCrCo-alloy, the $Ti_{0.52}Al_{0.48}N$ and $Ti_{0.34}Al_{0.66}N$ coated samples, listed from top to bottom. For each sample, gradual changes in the interference colors are observed that relate to evolving oxide scales. Particularly for the initially polished NiCrCo substrate, the evolution of the typical brownish NiO-scaling after 30 h is quite apparent.

On the right-hand side, the surfaces of the salt-loaded samples are shown before (0 h) and after the corrosion experiments (1–30 h). Significant corrosion can be observed for the uncoated NiCrCo-alloy. After 1 h, dark brown corrosion products appear at the border of the salt-deposit. As the duration of the corrosion experiment is prolonged, the corrosion front expands radially, whilst consuming the salt deposit (5 h). After 15 h, the entire alloy surface is covered with porous corrosion products, while the consumption of the salt deposit continues. After 30 h, all the salt has been taken up, leaving a completely deteriorated alloy-surface behind.

Contrarily, the corrosion progression and uptake of the salt-deposit for the $Ti_{1-x}Al_xN$ coated samples occurs much more delayed. After 1 h, no visible corrosion products form at the salt-deposit borders. After 5 h, an onset of surface degradation can be seen, which remains unchanged throughout 15 h. Only at 30 h, significant deterioration of the coating structure, as well as salt uptake is featured. We believe that the substantial consumption of the salt observed for the $Ti_{0.52}Al_{0.48}N$ is a sign for a breakthrough of the coating structure, where the salt has breached the protective coating and is able to react with the NiCrCo-substrate underneath.

### 3.3. *Oxidation behavior without salt deposits*

The oxidation behavior and scale formation of $Ti_{1-x}Al_xN$ coatings is well documented in literature, reporting the formation of a thin but continuous oxide scale in air at temperatures as low as 700–750 C [40, 41] However, depending on the coating's Al content and annealing temperature, distinct differences in the scale growth were observed. While coatings with lower Al-contents, such as $Ti_{0.75}Al_{0.25}N$ and $Ti_{0.56}Al_{0.44}N$ preferentially develop a double-layered oxide (so called type 1 oxidation, featuring an Al-rich upper layer and a Ti-rich sublayer), higher Al-content coatings like $Ti_{0.34}Al_{0.66}N$ tend to generate a mixed oxide scale (type 2 oxidation), with no separation between the Ti- and Al-diffusion profiles [41,42]. Coatings with Al concentrations falling between type 1 and type 2 follow a T-type oxidation behavior. Similar to type 1, the T-type oxidation exhibits a layered oxide, however, with less separation between the individual Al- and Ti-diffusion gradients.

By annealing $Ti_{0.52}Al_{0.48}N$ and $Ti_{0.34}Al_{0.66}N$ coatings in a 2800 ppm $SO_x$-rich atmosphere at 700 °C (control group), this behavior was only partially observed. While both coatings do feature the formation of $Al_2O_3$ and $TiO_2$ oxide scales, their scale structure appears quite similar and seem to follow a T-type oxidation (layered structure with an Al-rich upper layer, and a Ti-rich sublayer).

Figs. 4a and 4b, show EDX line scans obtained from the annealed $Ti_{0.52}Al_{0.48}N$ and $Ti_{0.34}Al_{0.66}N$ coatings, respectively, and intend to highlight the relative distribution of Al and Ti after 1, 5, 15, and 30 h at the coating surfaces. Apparent are layered diffusion profiles, where an Al-rich band forms on top and a Ti-rich zone underneath. As neither of the coatings demonstrates complete Al diffusion to the surface (substantial Al-content >10 at% remains within the Ti-rich sublayer), both coating fall within the type T oxidation regime. This only partially agrees with the model from Greczynski et al., which predicts a type 2 oxidation behavior for the higher Al-content $Ti_{0.34}Al_{0.66}N$ samples at 700 °C. At this point, the authors would like to point out that EDX may

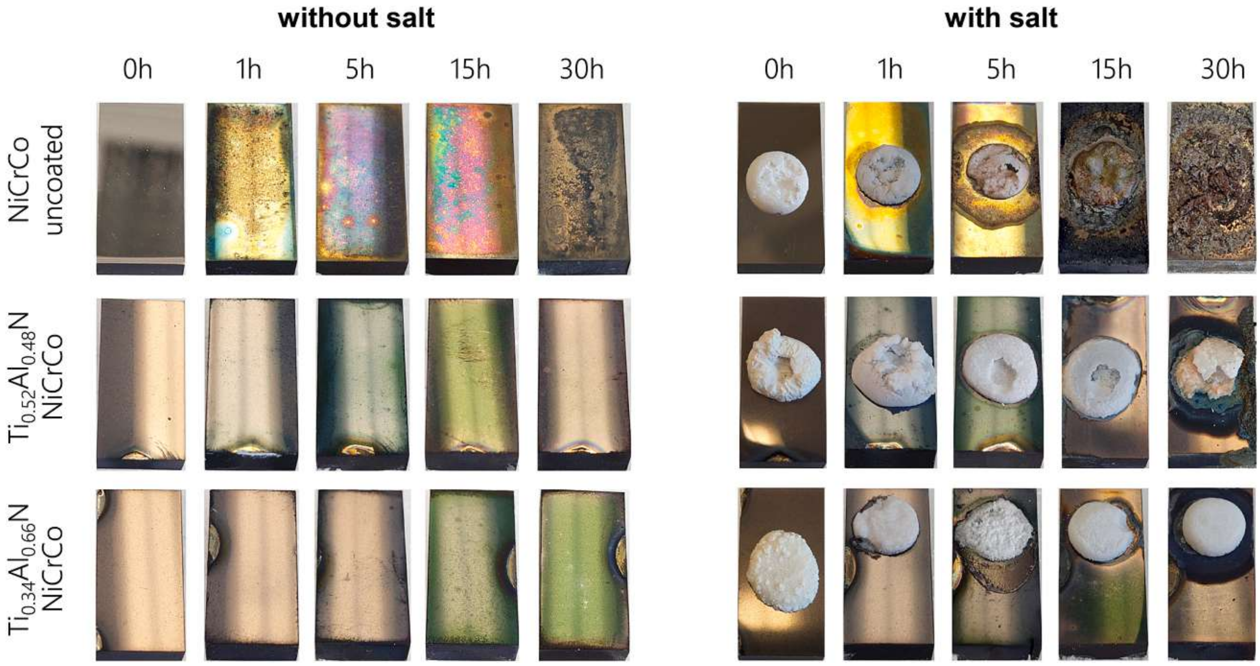

**Fig. 3.** Top-view images showing annealed samples at 700 °C in $SO_x$-rich atmosphere without salt-deposits for 0, 1 h, 5 h, 15 h and 30 h (left group), as well as annealed samples with salt-deposits under identical conditions (right group). The first row features uncoated Nimonic c-263 substrates, while the second and third row show $Ti_{0.52}Al_{0.48}N$ and $Ti_{0.34}Al_{0.66}N$ coated c-263 substrates, respectively.

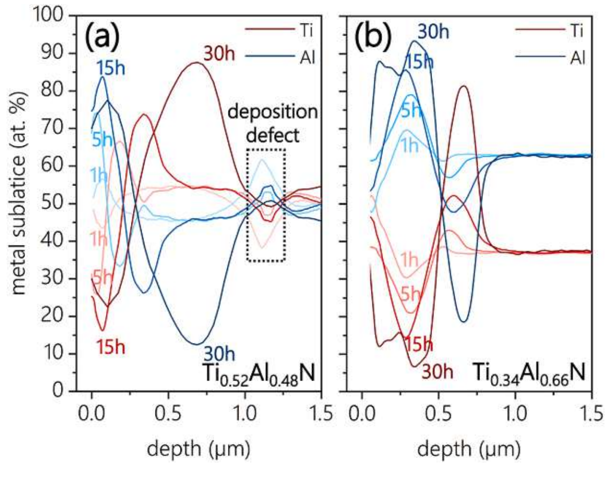

**Fig. 4.** EDX line scans for the annealed (a) $Ti_{0.52}Al_{0.48}N$ and (b) $Ti_{0.34}Al_{0.66}N$, highlighting the Al- and Ti-diffusion profiles of the metal sublattice after 1, 5, 15, and 30 h.

not be the most accurate analytical choice for making this observation and urge to treat this discrepancy with caution, particularly as the Al-chemistry $Ti_{0.34}Al_{0.66}N$ sits right at the border of the type-T and type-2 regimes.

As for the relative thicknesses of the Al- and Ti-rich layers, the $Ti_{0.52}Al_{0.48}N$ coatings feature a thinner Al-rich scale on top of a thicker Ti-dominated layer, whereas the $Ti_{0.34}Al_{0.66}N$ coatings develop a thicker Al-rich scale on top of a thinner Ti-band. This again stands in good agreement with observations made by Greczynski et al. [42], and Panjan et. al. [41], who reported that coatings with increasing AlN concentrations produce thinner overall oxides, but with a thicker Al-rich top layer.

Figs. 5a and 5b presents the structural evolution of $Ti_{0.52}Al_{0.48}N$ and $Ti_{0.34}Al_{0.66}N$ coatings without salt deposits annealed at 700 °C (1, 5, 15, and 30 h) in a 2800 ppm $SO_x$-rich atmosphere. Interestingly, indications of the rutile-$TiO_2$ structure are observed for both coatings in their as deposited state, which can be explained by a post-deposition venting strategy that facilitates oxygen to the not yet fully cooled coating surfaces [43]. As the coatings are annealed at 700 °C for 1 h, transformation of the metastable c-Ti(Al)N phase into the thermodynamically more favorable w-Al(Ti)N phase occurs for both compositions. While the $Ti_{0.52}Al_{0.48}N$ coating features intensified reflexes of the [002]-planes, the $Ti_{0.34}Al_{0.66}N$ coating exhibits more pronounced diffraction along the [100]-direction.

With increasing annealing time (5–15 h), the formation of additional oxides, such as α-$Al_2O_3$ and $TiO_2$ (anatase) occurs. For $Ti_{0.52}Al_{0.48}N$, reflexes of the α-$Al_2O_3$ and $TiO_2$ (anatase) are most pronounced in the [012]- and [101]-direction, respectively, while for the $Ti_{0.52}Al_{0.48}N$ coating, preferred diffraction of the same oxides occurs along the [202]- and [103]-planes.

Hereafter, no additional oxides develop, apart from the already mentioned $TiO_2$ (rutile), $TiO_2$ (anatase), and α-$Al_2O_3$. Interestingly, no sulphation of the surface oxides occurs for the duration of the annealing experiments despite the oxide to sulphate transformation being thermodynamically favored. This is a strong indication that an insufficiently high partial pressure of $SO_3$ is present [44]. By consulting the global kinetic model by Burdett et al. [45], together with studies from Wall et. al [29] and Anthony et. al. [46], an approximation of the homogeneous $SO_3/SO_2$ conversion rate was made, rendering a partial pressure of $p_{[SO3]}$ ~$2.0 \times 10^{-3}$ atm (or ~200 ppm by volume).

### 3.4. Oxidation behavior of salt-loaded samples

Compared to the coatings, which have been annealed solely in a $SO_x$-rich atmosphere (Fig. 5a & 5b), a significantly higher oxidation rate was observed for coatings that were loaded with salt deposits under identical annealing conditions (Fig. 6a & 6b). In order to retrieve information about the oxidized state of the coatings, the salt deposits were carefully removed from the samples prior to the XRD measurements.

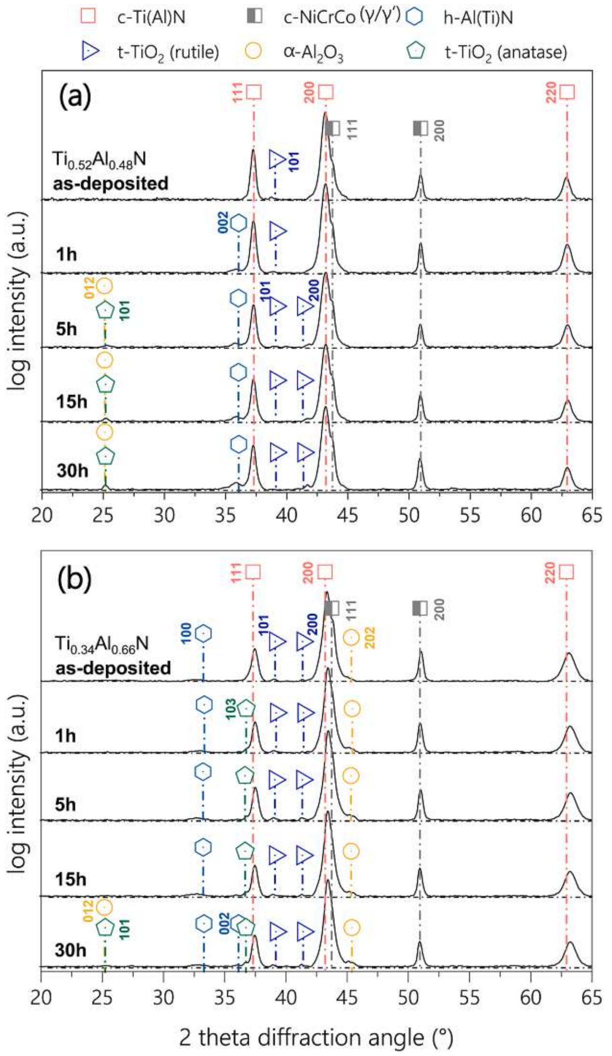

**Fig. 5.** XRD analysis of (a) $Ti_{0.52}Al_{0.48}N$ and (b) $Ti_{0.34}Al_{0.66}N$ coatings after annealing in $SO_x$-rich atmosphere at 700 °C for 0, 1, 5, 15, and 30 h (reference patterns were taken from ref. [37–39,47–49]).

By reviewing the respective diffractograms, a more prominent onset of oxide formation between 1 and 5 h is readily apparent. Both $Ti_{0.52}Al_{0.48}N$ and $Ti_{0.34}Al_{0.66}N$ coatings (Fig. 6a-b) feature more distinct reflexes of the $TiO_2$-anatase [101]-planes and α-$Al_2O_3$ [012]-planes, as well as additional peaks referring to the $TiO_2$-rutile [110]-planes.

After 15 h, more pronounced diffraction peaks of the previously mentioned $TiO_2$-anatase and α-$Al_2O_3$ are exhibited for both compositions, while additional diffraction peaks of $Cr_2O_3$ appear in the diffractogram for $Ti_{0.52}Al_{0.48}N$. As chromium can only originate from the substrate, the detection of $Cr_2O_3$ indicates a breakthrough of the corrosion front into the substrate material. Other oxides such as $Co_3O_4$ and NiO, which would also readily form in the case of substrate oxidation, unfortunately, overlap with other prominent diffraction peaks, and thus, cannot be clearly interpreted. Contrarily, no $Cr_2O_3$ reflexes are

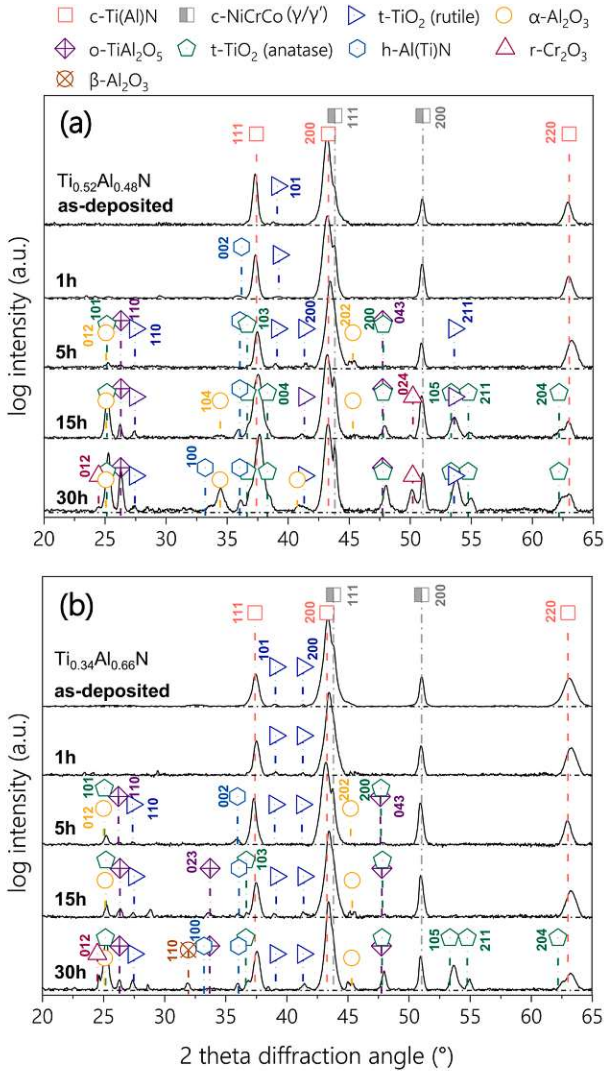

**Fig. 6.** XRD analysis of (a) $Ti_{0.52}Al_{0.48}N$ and (b) $Ti_{0.34}Al_{0.66}N$ coatings, which have been loaded with salt-deposits and annealed in an $SO_x$-rich atmosphere at 700 °C for 0, 1, 5, 15, and 30 h. Reference patterns were taken from ref. [37–39,47–51].

shown for the $Ti_{0.34}Al_{0.66}N$ coating after 15 h, suggesting that no breakthrough of the coating structure is present.

After 30 h of exposure to LTHC conditions, both coating variants feature severe oxidation and partial breakthrough of the corrosion front, validated by the structural evolution of rutile-$TiO_2$, α-$Al_2O_3$ and $Cr_2O_3$. Lastly, the formation of β-$Al_2O_3$ can be identified for the high Al-content $Ti_{0.34}Al_{0.66}N$ coating, which is a metastable structure that form in the presence of sodium aluminate ($NaAl_{11}O_{17}$).

### 3.5. *Localized corrosion of $Ti_{1-x}Al_xN$ coatings under LTHC conditions*

EDX line scans were collected along the cross-section of severely corroded coating sections. Fig. 7a & 7b show oxygen profiles, which serve as elemental indicators for the progression (depth) of the hot corrosion front. Since corrosion products that form during hot corrosion mostly comprise oxygen-containing compounds (oxides and sulfates), the diffusion depth of oxygen may provide first insights into the corrosion resistance of applied coating materials.

During the first 5 h of the corrosion experiments, the EDX profiles of both compositions display surface near oxygen enrichment, reaching diffusion depths of ~1 µm. After 15 h a significant increase in the oxygen diffusion rate is observed for the $Ti_{0.52}Al_{0.48}N$ coating variant, reaching a depth of ~8 µm. This is not the case for the higher Al-content $Ti_{0.34}Al_{0.66}N$ coating, which continues to exhibit a diffusion depth of only ~1 µm, however with a higher oxygen saturation than after 5 h.

Finally, after 30 h, accelerated oxygen diffusion is also observed for the high Al-containing $Ti_{0.34}Al_{0.66}N$ coating, with a diffusion depth of ~8 µm. As for the $Ti_{0.52}Al_{0.48}N$ coating, which already exhibited the accelerated diffusion behavior after 15 h, a complete bridging of the ~10 µm coating structure was measured, with the corrosion front reaching well into the underlying substrate material (>12 µm total diffusion).

Fig. 7c features a plot of the oxygen diffusion depths against the duration of the corrosion experiments, and highlights two stages: (i) an initiation stage, which involves surface-near oxygen enrichment and oxide scale development (~1 µm), and (ii) a propagation stage, which is characterized by accelerated oxygen inward diffusion. Apparent is that the higher Al-content $Ti_{0.34}Al_{0.66}N$ resides much longer within the initiation stage than the $Ti_{0.52}Al_{0.48}N$ coating (for 15 and 5 h, respectively), and consequently enters the propagation stage much later.

Unfortunately, LTHC is characterized by a pitting mechanism, which means that the corrosion progression of the coating occurs in a non-uniform (localized) manner. Therefore, the authors would like to emphasize that the oxygen profiles shown in Fig. 7a-c strictly pertain to the specific location they were obtained from and do not describe the overall state of the coating.

To further highlight this pitting behavior, Fig. 8 shows an EDX map of the salt-loaded $Ti_{0.52}Al_{0.48}N$ coating after 30 h, which has shown the highest oxygen inward diffusion (Fig. 7a) and exhibited $Cr_2O_3$ reflexes in the structural analysis as a clear indication for a corrosion front far beyond the coating ($Ti_{0.52}Al_{0.48}N$ loaded with salt after 30 h, Fig. 6a). Local corrosion pits emanate from regions where the coating structure has been breached, after which the corrosion front expands radially into the NiCrCo-base material. Also the corrosion of the coating itself occurs in homogeneously and is subject to local degradation. This is highlighted by the irregular diffusion profiles presented in Fig. 8 and can be summarized as follows:

i. Ti remains homogeneously distributed within the deposited coating.
ii. Al and N diffuse out of the coating structure and partially accumulate within the corrosion pit of the substrate.
iii. O diffuses into coating regions (lattice incorporation and/or atom replacement), where Al and N have defused outwards.
iv. O further diffuses into the NiCrCo-substrate material (radial pit-formation), where it reacts with Cr to form $Cr_2O_3$.
v. Ni and Co readily dissolve within the corrosion pit and diffuse outward.
vi. S accumulates at the corrosion front in the form of a highly concentrated S-band, however only within the pit of the substrate material.

### 3.6. *Salt chemistry after LTHC experiments*

Literature has shown that the LTHC mechanism hinges on the formation of a liquid salt/oxide interface [52]. The development of such a liquid interface, despite the corrosion temperature being well below the melting point of the salt-deposit, can occur in different ways. The so-called “gas phase induced acidic fluxing” is driven by high partial pressures of $SO_3$ in the atmosphere at relatively low temperatures (500–700 °C). First, sulphation of surface oxides that stand in direct contact with the atmosphere occurs, after which the development of low-melting eutectic mixtures between the newly formed sulphate scale and the salt-deposit follows (e.g. for $Na_2SO_4$ and $NiSO_4$ (mp= 680 °C) or

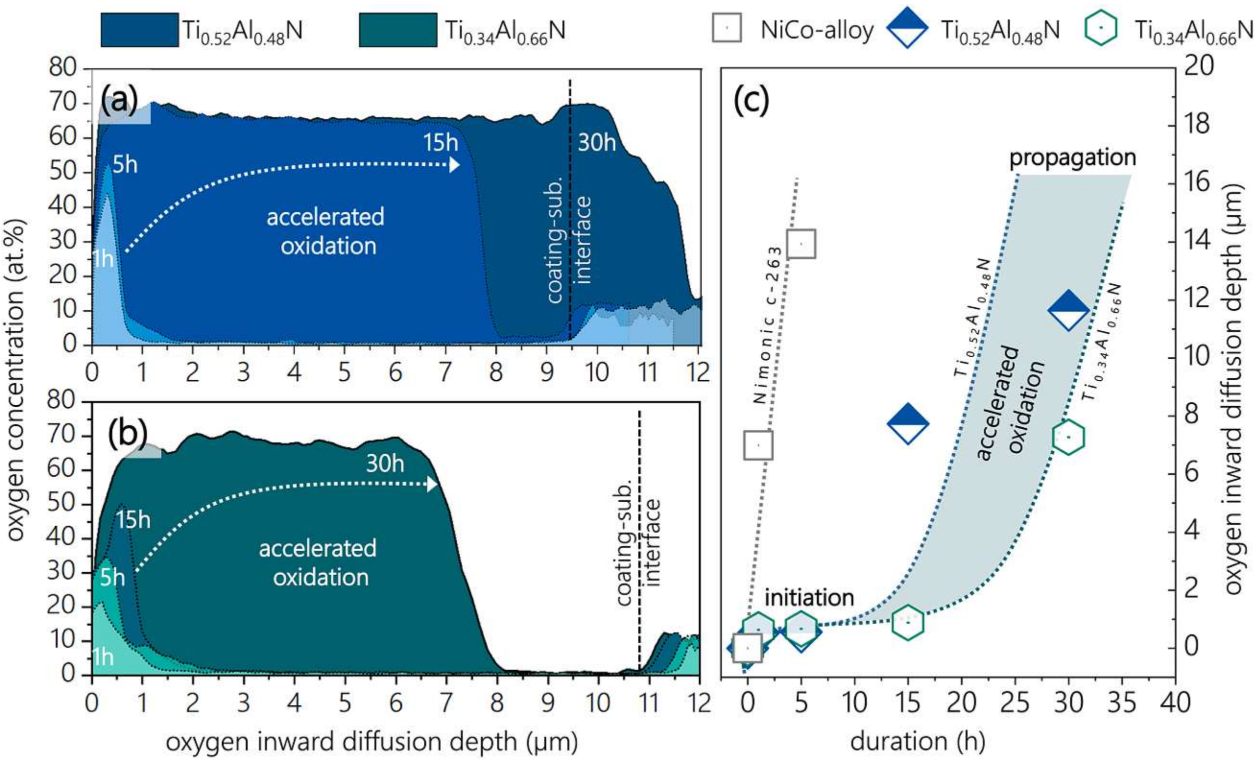

**Fig. 7.** EDX line-scan measurements of (a) the $Ti_{0.52}Al_{0.48}N$ and (b) the $Ti_{0.34}Al_{0.66}N$ coatings in their corroded states after 1, 5, 15, and 30 h. Depicted are the oxygen inward-diffusion profiles, which are indicative of the degree of oxidation that the coatings have suffered. (c) graphically highlights the prolonged oxidation resistance, due to the presence of the $Ti_{1-x}Al_xN$ coatings.

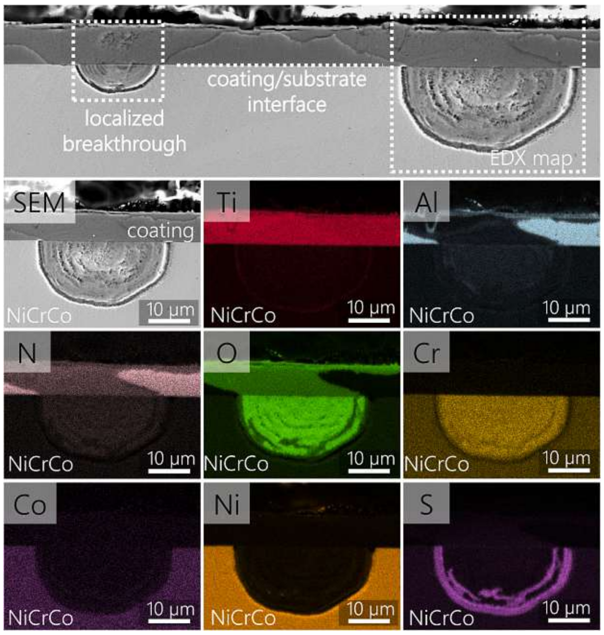

**Fig. 8.** Cross-section SEM imaging and EDX mapping showing localized breakthrough oxidation of the $Ti_{0.52}Al_{0.48}N$ coating, as well as the radial progression of the corrosion pit into the NiCrCo substrate material after 30 h of LTHC conditions.

$Na_2SO_4$ and $CoSO_4$ (mp= 575 °C) (see Eqs. 20–22). Other oxide-to-sulphate reactions are listed by Eqs. 23–25.

$$NiO_{(s)} + SO_{3(g)} = \mathrm{NiSO}_{4(s)} \tag{20}$$

$$CoO_{(s)} + SO_{3(g)} = \mathrm{CoSO}_{4(s)} \tag{21}$$

$$1/3Co_3O_{4(s)} + SO_{3(g)} = \mathrm{CoSO}_{4(s)} \quad + \quad 1/6O_2 \tag{22}$$

$$Al_2O_{3(s)} + 3SO_{3(g)} = 1/2\mathrm{Al}_2(\mathrm{SO}_4)_3 \tag{23}$$

$$Fe_2O_{3(s)} + 3SO_{3(g)} = 1/2\mathrm{Fe}_2(\mathrm{SO}_4)_3 \tag{24}$$

$$Cr_2O_{3(s)} + 3SO_{3(g)} = 1/2\mathrm{Cr}_2(\mathrm{SO}_4)_3 \tag{25}$$

Another way is the “alloy induced acidic fluxing” referring to alloying elements, such as W, Mo, or V, that readily diffuse to the surface, oxidize, and react with $Na_2SO_4$ to form low-melting complex oxides that in turn induce acidic fluxing of the protective oxide scale of the alloy (see Eqs. 26–29) [52].

$$2SO_{2(g)} + O_{2(g)} = 2\mathrm{SO}_{3(g)} \tag{26}$$

$$Mo + 3SO_{3(g)} = MoO_3 + 3SO_2 \tag{27}$$

$$MoO_{3(s)} + Na_2SO_{4(l)} = Na_2MoO_{4(diss.)} + SO_{3(g)} \tag{28}$$

$$MoO_{3(diss.in \quad Na_2SO_4)} + Al_2O_{3(s)} = Al_2(\mathrm{MoO}_4)_{3(diss.)} \tag{29}$$

In the case of a $Ti_{1-x}Al_xN$-coated NiCrCo-alloy, the latter alloy-induced fluxing mechanism may not be the most suitable model to explain the formation of a liquid salt/oxide interface, as a direct diffusion through the coating structure of such alloying elements has not been detected and is highly unlikely. Instead, the authors propose a gas-phase induced process, where the $SO_x/O_2$-rich atmosphere diffuses to locations where the deposit adheres to the coating surface. Due to the porous nature of the salt deposits, diffusion of the $SO_x/O_2$-rich gas through the salt-structure is possible, allowing the atmosphere to come in contact with the coating surface. There, the formation of oxides ($TiO_2$ and $Al_2O_3$) takes place, after which sulphation of the developed oxides (see Eqs. 20–25) and subsequent formation of low-melting eutectic sulfate mixtures with the $Na_2SO_4$ deposit occurs.

During the formation of the liquid interface between the sulphate and sintered $Na_2SO_4$ deposit, a liquid junction forms that slowly acidifies through the uptake of the $SO_3$-rich gas. It is important to keep in mind, that low partial pressures of $SO_3$ are not enough for sulphating surface-oxides such as t-$TiO_2$ and h-$Al_2O_3$ at 700 °C, as proven by the control group ($SO_3$-rich atmosphere without $Na_2SO_4$ deposit– revisit Fig. 3). This implies that the salt-oxide interface is a necessary requisite for the oxide-sulphate transformation and essential for establishing conditions for the subsequent accelerated oxidation of the remaining coating structure. Without the acidification of the $Na_2SO_4$ deposit at the salt-coating interface, no stable sulphation is possible and no low-melting liquid film can be generated. Luthra [35] first demonstrated that the transport of possible ionic species through a liquid $Na_2SO_4$ film (e.g. $S_2O_7^{2-}$, $SO_3^{2-}$, and $O^{2-}$), and therefore its acidity, is dominated by the solubility of $SO_3$ as $S_2O_7^{2-}$ through exchange reactions with $SO_4^-$. Luthra [35] also showed that gaseous species, such as $O_2$ and $SO_2$, have very low solubilities in $Na_2SO_4$ and are unlikely to play a major role in the corrosion mechanism within the liquid film [35], which was later confirmed by Shores, Fang and Rapp [53,54].

Fig. 9a shows the chemical analysis (by EDX) of the $Ti_{0.52}Al_{0.48}N$ coating surface that has been corroded with salt-deposits for 15 h at 700 °C in a $SO_x$-rich atmosphere. With the salt-deposits removed after the corrosion experiment, distinct differences in the severity of the corrosive attack are visible. Ring-like imprints reveal areas where the salt had contact with coating surface, and where voids/pores prevented the salt from causing corrosion (highlighted by the dotted circles). As the salt deposits are prepared by placing a drop of saturated salt-solution onto the surface of the coating, the subsequent drying process traps air within the slowly drying salt-deposit, and consequently forms a porous matrix. By reviewing the EDX-maps, significant depletion of Ti, Al and N is featured at places where the salt stood in contact with the coating surface. Simultaneously, O- and S-enrichment occurs where Al, N and Ti have diffused outward.

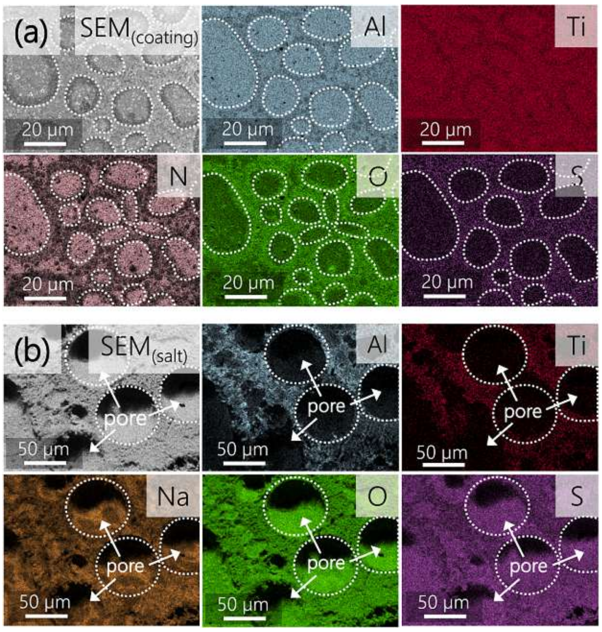

**Fig. 9.** EDX mapping showing (a) a top-view of the $Ti_{0.52}Al_{0.48}N$ coating surface after 15 h of corrosion time after the salt deposit removed, and (b) the underside of the respective salt-deposit extracted from the coating side shown in (a).

Fig. 9b, on the other hand, shows EDX-maps of the underside of the salt-deposit, revealing that indeed, Al and Ti are absorbed by the salt-deposit. This suggests that Al and Ti first migrate to the coating surface, where they oxidize and form $Al_2O_3$ and $TiO_2$ scales according to type T oxidation. Thereafter, an oxide to sulphate transformation takes place, after which a low melting sulphate-eutectic develops and a fluxing mechanism between the developing scales and salt-deposit proceeds.

In order to substantiate this claim, structural analyses were conducted of the as-deposited $Na_2SO_4$-$MgSO_4$ salt, as well as the salt-retrieval from the $Ti_{0.52}Al_{0.48}N$ coating after 15 h corrosion time at 700 °C (Figs. 10a and 10b, respectively). In the as-deposited form, the mixture is comprised solely of an orthorhombic $Na_2SO_4/MgSO_4$ mixture. After 15 h of corrosion time at 700 °C in a $SO_x$-rich atmosphere, the salt composition transitions to a predominantly monoclinic $Na_6Mg(SO4)_4$ and orthorhombic $Na_2Mg_3(SO_4)_4$ composition, with residual orthorhombic $Na_2SO_4$ and $MgSO_4$ grains. Furthermore, the presence of orthorhombic $TiO_2$ and monoclinic $NaAl(SO_4)_2$ could be confirmed, which provides further evidence for the dissolution of $Al_2O_3$ and $TiO_2$ by the $Na_2SO_4$-$MgSO_4$ melt.

### 3.7. *Detailed morphological analysis of $Ti_{1-x}Al_xN$ under LTHC conditions*

TEM analyses were conducted to further understand, to which degree the subsequent propagation mechanisms (accelerated oxidation) of the $Ti_{0.52}Al_{0.48}N$ and $Ti_{0.34}Al_{0.66}N$ coincide and/or differ from one another.

The propagation stage (accelerated oxidation) of the $Ti_{0.52}Al_{0.48}N$ and $Ti_{0.34}Al_{0.66}N$ coating is presented throughout Figs. 11–13. Fig. 11a shows a bright field TEM cross-section image of the salt-loaded $Ti_{0.52}Al_{0.48}N$ after 15 h at 700 °C. In order to provide better contrast between individual coating structures, especially corroded areas near the surface, STEM imaging was performed at the area highlighted by the dotted box and shown in Fig. 11b. There, three distinctly different

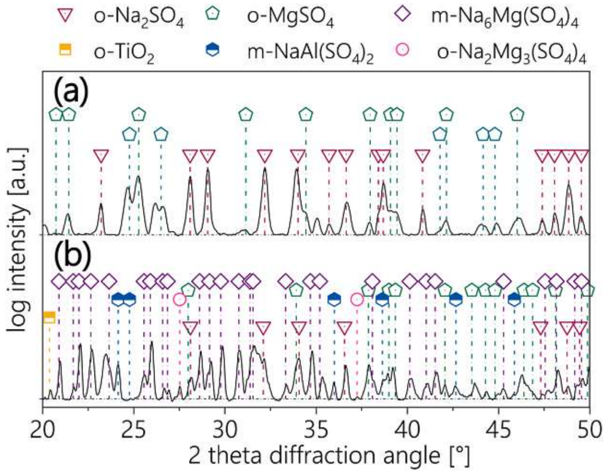

**Fig. 10.** X-ray diffractograms of (a) as-deposited 80/20 mol.% $Na_2SO_4/MgSO_4$ salt-mixture, and (b) salt-retrieval from the surface of a $Ti_{0.52}Al_{0.48}N$ coated Nimonic c-263 alloy after 15 h of annealing time in $SO_x$-rich atmosphere at 700 °C. Reference patterns were taken from ref. [55–60].

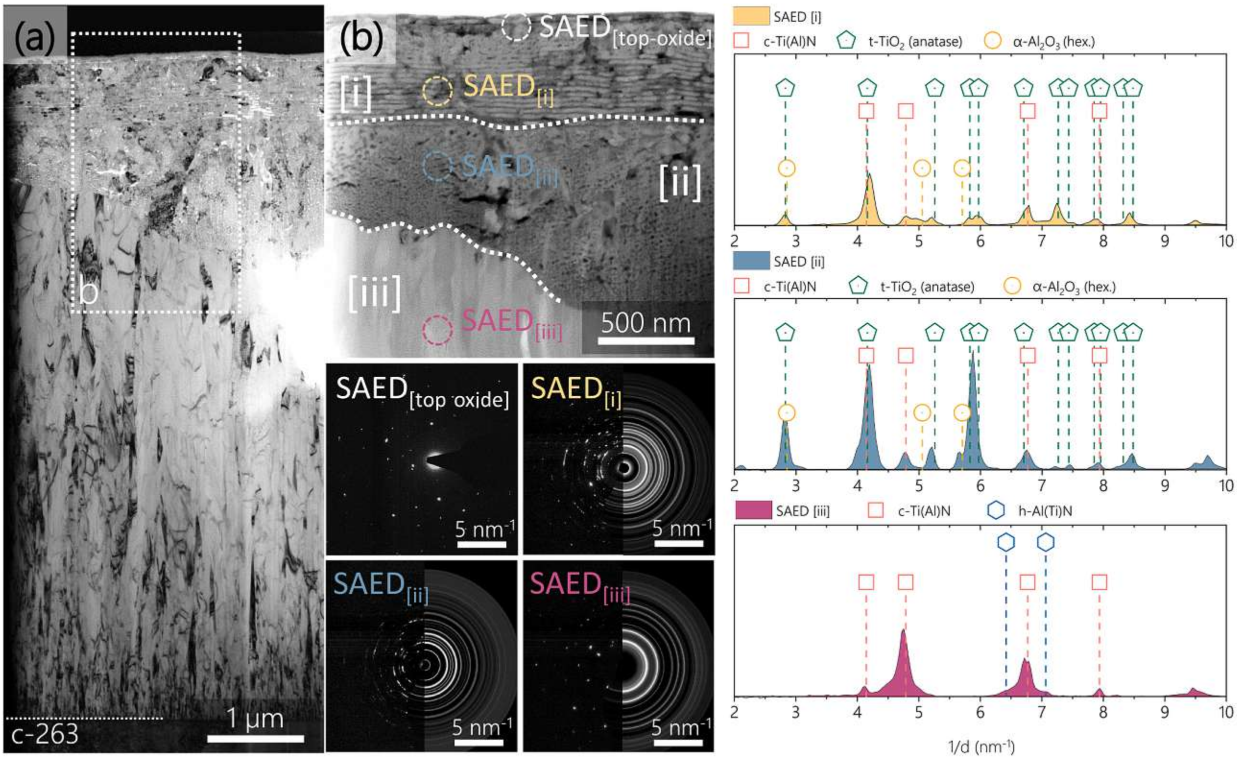

**Fig. 11.** TEM investigation featuring the propagation stage of the $Ti_{0.52}Al_{0.48}N$ coating after 15 h at 700 °C. (a) features a bright field TEM cross-section of the entire coating structure. (b) shows a STEM images of a selected surface near region (marked by the dotted box), highlighting the formation of three distinctly different coating microstructures (zone i,ii and iii). Lastly, SAEDs were obtained from each zone, whose integrated intensity plots are shown below.

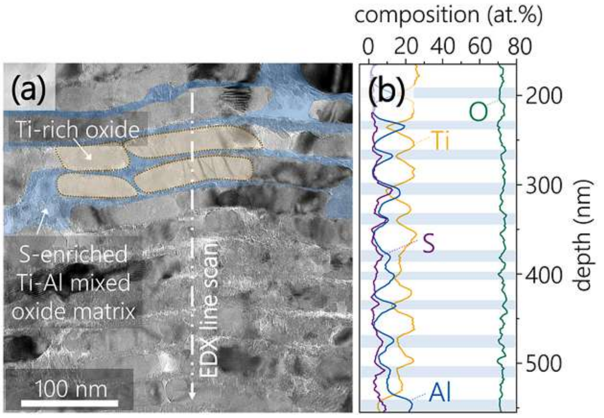

**Fig. 12.** TEM investigation of the highly lamellar coating structure (zone i), featuring the propagation stage of the $Ti_{0.52}Al_{0.48}N$ coating after 15 h at 700 °C: (a) bright-field image, featuring sequential Ti-rich crystalline domains, suspended in a disrupted S-enriched Ti-Al mixed oxide matrix. (b) provides the respective EDX line scan profiles.

coating morphologies are observed (labeled i, ii and iii). Starting from the top, a finely layered structure can be seen with distinct pore formations in between each layer (zone i). Underneath, a less ordered structure is featured with a more globular morphology and significant pore distribution (zone ii). Lastly, at the very bottom, the pristine coating morphology can be seen with its typical columnar structure (zone iii). In order to gain insight about the crystal structure of each distinct zone, SAEDs were collected. The location of each performed SAED is indicated in Fig. 11b and labeled according to the zones they were taken from ($SAED_{[i]}$, $SAED_{[ii]}$ and $SAED_{[iii]}$, pertain to the layered structure, globular feature, and pristine coating morphology, respectively, while the $SAED_{[top\ oxide]}$ refers to the oxide positioned at the surface). Starting from the top, the $SAED_{[top\ oxide]}$ renders single crystalline domains, as evident from the spot-pattern. Indexing of the pattern renders a trigonal crystal structure of the α-$Al_2O_3$ with the space group $R\bar{3}c$. $SAED_{[i]}$ and $SAED_{[ii]}$, on the other hand, exhibit smeared diffraction pattern, inferring a more distorted nanocrystalline structure. By integrating the SAED ring-patterns and plotting them over the reciprocal of the lattice-spacing, intensity plots with broadened but defined peaks are generated. The intensity plot obtained from zone i (layered structure, $SAED_{[i]}$) predominantly features $TiO_2$-reflexes, with minor diffraction intensity pertaining to α-$Al_2O_3$ and the c-Ti(Al)N crystal structure. Similarly, the intensity plot from zone ii exhibits the same constituents ($TiO_2$, α-$Al_2O_3$ and c-Ti(Al)N), however with different intensity distribution. Finally, the diffraction pattern from $SAED_{[iii]}$ provides spot like diffraction spots, whose integration render diffraction vectors that match the c-Ti(Al)N crystal structure with minor indication of the w-AlN phase.

By taking a closer look at zone ii (layered features) the presence of highly ordered $TiO_2$ is further validated. Fig. 12 shows a HR-TEM image from zone ii (Fig. 12a) together with an EDX-line scan (Fig. 12b). Quite evident are the formations of rod-like $TiO_2$-domains that are arranged periodically in a mesh composed of Ti, S, Al and O. While the individual $TiO_2$-domains measure around 100 × 30 nm in size, the mesh appears mostly amorphous with nanocrystalline grains suspended within.

Fig. 13 shows the corroded state of the $Ti_{0.34}Al_{0.66}N$ after 15 h at 700 °C, where four distinctly different coating morphologies can be observed (labeled i, ii, iii, and iv). Here too, the SAEDs provide insight

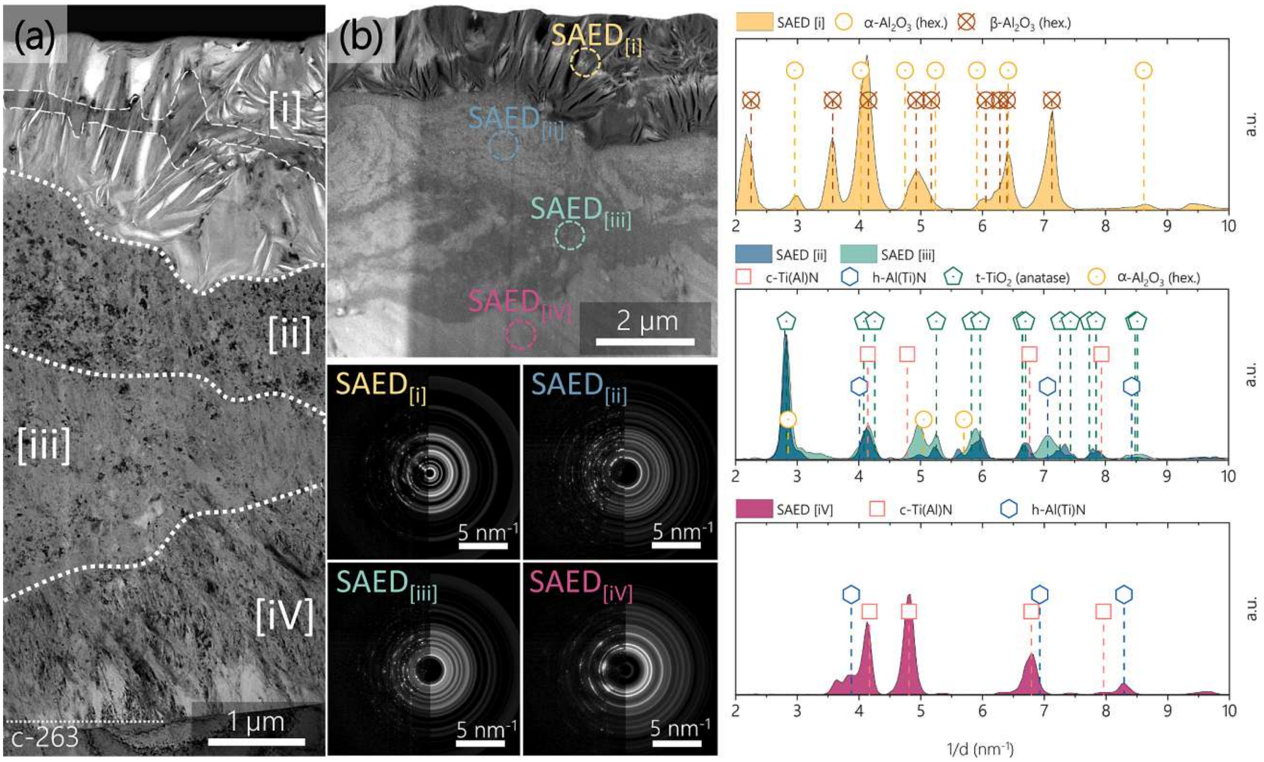

**Fig. 13.** TEM investigation featuring the propagation stage of the $Ti_{0.34}Al_{0.66}N$ coating after 15 h at 700 °C. (a) features a bright field TEM cross-section of the entire coating structure. (b) shows a STEM images of the face near region, highlighting the formation of four distinctly different coating microstructures (zone i, ii, iii, and iv). Lastly, SAEDs were obtained from each zone, whose integrated intensity plots are shown below.

about the crystal structure from each zone. Integration of the SAED$_{[i]}$ indicates diffraction vectors that match a mixed α-$Al_2O_3$ and β-$Al_2O_3$ oxide. While the α-configuration resembles the most common and thermodynamically stable form of $Al_2O_3$, the β-configuration represents a metastable structure, which forms together with sodium aluminate ($NaAl_{11}O_{17}$). The presence of both α- and β-crystal structures makes sense and validates the interaction between the $Na_2SO_4$ deposit and the forming Al-oxide scales.

Underneath, two globular morphologies can be seen (zone II and III). According to the respective SAED$_{[ii]}$ and SAED$_{[iii]}$, both zones feature a mixture of α-$Al_2O_3$, anatase-$TiO_2$ and residual c-Ti(Al)N. Unlike zone ii, zone iii (SAED$_{[iii]}$) features more pronounced α-$Al_2O_3$ reflexes, as well as peaks of the w-Al(Ti)N crystal structure.

Lastly, the SAED$_{[iv]}$ features diffraction vectors that fit the lattice spacing of the pristine as-deposited metastable c-Ti(Al)N crystal structure with indications of some indication of the w-Al(Ti)N phase.

## 4. Discussion

### 4.1. LTHC mechanism for $Ti_{1-x}Al_xN$ coatings

The LTHC mechanism for cathodic arc evaporated $Ti_{1-x}Al_xN$ coatings at 700 °C with a mixed $Na_2SO_4$-$MgSO_4$ salt-deposit is summarized schematically in Fig. 14.

#### 4.1.1. Incubation stage

The LTHC mechanism begins with the incubation stage and the formation of a passive oxide scale. For protective coatings, particularly nitride-based coating such as $Ti_{1-x}Al_xN$, this entails a nitride to oxide transformation. The porous structure of the salt deposit facilitates eased permeation and subsequent diffusion of the oxidizing atmosphere to the coating surface, where both $Ti_{1-x}Al_xN$ coating variants developed a layered oxide scale (see Fig. 14a-b). According to the control group of this study, the scale formation for both, $Ti_{0.52}Al_{0.48}N$ and $Ti_{0.34}Al_{0.66}N$ coatings follow a type-T oxidation mechanism, where an Al-rich oxide forms on top, followed by a Ti-rich oxide underneath.

#### 4.1.2. Initiation stage

The initiation stage comprises a sequence of changes in the materials environment that establishes the conditions where accelerated oxidation/degradation occurs. This is probably the most crucial step in the LTHC mechanism, as it roughly determines the longevity of protective coating. For LTHC, the initiations stage entails the formation of low-melting eutectics between the rigid salt-deposit and metal oxide surface. The formation of a liquid interface then allows for changes in the melt-basicity, and local depassivation of the oxide scale and/or nitride coating. For the establishment of a low-melting eutectic (liquid salt film) between the salt-deposit and the oxidized coating surface, sulphation of the oxide must occur. At sufficiently high $pSO_3$ in the atmosphere, the oxide-to-sulphate transition proceeds quite readily, but at low $pSO_3$, as is the case for this study, no sulphation of the coatings' top-oxides was observed (proven by control group, Fig. 5). Instead, $SO_3$ from the atmosphere permeates into the salt-deposit, where it accumulates, raises the local $pSO_3$ to a critical value (Fig. 14c-d) and initiates sulphation of the underlying oxide (Figs. 14e and 14e-*i*). As the formation of $Al_2(SO_4)_3$ progresses, a low melting eutectic $Al_2(SO_4)_3$-$Na_2SO_4$ mixture develops (Fig. 14f) and by extension transitions into a liquid salt interface (Fig. 14g). Within the liquid salt film, dissociation of $Na_2SO_4$ into its basic ($Na_2O$, $O^{2-}$) and acidic ($SO_3$) constituents (acid-base equilibrium $SO_4^{2-} \longleftrightarrow O^{2-}+SO_3$) proceeds. Acidic and basic fluxing mechanisms are now possible, depending on the local basicity (activity of $O^{2-}$ vs $S_2O_7^{2-}$). At the liquid-gas interface, $SO_3$ further acidifies the melt in the form of

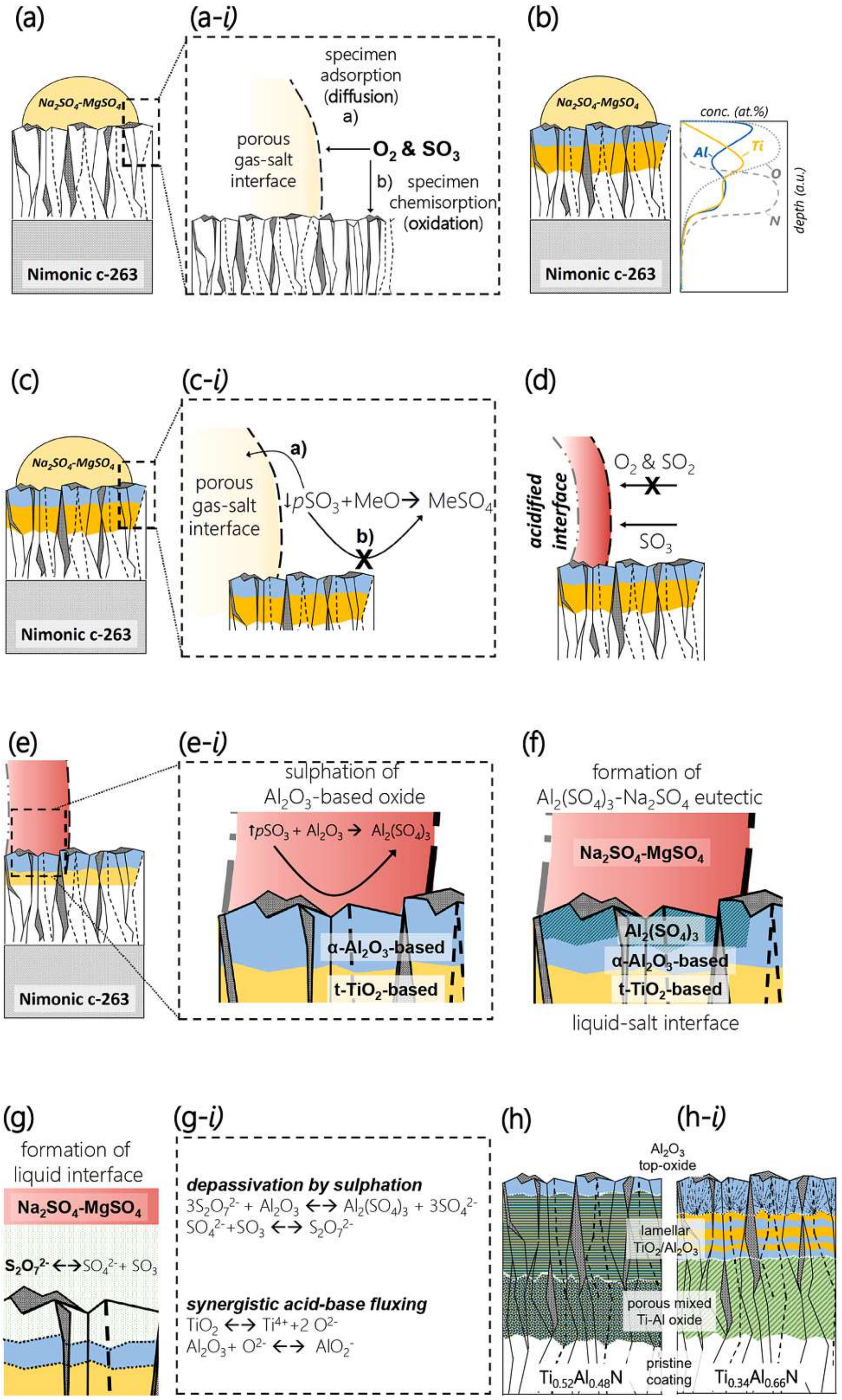

*depassivation by sulphation*

$3S_2O_7^{2-} + Al_2O_3 \leftrightarrow Al_2(SO_4)_3 + 3SO_4^{2-}$

$SO_4^{2-} + SO_3 \leftrightarrow S_2O_7^{2-}$

*synergistic acid-base fluxing*

$TiO_2 \leftrightarrow Ti^{4+} + 2\,O^{2-}$

$Al_2O_3 + O^{2-} \leftrightarrow AlO_2^-$

**Fig. 14.** Salt induced LTHC mechanism of cae-Ti$_{1-x}$Al$_x$N coatings annealed at 700 °C in a SO$_x$-rich atmosphere.

$S_2O_7^{2-}$, which has been shown to be the major ionic carrier between the gas-salt-interface and the sample surface. Accordingly, dissolution of $SO_3$ in the form of $S_2O_7^{2-}$ produces additional acidic character, which further promotes the acidic fluxing of the Al-rich top oxide. This so-called gas-phase induced acidification of the salt-deposit is thereby a critical link in the LTHC mechanism and plays a crucial role in the initial depassivation of the oxide scale (Fig. 14g-*i)*. Due to the relatively high stability of $Al_2O_3$ in acidic melts, its breakdown and acidic fluxing is proceeds quite slowly. This explains the different durations of the initiation stages, observed for both $Ti_{1-x}Al_xN$ coatings. Hence, a thicker $Al_2O_3$ top oxide contributes to a longer initiation stage ($Ti_{0.34}Al_{0.66}N$), whereas thinner $Al_2O_3$ scales provide less initial protection ($Ti_{0.52}Al_{0.48}N$).

### 4.1.3. *Propagation stage*

Once the $Al_2O_3$ top-oxide has been breached, a synergistic fluxing mechanism is proposed, where cooperative co-dissolution of $TiO_2$ and $Al_2O_3$ occurs. If the salt-melt basicity falls between the dissolution minima of two oxides (e.g. $Al_2O_3$ and $TiO_2$) then the more basic oxide ($TiO_2$ = more stable under basic conditions) undergoes acidic fluxing, whilst releasing oxide ($O^{2-}$) ions into the melt. The local increase in $O^{2-}$ (increased basicity) then induces basic dissolution of the more acidic oxide ($Al_2O_3$ = more stable under acidic conditions) and in turn stimulates the acidic dissolution (Fig. 14g-*i*). In other words, when two oxides support the dissolution of the other, a faster degradation of the protective scale is expected then if both oxides were present individually. When assessing the corrosion rates of the $Ti_{0.52}Al_{0.48}N$ and $Ti_{0.34}Al_{0.66}N$ coatings, a synergistic fluxing mechanism could explain the alternating layering of the Al-rich and Ti-rich oxide bands. The synergistic effect may also explain the highly frequent layering within the corrosion pit of the $Ti_{0.52}Al_{0.48}N$. If the Al:Ti $\approx$ 1, then the switching between acidic and basic fluxing may occur more frequently, whereas if the Al:Ti ‡ 1, then the changeover occurs in a more irregular manner (Fig. 14h and h-*i*).

## 5. Conclusion

The present work deals with the LTHC behavior of $Ti_{1-x}Al_xN$ coated c-263 alloy when treated with a $Na_2SO_4/MgSO_4$ salt mixture and isothermally annealed in a $SO_x$-rich atmosphere. A series of annealing experiments revealed that the LTHC mechanism for $Ti_{1-x}Al_xN$ coatings can be expressed in four distinct stages: incubation, initiation, propagation, and failure.

First, oxidation of the $Ti_{0.52}Al_{0.48}N$ and $Ti_{0.34}Al_{0.66}N$ coatings occurs, leading to the formation of a layered oxide scale that is composed of an Al-rich layer on top and a Ti-rich oxide layer underneath (incubation stage).

Thereafter, sulphation of the oxide scale proceeds due to the $SO_x$-rich atmosphere, followed by the formation of a low-melting eutectic $Al_2(SO_4)_3$-$Na_2SO_4$, providing the necessary liquid-salt interface for accelerated corrosion to commence (initiation stage).

The ensuing propagation stage for both $Ti_{1-x}Al_xN$ variants could best be described by a synergistic fluxing mechanism of the individual $Al_2O_3$-rich and $TiO_2$-rich oxide layers. Depending on the relative Al-contents of the $Ti_{1-x}Al_xN$ coatings, distinct differences in the development of the corrosion scales were observed. While low Al-containing $Ti_{0.52}Al_{0.48}N$ coatings featured a thin $Al_2O_3$ top-oxide, followed by a highly laminated structure of Al-rich and Ti-rich oxide domains, higher Al-containing $Ti_{0.34}Al_{0.66}N$ coatings exhibited a much thicker $Al_2O_3$ top-oxide with a more spread out layering of Al-rich and Ti-rich oxide bands. To explain these differences, the authors propose that a more frequent synergistic co-dissolution of individual oxide bands takes place when the coating composition on the metal sublattice approaches 1:1 (Ti:Al), while a more irregular and sluggish fluxing occurs when metal-sublattice compositions are further apart.

Synergistic corrosion phenomena, as presented here for the binary $Ti_{1-x}Al_xN$ system, pose a significant challenge for developing HC protective coatings. As future coating strategies and systems tend to increase in complexity, the authors would like to emphasize the profound effect that chemical composition and synergy between elements within a coating have on the corrosion behavior in HC settings.

## CRediT authorship contribution statement

O. E. H. and H. R. conceived the research. O. E. H. conducted the coating depositions, as well as the hot corrosion tests. P. K. prepared the TEM lamellas, whereas T. W. conducted the TEM measurements. O. H. and P. P. supported the research by providing indispensable funding, while L. S. and S. K. assisted the research with their thematic expertise. H. R. also provided funding acquisition and oversaw the research as supervisor. Finally, all authors have contributed in revising and approving the final version of the manuscript.

## Declaration of Competing Interest

The authors declare the following financial interests/personal relationships which may be considered as potential competing interests: Helmut Riedl reports financial support was provided by Christian Doppler Research Association.

## Data availability

The data that support the findings of this study are available from the corresponding author upon reasonable request.

## Acknowledgments

The financial support by the Austrian Federal Ministry for Digital and Economic Affairs, the National Foundation for Research, Technology and Development and the Christian Doppler Research Association is gratefully acknowledged (Christian Doppler Laboratory "Surface Engineering of high-performance Components"). We also thank for the financial support of Plansee SE, Plansee Composite Materials GmbH, and Oerlikon Balzers, Oerlikon Surface Solutions AG. In addition, we want to thank the X-ray center (XRC) of TU Wien for beam time as well as the electron microscopy center - USTEM TU Wien - for providing the TEM facilities. The authors would like to extend our gratitude to Dr. Eckhardt and VDM Metals International GmbH for their generosity and support throughout this study. Lastly, the authors acknowledge TU Wien library for financial support through its Open Access Funding Program.

## Appendices

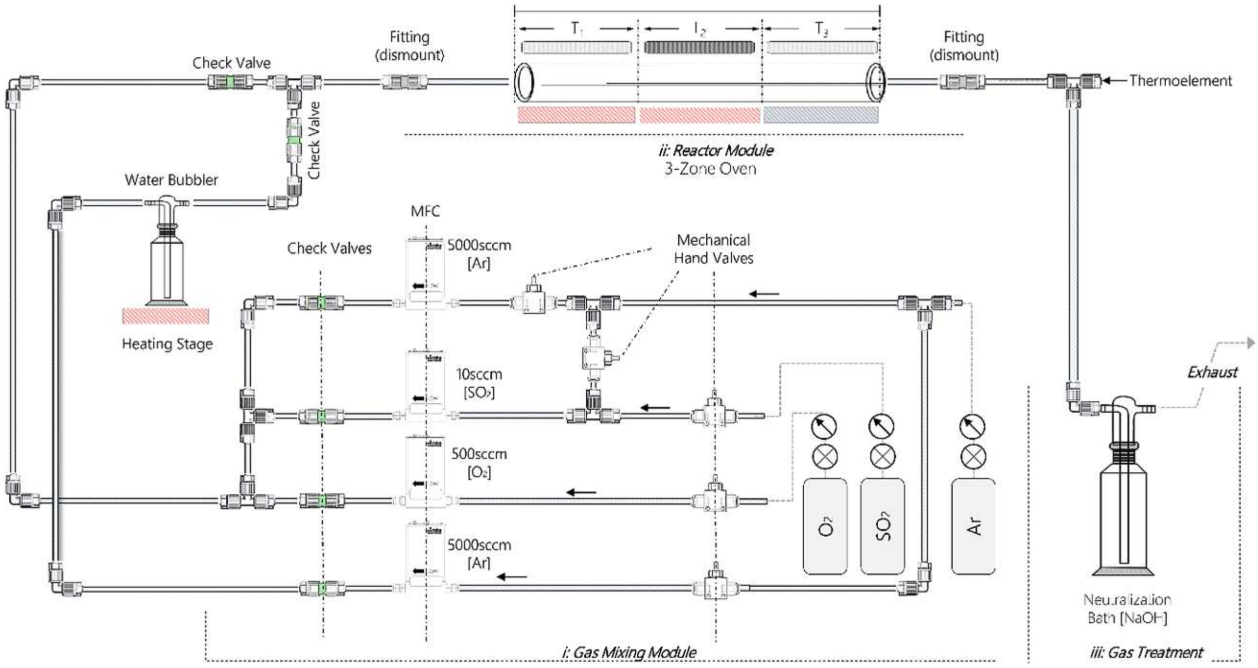

**Fig. A1.** Hot gas corrosion experimental set-up: (i) gas mixing system, (ii) quartz flow-reactor with a three-zone-gradient furnace, (iii) gas-treatment.

.

## References

[1] H. Bisaria, P. Shandilya, Experimental investigation on wire electric discharge machining (WEDM) of Nimonic C-263 superalloy, Mater. Manuf. Process. 34 (2019) 83–92, https://doi.org/10.1080/10426914.2018.1532589.

[2] X. Zhang, Y. Chen, J. Hu, Recent advances in the development of aerospace materials, Prog. Aerosp. Sci. 97 (2018) 22–34, https://doi.org/10.1016/j.paerosci.2018.01.001.

[3] H.L. Cockings, B.J. Cockings, W. Harrison, M. Dowd, K.M. Perkins, M.T. Whittaker, G.J. Gibson, The effect of near-surface plastic deformation on the hot corrosion and high temperature corrosion-fatigue response of a nickel-based superalloy, J. Alloy. Compd. 832 (2020), 154889, https://doi.org/10.1016/j.jallcom.2020.154889.

[4] J.C. Zhao, V. Ravikumar, A.M. Beltran, Phase precipitation and phase stability in Nimonic 263, Metall. Mater. Trans. A Phys. Metall. Mater. Sci. 32 (2001) 1271–1282, https://doi.org/10.1007/s11661-001-0217-4.

[5] I. Gurrappa, Hot corrosion behavior of CM 247 LC alloy in Na2SO4 and NaCl environments, Oxid. Met. 51 (1999) 353–382, https://doi.org/10.1023/a:1018831025272.

[6] T.M. Pollock, S. Tin, Nickel-based superalloys for advanced turbine engines: chemistry, microstructure, and properties, J. Propuls. Power 22 (2006) 361–374, https://doi.org/10.2514/1.18239.

[7] Y. Zhao, Y. Zhang, Y. Luo, D. Tang, H. Liu, H. Fu, Deformation behavior and creep properties of Co-Al-W-based superalloys: a review, Prog. Nat. Sci. Mater. Int. 31 (2021) 641–648, https://doi.org/10.1016/j.pnsc.2021.09.009.

[8] N. Rao, Materials for gas turbines – an overview, Adv. Gas. Turbine Technol. (2011), https://doi.org/10.5772/20730.

[9] N.S. Patel, V. Pavlík, M. Boča, High-temperature corrosion behavior of superalloys in molten salts–a review, Crit. Rev. Solid State Mater. Sci. 42 (2017) 83–97, https://doi.org/10.1080/10408436.2016.1243090.

[10] N. Otsuka, R.A. Rapp, Hot corrosion of preoxidized Ni by a thin fused Na2 SO 4 film at 900°C, J. Electrochem. Soc. 137 (1990) 46–52, https://doi.org/10.1149/1.2086436.

[11] P. Song, M. Liu, X. Jiang, Y. Feng, J. Wu, G. Zhang, D. Wang, J. Dong, X.Q. Chen, L. Lou, Influence of alloying elements on hot corrosion resistance of nickel-based single crystal superalloys coated with Na2SO4 salt at 900 °C, Mater. Des. 197 (2021), 109197, https://doi.org/10.1016/j.matdes.2020.109197.

[12] V. Patarini, N.S. Bornstein, M.A. DeCrescente, Hot corrosion of gas turbine components, J. Eng. Gas. Turbines Power 101 (1979) 177–185, https://doi.org/10.1115/1.3446441.

[13] S. Hu, H. Finklea, X. Liu, A review on molten sulfate salts induced hot corrosion, J. Mater. Sci. Technol. 90 (2021) 243–254, https://doi.org/10.1016/j.jmst.2021.03.013.

[14] X. Ren, F. Wang, High-temperature oxidation and hot-corrosion behavior of a sputtered NiCrAlY coating with and without aluminizing, Surf. Coat. Technol. 201 (2006) 30–37, https://doi.org/10.1016/j.surfcoat.2005.10.042.

[15] G. Sreedhar, M.M. Alam, V.S. Raja, Hot corrosion behaviour of plasma sprayed YSZ/Al2O3 dispersed NiCrAlY coatings on Inconel-718 superalloy, Surf. Coat. Technol. 204 (2009) 291–299, https://doi.org/10.1016/j.surfcoat.2009.07.026.

[16] R. Jafari, E. Sadeghi, High-temperature corrosion performance of HVAF-sprayed NiCr, NiAl, and NiCrAlY coatings with alkali sulfate/chloride exposed to ambient air, Corros. Sci. 160 (2019), 108066, https://doi.org/10.1016/j.corsci.2019.06.021.

[17] H. Lin, W. Liang, Y. Jia, Q. Miao, R. Hu, Z. Ding, L. Yu, Effect of Al–Y gradient coating on hot corrosion resistance of γ-TiAl alloy at different temperatures, Appl. Surf. Sci. 487 (2019) 868–875, https://doi.org/10.1016/j.apsusc.2019.05.168.

[18] L.K. Wu, J.J. Wu, W.Y. Wu, H.J. Yan, M.Y. Jiang, F.H. Cao, Hot corrosion behavior of electrodeposited SiO2 coating on TiAl alloy, Corros. Sci. 174 (2020), 108827, https://doi.org/10.1016/j.corsci.2020.108827.

[19] R. Li, C. Cheng, J. Pu, NaCl-induced hot corrosion behavior of TiAlN single-layer and TiAlN/Ti multilayer coatings at 500 °C, Mater. Today Commun. 33 (2022), 104421, https://doi.org/10.1016/j.mtcomm.2022.104421.

[20] M. Zhang, Y. Feng, Y. Wang, Y. Niu, L. Xin, Y. Li, J. Su, S. Zhu, F. Wang, Corrosion behaviors of nitride coatings on titanium alloy in NaCl-induced hot corrosion, Acta Metall. Sin. (Engl. Lett. 34 (2021) 1434–1446, https://doi.org/10.1007/s40195-021-01264-8.

[21] G. Biava, I.B. de Araujo Fernandes Siqueira, R.F. Vaz, G.B. de Souza, H.C. M. Jambo, A. Szogyenyi, A.G.M. Pukasiewicz, Evaluation of high temperature corrosion resistance of CrN, AlCrN, and TiAlN arc evaporation PVD coatings deposited on Waspaloy, Surf. Coat. Technol. 438 (2022), 128398, https://doi.org/10.1016/j.surfcoat.2022.128398.

[22] R.S. Bangari, S. Sahu, P.C. Yadav, Comparative evaluation of hot corrosion resistance of nanostructured AlCrN and TiAlN coatings on cobalt-based superalloys, J. Mater. Res. 33 (2018) 1023–1031, https://doi.org/10.1557/jmr.2018.53.

[23] Y. Qiao, X. Guo, X. Li, Hot corrosion behavior of silicide coating on an Nb-Ti-Si based ultrahigh temperature alloy, Corros. Sci. 91 (2015) 75–85, https://doi.org/10.1016/j.corsci.2014.10.053.

[24] J. He, X. Guo, Y. Qiao, F. Luo, A novel Zr-Y modified silicide coating on Nb-Si based alloys as protection against oxidation and hot corrosion, Corros. Sci. 177 (2020), 108948, https://doi.org/10.1016/j.corsci.2020.108948.

[25] H. Yu, Q. Fan, J. Li, D. Ma, J. Gong, C. Sun, Effect of Si addition to improve the performance of type II and type I hot corrosion resistance of aluminide coating, Corros. Sci. 212 (2023), 110937, https://doi.org/10.1016/j.corsci.2022.110937.

[26] Z. Tang, F. Wang, W. Wu, Effect of Al2O3 and enamel coatings on 900°C oxidation and hot corrosion behaviors of gamma-TiAl, Mater. Sci. Eng. A. 276 (2000) 70–75, https://doi.org/10.1016/S0921-5093(99)00513-4.

[27] H. Zhang, L. Yang, X. Zhang, Q. Wang, J. Wu, Z. Liu, C. Zeng, S. Zhu, Effect of enamel coating on the hot corrosion of 304 stainless steel beneath KCl–ZnCl2 deposits at 450 °C, J. Mater. Res. Technol. 23 (2023) 245–257, https://doi.org/10.1016/j.jmrt.2022.12.152.

[28] R.C. Brown, M.R. Anderson, C.E. Kolb, Aircr. Exhaust Sulfur Emiss. 23 (1996) 3603–3606.

[29] L.P. Belo, L.K. Elliott, R.J. Stanger, R. Spörl, K.V. Shah, J. Maier, T.F. Wall, High-temperature conversion of SO2 to SO3: homogeneous experiments and catalytic effect of fly ash from air and oxy-fuel firing, Energy Fuels 28 (2014) 7243–7251, https://doi.org/10.1021/ef5020346.

[30] S. Bose. High Temperature Coatings, 1st ed..,, Elsevier, 2007, https://doi.org/10.1016/B978-0-7506-8252-7.X5000-8.

[31] E. Yazhenskikh, T. Jantzen, D. Kobertz, K. Hack, M. Müller, Critical thermodynamic evaluation of the binary sub-systems of the core sulphate system Na2SO4–K2SO4–MgSO4–CaSO4, Calphad Comput. Coupling Phase Diagr. Thermochem. 72 (2021), https://doi.org/10.1016/j.calphad.2020.102234.

[32] J. Stringer, High-temperature corrosion of superalloys, Mater. Sci. Technol. 3 (1986) 482–493, https://doi.org/10.1080/02670836.1987.11782259.

[33] J.M. Alvarado-Orozco, J.E. Garcia-Herrera, B. Gleeson, F.S. Pettit, G.H. Meier, Reinterpretation of type II hot corrosion of Co-base alloys incorporating synergistic fluxing, Oxid. Met. 90 (2018) 527–553, https://doi.org/10.1007/s11085-018-9853-6.

[34] X. Zheng, R.A. Rapp, Electrochemical impedance of a platinum electrode in fused Na2 SO 4 melts in SO 2 – O 2 environments, J. Electrochem. Soc. 140 (1993) 2857–2862, https://doi.org/10.1149/1.2220922.

[35] K.L. Luthra, Low temperature hot corrosion of cobalt-base alloys" Part II, React. Mech. 13 (1982) 1853–1864.

[36] K.J. Meisner, E.J. Opila, Hot corrosion of shipboard gas turbine blades, Oxid. Met. 94 (2020) 301–322, https://doi.org/10.1007/s11085-020-09990-7.

[37] International Center of Diffraction Data, Powder diffraction file 04–001-3422, 2011.

[38] International Center of Diffraction Data, Powder diffractoin file 01–080-6097, 2013.

[39] International Center of Diffraction Data, Powder diffraction file 04–018-6856, 2022.

[40] L. Chavee, E. Serag, M. da Silva Pires, S. Lucas, E. Haye, A mechanistic approach of oxidation resistance, structural and mechanical behaviour of TiAlN coatings, Appl. Surf. Sci. 586 (2022), https://doi.org/10.1016/j.apsusc.2022.152851.

[41] P. Panjan, B. Navinšek, M. Čekada, A. Zalar, Oxidation behaviour of TiAlN coatings sputtered at low temperature, Vacuum 53 (1999) 127–131, https://doi.org/10.1016/S0042-207X(98)00407-2.

[42] G. Greczynski, L. Hultman, M. Odén, X-ray photoelectron spectroscopy studies of Ti1-xAlxN (0 ≤ x ≤ 0.83) high-temperature oxidation: the crucial role of Al concentration, Surf. Coat. Technol. 374 (2019) 923–934, https://doi.org/10.1016/j.surfcoat.2019.06.081.

[43] G. Greczynski, S. Mráz, L. Hultman, J.M. Schneider, Venting temperature determines surface chemistry of magnetron sputtered TiN films, Appl. Phys. Lett. 108 (2016), https://doi.org/10.1063/1.4940974.

[44] H.J. Maier, T. Niendorf, R. Bürgel, Handbuch Hochtemperatur- Werkstofftechnik, 6th ed., 2019.

[45] N. Burdett, W. Langdon, R.T. Squires, Rate coefficients for the reaction SO2+ O2→SO3+O in the temperature range 900–1350 K, J. Inst. Energy (1984) 373.

[46] Y. Sarbassov, L. Duan, V. Manovic, E.J. Anthony, Sulfur trioxide formation/emissions in coal-fired air- and oxy-fuel combustion processes: a review, Greenh. Gases Sci. Technol. 8 (2018) 402–428, https://doi.org/10.1002/ghg.1767.

[47] International Center of Diffraction Data, Powder diffraction file 01–086-4330, 2020.

[48] International Center of Diffraction Data, Powder diffraction file 01–071-1169, 2020.

[49] International Center of Diffraction Data, Powder diffraction file 01–071-1684, 2022.

[50] International Center of Diffraction Data, Powder diffraction file 04–001-9278, 2011.

[51] International Center of Diffraction Data, Powder diffraction file 00–010-0414, 2003.

[52] F. Pettit, Hot corrosion of metals and alloys, Oxid. Met. 76 (2011) 1–21, https://doi.org/10.1007/s11085-011-9254-6.

[53] D.A. Shores, W.C. Fang, Transport of oxidant in molten Na2 SO 4 in O 2 – SO 2 – SO 3 environments, J. Electrochem. Soc. 128 (1981) 346–348, https://doi.org/10.1149/1.2127417.

[54] W.C. Fang, R.A. Rapp, Electrochemical reactions in a pure Na2 SO 4 melt, J. Electrochem. Soc. 130 (1983) 2335–2341, https://doi.org/10.1149/1.2119581.

[55] International Center of Diffraction Data, Powder diffraction file 00–027-0631, 1972.

[56] International Center of Diffraction Data, powder diffraction file 04–026-7237, 2019.

[57] International Center of Diffraction Data, Powder diffraction file 00–029-1240, 1978.

[58] International Center of Diffraction Data, Powder diffraction file 04–012-5048, 2011.

[59] International Center of Diffraction Data, Powder diffraction file 00–049-1433, 2003.

[60] International Center of Diffraction Data, Powder diffraction file 04–002-8228, 2005.

# Publication IV

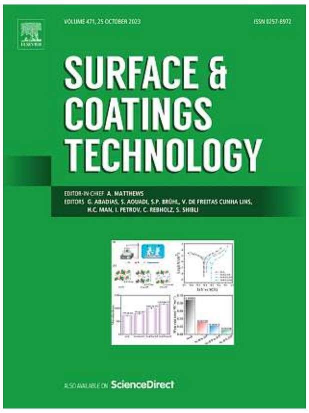

VOLUME 471, 25 OCTOBER 2023
ISSN 0257-8972

SURFACE & COATINGS TECHNOLOGY

EDITOR-IN-CHIEF A. MATTHEWS
EDITORS G. ABADIAS, S. AOUADI, S.P. BRÜHL, V. DE FREITAS CUNHA LINS, H.C. MAN, I. PETROV, C. REBHOLZ, S. SHIBLI

ALSO AVAILABLE ON ScienceDirect

## *High-temperature hot corrosion kinetics of arc evaporated Ti$_{1-x}$Al$_x$N on Ni-Cr-Co-based superalloys*

**O.E. Hudak**, A. Scheiber, P. Kutrowatz, T. Wojcik, R. Hahn, J. Ramm, O. Hunold, S. Kolozsvári, P. Polcik, and H. Riedl.

submitted at *Surface & Coatings Technology* since 31.10.2023

# High-temperature hot corrosion kinetics of PVD $Ti_{1-x}Al_xN$ on Ni-Cr-Co-based superalloys

O.E. Hudak,[1,*] A. Scheiber,[1] P. Kutrowatz,[1] T. Wojcik,[1] R. Hahn,[1]
O. Hunold,[2] J. Ramm,[2] S. Kolozsvári,[3] P. Polcik,[3] and H. Riedl[1,4]
[1] *Christian Doppler Laboratory for Surface Engineering of high-performance Components, Austria*
[2] *Oerlikon Balzers, Oerlikon Surface Solutions AG, Liechtenstein*
[3] *Plansee Composite Materials GmbH, Germany*
[4] *Institute of Materials Science and Technology, Austria*

(Dated: November 2, 2023)

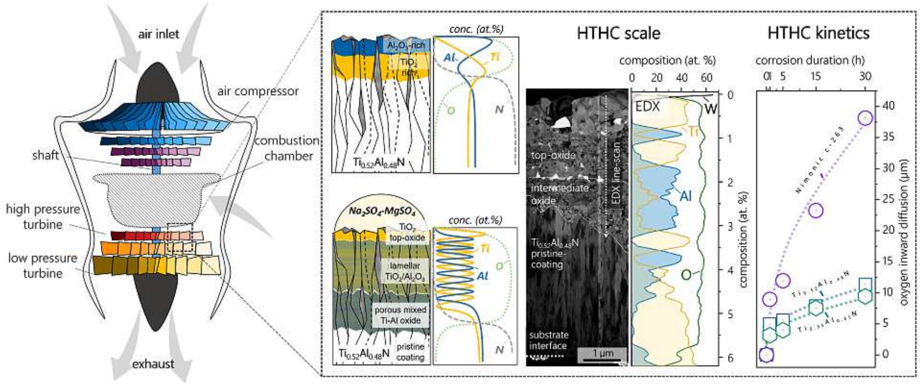

Throughout this study, the HTHC behavior of bare c-263 NiCrCo alloy and $Ti_{1-x}Al_xN$-coated specimens was studied with- and without an 80 mol% $Na_2SO_4/MgSO_4$ salt deposit at 850 °C in a $SO_x$-rich atmosphere. While the bare c-263 NiCrCo alloy and cathodic arc evaporated $Ti_{1-x}Al_xN$-coated specimens showed similar corrosion rates for the salt-free experiments, a significant acceleration in the corrosion progression was exhibited when salt deposits were added. By directly comparing the NiCrCo alloy and the $Ti_{1-x}Al_xN$ coated counterparts, a significantly lower corrosion rate was featured by the cae-$Ti_{1-x}Al_xN$ samples. The improved corrosion resistance by the $Ti_{1-x}Al_xN$ coatings is attributed to the lack of internal sulfidation, a key step of the HTHC mechanism found in most high-temperature alloys. Because there is little metallic substance in $Ti_{1-x}Al_xN$ for the corrosive media to attack after breaching the protective oxide, the rate-determining step of the HTHC mechanism appears to be the nitride-to-oxide transformation, followed by the basic fluxing of the newly formed oxide.

Keywords: Hot corrosion; Thin films; Oxidation kinetics; Fluxing; HTHC; PVD; TiAlN

## I. INTRODUCTION

In an attempt to improve the efficiency and robustness of gas turbines, engineers are constantly developing new strategies for increasing the in-service jet temperature and resorting to materials featuring excellent mechanical properties at high temperatures [1][2]. For these purposes, high-temperature nickel-based superalloys have become an indispensable choice in gas turbine construction [3–6]. Unfortunately, many of these high-temperature alloys are prone to accelerated salt-induced corrosion called "hot corrosion (HC)" [7–12], for which protective physical vapor deposited (PVD) coatings provide an attractive solution. Many coating systems have demonstrated beneficial corrosion resistance in high temperature settings, such as metallic gradient coatings [13], NiCrAlY [14–16], ceramic coatings [17–24], and enamel [25, 26], but remain far from being optimal.

With a focus on industrially established Ni- and Co-based superalloys that readily find application in high-temperature settings, the objective of this study is to investigate the hot-corrosion behavior of a Nimonic c-263 alloy and to improve its corrosion behavior through the application of protective PVD $Ti_{1-x}Al_xN$ coatings. Furthermore, we aim to provide a fundamental understanding of the respective HC rates and mechanisms. Throughout the following sections, the authors would like to provide a condensed background around hot corrosion, high-temperature hot corrosion, and the underlying chemical reaction mechanisms that are relevant to this study.

---

[*] oliver.hudakr@tuwien.ac.at

### A. Hot corrosion (HC)

Within a temperature range of 575-950 °C, formations of salt deposits give rise to accelerated degradation of machining components, particularly transition lines from the combustion chamber, as well as blades and vanes of the high-pressure turbine (HPT) and low-pressure turbine (LPT). When sulfur from the kerosene (<0.3 m.%) is combusted, it oxidizes entirely and forms a mixture of $SO_2$ and $SO_3$ ($SO_x$), as shown by Eq.1-2 [27].

$$S + O_2 \rightarrow SO_2 \tag{1}$$

$$SO_2 + \frac{1}{2}O_2 \leftrightarrow SO_3 \tag{2}$$

When operating in marine environments, salt-rich aerosols can enter the turbine sections through the air intake (e.g., $Na^+$, $K^+$, $Mg^{2+}$, $Ca^{2+}$), where they react with the $SO_x$-rich exhaust gases and form high-melting sulfate-salt deposits (Eq.3-4) [28, 29].

$$2NaCl + S + 2O_2 \rightarrow Na_2SO_4 + Cl_2 \quad (T_m = 884°C) \tag{3}$$

$$MgCl_2 + S + 2O_2 \rightarrow MgSO_4 + Cl_2 \quad (T_m = 1124°) \tag{4}$$

Depending on the physical aggregate of the salt deposit, one of two corrosion mechanisms can ensue: High-temperature hot corrosion (HTHC, Type 1), where the salt deposit exits in a molten state, or low-temperature hot corrosion (LTHC, Type 2), where the salt adheres in a solid form.

This significantly complicates the study of hot corrosion phenomena in industrial settings, as both temperature and mole-fractions of multi-component salt deposits substantially influence the predominant corrosion mechanism. For instance, while $Na_2SO_4$- and $MgSO_4$ deposits have melting points of 884 °C and 1124 °C, respectively, their binary system features a eutectic temperature of merely 665 °C [29]. Thus, machining elements that operate at 850 °C and are exposed to either $Na_2SO_4$ or $MgSO_4$ individually would likely experience a LTHC attack, while surfaces exposed to the eutectic mixture of $Na_2SO_4/MgSO_4$ experience HTHC. In order to set the stage for investigating HTHC phenomena, strict measures were set throughout this study to ensure the proper corrosion environment. That is, isothermal annealing experiments were conducted at 850 °C with an 80 mol% $Na_2SO_4/MgSO_4$ salt mixture ($T_m$= ~800 °C) to ensure the liquefaction of the salt deposit.

### B. High-temperature hot corrosion (HTHC)

HTHC of metals and alloys may involve various degenerative processes: A sulfidation-oxidation mechanism [7, 30–33] acidic or basic dissolution of the protective oxide scale (fluxing) [33–37] or a synergistic co-dissolution mechanism, referred to as synergistic fluxing. Whether or not conditions for sulfidation or fluxing are met depends on the material's chemical makeup, temperature profile, chemical composition of the atmosphere, and, as a result, on the melt basicity of the salt deposit.

For many metals, sulfur behaves much more aggressively than oxygen. Many metals such as iron (Fe), Nickel (Ni), Cobalt (Co), and Chromium (Cr) react readily with sulfur, achieving reaction rates that are several magnitudes higher compared to oxygen under the same conditions [35]. Reasons for the higher reaction rates for metal-sulfides include: (i) metal-sulfide formations that are accompanied by larger concentrations of lattice defects than their related metal-oxide variants. Consequently, diffusion rates in sulfides are significantly higher, allowing further sulfidation and/or oxygen to ensue; (ii) many metal-sulfides feature low melting points. This is especially true for alloying elements used in Ni-based superalloys, such as Co, and Fe, whose sulfides ($Ni_3S_2$, $Co_4S_3$ and FeS) have melting temperatures of 635 °C, 880 °C and 985 °C, respectively. Ni-sulfides also tend to form low-melting eutectics, which further lower the liquidus line. Lastly, (iii) metal-sulfides exhibit much greater dissociation pressures than their metal-oxide counterparts. As a result, high sulfur partial pressures develop at the scale-metal interface, leading to accelerated intergranular corrosion [38].

Fluxing, on the other hand, describes the reaction between protective oxide scales and components of the salt deposit, by which the product barrier becomes non-protective and produces species that are soluble within the salt. When considering a melt of pure $Na_2SO_4$, it partially dissociates into its basic ($Na_2O$) and acidic ($SO_3$) components (Eq.5). Depending on which species reacts with the protective oxide scale of a material, it is referred to as a basic or acidic fluxing mechanism.

$$Na_2SO_{4(l)} \leftrightarrow Na_2O_{(diss)} + SO_{3(g)} \tag{5}$$

### C. Salt-induced basic fluxing & alloy induced acidic fluxing

For many Ni-based superalloys, an alloy-induced acidic fluxing mechanism represents the most dominant form of HTHC, where acidic transient oxides of elements, such as W, Mo, and V (solid solution hardeners in Ni-based superalloys) form and acidify the melt [33]. For instance, $MoO_3$ reacts with $Na_2O$ from the $Na_2SO_4$ melt and forms a complex metal oxide ($Na_2MoO_4$). By doing so, the local activity of $Na_2O$ (basicity of the melt) is lowered, allowing for the acidic fluxing of $Al_2O_3$ by expendable $MoO_3$ (Eq.6-7). Soluble within the $Na_2SO_4$ melt, the metal oxyanions ($MoO_4{}^{2-}$) and $Al^{3+}$ cations diffuse towards the melt surface, where $MoO_3$ evaporates (900 °C) and $Al_2O_3$ precipitates as a porous non-protective oxide due to the higher $O^{2-}$ activity. Through the evaporation of $MoO_3$ and thus the transport of $O^{2-}$-species to the salt-gas interface, a negative concentration gradient for the $Al_2O_3$ is ensured and provides a self-sustaining character [12].

$$Al_2O_3 + 3MoO_3 \leftrightarrow Al_2(MoO_4)_3 \quad (6)$$

$$Al_2(MoO_4)_3 \leftrightarrow 2Al^{3+} + 3MoO_4^{2-} \quad (7)$$

On the contrary, HTHC may also elicit basic fluxing of the protective oxides, which applies to alloys with low concentrations of transient oxide formers. In the event of basic dissolution of protective oxide scales, $Na_2O$ ($O^{2-}$) in the liquid salt film reacts with the metal-oxide and forms soluble anionic species. Basic fluxing predominates typically at higher temperatures ( 900 °C), where the production of $O^{2-}$-ions through decomposition of the salt melt is sufficiently high, and the acidic component of the atmosphere (e.g., $SO_3$) is negligible. Unlike acidic fluxing, basic fluxing is considered non-self-sustaining and ultimately depends on the amount of salt deposit available for the reactions. If, however, sufficient salt deposit is present, and therefore a sufficiently high reservoir of $O^{2-}$, a long-term investigation of such a basic fluxing mechanism is possible. While an alloy-induced fluxing mechanism can be disregarded with confidence, since no refractory metals are present in $Ti_{1-x}Al_xN$, the latter shall be investigated more closely.

## II. EXPERIMENTAL

### A. Coating depositions

All coatings were deposited using an industrial-scale cathodic arc-evaporation system (Oerlikon Innova 1.0, Oerlikon Surface Solutions AG). $Ti_{1-x}Al_xN$ coatings with varied Al contents ($Ti_{0.52}Al_{0.48}N$ and $Ti_{0.34}Al_{0.66}N$) were deposited using TiAl (50/50 at.%) and TiAl(35/65 at.%) targets, respectively (Plansee Composite Materials GmbH).

Single-crystalline Si stripes (100-oriented, 20x7x0.38 mm) and Nimonic c-263 (VDM-Metals, Germany) were used as substrate materials (detailed chemical composition, see Table I). Whereas coated Si-substrates were solely used for coating-characterization purposes (e.g., analysis of the coating morphologies via fracture cross-sections, coating thickness measurements, and crystal-phase determination by X-ray diffraction), the coated c-263 alloys were exclusively used for hot gas corrosion experiments and post-corrosion analysis. Prior to the depositions, the substrates were ultrasonically cleaned with acetone and ethanol before mounting them onto the carousel of the deposition chamber. At a base pressure of <$5.0^{-3}$ Pa, the substrates were further cleaned for 25 min by a central-beam argon plasma etching procedure (Oerlikon Surface Solutions AG).Arc-evaporated coatings with thicknesses of 10 $\mu$m were deposited at a temperature of 450 °C in a pure $N_2$ atmosphere (total deposition pressure 3.2 Pa), with a target current of 200 A and a DC bias of -40 V, respectively.

TABLE I. Nominal chemical composition (wt.%) of the Nimonic c-263 superalloy [39].

| alloy | Ni | Co | Cr | Mo | Ti | Al | Fe | Si |
|---|---|---|---|---|---|---|---|---|
| **c − 263** | 47-54 | 19-21 | 19-21 | 5.6-6.1 | 1.9-2.4 | 0.3-0.6 | 0-0.7 | 0-0.4 |

### B. Corrosion experiments

The hot gas corrosion testing rig was conceptualized in three sections: (i) the gas-mixing system (inlet), (ii) a reaction module, and (iii) a gas-treatment system (outlet). A combination of three gas-inlet feeds was controlled via mass-flow controllers to regulate the experiment's atmosphere. A total gas flow (total pressure, $\rho$) of 2500 sccm was chosen, comprised of 2118 sccm [Ar], 375 sccm [$O_2$], and 7 sccm [$SO_2$]. This translates to partial pressures of $\rho$[Ar]= $8.47{\cdot}10^{-1}$ atm, $\rho$[$O_2$]= $1.5{\cdot}10^{-1}$ atm, and $\rho$[$SO_2$]=$2.8{\cdot}10^{-3}$ atm, respectively. The mixed gases enter the reaction chamber inside a three-zone gradient oven (Carbolite Gero GmbH & Co. KG). A quartz-tube flow reactor safely accommodates the aggressive SOx-rich atmosphere in liaison with the high temperatures (850 °C) needed for the HC experiments. Lastly, the exhaust gases are washed in a NaOH bath before exiting the set-up. A detailed illustration of the HC-testing rig can be found in [40].

For every corrosion experiment, two sets of sample arrangements were considered: (i) a control arrangement, where no salt was added to the sample surfaces, and (ii) an experimental arrangement, where samples were prepped with salt coupons to mimic hot-corrosion conditions. A mixture of anhydrous $MgSO_4$ and $Na_2SO_4$ (Merck KGaA) with a molar ratio of 20:80 or mass ratio of 15.21:84.78, respectively, was chosen for all experiments. A saturated aqueous solution was then prepared. By using a pipette, small droplets were applied onto the sample surfaces and dried under ambient conditions for several days.

Regarding the calculated binary-phase diagram from Yazhenskikh et al., a solidus temperature of ~725 °C and a liquidus temperature of ∼810 °C were estimated for the prepared salt coupons, which was later confirmed in a series of annealing experiments [29]. Thus, by choosing 850 °C for the corrosion experiments, the salt deposits would melt and fulfill the prerequisite for HTHC.

After loading the quartz tube with the control arrangement and the salt-loaded samples, the chamber was sealed and purged for 10 min with 2000 sccm Ar. Subsequently, the furnace was turned on while continuing purging with Ar. With a ramp setting of 20 °C/min, 45 min were allocated for reaching the desired 850 °C, after which an additional 15 min were allotted for ensuring a homogeneous temperature distribution within the quartz tube. Following the heat-up sequence, the Ar, $O_2$, and $SO_2$ mass-flow controllers were opened, marking the beginning ($t_h$) of the corrosion experiment. After the desired duration of the experiment has elapsed (e.g., t=1, 5, 15, and 30 h), the furnace was turned off, the hand valves for the $O_2$ and $SO_2$ feeds closed, and the chamber purged with 2000 sccm Ar until the temperature within the quartz tube was <200 °C.

### C. Analytical methods

For studying the morphological properties, such as coating thickness, surface texture, and the integrity of the substrate-coating interfaces, a Zeiss Sigma 500 VP high-resolution field emission gun scanning electron microscope (FEGSEM) was used. Using an acceleration voltage of 3 to 6 kV, coating thickness and morphology were characterized on fracture cross sections of coated Si-substrates. Furthermore, the FEGSEM, combined with an EDAX Octane elect system for energy dispersive X-ray spectroscopy (EDX), was used for quantitative chemical investigations.

Bragg-Brentano X-ray diffraction (BBHD) was utilized for crystallographic analysis using a PANalytical XPert Pro MPD system equipped with a Cu-$K_\alpha$ radiation source (wavelength $\lambda$ =1.54 Å).

For post-corrosion characterization, top-view images were taken using a digital light microscope. The deposit was carefully removed for salt-loaded samples, and any remnant salt was washed off with distilled water to expose the oxidized coating surfaces. Subsequently, XRD measurements were conducted, after which the samples were embedded in a conductive polymer matrix, their cross-sections thoroughly ground, polished, and analyzed using a Zeiss Sigma 500 VP high-resolution FEGSEM. EDX line scans and EDX mapping were utilized for identifying diffusion pathways, phase transformations, and coating breakdown.

Lastly, transmission electron microscopy (TEM), FEI TECNAI F20, equipped with a field emission gun and operated at an accelerating voltage of 200 kV) was conducted. Bright-field (BF) imaging was utilized to learn more about the microstructure, diffusion processes, and the overall corrosion mechanism. To prepare the TEM lamella, a standardized focused-ion beam (FIB) lift-out technique was used (Scios 2 DualBeam system, ThermoFisher Scientific).

## III. RESULTS

### A. Structure and morphology

The as-deposited fracture cross-sections of both, low Al-content $Ti_{0.52}Al_{0.48}N$ and high Al-content $Ti_{0.34}Al_{0.66}N$ coatings are shown in Fig.1a and 1b, respectively. Both coating variants feature a homogeneous and dense columnar microstructure with thicknesses of 9.8 $\mu$m ($Ti_{0.52}Al_{0.48}N$) and 10.1 $\mu$m ($Ti_{0.34}Al_{0.66}N$). The chemical compositions of the $Ti_{0.52}Al_{0.48}N$ and $Ti_{0.34}Al_{0.66}N$ coatings, normalized to the metallic sublattice, were determined by EDX and deviate only slightly from their target compositions (50/50 and 35/65 at.%, respectively). Structural analysis by XRD indicates a dominant c-Ti(Al)N crystal structure (B1, NaCl-prototype) for both coating variants, with only slight indications of the thermodynamically favored h-Al(Ti)N phase (B4, wurzite-prototype) visible for the higher-Al containing $Ti_{0.34}Al_{0.66}N$ coating (Fig.1c).

Fig.2 presents top-view images of all samples subject to hot-corrosion experiments. All samples were exposed to the same corrosive atmosphere and annealed at 850 °C with a partial pressure of $\rho[SO_2]= 2.8{\cdot}10^{-3}$ atm (2800 ppm by volume). Shown on the top is the so-called control group (salt-free samples), comprised of the uncoated NiCrCo alloy, $Ti_{0.52}Al_{0.48}N$, and $Ti_{0.34}Al_{0.66}N$ coated samples, listed from top to bottom. A gradual change in the interference colors is observed that relates to evolving oxide scales.

On the bottom half of 2, the surfaces of the salt-loaded samples are shown in their as-deposited state (0 h) and after corrosion times of 1, 5, 15, and 30 h. The molten salt deposit prerequisite is clearly met and provides the foundation for high-temperature hot corrosion (HTHC). Significant uptake (consumption) of the salt deposit can be seen for the uncoated NiCrCo alloy, which is indicative of significant corrosion. During the first hour, the salt deposit melts and adheres to the alloy surface. A brown oxide scale develops at the bare alloy surface, identified as a mixed NiO-$Cr_2O_3$ oxide scale. As the duration of the corrosion experiment is prolonged, a gradual consumption of the salt deposit (5-15 h) is observed. After 30 h, the entire salt deposited has been consumed by the alloy, which is now covered with a porous corrosion scale.

Contrarily, the corrosion progression and uptake of the salt deposit for the $Ti_{1-x}Al_xN$ coated samples occur

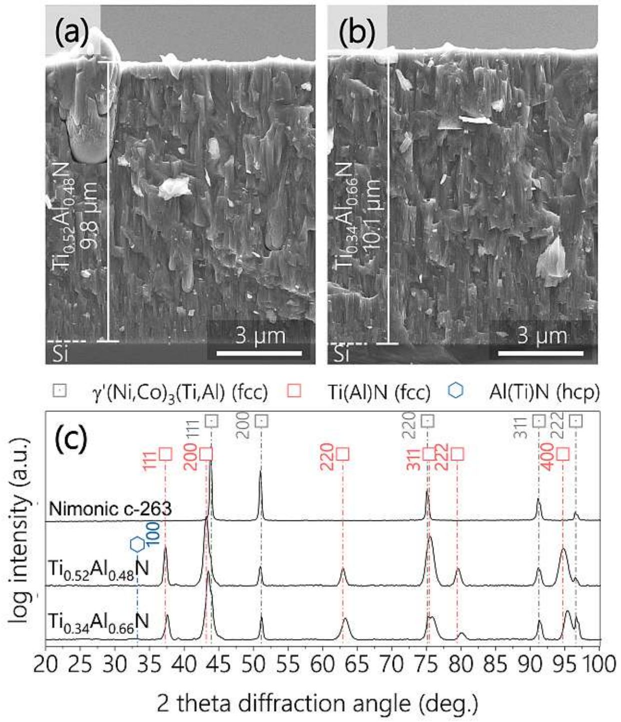

**Fig.** 1. Characterization of as-deposited $Ti_{1-x}Al_xN$ coatings: (a-b) show the fracture cross-sections of the $Ti_{0.52}Al_{0.48}N$ and $Ti_{0.34}Al_{0.66}N$ on Si, respectively, whereas (c) features XRD analysis of their crystal structure and NiCrCo substrate material. Reference patterns were taken from ref. [41–43].

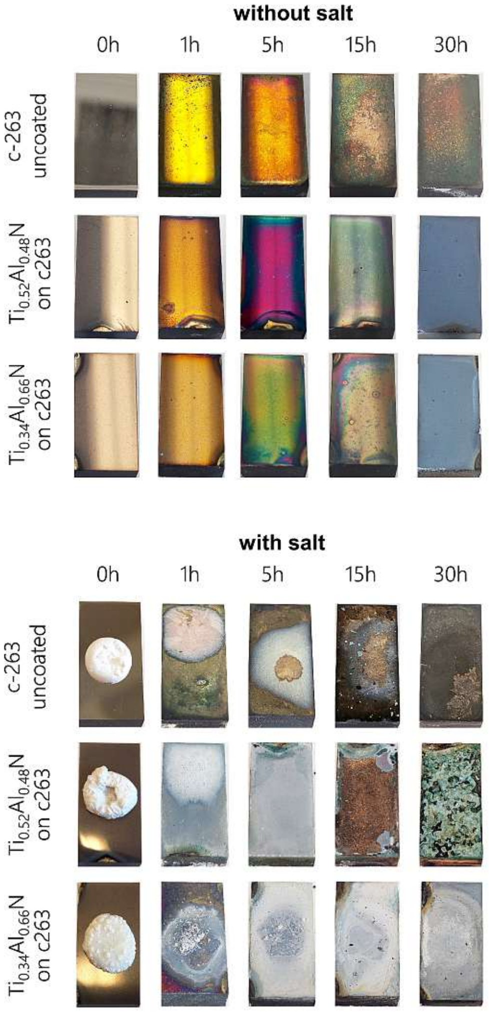

**Fig.** 2. Top-view images showing annealed samples at 850 °C in a $SO_x$-rich atmosphere without salt deposits for 0, 1, 5, 15, and 30 h (top group), as well as annealed samples with salt deposits under identical conditions (bottom group). The first row features uncoated Nimonic c-263 substrates, while the second and third rows show $Ti_{0.52}Al_{0.48}N$ and $Ti_{0.34}Al_{0.66}N$ coated c-263 substrates, respectively.

much more delayed. First, clear indications of salt uptake can be seen after 15 h for the $Ti_{0.52}Al_{0.48}N$ coated samples. Significant scaling and spalling of the surface oxides can be seen after a corrosion duration of 30 h. Especially, the $Ti_{0.34}Al_{0.66}N$ coated samples feature minor salt uptake throughout 30 h of the corrosion experiments. The authors believe that the substantial consumption of the salt observed for the $Ti_{0.52}Al_{0.48}N$ is a sign of a breakthrough of the coating structure, where the salt has breached the protective coating and can react with the NiCrCo-substrate underneath.

### B. Structural evolution of annealed $Ti_{1-x}Al_xN$ in $SO_x$-enriched atmosphere

To gain insights into the formation of corrosion products throughout the HTHC experiments, structural analysis by XRD was conducted. Fig.3a presents the structural evolution of the salt-free $Ti_{0.52}Al_{0.48}N$ and $Ti_{0.34}Al_{0.66}N$ coatings annealed at 850 °C in a 2800 ppm $SO_x$-rich atmosphere. In contrast, Fig.3b features the structural evolution for the salt-loaded samples, annealed under identical atmospheric conditions. For reference purposes, the diffractograms of the as-deposited coating states are included.

Starting with the salt-free $Ti_{0.52}Al_{0.48}N$ coating, immediate onset of fast-growing tetragonal-$TiO_2$ anatase and rutile oxides is observed after 1 h exposure time, which is accompanied by a phase transition from the c-Ti(Al)N to the thermodynamically favored h-Al(Ti)N (Fig.3a). Also apparent is the development of an Al-O-phase, which will crystalize into r-$Al_2O_3$ as the annealing duration is prolonged. More distinct reflexes are measured between 1 h and 30 h, suggesting further development of each aforementioned oxide. Notably, the contribution of rutile-$TiO_2$ and r-$Al_2O_3$ phases seem to gain dominance throughout the oxide scale, indicated by the relative intensities and the receding anatase-$TiO_2$. Similar to the salt-free $Ti_{0.52}Al_{0.48}N$, the higher Al-content salt-free $Ti_{0.34}Al_{0.66}N$ instantaneously forms a mixed-oxide scale within 1 h at 850 °C, evident from the rutile-$TiO_2$, anatase-$TiO_2$ and r-$Al_2O_3$ diffraction peaks.

For both compositions further annealing at 850 °C leads to thermally induced spinodal decomposition of the c-$Ti_{1-x}Al_xN$ solid solution, which is accompanied by the precipitation of coherent AlN particles. By reference to the preferential [200]-reflex at 43.27°, unmixing of the c-TiAlN solid solution into Ti-rich c-Ti(Al)N and metastable Al-rich c-Al(Ti)N domains occurs, which we interpret according to the peak-broadening of the initial (as-deposited) c-Ti(Al)N [200]-reflex. As the $Ti_{0.34}Al_{0.66}N$ chemistry falls closer to the solubility limit of c-Ti(Al)N, more pronounced w-AlN formation is prevalent throughout the annealing experiments. Despite literature reporting significantly higher temperatures (>1000 °C) as a precondition for w-AlN nucleation, the [100]-reflex positioned at 33.18° in Fig.3a provides a significant argument that nucleation and growth of w-AlN in supersaturated c-Ti(Al)N coatings may already form at much lower temperatures (850 °C). This, in fact, has also been observed by Rogström et al. in a series of in-situ high-energy X-ray diffraction (XRD) experiments while studying the strain and microstructure evolution during decomposition. This discrepancy may be due to the significantly longer annealing time.

The structural evoluation of the $Ti_{0.52}Al_{0.48}N$ and $Ti_{0.34}Al_{0.66}N$ coatings after 30 h of annealing at 850 °C in an $SO_2$-enriched atmosphere without salt deposits can be summarized as follows: Both coatings develop a fast-growing mixed $TiO_2/Al_2O_3$ oxide scale, where the $TiO_2$ phases consist of both, rutile and anatase. Judging from the relative peak intensities, the scale formation for the lower Al-content $Ti_{0.52}Al_{0.48}N$ coating seems to be $TiO_2$ dominated, whereas a more balanced contribution between $TiO_2$ and $Al_2O_3$ exists for the higher Al-containing $Ti_{0.34}Al_{0.66}N$ coating. Lastly, significant nucleation and growth of w-Al(Ti)N and spinodal decomposition of the c-Ti(Al)N solid solution are observed throughout the annealing experiments for the high Al-content $Ti_{0.34}Al_{0.66}N$ coating.

On the other hand, the structural evolution for salt-loaded $Ti_{1-x}Al_xN$ coatings is much more dynamic (see Fig.3b). After 1 h, a significantly pronounced scale formation can be seen. Distinct diffraction intensities of the r-$TiO_2$ and a-$TiO_2$ structure, as well as an onset of the r-$Al_2O_3$ structure, are featured by both coating variants. Again, the $Al_2O_3$ contribution is more dominant for the higher Al-containing $Ti_{0.34}Al_{0.66}N$ coating. Moreover, the thermally unstable tialite structure (o-$TiAl_2O_5$) develops throughout the first 5 h of the salt-loaded experiments as one of the dominant structural constituents of the developing oxide scale. As the annealing duration is prolonged, the initially fast-growing tialite phase decompose into its parent oxides, alumina and rutile.

### C. Oxidation and corrosion kinetics in $SO_2$-rich atmosphere

Since HTHC most often occurs in the presence of a $SO_x$-enriched atmosphere, all annealing and corrosion experiments were performed at a partial pressure of $\rho[SO_2]= 2.8\cdot10^{-3}$ atm (2800 ppm by volume). In order to describe the oxidation behavior for such an environment, annealing experiments were first conducted without any salt deposits to determine the oxygen diffusion kinetics experimentally. Over periods of 1, 5, 15, and 30 h, $Ti_{1-x}Al_xN$ coated, as well as uncoated NiCoCr samples were annealed at temperatures of 700, 775, and 850 °C – temperatures, where HTHC begins to play a factor. Depth profiles for the oxygen inward diffusion were obtained by conducting EDX line scans along the cross-section of each annealed sample and are shown in Fig.4(a-i).

Material-specific diffusion rate laws were determined by plotting the diffusion depth over time. A quasi-cubic rate function (n=~3) was found to best fit the oxygen inward diffusion for the NiCrCo c-263 alloy, the $Ti_{0.52}Al_{0.48}N$ and $Ti_{0.34}Al_{0.66}N$ coated samples at each annealing temperature (Fig.4j, k and l, respectively). In Eq.8, the generic rate law is described, where x refers to the distance, dox to the rate constant, t corresponds to the time, and n is a constant.

$$x_{ox}^{n} = d_{ox} \cdot t \tag{8}$$

The rate law allows for determining temperature-dependent rate constants ($d_{ox}$), which can be plotted in an Arrhenius plot (Eq.9) to further describe the oxygen diffusion kinetics. By plotting the ln function of the Arrhenius plot, the pre-exponential factors ($d_{0,ox}$) could be determined from the intersection of the linear fit with the ordinate, and the activation energies ($q_{ox}$) were derived from the slope.

$$d_{ox} = d_{0,ox} \cdot e^{\frac{q_{ox}}{RT}} \tag{9}$$

$$ln(d_{ox}) = -\frac{q_{ox}}{R} \cdot \frac{1}{T} + ln(d_{0,ox}) \tag{10}$$

where $d_{ox}$ denotes the mean diffusion rate, $d_{0,ox}$ the pre-exponential factor, $q_{ox}$ the activation energy, R the gas constant, and T the temperature.

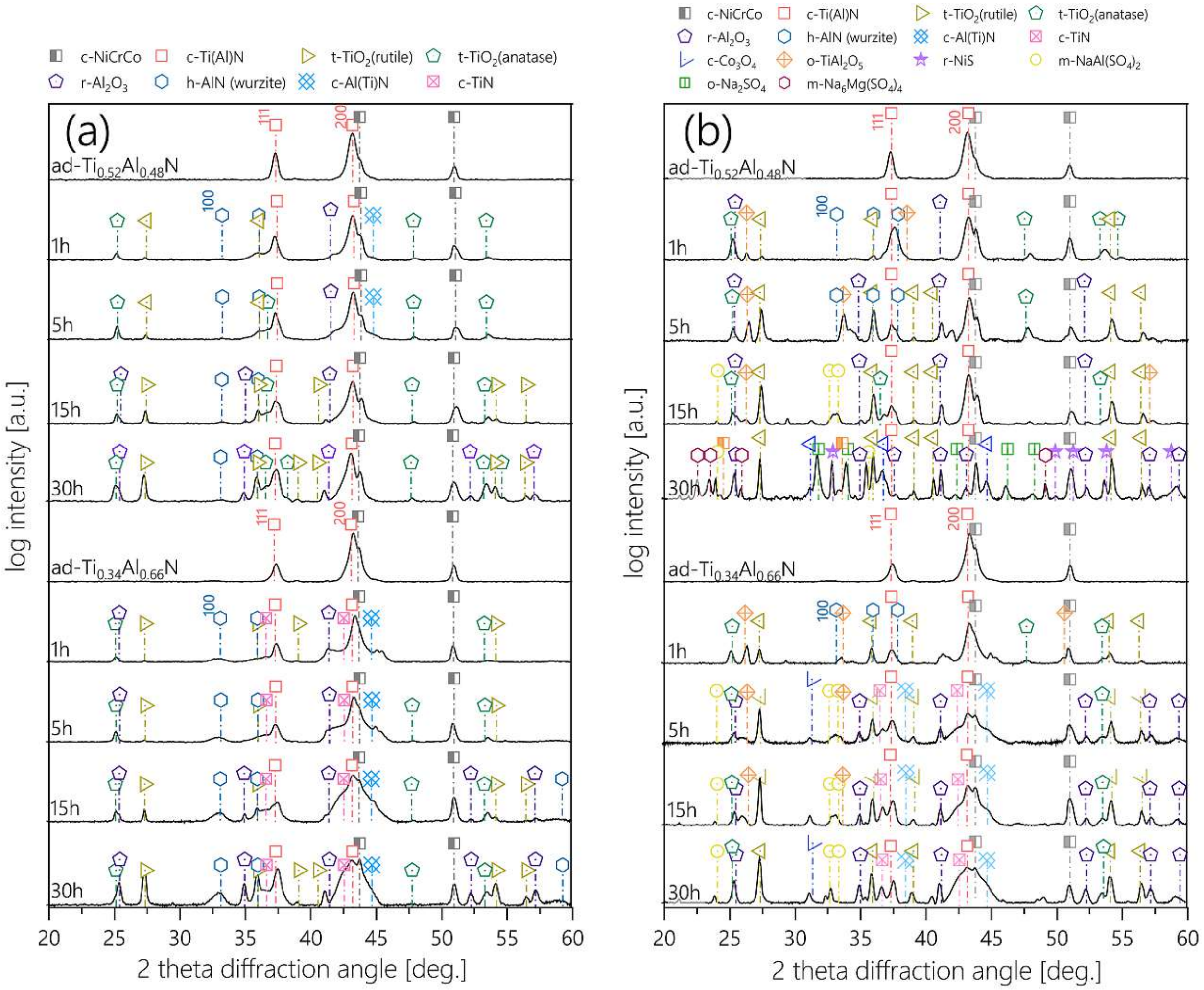

**Fig.** 3. Crystal structure analysis of $Ti_{0.52}Al_{0.48}N$ and $Ti_{0.34}Al_{0.66}N$ coatings annealed in an $SO_x$-rich atmosphere at 850 °C (a) without salt deposits and (b) with salt deposits [41–54].

The derived activation energies for oxygen follow the order of $Q_{(c\text{-}263)} < Q_{(Ti_{0.36}Al_{0.66}N)} < Q_{(Ti_{0.52}Al_{0.48}N)}$ (Table II) and fall significantly lower to literature values that have been calculated from annealing experiments conducted in air. Particularly, the uncoated c-263 alloy shows a drastic reduction in the $Q_a$-value when $SO_2$ is present in the atmosphere ($Q_a$=51 kJ/mol) compared to pure air exposure (∼110 kJ/mol) [55]. This may be due to two key reasons: (i) a not sufficiently evolved native oxide scale prior to the annealing experiments, where the alloy was in a polished state. Higher diffusion rates are thus observed during the first hour of the annealing experiments, where a passive scale is still developing. (ii) $SO_2$ acts as a reducing agent. It is well understood that $SO_2$ may further oxidize to $SO_3$ in an oxidizing atmosphere such as air (homogeneous conversion), which is thermodynamically favored at lower temperatures [56, 57]. Moreover, fly ash or metal oxide surfaces of machining components can lead to catalytic effects that accelerate the conversion of $SO_2$ to $SO_3$ (heterogeneous conversion) [57–59]. We associate this latter case with the drop in activation energies derived throughout the annealing experiments of this study. Thus, elevated $SO_2$ concentrations can considerably restrict the ability to thermally grow a passive oxide scale to function as an oxygen diffusion barrier, whether this entails the formation of a $Cr_2O_3$/NiO dominated scale (c-263 alloy) or a mixed $TiO_2$/$Al_2O_3$ scale ($Ti_{1\text{-}x}Al_xN$ coatings).

Lastly, the oxidation rate law constants (n) were determined for the salt-loaded HTHC sample group at 850 °C. Unlike the derivations of the activation energies calculated across a temperature range (700-850 °C), the oxygen rate constants for the salt-loaded corrosion experiments were solely conducted at 850 °C. The reason for this is the prerequisite for a molten salt film, which would not be

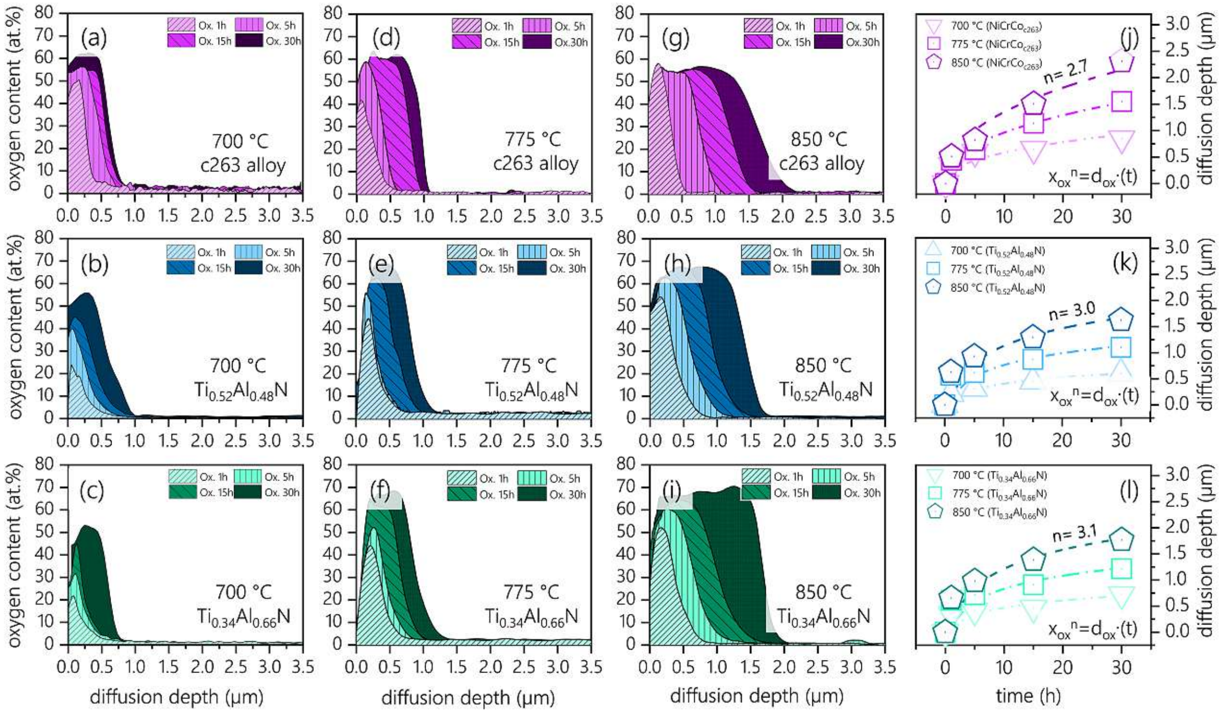

**Fig.** 4. (a-i) show oxygen diffusion profiles of bare c-263 alloy, $Ti_{0.52}Al_{0.48}N$ and $Ti_{0.36}Al_{0.66}N$ coated samples that have been annealed at 700, 775, and 850 °C in a $SO_x$-rich atmosphere for 1, 5, 15 and 30 h without salt deposits. (j-k) features the graphical representation of the oxygen diffusion profiles, intended to manifest the diffusion rate law and related rate constants ($d_{ox}$), which best pertain to each sample

met at lower temperatures. Presented in Fig.5 are the diffusion depth-time plots for the salt-loaded and salt-free samples that were annealed at 850 °C. While the samples without salt deposits exhibit fairly similar oxidation kinetics– as previously described by their activation energies and quasi-cubic diffusion rate laws– the oxidation rates drastically change when salt is introduced.

Firstly, the oxidation rate law of the c-263 alloy changes from a quasi-cubic rate law (n= 2.7) when exposed to a $SO_x$-rich atmosphere towards a compounded parabolic-linear rate law (n= 1.5) when salt deposits are added. For the latter case, a parabolic oxidation behavior governs the first few hours of the corrosion experiments (0-15 h), after which a linear oxidation rate takes over. Such linear rates are characteristic of HTHC of high-temperature alloys and essentially motivate the application of protective coatings [60–62].

In contrast to the uncoated c-263 alloy, the oxidation rate laws for both, $Ti_{0.52}Al_{0.48}N$ and $Ti_{0.34}Al_{0.66}N$ coated samples change from a cubic-diffusion rate (n= 3.0 and 3.1, respectively) to a near-parabolic rate behavior with n= 2.3 and n= 2.2, respectively (see Fig.5).

### D. HTHC mechanism for $Ti_{1-x}Al_xN$ coatings

Over the last few decades, a general understanding has evolved around the behavior and stability of various metals and their oxides when exposed to sulfate salts at high temperatures. Particularly, $Na_2SO_4$ has stood at the forefront of many high-temperature corrosion studies due to its relatively high thermal stability, ability to form low melting mixtures with other salts, and its presence and relevance in many high-temperature applications. However, little knowledge exists about the stability and behavior of metal nitrides in conjunction with $Na_2SO_4$ deposits at high temperatures. For this reason, this section intends to provide a time-resolved description of the stability of $Ti_{1-x}Al_xN$ when brought in contact with a $Na_2SO_4$-based (80 mol% $Na_2SO_4$-$MgSO_4$) at 850 °C.

The corrosion of metals and alloys by hot corrosion proceeds in several key steps: An incubation stage, an initiation stage, and a propagation stage, followed by failure [63].

i. Incubation: In absence of any salt deposit, the incubation stage features the formation of stable oxide scales (e.g., $Al_2O_3$ and $Cr_2O_3$), whereby a stable state (passivity) against further oxidation is provided.

TABLE II. List of logarithmic rate constants ($d_{ox}$) for the oxygen inward diffusion of $Ti_{0.52}Al_{0.48}N$, $Ti_{0.34}Al_{0.66}N$ and the parabolic-like rate constants ($d_{ox}$,n= 2.38) for the uncoated c-263 at 700, 775, and 850 °C. Moreover, pre-exponential factors ($d_{0,ox}$) and activation energies ($Q_{ox}$) are provided, which have been derived with respect to the diffusion coefficients.

| T (°C) | $Ti_{0.52}Al_{0.48}N$ | | | $Ti_{0.34}Al_{0.66}N$ | | | c-263 alloy | | |
|---|---|---|---|---|---|---|---|---|---|
| | $d_{ox}$ $cm^n/h$ | $d_{0,ox}$ $cm^n/h$ | $Q_{ox}$ kJ/mol | $d_{ox}$ $cm^n/h$ | $d_{0,ox}$ $cm^n/h$ | $Q_{ox}$ kJ/mol | $d_{ox}$ $cm^n/h$ | $d_{0,ox}$ $cm^n/h$ | $Q_{ox}$ kJ/mol |
| 700 | $1.89 \cdot 10^{-5} \pm 3.90 \cdot 10^{-7}$ | | | $2.25 \cdot 10^{-5} \pm 1.57 \cdot 10^{-6}$ | | | $2.57 \cdot 10^{-5} \pm 2.07 \cdot 10^{-6}$ | | |
| 775 | $3.56 \cdot 10^{-5} \pm 1.98 \cdot 10^{-7}$ | $4.32 \cdot 10^{-2}$ | 62.3 | $4.00 \cdot 10^{-5} \pm 1.17 \cdot 10^{-6}$ | $2.97 \cdot 10^{-2}$ | 57.9 | $4.21 \cdot 10^{-5} \pm 2.04 \cdot 10^{-6}$ | $1.41 \cdot 10^{-2}$ | 51.1 |
| 850 | $5.27 \cdot 10^{-5} \pm 4.98 \cdot 10^{-7}$ | | | $5.84 \cdot 10^{-5} \pm 3.68 \cdot 10^{-7}$ | | | $5.94 \cdot 10^{-5} \pm 5.25 \cdot 10^{-6}$ | | |

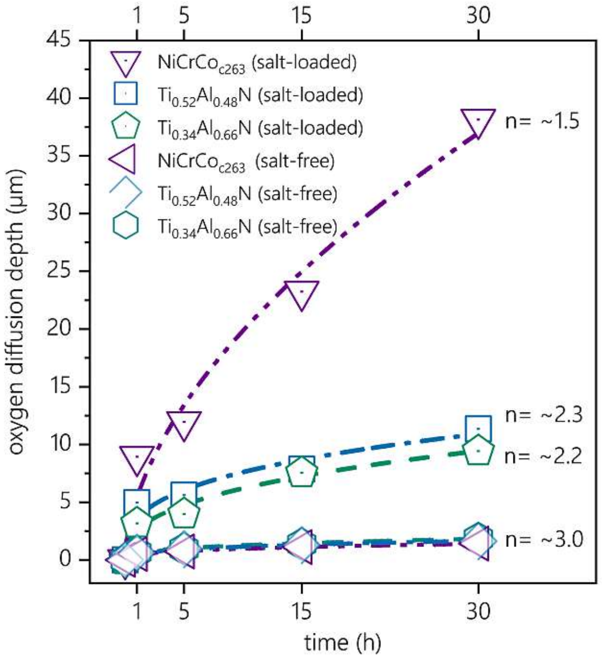

**Fig.** 5. Oxygen kinetics of uncoated c-263 alloy and $Ti_{1-x}Al_xN$ coated samples, showing the diffusion depth-time plot used for determining the corrosion rates of salt-loaded and salt-free samples.

ii. Initiation: The initiation stage comprises a sequence of changes in the material's environment that establishes accelerated oxidation/degradation conditions. This comprises the deposition of a salt film, the melting of the salt deposit (HTHC), the formation of low-melting eutectics between the salt deposit and metal oxide surface (LTHC), changes in the melt-basicity, and local depassivation of the oxide scale that allows for accelerated attack of the underlying alloy/metal.

iii. Propagation: Propagation describes the accelerated depassivation of the protective metal oxide scale and internal sulfidation and oxidation of the unprotected bulk material.

iv. Failure: Lastly, after a given duration, the corrosion front has infiltrated the material to such an extent that the integrity of the component fails.

In relation to these well-known sequences, the HTHC behavior of the ceramic $Ti_{1-x}Al_xN$ coatings is discussed in the following.

### *1. Incubation stage*

The mechanism begins with the incubation stage, which generally comprises the formation of a passive oxide scale, followed by the deposition of salts onto that protective oxide. Particularly for a nitride-based coating, such as $Ti_{1-x}Al_xN$, the growth of a passivating oxide scale is significant for ensuring their longevity in high-temperature environments. This entails a nitride-to-oxide transformation, which, as discussed in section 3.2, produces a mixed $Al_2O_3/TiO_2$ scale under atmospheric conditions (salt-free). Fig. 6a and 6b show the diffusion profiles of Ti, Al, and O in $Ti_{0.52}Al_{0.48}N$ and $Ti_{0.34}Al_{0.66}N$ coatings after isothermal annealing in an $SO_2$-rich atmosphere at 850 °C for a duration of 1, 5, 15, and 30 h. While after 1 h, a mixed oxide appears to develop at the coating surface, a gradual separation of Al and Ti is exhibited for longer annealing times. After 30 h, both $Ti_{1-x}Al_xN$ scales follow a layered arrangement, generating an Al-rich layer near the surface and a Ti-rich layer below. This scaling behavior stands in good agreement with works from Panjan et al. [64] and Greczynski et al. [65], who have reported similar results throughout various annealing experiments conducted in air (no additional $SO_2$).

However, as these coatings were exposed to salt deposits while being in their native (unoxidized) state, the incubation stage solely involves the preparation of the salt deposits on the $Ti_{1-x}Al_xN$ coatings.

### 2. *Initiation stage*

The initiation stage entails a sequence of changes in the overall environment, establishing accelerated oxidation/degradation conditions. This is the most crucial step in the HTHC mechanism, as it determines the longevity of the protective coating. For HTHC, such changes include the salt deposit's solid-to-liquid transformation, the salt-basicity's equilibration according to the existing temperature and present atmospheric partial pressures, and finally, the formation of a protective oxide.

As the salt deposit liquefies at some fixed temperature, its composition and, ultimately, its character is described by the oxygen partial pressure and the activity of $Na_2O$ ($\alpha Na_2O$), or the partial pressure of $\rho(SO_3)$, as it is directly associated with Na2O by the equilibrium constant in Eq.11.

$$Na_2SO_4 \leftrightarrow \rho SO_3 + \alpha Na_2O \qquad (11)$$

As the thermodynamic equilibrium between $SO_2$ and $SO_3$ shifts towards $SO_2$ with increasing temperature, the equilibrium between $Na_2O$ and $SO_3$ shifts towards $Na_2O$, increasing the $Na_2O$ activity and providing a more basic character to the salt deposit. Together with a low $\rho(SO_2)$ and high $\rho(O_2)$ in the atmosphere, it is safe to say that the $Ti_{0.52}Al_{0.48}N$-coated samples are exposed to a $Na_2SO_4$ deposit with a highly basic character.

Regarding the formation of the protective top-oxide, a similar scaling behavior is observed as for salt-free samples, featuring an Al-rich top layer and a Ti-rich sublayer (Fig.6c and 6d). By revisiting the sequence of the corrosion experiments presented in the experimental section, it was stated that $O_2$ and $SO_2$ were added to the atmosphere after the desired temperature of 850 °C and liquefaction of the salt deposit was achieved. Since the solubility of molecular $O_2$ and $SO_2$ exhibit poor solubility and slow transport in $Na_2SO_4$ slags, the observed oxidation of the coating must originate from an ionic $O^{2-}$ transport of the salt-deposit rather than from dissociation and absorption processes out of the gas-phase. This also explains why the oxidation rates (inward diffusion depth) for the salt-loaded samples are much faster (deeper) than for the atmospheric annealing experiments. Conducted under identical thermal and atmospheric conditions, the salt-induced oxidation of the $Ti_{1-x}Al_xN$ coatings solely relies on the ionic diffusion of $O^{2-}$- species from the salt-coating interface (high $\alpha Na_2O$ in basic melts) into the coating and does not rely on the kinetics of oxygen-adsorption, -dissociation and –absorption.

### 3. *Propagation stage*

Now that a top oxide has been established, the HTHC mechanisms transitions into its propagation stage. At this point, an oxygen gradient is established across the liquid film, as the coating has already consumed $O^{2-}$-ions from the salt film, while molecular oxygen from the atmosphere slowly dissolves according to Eq.12 and diffuses into the melt [36].

$$O_2 + 2O^{2-} \leftrightarrow 2O_2^{2-}(dissolution\ of\ oxygen) \qquad (12)$$

Therefore, a lower oxygen activity develops at the oxide-melt interface and increases towards the salt-gas interface. For very thin salt films, which can only accommodate a limited amount of $O^{2-}$ as the fluxing mechanisms progress, the activity of sulphur begins to rise at regions of low $O^{2-}$ concentrations, resulting in the sulfidation of unprotected material. In the case of the Ni-based superalloys and other high-temperature alloys with high contents of Cr and Ni, a common feature of HTHC is a precursive sulfide band, which forms at the corrosion front. Kinetically favored in their evolution, non-protective Cr- and Ni-sulfides develop first, after which a corrosive medium can penetrate the porous corrosion scale. Once the $O^{2-}$ activity recovers, the sulfides are oxidized to a porous oxide scale, after which the sulfur activity rises again and reacts with the new unprotected metal below.

This typical progression, however, was not observed throughout this study. As the coating's metal constituents (Ti and Al) are covalently bound to nitrogen, the formation of a metal sulfide band is impeded. Therefore, the propagation stage follows a strict basic fluxing mechanism of repetitive oxidation of the Ti(Al)N nitride matrix, followed by the basic dissolution of its developing oxides. The result is a porous, layered corrosion scale consisting of individual Al-rich and Ti-rich bands. Unlike the dual scale structure obtained when the $Ti_{1-x}Al_xN$ coatings were annealed without a salt deposit, a multitude of alternating Ti-rich and Al-rich bands develop. Illustrated in Fig.6c and 6d are EDX depth profiles of the corroded $Ti_{0.52}Al_{0.48}N$ and $Ti_{0.34}Al_{0.66}N$ coatings, respectively, highlighting the elemental distribution of Ti, Al, and O after 1, 5, 15 and 30 h. Moreover, a gradual switching of the topmost layer can be observed for both coatings. While both coating variants begin to oxidize by developing an Al-rich top-oxide with a Ti-rich oxide layer below, the contribution of the Al-rich layer successively diminishes, and a Ti-rich oxide begins to occupy the topmost layer. This can be attributed to the fact that $Al_2O_3$ is a highly acidic oxide ($Al_2O_3$ is more stable under acidic conditions), which is thus more prone to basic fluxing than the more basic $TiO_2$ oxide ($TiO_2$ is more stable under basic conditions).

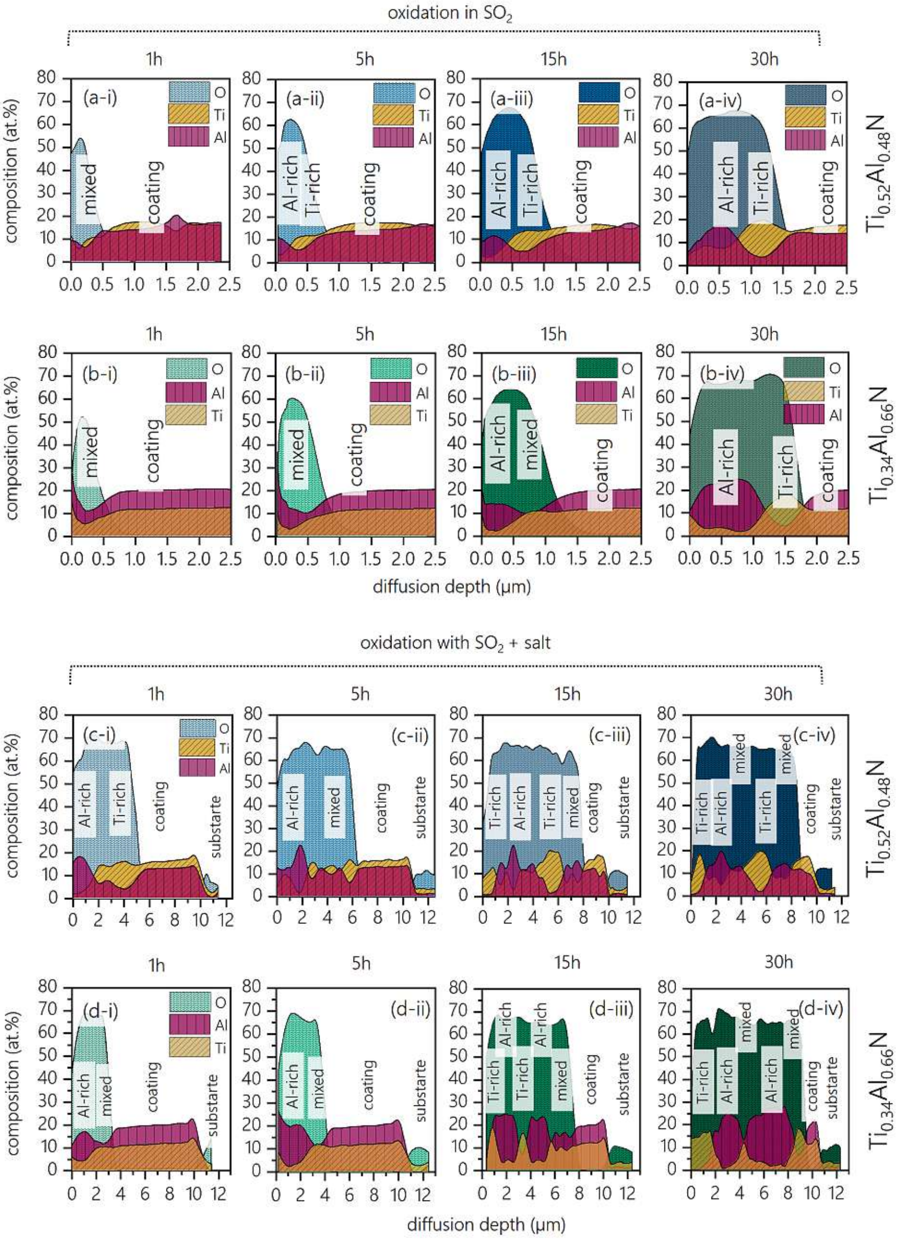

**Fig.** 6. EDX diffusion profiles highlighting the scale development of salt-free annealed $Ti_{0.52}Al_{0.48}N$ (ai-iv) and $Ti_{0.34}Al_{0.66}N$ coatings (bi-iv), as well as salt-loaded $Ti_{0.52}Al_{0.48}N$ (ci-iv) and $Ti_{0.34}Al_{0.66}N$ (di-iv) over the course of 30 h.

The development of a $TiO_2$-dominated top-oxide after longer durations of salt exposure (>15 h) is further substantiated by TEM analysis and presented in Fig. 7. A highly porous corrosion scale is observed for both, $Ti_{0.52}Al_{0.48}N$ and $Ti_{0.34}Al_{0.66}N$ coatings, and shown in the bright-field images Fig. 7a and 7c, respectively. Differences in the granularity of the corrosion scale are attributed to the inherently different grain sizes making up both coatings' morphologies. That is, an increased granularity of the corrosion scale is produced by the more coarse-grained $Ti_{0.52}Al_{0.48}N$ morphology, while a decreased granularity is obtained due to the more fine-grained $Ti_{0.34}Al_{0.66}N$ structure. Both coatings feature large $TiO_2$ grains that have formed at the scale-melt interface, shown in (7b) and (7d). Indexing of the respective spot patterns obtained from the SAEDs

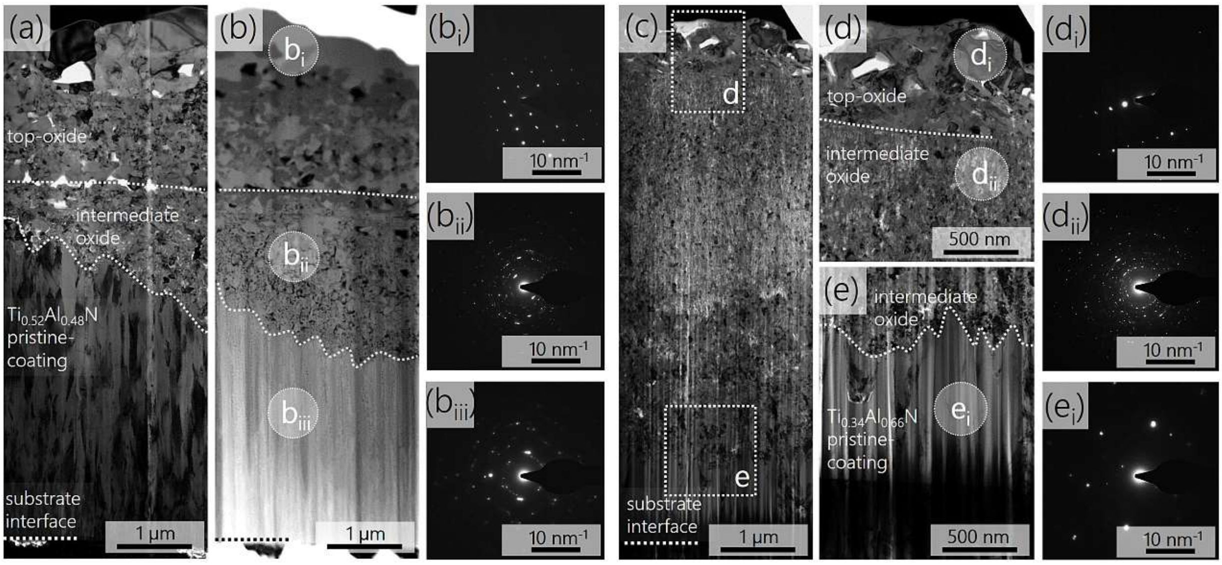

**Fig.** 7. TEM investigation featuring progressed hot corrosion of salt-loaded $Ti_{0.52}Al_{0.48}N$ (a-b) and $Ti_{0.34}Al_{0.66}N$ (c-e) after 15 h at 850 °C. (a) Features a bright field TEM cross-section of the entire $Ti_{0.52}Al_{0.48}N$ coating structure, while (b) shows its respective STEM with enhanced mass-contrast of present elements. Similarly, a bright field image of the $Ti_{0.34}Al_{0.66}N$ cross section is shown in (c), with enlarged highlights of the top-oxide and corrosion front shown in (d) and (e), respectively. For both $Ti_{0.52}Al_{0.48}N$ and $Ti_{0.34}Al_{0.66}N$, SAEDs were taken from the top-oxide scales (bi and di), underlying corroded coating morphology ($b_{ii}$ and $d_{ii}$), as well as remaining pristine coating near the coating substrate interface ($b_{iii}$ and $e_i$).

($b_i$) and ($d_i$) renders a tetragonal rutile crystal structure (P42/mnm, space group 136), which strands in good agreement with the previously discussed EDX results.

Further crystallographic information was gained by integrating the SAED ring-patterns and plotting them over the reciprocal of the lattice-spacings. The diffraction angles and correlating lattice parameters obtained by the SAED ($7b_{ii}$) and SAED ($7d_{ii}$) ring patterns the development of a mixed $\alpha$-$Al_2O_3$, anatase-$TiO_2$, w-Al(Ti)N and residual c-Ti(Al)N corrosion scale by $Ti_{1-x}Al_xN$ coatings, which coincides with the earlier presented XRD data describing the structural evolution during HTHC conditions.

Lastly, SAED ($7b_{iii}$) and ($7e_i$) reveal the presence of residual single-phased c-Ti(Al)N structure, which remained unaffected by the corrosive attack.

## IV. CONCLUSIONS

The present work deals with the HTHC behavior of $Ti_{1-x}Al_xN$ coated c-263 alloy when loaded with a $Na_2SO_4$/$MgSO_4$ salt mixture and isothermally annealed in an $SO_x$-rich atmosphere. In an attempt to first describe the oxidation kinetics of the $Ti_{1-x}Al_xN$ and bare c-263-substrate in said $SO_x$ atmosphere, a series of salt-free annealing experiments was conducted at 700, 775, and 850 °C. Next, EDX line-scan measurements were performed of both, uncoated and $Ti_{1-x}Al_xN$-coated samples, which rendered oxygen diffusion profiles that best fit a quasi-cubic rate-law (n=~3). Activation energies of 51, 62 and 58 kJ/mol, as well as pre-exponential factors of $1.41{\cdot}10^{-2}$, $4.32{\cdot}10^{-2}$, and $2.97{\cdot}10^{-2}$ $cm^n/h$ were derived for the bare c-263 alloy, $Ti_{0.52}Al_{0.48}N$ and $Ti_{0.34}Al_{0.66}N$ coated samples, respectively.

A significant increase in the oxidation kinetics was observed when salt deposits were added in a new series of experiments and annealed at 850 °C under identical $SO_x$-enriched atmospheric conditions. Compared to the quasi-cubic rate laws exhibited for the c-263 alloy and $Ti_{1-x}Al_xN$ coatings in the absence of a salt deposit, the c-263 alloy now followed a compounded parabolic-linear rate law (n= 1.5). At the same time, both $Ti_{0.52}Al_{0.48}N$ and $Ti_{0.34}Al_{0.66}N$ feature a parabolic-like rate behavior (n= 2.3 and n= 2.2, respectively). Thus, a significantly improved corrosion resistance is expressed by the cae-$Ti_{1-x}Al_xN$ samples over the bare c-263 alloy.

The HTHC mechanism of $Ti_{1-x}Al_xN$ can best be described by an initial oxidation step of the $Ti_{1-x}Al_xN$ matrix, followed by the basic fluxing of the aforementioned oxide scale. A sequential fluxing of Ti-rich and Al-rich was found to be the dominating corrosion mechanism, resulting in the formation of a layered and porous corrosion scale. Due to the more basic character of $TiO_2$ (more stable under basic conditions) over $Al_2O_3$, a porous $TiO_2$

scale predominantly develops at the scale-salt interface, followed by a voluminous Al-rich oxide band below. Depending on the available Al-reservoir of the $Ti_{1-x}Al_xN$, the more pronounced the Al-rich band becomes. No internal sulfidation was observed at the corrosion front of TiAlN-coated samples, which is regarded as one of the reasons for the improved corrosion resistance over the NiCrCo superalloy.

## ACKNOWLEDGMENTS

The financial support by the Austrian Federal Ministry for Digital and Economic Affairs, the National Foundation for Research, Technology and Development and the Christian Doppler Research Association is gratefully acknowledged (Christian Doppler Laboratory "Surface Engineering of high-performance Components"). We also thank for the financial support of Plansee SE, Plansee Composite Materials GmbH, and Oerlikon Balzers, Oerlikon Surface Solutions AG. In addition, we want to thank the X-ray center (XRC) of TU Wien for beam time as well as the electron microscopy center - USTEM TU Wien - for providing the SEM and TEM facilities. We also thank Dr. M. Weiss and Prof. A. Limbeck from the Institute of Chemical Technologies and Analytics, TU Wien, for their support with chemical analysis of our samples. The authors acknowledge TU Wien Bibliothek for financial support through its Open Access Funding Programme.

## DATA AVAILABILITY STATEMENT

The data that support the findings of this study are available from the corresponding author upon reasonable request.

## DECLARATION OF INTEREST STATEMENT

The authors declare that they have no known competing financial interests or personal relationships that could have appeared to influence the work reported in this paper.

## REFERENCES

[1] A. H. Epstein, AIAA Journal **52**, 901 (2014).
[2] A. Poullikkas, Renewable and Sustainable Energy Reviews **9**, 409 (2005).
[3] M. Young and H. H. Hanink, SAE Technical Papers (1943), 10.4271/430133.
[4] A. Czyrska-Filemonowicz, B. Dubiel, M. Ziętara, and A. Cetel, Inżynieria Materiałowa **3-4**, 1 (2007).
[5] P. Caron and T. Khan, Aerospace Science and Technology **3**, 513 (1999).
[6] R. Darolia, International Materials Reviews **64**, 355 (2019).
[7] F. Pettit, Oxidation of Metals **76**, 1 (2011).
[8] G. A. El-Awadi, S. Abdel-Samad, and E. S. Elshazly, Applied Surface Science **378**, 224 (2016).
[9] D. Mudgal, S. Singh, and S. Prakash, Journal of Materials Engineering and Performance **23**, 238 (2014).
[10] S. Kamal, K. V. Sharma, and A. M. Abdul-Rani, Journal of Minerals and Materials Characterization and Engineering **03**, 26 (2015).
[11] J. K. Sahu, B. Ravi Kumar, S. K. Das, N. Paulose, and S. L. Mannan, Materials Science and Engineering: A **622**, 131 (2015).
[12] B. S. Lutz, J. M. Alvarado-Orozco, L. Garcia-Fresnillo, and G. H. Meier, Oxidation of Metals **88**, 599 (2017).
[13] H. Lin, W. Liang, Y. Jia, Q. Miao, R. Hu, Z. Ding, and L. Yu, Applied Surface Science **487**, 868 (2019).
[14] X. Ren and F. Wang, Surface and Coatings Technology **201**, 30 (2006).
[15] G. Sreedhar, M. M. Alam, and V. S. Raja, Surface and Coatings Technology **204**, 291 (2009).
[16] R. Jafari and E. Sadeghi, Corrosion Science **160**, 108066 (2019).
[17] L. K. Wu, J. J. Wu, W. Y. Wu, H. J. Yan, M. Y. Jiang, and F. H. Cao, Corrosion Science **174**, 108827 (2020).
[18] R. Li, C. Cheng, and J. Pu, Materials Today Communications **33**, 104421 (2022).
[19] M. Zhang, Y. Feng, Y. Wang, Y. Niu, L. Xin, Y. Li, J. Su, S. Zhu, and F. Wang, Acta Metallurgica Sinica (English Letters) **34**, 1434 (2021).
[20] G. Biava, I. B. de Araujo Fernandes Siqueira, R. F. Vaz, G. B. de Souza, H. C. M. Jambo, A. Szogyenyi, and A. G. Pukasiewicz, Surface and Coatings Technology **438**, 128398 (2022).
[21] R. S. Bangari, S. Sahu, and P. C. Yadav, Journal of Materials Research **33**, 1023 (2018).
[22] Y. Qiao, X. Guo, and X. Li, Corrosion Science **91**, 75 (2015).
[23] J. He, X. Guo, Y. Qiao, and F. Luo, Corrosion Science **177**, 108948 (2020).
[24] H. Yu, Q. Fan, J. Li, D. Ma, J. Gong, and C. Sun, Corrosion Science **212**, 110937 (2023).
[25] Z. Tang, F. Wang, and W. Wu, Materials Science and Engineering A **276**, 70 (2000).
[26] H. Zhang, L. Yang, X. Zhang, Q. Wang, J. Wu, Z. Liu, C. Zeng, and S. Zhu, Journal of Materials Research and Technology **23**, 245 (2023).
[27] R. C. Brown, M. R. Anderson, and C. E. Kolb, **23**, 3603 (1996).
[28] S. Bose, *High Temperature Coatings*, 1st ed. (Elsevier, 2007) p. 299.
[29] E. Yazhenskikh, T. Jantzen, D. Kobertz, K. Hack, and M. Müller, Calphad: Computer Coupling of Phase Diagrams and Thermochemistry **72** (2021), 10.1016/j.calphad.2020.102234.
[30] Z. Rizhang, G. Manjiou, and Z. Yu, Oxidation of Metals **27**, 253 (1987).
[31] R. A. Rapp, Corrosion Science **44**, 209 (2002).
[32] S. Mrowec, Oxidation of Metals **44**, 177 (1995).
[33] S. Gialanella and A. Malandruccolo, *Book* (2020) pp. 480–492.
[34] H. H. Strehblow and P. Marcus, Corrosion Mechanisms in Theory and Practice: Third Edition , 1 (2011).
[35] A. S. Khanna, *Handbook of Environmental Degradation of Materials: Second Edition*, 2nd ed. (Elsevier Inc., 2012) pp. 127–194.
[36] W. Gao and Z. Li, *Developments in high-temperature corrosion and protection of materials*, April (2008).
[37] M. Fukumoto, T. Suzuki, M. Sano, M. Hirade, and M. Kara, Materials Transactions **45**, 2994 (2004).
[38] A. S. Khanna, Handbook of Environmental Degradation of Materials: Second Edition , 127 (2012).
[39] J. C. Zhao, V. Ravikumar, and A. M. Beltran, Metallurgical and Materials Transactions A: Physical Metallurgy and Materials Science **32**, 1271 (2001).
[40] O. E. Hudak, A. Scheiber, P. Kutrowatz, T. Wojcik, L. Shang, O. Hunold, S. Kolozsvári, P. Polcik, and H. Riedl, Corrosion Science **224** (2023), 10.1016/j.corsci.2023.111565.
[41] International Center of Diffraction Data, "Powder diffraction file 04-001-3422," Tech. Rep. (2011).
[42] International Center of Diffraction Data, "Powder diffractoin file 01-080-6097," Tech. Rep. (2013).
[43] International Center of Diffraction Data, "Powder diffraction file 04-018-6856," Tech. Rep. (2022).
[44] International Center of Diffraction Data, "Powder diffraction file 04-015-2554," Tech. Rep. (2011).
[45] International Center of Diffraction Data, "Powder diffraction file 01-086-4330," Tech. Rep. (2020).
[46] International Center of Diffraction Data, "Powder diffraction file 01-071-1169," Tech. Rep. (2020).
[47] International Center of Diffraction Data, "Powder diffraction file 04-015-8610," Tech. Rep.
[48] International Center of Diffraction Data, "Powder fiffraction file 00-046-1200," Tech. Rep. (1996).
[49] International Center of Diffraction Data, "Powder diffraction file 04-004-8138," Tech. Rep. (2020).
[50] International Center of Diffraction Data, "Powder diffraction file 04-011-9497," Tech. Rep. (2011).
[51] International Center of Diffraction Data, "Powder diffraction file 04-014-3038," Tech. Rep. (2011).
[52] International Center of Diffraction Data, "Powder diffraction file 00-027-0631," Tech. Rep. (1972).
[53] International Center of Diffraction Data, "Powder diffraction file 04-012-5048," Tech. Rep. (2011).
[54] International Center of Diffraction Data, "Powder diffraction file 00-029-1240," Tech. Rep. (1978).

[55] N. Sheng, K. Horke, A. Meyer, M. R. Gotterbarm, R. Rettig, and R. F. Singer, Corrosion Science **128**, 186 (2017).

[56] D. Fleig, K. Andersson, F. Normann, and F. Johnsson, Industrial and Engineering Chemistry Research **50**, 8505 (2011).

[57] L. P. Belo, L. K. Elliott, R. J. Stanger, R. Spörl, K. V. Shah, J. Maier, and T. F. Wall, Energy and Fuels **28**, 7243 (2014).

[58] Y. Sarbassov, L. Duan, V. Manovic, and E. J. Anthony, Greenhouse Gases: Science and Technology **8**, 402 (2018).

[59] J. P. Dunn, P. R. Koppula, H. G. Stenger, and I. E. Wachs, Applied Catalysis B: Environmental **19**, 103 (1998).

[60] J. hua HE, X. ping GUO, and Y. qiang QIAO, Transactions of Nonferrous Metals Society of China (English Edition) **31**, 207 (2021).

[61] Z. Lin, M. Li, J. Wang, and Y. Zhou, Journal of the American Ceramic Society **90**, 3930 (2007).

[62] G. C. Fryburg, F. J. Kohl, C. A. Stearns, and W. L. Fielder, Journal of The Electrochemical Society **129**, 571 (1982).

[63] J. Stringer, Materials Science and Technology **3**, 482 (1986).

[64] P. Panjan, B. Navinšek, M. Čekada, and A. Zalar, Vacuum **53**, 127 (1999).

[65] G. Greczynski, L. Hultman, and M. Odén, Surface and Coatings Technology **374**, 923 (2019).